PhD Dissertation

Design and Analysis of 5G/IoT Antennas for sub-6 GHz Applications using Characteristic Modes Analysis

Universitat Politècnica de València

Departamento de Comunicaciones

Author

Jaime Molins Benlliure

Advisors

Prof. Dr. Eva Antonino Daviu
Dr. Marta Cabedo Fabrés

València, September, 2024

"It's the one thing you can control.
You are responsible for how people remember you."
— Kobe Bryant

Agradecimientos

Es curioso mirar hacia atrás y recordar todo el camino que me ha llevado hasta aquí. Siendo franco, nunca pensé que podría llegar a convertirme en doctor, de hecho, aun me produce tanto vértigo como ilusión. Creo que los finales son más felices si los inicios son accidentados, y en mi caso, mi inmadurez y falta de hábito de estudio convirtieron mis primeros años como estudiante en un auténtico tormento. Por suerte, aprendí que el trabajo y la disciplina alcanzan al talento y que más importante que una meta es el camino y los compañeros que te encuentras. Esta tesis, aunque lleve mi nombre, debería incluir el de muchas personas que la han hecho posible.

A Alba, mi mayor apoyo, mi confidente, mi todo. Por cuidarme, preocuparte y confiar en mi más de lo que yo mismo lo hago. Por siempre encontrar las palabras justas para disolver mis dudas y tranquilizarme. Por nunca cortarme las alas en ninguno de mis objetivos por más locos que parezcan y acompañarme hasta el final. Mi mejor versión como persona ha llegado de tu mano.

A mi madre, por los valores que me ha inculcado, por siempre pedirme más y por transmitirme ese carácter perseverante y de nunca rendirme. Por las incalculables horas que has invertido en mi educación y en la de Ana. Por tantas veces que te tocó sacarme de la cama y por hacerme entender que el sacrificio y la disciplina es el único camino. Por eso y mil cosas más, eres los cimientos de esta tesis y sobre todo, y más importante, de la persona que soy.

A mi padre por su apoyo incondicional, por su infinita disposición para ayudarme en cualquier aspecto y por todos los valores que junto a mi madre me ha transmitido. Por siempre dejar que recorra mi propio camino sabiendo que cuento con él como salvavidas.

A Ana por siempre haber conservado ese instinto de hermana mayor de cuidarme y preocuparse por mi. Por su vitalidad y por ser un ejemplo de cómo afrontar cualquier embiste de la vida.

A toda mi familia por su cariño y apoyo. A mi abuelo Paco por ser un ejemplo de esfuerzo y sacrificio y por enseñarme tanto. Por tantos momentos viendo y hablando de nuestro Valencia CF, el Tour, las motos, la F1 o Roland Garros. Mi pasión por el deporte ha venido de tu mano. A mi abuela Maruja, por ser la persona más

bondadosa que he conocido, por tanto amor y por desvivirse por su familia. Tus valores y tu recuerdo han dejado una huella tan grande como el vacío que dejaste al marcharte.

A mis compañeros de carrera y de IEEE: Borja, Enrique, Manu, Vicent, Fito, Rubén, Juan, Acha, Alin y Redo. Por haber sido un apoyo tan grande en mis años de carrera y haber encontrado en vosotros un oasis cuando los resultados no acompañaban. Qué feliz he sido y cuantas anécdotas tengo con vosotros. Estoy seguro de que muchas más están por venir.

A Miguel Ferrando, por haber sido como un padre en el ámbito profesional. Por tu conocimiento y lecciones infinitas, por la pasión que transmites y por guiarme tan bien. Te estaré infinitamente agradecido por haber tenido fe en mí. A Eva y Marta, por haberme acogido desde el primer momento y por guiarme como doctorando. Por haberme dado la oportunidad de descubrir algo que me apasiona y por vuestro apoyo.

A Dani, por su paciencia infinita, por sus incontables enseñanzas y sobre todo por ser tan buen compañero. Tu ejemplo de profesionalidad y compañerismo lo intentaré aplicar allá donde esté. A Ferdaous por haber sido un apoyo incondicional durante todo este proceso. Por tu vitalidad, tu valentía, tu generosidad y por tu bendita montaña rusa de emociones. Qué suerte he tenido de compartir viaje de doctorado contigo. A Miguel Ferrando Rocher, por siempre ser un referente y un espejo donde mirarme. Por sus consejos y por su apoyo en el proceso de publicación y revisión de artículos. Si Miguel Ferrando ha sido mi padre profesional, Miguel hijo ha sido mi hermano mayor. A Damián y Adrián por traer tanta alegría al laboratorio cuando más apagado estaba. Por ser más amigos que compañeros. Me quedo con grandes recuerdos como nuestros almuerzos en el Ximo y como vuestra visita en Dublín.

Por gente maravillosa que he podido conocer en el APL. A José Ignacio por su sabiduría y sus consejos. A María por sus aventuras y su sonrisa eterna. A Felipe, y nuestra maravillosa odisea en Singapur. A Bernat, por darle vida a nuestras creaciones y por su trato tan cercano. A Marc, Daniel, Carlos, Toni, M.Ángel, Alejandro, Zakaria, Kaouding, Hakim, Yousra, Laura y Álvaro. Por úlitmo me gustaría agradecer a la empresa Taoglas, en especial a Ben y Jinsong su apoyo en mi transición al sector privado.

Todos habéis sido participes de esta historia, mi historia, que por dura que haya sido por momentos, siempre la recordaré con mucho cariño y sobre todo, por haber sido tan feliz. Gracias.

Abstract

The current wireless communication scenario is defined by the progressive deployment of the 5th generation (5G) wireless communication system, which has established high standards in data rate, reliability, efficiency, number of connections, and latency. The early deployment of the 5G has taken place in the so-called sub-6 GHz bands due to its compatibility with the previously deployed infrastructure. One of the novelties of the 5G is the subdivision into small cell coverage areas, which will require the installation of indoor access points requiring multiple port antennas with high efficiency compatible with the Multiple-Input Multiple-Output (MIMO) technology. As a result, the need for this kind of antenna has increased. The design of these antennas becomes complex and time-demanding when the number of ports is increased. This thesis deals with the design and analysis of multiple-fed cavity-backed solutions with the novelty of introducing new characteristic modes analysis (CMA) based methodologies for the systematic design of this kind of solution, which simplifies the design and calculation process. In addition, all the solutions are analyzed regarding the channel perspective for their evaluation in a real MIMO system environment.

Another challenge that brings the 5G system is the exponential growth in the demand for the integration of small antennas in size-limited devices introduced by the all-connected concept and the development of new applications for the Internet of Things (IoT). In particular, the 433 MHz, 868/915 MHz, and 2.4 GHz ISM bands are mainly used for these applications. Miniaturization techniques become imperative in such a limited space, considering that the device can be even 10-20 times smaller than the wavelength of the operating band. Antenna manufacturers have introduced ceramic chip antennas installed in printed circuit boards (PCBs) as the solution for this scenario. They are provided with generic installation guidelines without further physical insight. In this thesis, low-temperature co-fired ceramic (LTCC) chip antennas have been designed and fabricated in-house to provide more information about their radiation performance and optimum allocation to excite the desired modes on the installed PCB. A novel CMA parameter based on the correlation between total and modal fields is introduced to provide physical insight into this topic.

Resumen

El escenario actual de las comunicaciones inalámbricas está definido
por el progresivo despliegue del 5G que ha establecido altos estándares
en tasas binarias, fiabilidad, eficiencia, número de conexiones y la-
tencia. El despliegue inicial del 5G se ha producido en las ban-
das denominadas sub-6 GHz debido a su compatibilidad con la in-
fraestructura ya desplegada. Una de las novedades del 5G es la sub-
división en pequeñas celdas que requerirá la instalación de puntos de
acceso interiores mediante antenas de múltiples puertos, altamente
eficientes y compatibles con la tecnología MIMO. Como consecuen-
cia, la necesidad de este tipo de antenas ha experimentado un crec-
imiento en su demanda. El diseño de este tipo de antenas resulta
complejo y requiere de muchos recursos computacionales cuando el
número de puertos es elevado. Esta tesis aborda el diseño y análisis
de antenas respaldadas por cavidades con alimentación múltiple con
la novedad de introducir nuevas metodologías basadas en el análisis
de modos característicos (CMA) para el diseño sistemático de este
tipo de soluciones para simplificar el proceso de diseño y simulación.
Además, todas las soluciones se analizan desde la perspectiva de
canal para su evaluación en un entorno real de un sistema con tec-
nología MIMO.

Otro desafío que ha supuesto el sistema 5G es el crecimiento ex-
ponencial en la demanda de pequeñas antenas para su integración
en dispositivos de tamaño reducido debido al desarrollo de nuevas
aplicaciones para el Internet de las Cosas (IoT). En particular, las
bandas ISM de 433 MHz, 868/915 MHz y 2.4 GHz son las que
más atención han recibido para albergar estas aplicaciones. Las
técnicas de miniaturización se vuelven imprescindibles cuando el
espacio es tan limitado y considerando que el dispositivo puede ser
incluso entre 10 y 20 veces más pequeño que la longitud de onda
de la frecuencia de la banda utilizada. Los fabricantes de antenas
han introducido antenas cerámicas conocidas como chip antenas
que se instalan en placas de circuito impreso (PCB) como solución
a esta problemática. Junto con las antenas chip, se proporcionan
unas pautas de instalación genéricas en las que falta información
del funcionamiento físico de la antena. En esta tesis, varias antenas
tipo chip se han diseñado y fabricado con tecnología LTCC para
proporcionar más información sobre sus propiedades de radiación y

su localización óptima para excitar los modos deseados de la PCB donde se instalan. Un nuevo parámetro basado en CMA se ha propuesto mediante la correlación entre los campos totales y modales para proporcionar información física sobre esta temática.

Resum

L'escenari actual de les comunicacions sense fils està definit pel progressiu desplegament del 5G que ha establit alts estàndards en taxes binàries, fiabilitat, eficiència, nombre de connexions i latència. El desplegament inicial del 5G s'ha produït en les bandes denominades sub-6 GHz a causa de la seua compatibilitat amb la infraestructura ja desplegada. Una de les novetats del 5G és la subdivisió en xicotetes cèl·lules que requerirà la instal·lació de punts d'accés interiors que requeriran antenes de múltiples ports altament eficients compatibles amb la tecnologia MIMO. Com a consequencia, la necessitat d'este tipus d'antenes ha experimentat un creixement en la seua demanda. El disseny d'estes antenes es torna complex i requerix molts recursos computacionals quan s'augmenta el nombre de ports. Esta tesi aborda el disseny i anàlisi de solucions recolzades per cavitats amb alimentació múltiple amb la novetat d'introduir noves metodologies basades en l'anàlisi de modes característics (CMA) per simplificar el procés de disseny i simulació de estes antenes. A més, totes les solucions s'analitzen des de la perspectiva de canal per a la seua avaluació en un entorn real de sistema MIMO.

Un altre desafiament que ha suposat el sistema 5G és el creixement exponencial en la demanda d'integració de xicotetes antenes en dispositius de tamany reduït i el desenvolupament de noves aplicacions per a la Internet de les Coses (IoT). En particular, les bandes ISM que operen a 433 MHz, 868/915 MHz i 2.4 GHz són les mes demandades per a estes aplicacions. Les tècniques de miniaturització es tornen imprescindibles quan l'espai és tan limitat i considerant que el dispositiu pot ser fins i tot entre 10 i 20 vegades més xicotet que la longitud d'ona de la banda de freqüència utilitzada. Els fabricants d'antenes han introduït antenes tipus xip ceràmiques instal·lades en plaques de circuit imprés (PCB) com a solució a esta problematica. Juntament amb les antenes xip, es proporcionen unes pautes d'instal·lació genèriques sense cap justificació física adicional. En esta tesi, diverses antenes tipus xip s'han dissenyat i fabricat internament amb tecnologia LTCC per a proporcionar més informació sobre les seues propietats de radiació i la seua localització òptima per a excitar els modes desitjats de la PCB on s'instal·len. Un nou

paràmetre basat en CMA s'ha proposat mitjançant la correlació entre els camps totals i modals per a proporcionar informació física sobre esta temàtica.

Table of contents

Chapter 1

Introduction

In the last decade, wireless communications have experienced exponential growth in mobile data traffic and the number of connected devices. This enormous data demand has challenged the features of previous standards and fuelled the upgrade to a new wireless communications system.

The fifth generation (5G) communication system [1, 2] blooms as the solution to fulfill the new requirements in terms of data rate, number of simultaneous connections, latency, efficiency, and reliability regardless of the location of the connected devices:

- Peak data rates of 20 Gbit/s (Downlink) and 10 Gbit/s (Uplink)

- Maximum latency ranging from 8 to 12 ms

- Peak spectral efficiencies of 30 bit/s/Hz (Downlink) and 15 bit/s/Hz (Uplink)

- Support for on-board users at high-speed traveling (300-500km/h)

- Up to 100x number of connected users per unit area (compared with 4G LTE)

- 100% coverage and reduction in network energy usage

The need to meet the high requirements of the new standard has also increased the demand for new solutions for the antenna field as part of the system. The spectrum of the 5G system has an extensive dynamic range and has been divided into two frequency ranges, the FR1 and the FR2. The FR1 comprehends the so-called sub-6GHz bands ranging from 0.6 GHz to 7.1 GHz. On the other hand, the FR2 is composed of millimeter wave frequency bands, which

	FR1					FR2		
	<1 GHz		3 GHz	4 GHz	5 GHz	24-30 GHz	37-50 GHz	64-71 GHz
🇺🇸	600 MHz	2.5/2.6 GHz (B41/n41)	3.1-3.45 GHz 3.45-3.55 GHz 3.55-3.7 GHz 3.7-4.2 GHz		5.9-7.1 GHz	24.25-24.45 GHz 24.75-25.25 GHz 27.5-28.35 GHz	37-37.6 GHz 37.6-40 GHz 47.2-48.2 GHz	57.2-64 GHz 64-71 GHz
🇪🇺	700 MHz		3.4-3.8 GHz		5.9-6.4 GHz	24.5-27.5 GHz		
🇬🇧	700 MHz		3.4-3.8 GHz			26 GHz		
🇩🇪	700 MHz		3.4-3.8 GHz			26 GHz		
🇫🇷	700 MHz		3.46-3.8 GHz			26 GHz		
🇮🇹	700 MHz		3.6-3.8 GHz			26.5-27.5 GHz		
🇨🇳	700 MHz	2.5/2.6 GHz (B41/n41)	3.3-3.6 GHz	4.8-5 GHz		24.75-27.5 GHz	40-43.5 GHz	
🇯🇵			3.6-4.1 GHz	4.5-4.9 GHz		26.6-27 GHz 27-29.5 GHz	39-43.5 GHz	
🇮🇳	700 MHz		3.3-3.6 GHz			24.25-27.5 GHz 27.5-29.5 GHz	37-43.5 GHz	
🇦🇺			3.4-3.7 GHz			24.25-27.5 GHz	39 GHz	

Figure 1.1: 5G bands including FR1 and FR2 for different worldwide locations.

range from 24 GHz to above 95 GHz [3–6]. Providing services in such high-frequency bands poses additional challenges still under investigation. Different sub-6 GHz bands have been licensed depending on the location and legislation. In Fig. 1.1, most bands, including FR1 and FR2, are detailed for different worldwide locations.

Indoor Access Points

The early deployment of the 5G system has taken place at the FR1 bands [7] due to the already deployed infrastructure (4G), which works at frequencies below 6 GHz. Hence, the integration of the 5G network is much simpler. On the other hand, new bands and technologies have been established to support new applications [8, 9], and many upgrades must be applied to the infrastructure. One of the novelties of the latest communication system is simplifying coverage cells into multiple smaller-sized cells to provide higher-quality service.

The cell distribution proposed by 5G will be made more efficient to ensure 5G performance in areas with a high density of users. One of the features incorporated in the new system is the small cell concept [10–12]. This scalable solution allows for replacing one cell with a high load with multiple small cells. These cells will require low-power, low-cost, local range base stations, providing coverage in open and indoor areas with poor signal levels caused by penetration losses. These will benefit from this new base station arrangement as they will guarantee coverage in such conditions. This new feature will allow the substitution of complex base stations by multiple access points spread over

Figure 1.2: a) Picture of a compact wideband dual-polarized magnetoelectric dipole antenna [13] and, b) Dual-polarized wideband omnidirectional ceiling antenna with low gain variations (GVs) [14].

the same coverage area. They will be simple to install, allowing for rapid restructuring if conditions change.

This scenario has triggered the design of multiple solutions using wideband or multi-resonant antennas to provide numerous independent ports for Multiple-Input Multiple-Output (MIMO) technology, high radiation efficiency, and connection to the 5G sub-6GHz bands and, if possible, to the previous 2G/3G/4G bands, which are still in use.

Most solutions are based on dual-polarized antennas [13–20] due to their orthogonal and highly isolated ports. A recent wideband solution proposes a compact wideband dual-polarized magnetoelectric dipole antenna [13] (see Fig. 1.2(a)) that can cover 5G NR n77/78/79 bands ranging from 3.06 GHz to 5.28 GHz and an isolation between ports higher than 22 dB. An alternative solution is proposed in [19] with a dual-polarized bandwidth-enhanced dipole antenna with filtering capabilities by using parasitic elements presenting 76% impedance bandwidth (2.49-5.59 GHz) and isolation of minimum 22 dB. Solutions with dielectric resonator antennas (DRA) have also been investigated [16,21] like in [16] where a compact wideband dual-polarized DRA is composed of a monolithic cross-shaped dielectric block covering from 3.25 GHz to 3.85 GHz including the n78 band. Furthermore, a dual-polarized wideband omnidirectional ceiling antenna with low gain variations (GVs) is presented in [14] for 2G/3G/4G/5G sub-6 GHz indoor applications with a vertical-polarized antenna element arranged in the center with semicircular plates and a top-loaded disk and the horizontal-polarized element is obtained with four printed dipoles
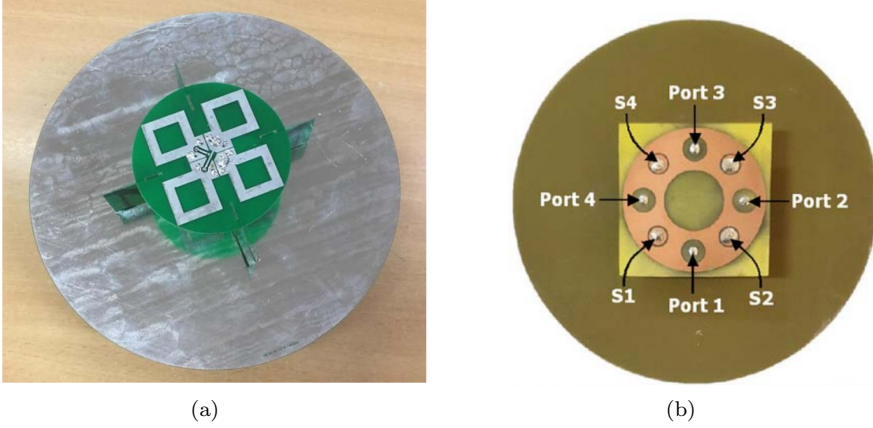
Figure 1.3: a) Picture of a tripolarized antenna composed of two crossed-stepped dipoles and a monopole-equivalent structure [23] and, b) Picture of a 4-port single-patch based on a quasi $TM_{1/2,1/2}$ [25].

with truncated corners (See Fig. 1.2(b)). Results show an impedance bandwidth ranging from 1.66 GHz to 3.65 GHz with an isolation higher than 40 dB. Lastly, an alternative solution using an AMC reflector [22] operating at n78/n79 bands has also been proposed.

Dual-polarized antennas are a great solution with high port isolation but are limited to two independent ports. Different solutions with alternative antenna arrangements are proposed to increase the number of ports. A tripolarized antenna composed of two crossed-stepped dipoles and a monopole-equivalent structure (see Fig. 1.3(a)) is proposed in [23] operating at n77/n78 bands showing 30 dB isolation and 85% of efficiency. Another 3-port solution is presented in [24] with an equilateral triangular patch antenna ranging from 3.3 GHz to 4.2 GHz with 82% efficiency and 15 dB of minimum isolation.

Regarding 4-port solutions, an antenna is proposed in [25] with a single-patch (see Fig. 1.3(b)) based on a quasi $TM_{1/2,1/2}$ mode ranging at 3.3-4.5 GHz band (15 dB isolation and 80% total efficiency). A similar solution with an annular-ring patch is presented in [26] with an impedance bandwidth ranging at 3.3-5 GHz (16.5 dB isolation and 84% total efficiency). Lastly, a solution with six ports is proposed in [27] with a circular patch antenna with six feeds ranging from 3.1 GHz to 7.2 GHz with 20 dB of minimum isolation and 85% efficiency.

Increasing the number of ports has led to complex designs with time— and memory-consuming simulations. In this thesis, different methodologies and strategies based on CMA will be presented to ease the design process

of multiple-port broadband antennas, providing physical insight throughout. Their performance will be tested in different environments, ensuring their performance on a MIMO system.

Small Antennas for IoT Devices

Another challenge that brings the installation of the new wireless system (5G) is managing the exponential growth of connections sparked by the apparition of new applications for the Internet of Things (IoT) and the need to install small antennas even in quotidian size-limited devices (See Fig.1.4(a)). These reduced-size antennas are widely known as small antennas (ESAs) and, by definition, satisfy $ka < 1$ (where k is the wavenumber and a is the smallest radius of a sphere containing the antenna). Miniaturization techniques allow antennas to be installed in these restricted scenarios, but in general, reducing the size of an antenna leads to a reduction in bandwidth and efficiency, compromising its radiation properties. Thus, the design and integration of ESAs have received much attention in the last years.

| (a) | (b) |

Figure 1.4:   a) IoT size-limited devices b) Chip antennas from Taoglas.

Industrial, scientific, and medical (ISM) radio bands are reserved for industrial, scientific, and medical purposes. In particular, the 433 MHz, 868 MHz (Europe), 915 MHz (USA), and the 2.4 GHz are mainly used for IoT applications [28]. With the installation of the 5G system and its "all connected" philosophy, specific 5G IoT bands have been established, operating at 600 MHz in the U.S. and at 700 MHz in Europe. The proximity of the two bands (ISM and IoT 5G) and the overlap of their applications has initiated an increasing demand for antennas operating at these frequencies.

Miniaturization plays an essential role in the integration of antennas in size-limited devices. The length of a resonant antenna is limited by the length $\lambda/4$ corresponding to a resonant monopole. For the 600 MHz band, the wavelength is λ=500 mm, and a resonant monopole at that frequency has a length of $\lambda/4$= 125 mm. Integrating an antenna with a 125 mm length in such a scenario is challenging, especially considering that the devices manufacturer leaves a limited area for the antenna to be installed. Most of the classic solutions are based on PCB-based antennas with the use of inverted L-shaped (ILA) [29,30] and inverted F-shaped (IFA) [31,32] antennas but in some cases, further miniaturization techniques [33] must be used.

In recent years, multiple companies have designed miniaturized antennas, also known as chip antennas, embedded in a high electric permittivity substrate, obtaining a low-frequency antenna with compact size (See Fig.1.4(b)). These antennas are installed on printed circuit boards (PCBs), and manufacturers provide instructions for proper installation. Due to fundamental limits, the radiation properties of chip antennas are limited [34, 35]. Therefore, the main contribution is produced by the ground plane [36] connected to the antenna. There is a growing interest in this topic, including different factors, such as the size and shape of the PCB where the antenna is placed, the location of the antenna, and possible cancellations due to interaction with the surrounding elements. This thesis will provide multiple studies based on characteristic modes analysis to give physical insight into this topic.

Characteristic Modes Analysis

Characteristic Modes Analysis (CMA) has been applied throughout the thesis thanks to the physical insight that provides the study of the natural resonances of the analyzed structure. It simplifies the design process and gives the reader a visual insight to properly understand the radiation mechanism of any antenna through its operating band. After this brief introduction, in Chapter 2, the theory of characteristic modes (TCM) will be further explained.

The theory of characteristic modes was initially formulated by Garbacz in [37] and refined by Harrington and Mautz [38, 39] in the seventies. It was initially used in antenna geometry synthesis and scattering before it became a niche topic and has not received enough attention from the antenna community. This situation turned in 2007 (see Fig. 1.5) when the antennas and propagation lab (APL) from the Universitat Politècnica de València published an article [40] introducing the theory of characteristic modes to simplify the design of antennas for hot topic applications such as the excitation of a mobile phone chassis modes.

In Fig. 1.5, the number of CMA-based published articles in the Transactions in Antennas and Propagation journal during the last 50 years is rep-
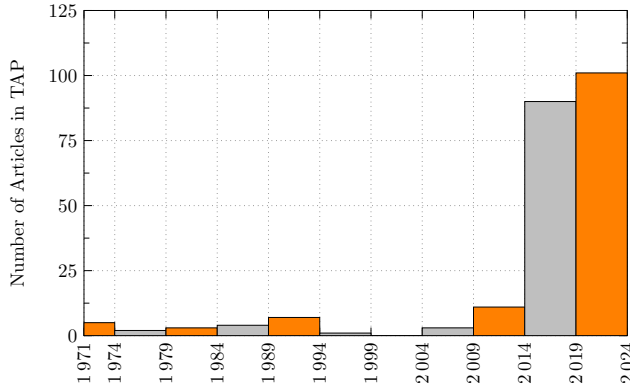
Figure 1.5: Number of articles based on characteristic modes published in IEEE Transactions on Antennas and Propagation journal since their formulation in 1971.

resented where the exponential increment in the last decade can be noticed. Demonstrating the usefulness of the characteristic modes analysis (CMA) in the design process of standard antennas and including the modal solution in electromagnetic software led to an exponential growth in published articles in the last decade. Unlike classical design methods, CMA brings physical insight into the radiating performance of an antenna and provides a systematic strategy to develop new designs with specific radiation characteristics. CMA helps to understand the analyzed antennas' operating principle and provides useful instructions for the design process.

The design and model of antennas with arbitrary geometries require electromagnetic simulation software due to the lack of analytic solutions. These antenna models need to be discretized and solved with numerical methods, which, depending on the complexity of the antenna, the frequency, and the accuracy of the results, may require fine meshing, which increases the simulation time.

The design of antennas integrated in platforms with different geometries is complex for antenna designers since multiple operating principles are combined in the same resonating structure. This situation leads to increased simulations due to the unknown of the optimum location and the kind of excitation. Characteristic modes (CM) come as a solution to provide enough information about the natural resonances of any platform and the location and type of feeding that is required to tune and excite each of those resonances. Hence, using CM simplifies the design process of any structure that requires feeding. In addi-

7

tion, it provides much information in advance about the operating principle and potential performance of the analyzed antenna.

Characteristic modes permit the decomposition of the total current on the surface of a conducting body into a set of orthogonal functions (characteristic modes). These current modes can be numerically calculated from an arbitrary conducting structure. They provide suitable information for antenna design due to the physical interpretation of the radiation performance on the surface of an antenna.

Characteristic modes are calculated without excitation (independent of any excitation) and only depend on the size and shape of the analyzed body. This independence from any kind of excitation is convenient for analyzing the currents of a conducting body at first glance to later properly choose the type and location of the excitation.

The design process of an antenna with CMA can be divided into two steps: first, the antenna's geometry is optimized to bring the modal resonance at the desired frequency, and the second step focuses on feeding optimization to excite the desired modes properly. The number of possible excited modes permits the approximation of the potential bandwidth that can be achieved. In summary, using characteristic modes guides the design of antennas with a controlled methodology that provides the user with a graphical insight into the operating principle of the antenna.

1.1 Motivation and Context

This thesis was developed in the framework of a research fellowship ("Ayuda para Contratos Predoctorales para la Formación de Doctores 2017") funded by the Spanish Science Research Agency ("Agencia Estatal de Investigación. Ministerio de Ciencia, Innovación y Universidades") and realized in the Antennas and Propagation Lab (APL) from the Universitat Politècnica de València (UPV). The associated project is Multimode Multiple-beam reconfigurable X-Wave antennas for communication and sensor systems.

Antennas and Propagation Lab (APL) has a long tradition in the design and study of antennas with the use of CMA, and they have published multiple high-impact journals, which have gathered a lot of attention. They were pioneers in using CMA to design antennas for modern applications [41], and they exposed the TCM to the antenna community, which has been a niche topic since its creation. Since then, the CMA has been widely used to design and analyze antennas. The APL has also published many journals on the design of wideband antennas with multiple feedings. That fact, and the need for this kind of solution for the 5G indoor access points, responds to the reason for focusing on

half of the thesis on designing Multiple-fed wideband 5G access point antennas with CMA.

In addition, the group is constantly exposed to national and international projects regarding the design and integration of antennas for IoT, LTE/5G, and satellite communications applications. This thesis was started following a project between Huawei Finland and the APL for the design, integration, and fabrication of antennas to be integrated into a Huawei terminal for sub-6 GHz 5G MIMO applications. This project was a convenient prologue to be exposed to the limitations of small antennas and the main issues for their integration in platforms. In addition, during the thesis, projects with private companies (Fermax and Celestica) were carried out to design antennas for their installation in size-limited devices for IoT applications. Due to these factors, half of this thesis focused on the study of small antennas using CMA, one of the main areas of expertise for the APL team.

Thanks to the experience obtained in this thesis with design, analysis, and integration of multiple chip antennas, an Antenna/RF Engineer position was obtained in Dublin for one of the top small antenna manufacturers (Taoglas).

1.2   Objectives

This thesis chases two global objectives. The first one is the use of CMA to ease the design process of wideband multiple-fed antennas for 5G MIMO applications due to their growing complexity when a higher number of ports is required, not only computationally but also to achieve proper isolation and uncorrelated radiation pattern with a reduced size design.

The second objective is to analyze the allocation of chip antennas on metallic elements with CMA to emulate their installation on a real device. Chip antennas are widely installed in size-limited devices, and manufacturers provide installation guidelines without further physical explanation. In this thesis, an explanation based on CMA will be carried out for the optimum allocation of chip antennas.

The following specific objectives have been defined:

1. Design wideband multiple-fed indoor access point antennas for 5G MIMO applications with high efficiency, high isolation, unidirectional radiation pattern, and compact.

2. Establish new design methodologies based on CMA for the previous antennas for their design and the proper port isolation.

3. Analyze the designed antennas in real environments to check their MIMO performance, calculating the channel capacity and the envelope carrier

correlation (ECC) in different scenarios modeled by different distributions (Uniform, Gaussian, Laplace).

4. Design and Fabrication in LTCC technology chip antennas on high permittivity ceramic substrates for 5G and IoT applications. The fabrication will be carried out in a clean laboratory from the UPV.

5. Analyze with CMA the modes of the PCB that are excited by the chip antennas and give physical insight into the optimum location of these antennas depending on the excited modes.

6. Define new parameters based on CMA to properly evaluate the excitation of the structure modes where the chip antenna is installed.

1.3 Methodology

The **first phase** of the thesis focused on the bibliographic review. It will be carried out more fundamentally in the documentation and state-of-the-art phase, while it will become more specific throughout the thesis. The review of scientific documentation will be done mainly through the databases indexed in the WoS (Web of Science), which specializes in antennas and microwaves, especially in the IEEE Xplore database. In support of this constant input of information, active participation in congresses related to the subject at national and international levels is foreseen. In addition, several PhD level courses at the European School of Antennas (ESoA) were attended.

The **second phase** of the thesis is based on the analysis and design of wideband antennas to be used in 5G indoor access points. In this phase, different broadband designs will be carried out, with the primary objective of obtaining multiple highly efficient independent ports with high efficiency. During the design process, CMA was used, and different methodologies for the design and the isolation of multiple-fed antennas were presented.

The **third phase** of the thesis addresses the analysis and design of small antennas and their location on metallic structures such as PCB. The third phase will focus on the research of how the radiation properties of small-size antennas are affected by the PCB's size and location on them. In addition, design strategies will be defined to minimize these effects. A new parameter based on CMA has been created to evaluate the excitation of the modes of the PCB, providing information about the optimum location of the antennas.

The **fourth phase** focused on validating the designs with their fabrication and measurement. The Antennas and Propagation Lab (APL) laboratory of the Institute of Telecommunications and Multimedia Applications (iTEAM) has provided the equipment to perform this process.

Throughout the thesis, the most relevant results will be presented to the scientific community through articles in journals and congresses related to the research topic due to their novelty in the field.

1.4   Thesis Structure

The thesis is divided as follows:

Chapter 1 provides an introduction of the topics the thesis is focused on. In addition, the main objectives, methodology, motivation, and context are also detailed.

Chapter 2 focuses on introducing the mathematical formulation of the theory of characteristic modes and enumerates the main parameters used in the CMA. These parameters are detailed using a rectangular metallic plate. Furthermore, the main applications where CMA has been lately applied are also detailed.

Chapter 3 is based on wideband monopoles with different geometries and the excitation of the modes of a square plate depending on the location of the monopole. A new parameter based on CMA is presented to correlate modal and total fields.

Chapter 4 presents a procedure for designing cavity-backed antennas. The procedure presents multiple cavity-backed antennas for 5G MIMO indoor access point applications.

Chapter 5 introduces two novel methodologies based on CMA. The first one is to increase the isolation between ports, and the second is to divide antennas into sectors with revolution symmetry to significantly minimize this kind of solution's simulation and design process. In addition, the MIMO channel using the proposed antennas is analyzed in different scattering scenarios.

Chapter 6 is based on small antennas and introduces the main miniaturization techniques used in the last decades. A deep parametric study is introduced to analyze chip antenna installation further and find the optimum configuration.

Chapter 7 details the design, analysis, and fabrication of three LTCC On-Ground chip antennas working at 868 MHz, 2.4 GHz, and 3.6 GHz. The new parameter based on CMA is used to analyze the excitation of different modes of the metallic ground planes where the chip antennas are installed.

Chapter 8 enumerates the main conclusions of the thesis.

Chapter 2

Characteristic Modes Analysis (CMA)

Characteristic modes analysis (CMA) is a powerful tool for analyzing and providing visual insight into the radiation performance of metallic structures. CMA will be applied throughout this thesis, and in this chapter, the mathematical formulation of the Theory of Characteristic Modes (TCM) is introduced. In addition, the main applications during the last decades and the state of the art will be carried out to understand the rest of the thesis appropriately.

2.1   Mathematical Formulation of the TCM

Garbacz first proposed characteristic modes [37] by diagonalizing the scattering matrix and demonstrating that the modal currents are real and the tangential modal electric field presents a constant phase over the body's surface. After this first approach, Harrington [38] presented a refined approximation with a more convenient formulation approaching the problem by diagonalizing the operator, which related the current to the tangential electric field on a body. He proposed a particular weighted eigenvalue equation to obtain the same modes introduced by Garbacz more understandably.

Consider the scenario depicted in Fig. 2.1 with an arbitrarily shaped perfect electric conductor (PEC) defined by the surface S and an incident electric field E^i. The definition of characteristic modes begins from the operator equation (2.1), which relates the current J on surface S and the tangential component of an electric incident field E^i.
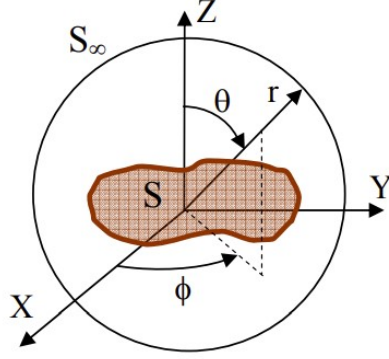
$$[L(J) - E^i]_{tan} = 0 \qquad (2.1)$$

Figure 2.1: Computation of characteristic modes scenario, and system coordinates.

where the subscript tan denotes tangential components on S. Operator L is defined as follows:

$$L(J) = jwA(J) + \nabla\Phi(J) \tag{2.2}$$

$$A(J) = \mu \oiint_S J(r')\psi(r, r')ds' \tag{2.3}$$

$$\Phi(J) = -\frac{1}{jw\varepsilon} \oiint_S \nabla' J(r')\psi(r, r')ds' \tag{2.4}$$

$$\psi(r, r') = \frac{e^{-jk|r-r'|}}{4\pi|r-r'|} \tag{2.5}$$

where r' denotes a source point, r a field point, k the wavenumber, ε the permittivity and μ the permeability on free space. $-L(J)$ can be physically interpreted as the electric intensity at any point in the space produced by the current J on S.

The operator in 2.1 can be redefined as the following notation since it has the dimensions of impedance:

$$Z(J) = [L(J)]_{tan} \tag{2.6}$$

where the Z operator is complex and defined as:

$$Z(J) = R(J) + jX(J) \tag{2.7}$$

2.1.1   Characteristic Currents and Fields

Next, we consider the approach introduced in [38] where the characteristic current modes can be obtained as the eigenfunctions of a weighted eigenvalue equation:

$$X(\vec{J_n}) = \lambda_n R(\vec{J_n}) \tag{2.8}$$

where X and R are the imaginary and real part of the impedance operator Z, λ_n the eigenvalues, and $\vec{J_n}$ the eigenfunctions (also called characteristic currents or eigencurrents), both X and R are real symmetric operators; hence, λ_n and $\vec{J_n}$ must be real and satisfy orthogonality relationships. The selection of $\vec{J_n}$ as basis functions permits the diagonal matrix representation of R, X, and Z.

According to [38], when each eigencurrent which radiates is normalized ($\langle J_n{}^*, RJ_n \rangle = 1$), they satisfy the following orthgonality relationships:

$$\langle J_m, RJ_n \rangle = \langle J_m^*, RJ_n \rangle = \delta_{mn} \tag{2.9}$$

$$\langle J_m, XJ_n \rangle = \langle J_m^*, XJ_n \rangle = \lambda_n \delta_{mn} \tag{2.10}$$

$$\langle J_m, ZJ_n \rangle = \langle J_m^*, ZJ_n \rangle = (1 + j\lambda_n)\delta_{mn} \tag{2.11}$$

where δ_{mn} is the Kronecker delta ($\delta_{mn} = 1$ if $m = n$,and $\delta_{mn} = 0$ if $m \neq n$).

The eigencurrents J_n produce electric E_n and magnetic H_n fields known as characteristic fields or eigenfields. The orthogonality relationship for the characteristic fields from the ones for characteristic currents is obtained using the complex Poynting theorem:

$$P(J_m, J_n) = \langle J_m^*, ZJ_n \rangle = \langle J_m^*, RJ_n \rangle + j\langle J_m^*, XJ_n \rangle$$
$$= \oiint_{S'} \vec{E}_n \times \vec{H}_n^* ds + jw \iiint_{\tau'} (\mu \vec{H}_m \cdot \vec{H}_n^* - \varepsilon \vec{E}_m \cdot \vec{E}_n^*) d\tau \tag{2.12}$$
$$= (1 + j\lambda_n)\delta_{mn}$$

With the assumptions of surface finite surface S and S' to be the radiation sphere S_∞, it can be demonstrated:

$$\frac{1}{\eta} \oiint_{S_\infty} \vec{E}_n \cdot \vec{E}_m^* ds = \delta_{mn} \tag{2.13}$$

Then, characteristic electric fields form an orthogonal set in the far field.

2.1.2 Characteristic Modes Computation

The computation of characteristic modes requires standard algorithms to get the eigencurrents and eigenvalues. Since their formulation, characteristic modes have been computed with different procedures, and due to computational difficulties, a few modes for only revolution symmetry shapes or wire bodies were calculated in their early stage. Harrington was a pioneer in applying his previously published numerical method called Method of Moments (MoM) [42] for the computation of characteristic modes of arbitrary shapes bodies [39].

For modes calculation, in practice, equation (2.8) can be approximated with the Galerkin formulation matrix eigenvalue equation:

$$[X]\vec{J_n} = \lambda_n[R]\vec{J_n} \tag{2.14}$$

where $[R]$ and $[X]$ are the real and imaginary components of the generalized impedance matrix defined as $[Z] = [R + jX]$. Characteristic modes are calculated with the generalized impedance matrix computed with MoM and Rao-Wilton-Glisson (RWG) edge elements.

The general formulation used to compute the generalized impedance matrix combines Maxwell Equations and boundary conditions to derive the Electric Field Integral Equation (EFIE), which provides the induced surface currents by an incident electric field on a conducting body surface S. A different formulation is sometimes preferred with The Mixed Potential Integral Equation (MPIE), a particularization of the EFIE. The EFIE relates the surface currents with the vector potential and the gradient of the scalar potential. RWG edge elements are used as basis functions to represent unknown currents on planar structures due to their convenience involving EFIE and triangular patch modeling.
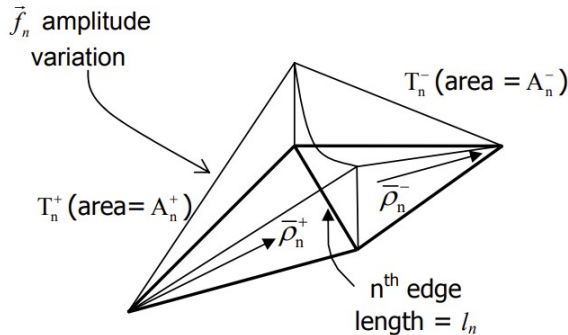

Figure 2.2: RWG basis function description.

A surface S of a conducting object can be approximated with proper triangle patch meshing. Each pair of triangles with a common edge corresponds to an RWG edge element, as seen in Fig. 2.2. Each basis function is linked to an edge and two annexed triangles labeled as T_n^+ and T_n^- and null outside the two annexed triangles. A position vector $\vec{\rho_n}^+$ is defined to designate the points in T_n^+ from the free corner or the non-contiguous corner of the edge. At the same time, the vector $\vec{\rho_n}^-$ is also defined for T_n^- but with the vector pointing towards the free corner. Labeling positive or negative triangles is determined by choosing a reference current direction for the nth edge assumed to flow from T_n^+ to T_n^-. The vector basis function associated with the nth edge is defined as follows:

$$f_n(\vec{r}) = \begin{cases} \frac{l_n}{2A_n^+}\vec{\rho_n}^+ & , \vec{r} \text{ in } T_n^+ \\ \frac{l_n}{2A_n^-}\vec{\rho_n}^- & , \vec{r} \text{ in } T_n^- \\ 0 & , \text{ outside} \end{cases}$$

where $A_n^{\pm}$ is the area of the triangle $T_n^{\pm}$ and l_n is the length of the edge.

The total current on surface S can be approximated by the sum of all the contributions from the interior edge elements

$$\vec{J_n} = \sum_{n=1}^{N} I_n \vec{f_n} \qquad (2.15)$$

where N is the number of interior edges, and I_n is the unknown coefficient, calculated with classical moment equations.

2.1.3 Modal Solutions

The orthogonal properties of characteristic modes on the body's surface permit the decomposition of the total current J on a summation of independent currents, which are the characteristic modes. Characteristic modes can then be used as a basis to expand the unknown total current J on a conducting body. The contribution of each mode to the total current J is determined by the coefficient α_n and must be computed:

$$J = \sum_n \alpha_n J_n \qquad (2.16)$$

The total current can also be expressed in a different form with the substitution of 2.17 into 2.1 and the use of the modes orthogonality properties:

$$J = \sum_n \frac{\langle J_n, E^i \rangle}{1 + j\lambda_n} J_n = \sum_n \frac{V_n^i}{1 + j\lambda_n} J_n \qquad (2.17)$$

where V_n^i is the modal excitation coefficient, which determines if a particular mode is excited depending on the type of feeding applied.

The expression detailed in 2.17 details the dependence of the total current and λ_n, the eigenvalue associated with the nth mode. The analysis of eigenvalues plays a significant role in characteristic modes analysis due to the information about the resonance frequency and the radiation behavior and performance that eigenvalues provide of their associated modes.

To properly give a physical insight into characteristic modes, a 150x100 mm^2 metallic rectangular plate (Fig. 2.3(a)) has been analyzed by calculating the first six modes. The current distribution of these modes J_n is depicted in Fig. 2.3(b), and the different current distributions of the natural resonances of a square plane can be observed.

The following section reviews the different parameters obtained from the eigenvalues to give physical insight into the radiation performance of the analyzed modes.

2.2 Physical Interpretation of Characteristic Modes

The interpretation and study of the eigenvalues are of great importance in understanding the radiation performance of the associated modes through frequency. The relation between eigenvalues and the radiation power of modes is analyzed by 2.12, where it can be deduced that the radiated power is normalized to the unit. Still, the reactive power depends on the magnitude of the eigenvalues.

It is, therefore, essential to notice that the eigenvalues provide information regarding the resonance of the associated mode and its capacitive or inductive behavior. Eigenvalues λ_n present values from $-\infty$ to ∞, and when λ_n is equal to 0, the associated mode is considered at resonance since the reactive power is also 0. It is desired to excite the modes when they are close to resonance since they radiate more efficiently. Furthermore, the sign of the eigenvalues defines if the mode contributes to storing magnetic energy ($\lambda_n > 0$ inductive behavior) or if it contributes to storing electric energy ($\lambda_n < 0$ capacitive behavior).

To better interpret the eigenvalues, the reference design of the metallic plate (Fig. 2.3(a)) analyzed in the previous section is used, and its eigenvalues are represented in Fig. 2.4. It can be observed the capacitive behavior (negative eigenvalue values) that the first resonant modes present before resonance. After resonance ($\lambda_n = 0$), all the modes become inductive with low positive eigenvalues close to 0, which can be interpreted as a potential wide bandwidth performance that a metallic ground plane can exhibit if appropriately excited. It can be observed that modes are consecutively resonating from The first mode or fundamental mode J_1 which resonates at $f_1 = 0.9$ GHz, then
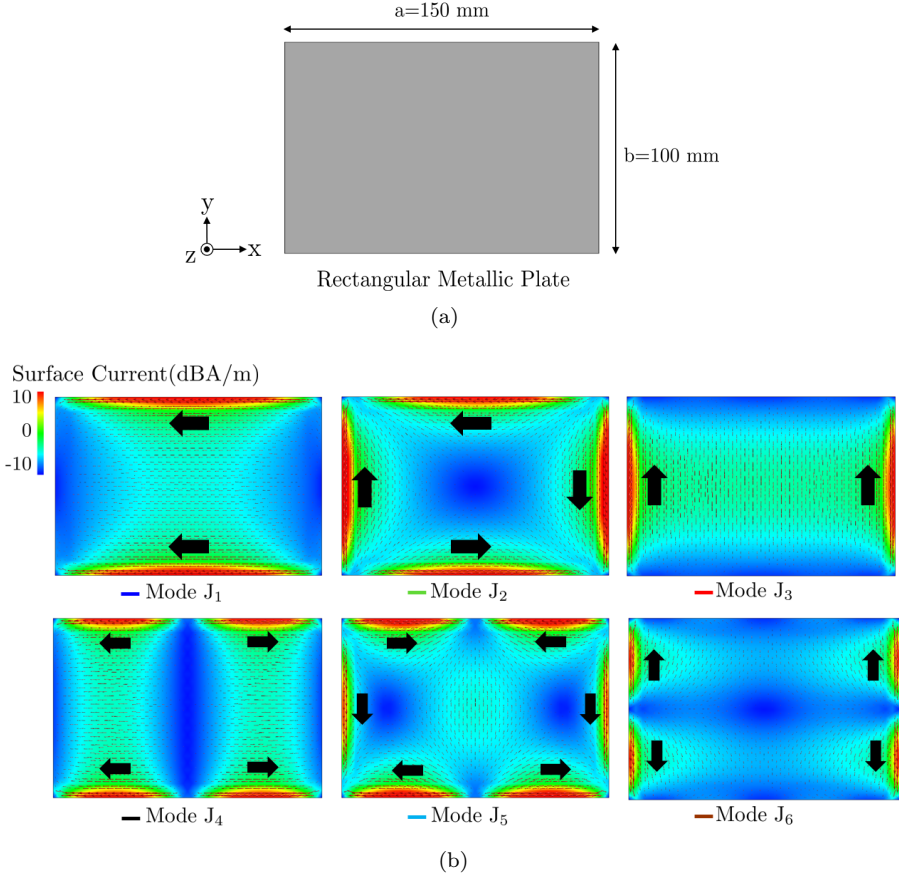
Figure 2.3: a) Analyzed 150x100 metallic square plate, and b) Current distributions of the first six characteristic modes of the rectangular plate.

mode J_2 at f_1=1.65 GHz, mode J_3 at f_3=2 GHz, J_4 at f_4=2.3 GHz, and J_5 and J_6 which resonate out the analyzed frequency range.

2.2.1 Modal Significance

Since the eigenvalues provide information regarding the resonance and behavior of the modes with the frequency, additional parameters calculated from the eigenvalues have been proposed in the literature. Formulating other parameters responds to using different figures of merit, which aids the analysis of eigenval-
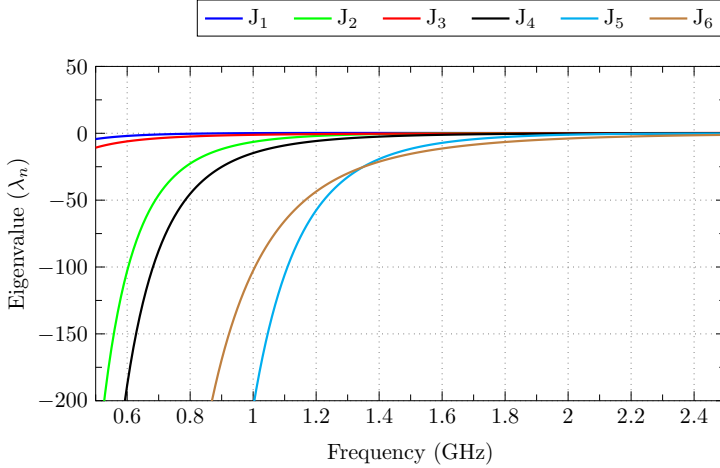
Figure 2.4: Eigenvalues of the first six modes of the 150x100 mm^2 rectangular metallic plate.

ues and provides more information. Most CMA articles offer information on eigenvalues with alternative parameters, such as modal significance.

The modal significance (MS_n) is obtained from the modal expansion of the current detailed in 2.16, which has an inverse dependence on the eigenvalues. The modal excitation coefficient and the modal current are taken away, and only the term that includes the eigenvalues is analyzed:

$$MS_n = \left| \frac{1}{1 + j\lambda_n} \right| \tag{2.18}$$

The modal significance 2.18 is a parameter that shows values from 0 to 1 and obtains a unit value when the mode is at resonance. It represents the normalized amplitude of the current modes and only depends on the shape of the analyzed structure without excitation.

Fig. 2.5 represents the modal significance of the six first resonance modes of the square metallic plate from Fig. 2.3(a). It can be observed that modes exhibit a peak value of one when they are at resonance, and the closer they are to that value with frequency, the wider the potential bandwidth of each mode will be.

A figure-of-merit regarding the radiating bandwidth of a mode BW_n can be established by analyzing the width of the modal significance at its resonance $(MS_n=1)$ and the frequencies close to it, which exhibit an MS_n higher than a specific value. The modal radiation bandwidth BW_n is the frequency range
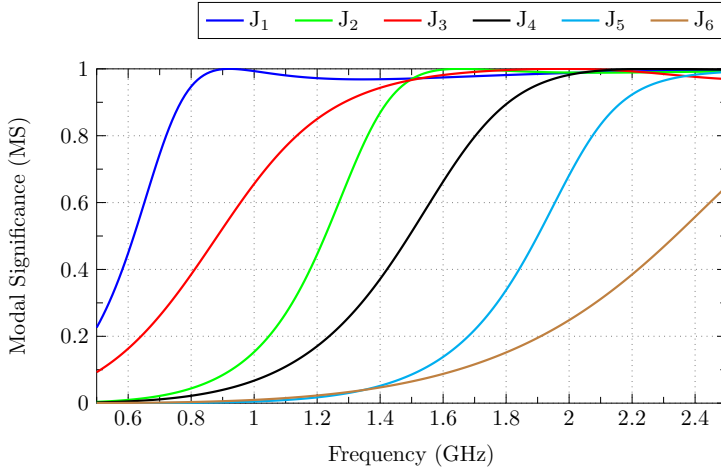
Figure 2.5: Modal Significance of the first six modes of the 150x100 mm^2 rectangular metallic plate.

where the radiated power is higher than half of the power radiated at the mode resonance.

The half power of the power radiated at the mode resonance is traduced in a reduction of $\sqrt{2}$:

$$MS_{HP_n} = \left| \frac{1}{1 + j\lambda_n} \right| = \left| \frac{1}{\sqrt{2}} \right| = 0.707 \tag{2.19}$$

With the MS_n=0.707 value, the maximum and minimum frequency of the frequency bandwidth of each mode can be found. The radiation bandwidth is calculated as follows:

$$BW_n = \frac{f_{max} - f_{min}}{f_{res}} \tag{2.20}$$

Another parameter that is also used in modal analysis and is calculated with the use of the radiation bandwidth is the modal quality factor Q$_{rad,n}$:

$$Q_{rad,n} = \frac{1}{BW_n} \tag{2.21}$$

The modal quality factor Q$_{rad,n}$ measures how narrow each mode's resonance is. The higher the quality factor, the narrower the modal bandwidth.

2.2.2 Characteristic Angle

The Characteristic angle (α_n) is another widely used parameter due to its intuitive way of interpreting the analyzed eigenvalues. It represents the phase angle between the characteristic current J_n and the associated characteristic field E_n, and it is calculated as follows:

$$\alpha_n = 180° - \tan^{-1}(\lambda_n) \tag{2.22}$$

From 2.22 it can be deduced that when the mode is at resonance (λ_n=0) the characteristic angle is α_n=180°. On the other hand, when the characteristic angle is lower than 180°, it stores magnetic electric (inductive behavior), increasing the stored energy when it approaches 90°. Alternatively, when the characteristic angle presents values higher than 180°, it stores electric energy (capacitive behavior), and that energy rises when the angle is closer to 270°.
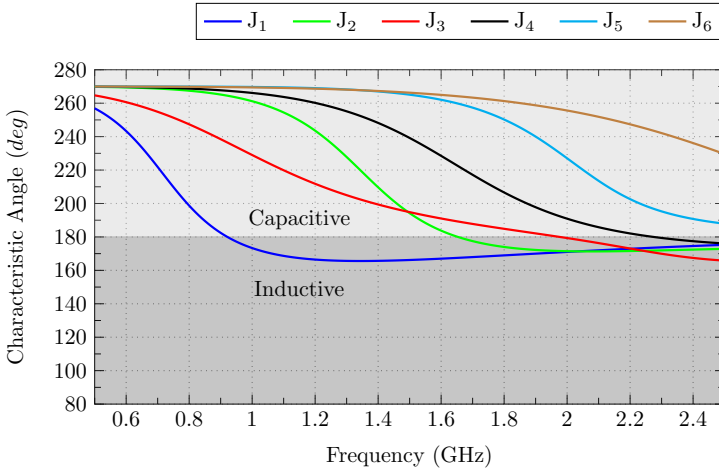

Figure 2.6: Characteristic Angle of the first six modes of the 150x100 mm^2 rectangular metallic plate.

Fig. 2.6 depicts the characteristic angle of the first six resonant modes of the analyzed rectangular metal plate. The resonance borderline (α_n=180°) can be observed, which separates the two areas where the modes present capacitive or inductive performance.

To calculate the radiating bandwidth 2.20 according to the half-radiated power from resonance (MS_n=0.707 values), the corresponding eigenvalues are λ_n=1 and λ_n=-1 which if substituted in 2.22, the obtained values are $\alpha_n = 135°$ and $\alpha_n = 225°$. The radiating bandwidth can also be computed using the frequencies obtained at each mode's $\alpha_n = 135°$ and $\alpha_n = 225°$ values.

2.3 Excitation of Characteristic Modes

In the previous section, all the parameters introduced were independent of any excitation and used to feed the analyzed structure properly. In this section, by applying any kind of feeding, we introduce parameters to determine which modes are excited and their contribution to the total radiated power.

To calculate the contribution of each mode on the input bandwidth, the input admittance Y_{in} is analyzed. For its calculation, the excitation is assumed as 1V. Hence, the input impedance becomes equal to the total current $J(P)$ (2.17) measured at the feeding point P, and it is derived as follows:

$$Y_{in} = \frac{J(P)}{1V} = \sum_n \frac{V_n^i}{1 + j\lambda_n} J_n \tag{2.23}$$

The input impedance can also be derived with the summation of modal admittances:

$$Y_{in} = \sum_n Y_n = \sum_n G_n + jB_n \tag{2.24}$$

Generally, the parameters used to evaluate the contribution to each characteristic mode's power are the modal weighting coefficient (MWC) α_n and the modal radiated power.

To further explain the concept, the metallic plate presented in 2.3(a) analyzes the excitation of the six first modes of the metallic plate. The modes of the metallic plate are depicted in Fig. 2.7(b) for the analysis. Two kinds of coupling elements excite the modes of a metallic platform due to their different nature. They are the capacitive coupling element (CCE) and the inductive coupling element (ICE).

Capacitive coupling elements (CCEs) are resonant or non-resonant elements located close to the platform to create a capacitive effect, as seen in Fig. Fig. 2.7(a). They must be located where the electric field of the characteristic mode exhibits a maximum (minimum of current) to excite the mode. CCEs are generally placed on the corner of the metallic platforms due to the number of modes that exhibit a minimum of currents. From Fig. 2.7(b), if the CCE is placed in the corner of the metallic plate, the first six modes of the metallic plate could be excited.

Inductive coupling elements (ICE) are also resonant or non-resonant elements that couple via a magnetic field (inductively). Hence, they must be placed where the characteristic mode exhibits a current maximum. They are generally based on loop elements, as seen in Fig. Fig. 2.7(a). In contrast to CCEs, ICEs are usually placed in the middle of the sides of a metallic structure, as seen in Fig. 2.7(a). Modes J_1 and J_2 would be mainly excited. Modes J_4 and J_5 may also be excited if the ICE was moved slightly to the left or right.
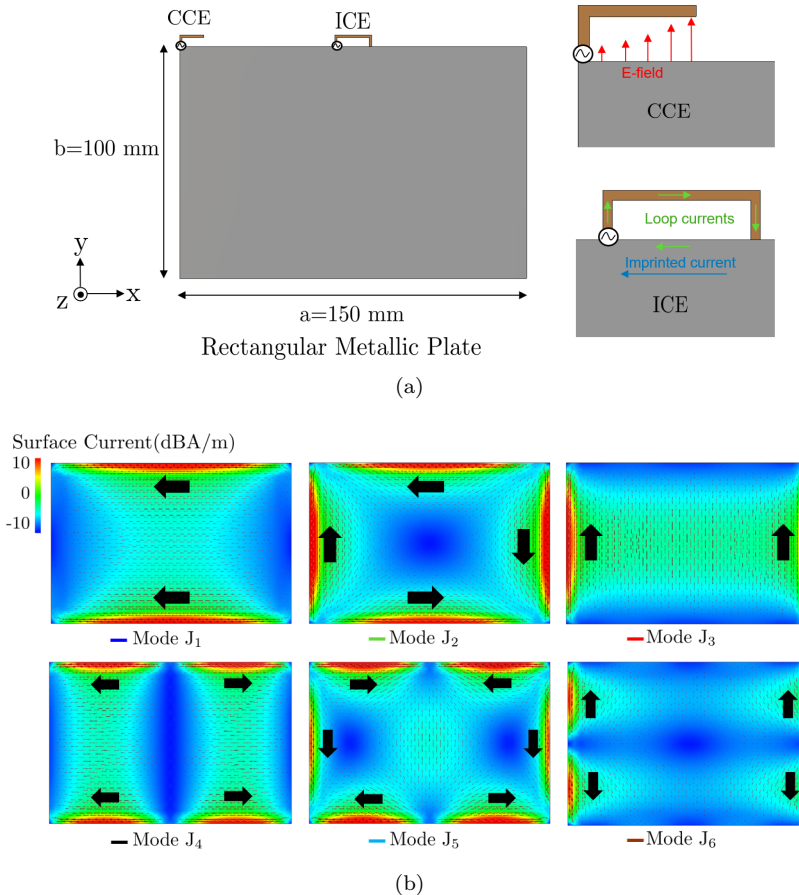
(a)

(b)

Figure 2.7: a) 150x100 metallic square plate with an ICE and a CCE and, b) Current distributions of the first six characteristic modes of the rectangular plate.

2.4 Review on the CMA Applications

Characteristic modes have been applied to many different applications in the last decades. The journal published by M.Cabedo and E.Antonino [40] was a pioneer in applying CMA for the design of state-of-the-art planar antennas such as patch-antennas, reflectarrays, planar-monopoles, and a handset platform. This publication triggered the use of CMA to excite the modes of different platforms in modern applications. They analyzed different shape structures
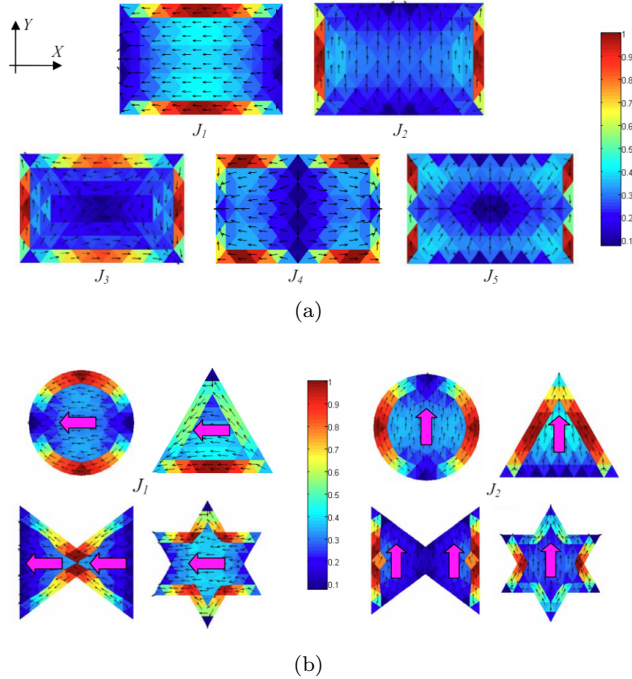
Figure 2.8: a) Current distribution of the first five modes of a rectangular plate and, b) Current distribution of Mode J_1 (horizontal) and Mode J_2 (Vertical) from a circular, triangular, bow-tie and star plates. [40]

(Fig. 2.8) and calculated the first resonant modes, showing their current distributions and detailing how to excite them. In addition, they analyzed different planar geometries such as circular, triangular, bow-tie, and star shapes, calculating and representing the first resonant modes, the horizontal/vertical (J_1/J_2) modes (Fig. 2.8(b)).

In addition, they used a triangular shape monopole (Fig. 2.9(a)) placed in parallel to a ground plane and demonstrated how to feed it in the optimum position to get circular polarization with the combination of two orthogonal and linearly polarized modes. The orthogonality properties of the CM and their current distribution analysis made the design process easy and intuitive.

Another study carried out was the bandwidth enhancement of a square monopole (Fig. 2.9(b)) with dual feeding, which permitted only the existence of the vertical mode, which showed wider bandwidth than the horizontal one. The last design proposed in [40] demonstrated the use of the chassis of a cell phone as the main radiator, analyzing a folded ground plane and exciting its
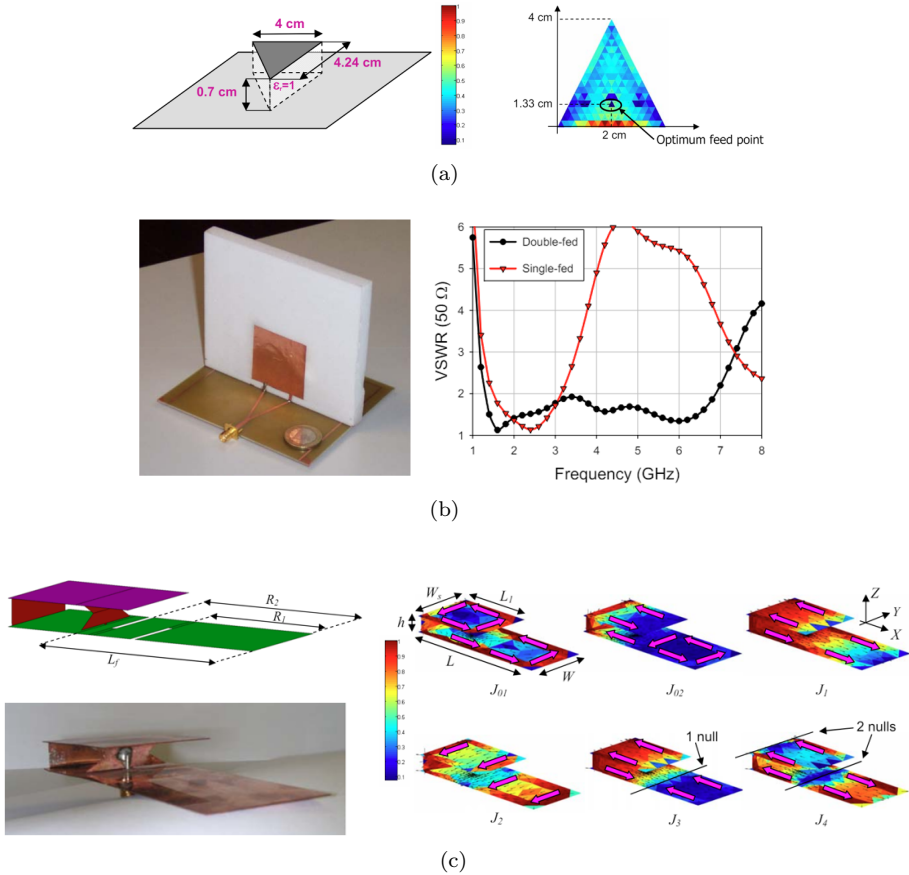
(a)

(b)

(c)

Figure 2.9: a) Current distribution of a triangular shape monopole (Fig. 2.9(a)) placed in parallel to a ground plane and, b) Picture and VSWR of a dual fed monopole and c) Picture and current distribution of the first six modes of a folded ground plane excited by a bowtie-shaped monopole. [40]

modes with the use of a bowtie-shaped monopole (Fig. 2.9(c)). This last design was the most relevant due to its high application in designing GSM antennas for integration in the first decade of the 2000s phones.

After showing the benefits of using CM in the design process of different antennas, CM has been widely used for different aspects of the model and optimization of different antennas during the last decades.

(a)

(b)
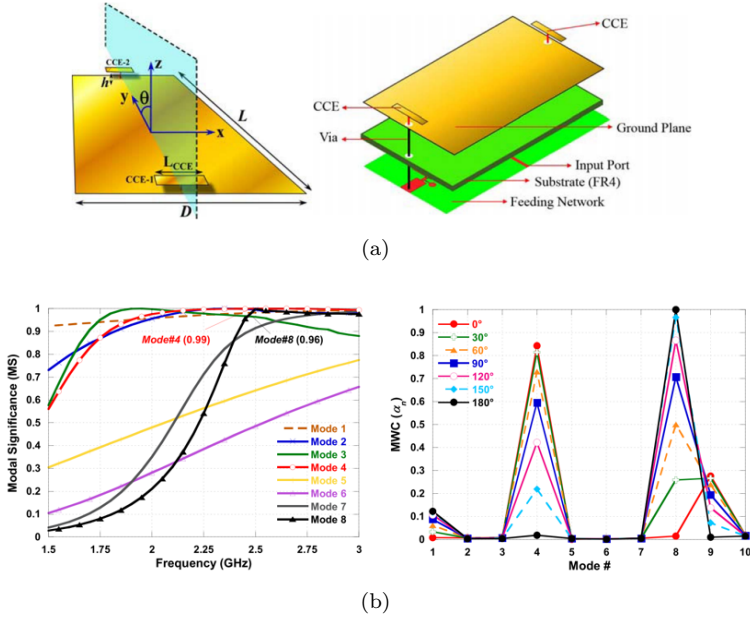
Figure 2.10: a) Null-steering antenna on a 150×75 mm^2 ground plane of a mobile terminal and, b) Modal Significance and modal weighting coefficient (MWC). In [43]

One application where CM has been applied is the optimization of radiation patterns by excitation of the modes showing the desired radiation characteristics to obtain specific radiation patterns with specific polarization.

Many authors applied CM for pattern optimization, such as F.A.Dicandia, S.Genovesi, and A.Monorchio who presented several articles [43,44] about null-steering antennas exciting different modes of a rectangular plane with capacitive exciters (CCEs) and using phase shifters to steer the beam. Two ways of exciting any structure's modes are using inductive coupling elements (ICEs) or capacitive coupling elements (CCEs). To properly excite a mode with an ICE, it must be placed at the maximum of the current mode distribution, while with a CCE, the excitation must be located on a current minimum.

In [43], a null-steering antenna on a 150×75 mm^2 ground plane of a mobile terminal is proposed with the use of two CCEs placed on both short sides of the rectangular ground plane (Fig. 2.10(a)). Using two ICEs permits to excite Mode 4 and Mode 8 (Fig. 2.10(b)). These two modes are asymmetrically excited at 2.45 GHz, including a phase difference between them, which allows
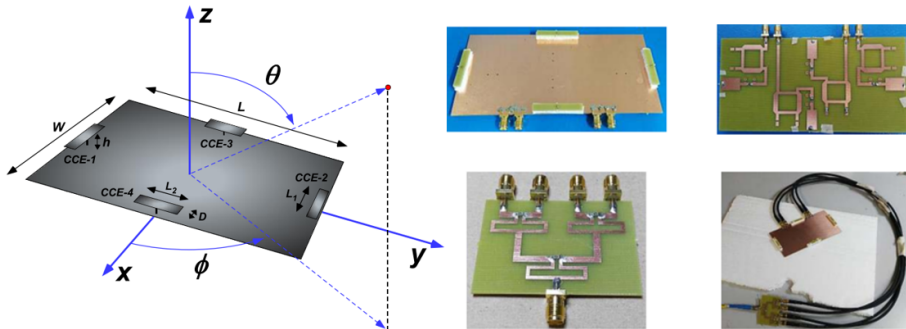
27

Figure 2.11: 3-D null-scanning antenna consisted of four CCEs placed on each side of a 150×75 mm² rectangular ground plane. [44]

steering the radiation pattern null 64° from broadside direction (θ=0°) with a null depth greater than 18 dB. In Fig. 2.10(b), the modal weighting coefficient at 2.45 GHz is represented where Mode 4 and 8 contribute to the total current. In the graph, the shift in the contribution of each mode can also be observed depending on the phase difference between the excitation of each CCE.

The same authors presented a design strategy based on CMA [44] to design 3-D null-scanning antennas to place a null in any desired direction in the upper hemisphere. The proposed antenna consists of four CCEs on each side of a 150×75 mm² rectangular ground plane, the main radiator 2.11. The article aims to demonstrate that with four excitations whose phase and amplitude can be controlled, different modes can be excited in various degrees, consequently driving the null in the desired direction. For that purpose, the authors use a reconfigurable feeding network that permits the excitation control of the preferred modes of the ground plane.

In Fig.2.12(a) left, the eigenvalues of the first ten modes and on the left are the main contributing ones to the radiation when each port is excited with the modal weighting coefficient. The modes which show the highest values are Mode 2, Mode 5, and Mode 8. Their current distribution can be observed in Fig.2.12(b). Since a CCE must be placed on a current minimum, the correlation between feeding each CCE separately and the excited modes can be observed.

Another design strategy based on CMA was presented in [45] for improving the radiation efficiency of a mounted-on-platform radiator. A novel feeding strategy called balanced inductive exciter (BIE) is introduced to improve the modal excitation purity of some characteristic modes. The approach reduces the reactive power stored in the near-field of the antenna to optimize the radiated power of the antenna. The authors stated that even when locating the exciters into the optimum position, the modal excitation purity of the employed
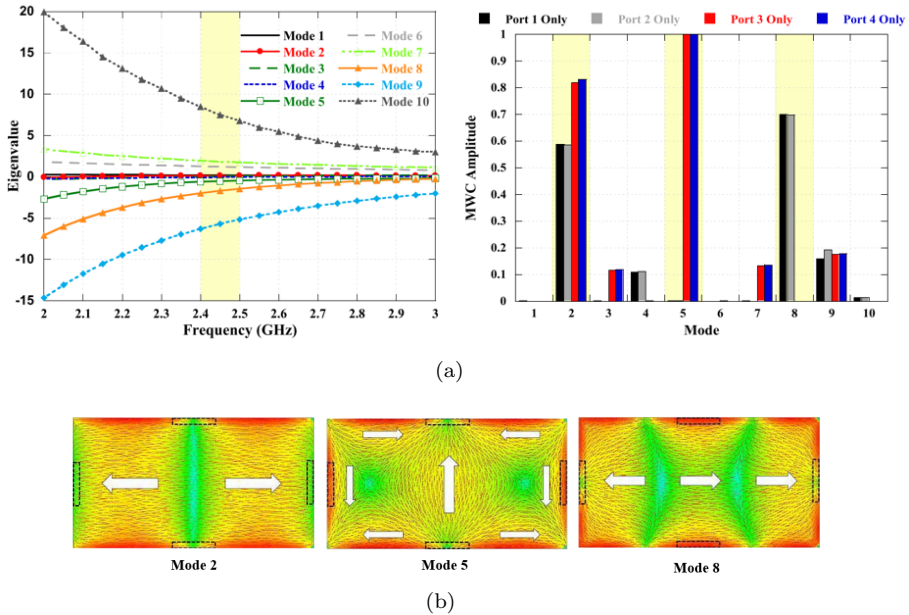
(a)

(b)

Figure 2.12: a) Eigenvalues of the first 10 modes of the antenna shown in Fig. 2.11 and b) Current distribution of Mode 2, 5 and 8.

exciters plays an essential role in the radiation efficiency of the whole radiating system. The proposed solution includes four ICEs over a $3.4{\times}2{\times}1$ m^3 box with a novel BIEs configuration (Fig. 2.13(a) right) and compare it with a classical ICE excitation (Fig. 2.13(a) left).

In Fig.2.13(b), the MWC when each port is excited individually is represented for the classic ICEs (blue) solution and the novel BIEs (red) solution. It can be a higher value for the MWC on the desired modes with the use of the BIEs; hence, the radiation efficiency of the whole system is increased.

The design of stable and omnidirectional radiation patterns has also been studied with CMA, and in [46] a wideband antenna working at 1.85-2.9 GHz consisting of a dipole and a loop antenna (Fig. 2.14(a) left) is presented with the excitation of the two first modes simultaneously taking advantage of their omnidirectional properties. Firstly, the antenna is analyzed without excitation to calculate the first characteristic modes (Fig. 2.14(a) right).

After analyzing the current distribution (Fig. 2.14(b)) and radiation patterns of the four modes, Mode 1 and Mode 2 have omnidirectional properties. They are the desired modes that will be excited; with the inspection of the current distribution, Mode 1 and Mode 2 have a current maximum in the center of
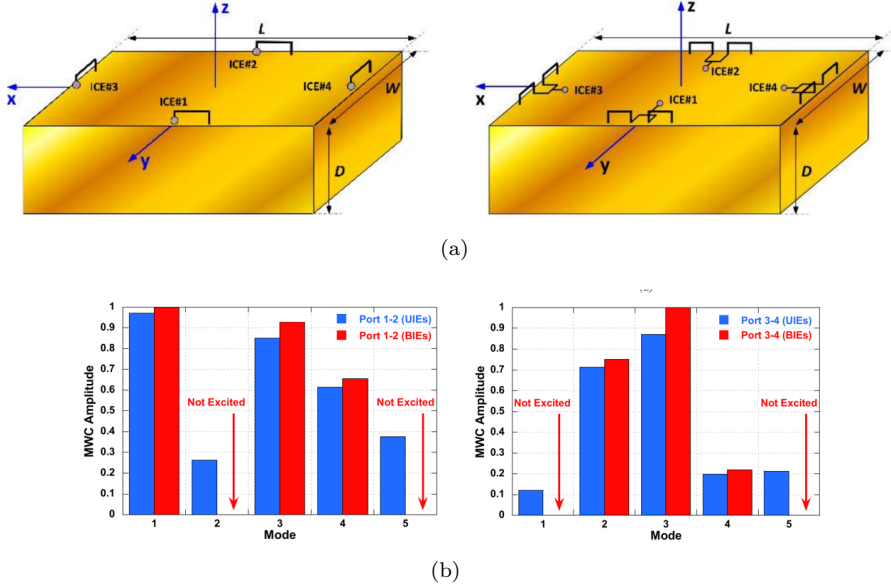
(a)

(b)

Figure 2.13: a) Clasic ICEs on a platform (left) and A novel feeding strategy called balanced inductive exciter (BIE) (right) and, b) MWC comparison between classical feeding (left) and BIE feeding (right). [45]

the monopole (Mode 1) and the middle of both long sides of the loop antenna (Mode 2). In addition, in those positions, Mode 3 and Mode 4 have a current minimum, hence if at any of those positions an inductive feeding is used, only Mode 1 and Mode 2 would be excited.

The three locations of the current maximums of Mode 1 and Mode 2 are analyzed (A, B, and C), placing an inductive feeding. In Fig. 2.14(c), the modal weighting coefficient is depicted depending on the feeding location. Finally, position A is chosen to feed the antenna with a coaxial cable due to its potential bandwidth, which is exciting modes Mode 1 and Mode 2. The final design is presented in Fig. 2.14(c) left.

The study of how to keep the roundness of a 2.4 GHz monopole antenna when placed off-center is analyzed in [47]. This article aims to investigate the radiation pattern roundness of an eccentrically allocated monopole on a circular ground plane (see Fig. 2.15(a)) with the use of CMA to show the physical insight of the unroundness of the radiation pattern when the monopole is not placed in the center. An annular ring structure surrounds the monopole to reinforce radial current modes with omnidirectional radiation properties.
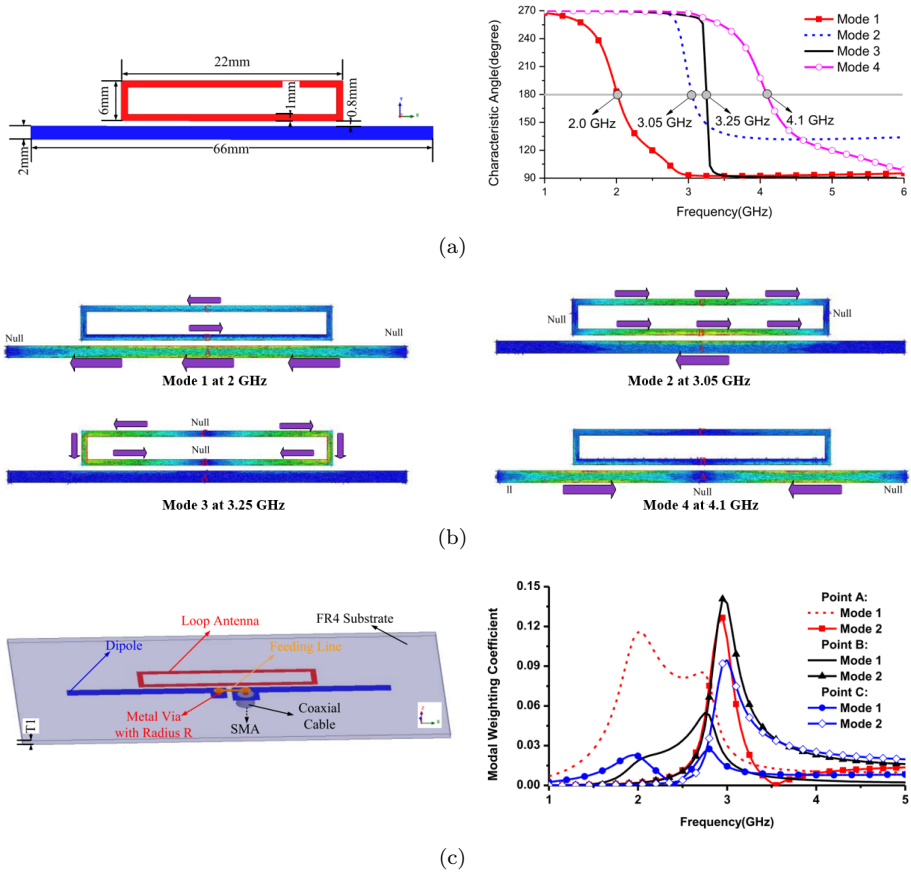
(a)

(b)

(c)

Figure 2.14: a) Dipole and loop antenna (left) and their characteristic angle, b) Current distributions of Mode 1, 2, 3 and 4 at resonance and, c) Proposed design and the modal weighting coefficient depending on the feeding location [46].

In Fig. 2.15(b) left, the radiation patterns and currents of the six first modes of the annular ring are represented. The mode J_{R1} is the only mode with radial contribution and omnidirectional properties, and it is the only mode that is excited, placing a monopole in the center of the ring. In addition, in Fig. 2.15(b) right, the modes of the ring-loaded monopole are depicted where it can be observed that modes J_1 and J_6 exhibit in-phase and radial currents with omnidirectional patterns and will be the ones excited feeding the monopole with a sma connector on the base. The roundness of the radiation pattern is
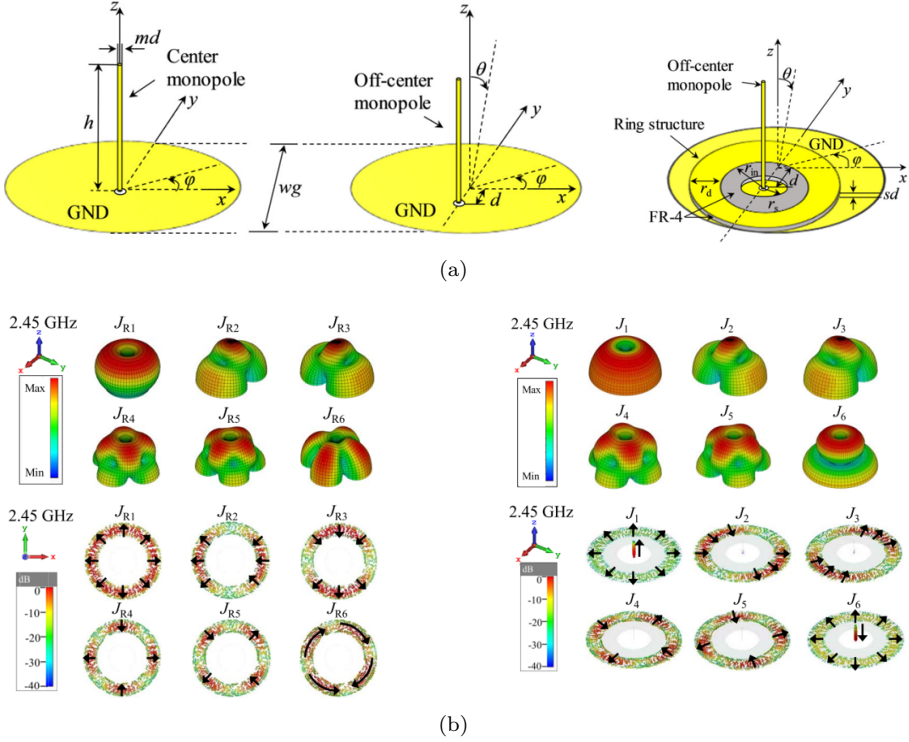
31

(a)

(b)

Figure 2.15: a) Study of the roundness of a 2.4 GHz monopole antenna when it is placed in the center (left), off-center (middle), and off-center with a ring structure (right) and, b) Radiation patterns and current distributions of the six first modes of the annular ring (left) and, the ring-loaded monopole (right) [47].

then maintained thanks to the use of the annular ring and the insight provided by the CMA.

Several studies have been published on antenna polarization control to obtain the desired polarization using CMA. In [48], a characteristic mode-based design procedure is presented for the design of wideband circularly polarized antennas in three steps. For the demonstration, a CP patch antenna using H-shaped unit cells in a 4×4 disposition fed with a cross-shaped aperture (Fig. 2.16(a)) with an impedance bandwidth from 4.42 GHz to 6.55 GHz (38.8%) and a 3 dB axial ratio bandwidth of 14.3%.

Two orthogonal modes are excited to obtain the circular polarization with a constant phase difference. In this case, Modes 1 and 3 are the desired ones
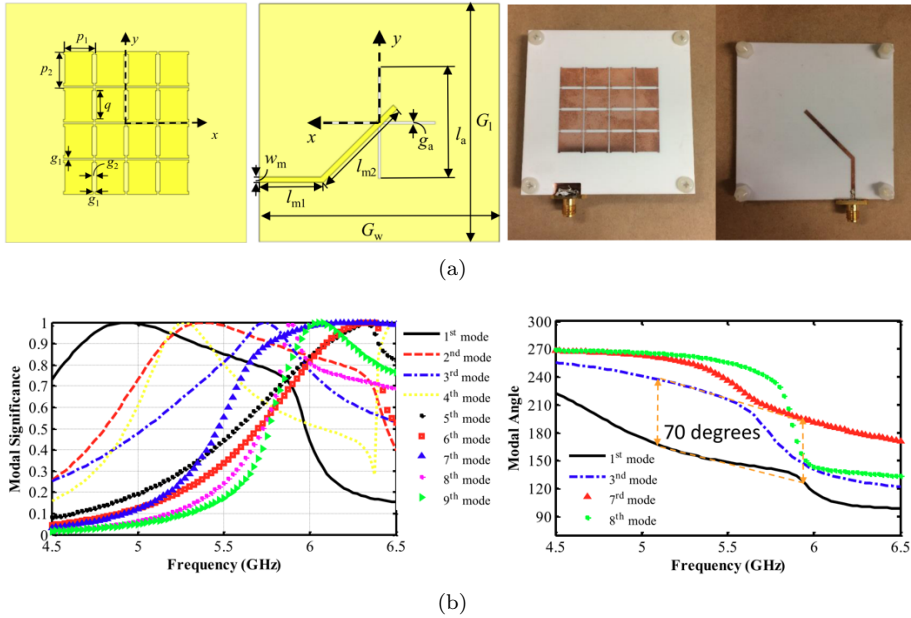
(a)

(b)

Figure 2.16: a) A CP patch antenna using H-shaped unit cells in a 4×4 disposition fed with a cross-shaped aperture and, b) Modal Significance and Modal Angle of the proposes design [48].

because they are the fundamental modes in x and y with single lobe broadside radiation patterns. With a constant 70° difference between Modes 1 and 3 until 5.5 GHz (Fig. 2.16(b)), the CP antenna is obtained. From 5.5 GHz, Mode 3 is no longer excited, and Mode 7 is excited.

Another article that applied CMA for polarization rotation is detailed in [49] where a novel transmission type polarization rotator of linearly polarized plane waves is described. Two current modes on a frequency selective surface (FSS) with CP patterns are provided to rotate the polarization. It gives a polarization-insensitive and angularly stable response.

The FSS design's unit cell is analyzed using CMA. This is the first time that CMA has been applied for the polarization rotation and the first time that a CP has been obtained with the only excitation of a characteristic mode.

The unit cell consists of four 3-D meandered dipoles arranged with a 90 rotational fourfold symmetry (Fig. 2.17(a)) based on Pierrot's cell, a famous structure supporting a CP scattered field. In Fig. 2.17(b), the MS is represented where Mode 1 and Mode 2 are degenerate modes, and both resonate at 8 GHz and are the desired ones due to their CP radiation patterns. In addition,
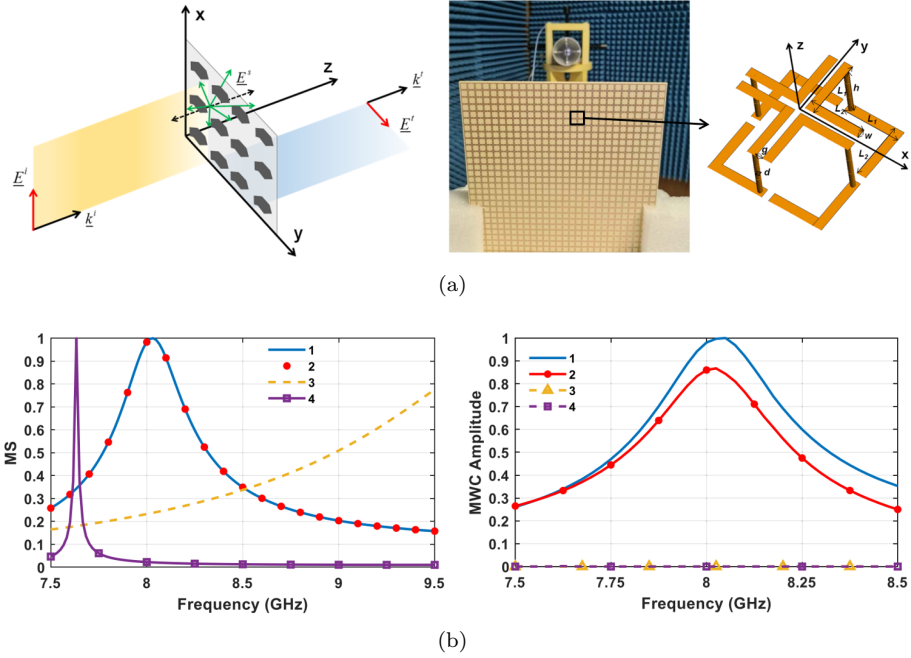
(a)

(b)

Figure 2.17: a) Frequency selective surface (FSS) with polarization rotator of linearly polarized plane waves composed by four 3-D meandered dipoles arranged with a 90 rotational fourfold symmetry unit cells and, b) Modal Significance and MWC of the four first modes of the FSS unit cell [49].

the MWC is depicted, where the contribution of both modes can be observed when an LP plane wave impinges.

Characteristic modes have also shown their efficiency for antenna loading [51] and bandwidth enhancement [50, 52–54]. With the physical insight provided by the characteristic modes, it is possible to precisely tune the modes to the desired frequency and, if desired, excite multiple modes simultaneously to enhance the impedance bandwidth.

In [50], a stub-loaded dipole 2.18(a) resonating at high-order modes is proposed to enhance the bandwidth and directivity of a conventional dipole. Characteristic modes analysis demonstrates that stubs permit shifting the fifth-order mode close to the third-order mode to achieve wideband behavior, as observed with the modal significance (MS) in Fig. 2.18(b) left. It can also be observed as a comparison of the S_{11} for a dipole with and without the stubs, where the increment in bandwidth is depicted.
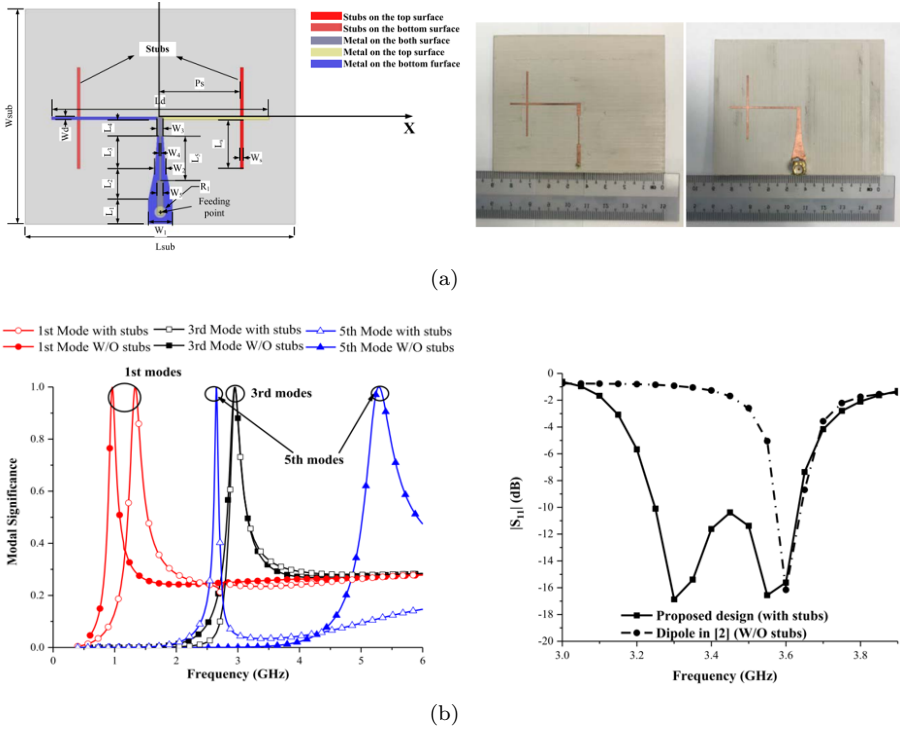
(a)

(b)

Figure 2.18:   a) Stub-loaded dipole 2.18(a) resonating at high-order modes and, b) Modal Significance and Return loss of the Proposed design against a classical Dipole [50].

Using CM, it is demonstrated simply that, with the addition of the stubs, it is possible to tune and excite higher-order modes if desired. In this case, since a wider bandwidth and higher directivity are required, the excitation of higher-order modes was a must, and they were successfully excited together, obtaining a high-gain antenna for array applications in 5G mobile communications working from 3.3 to 3.6 GHz.

Characteristic modes have also been successfully applied to enhance the bandwidth in platform-mounted antennas. The goal is to analyze the radiation properties of the platform itself, obtain its modes, and use the antenna as a coupling mechanism to convert the platform to the main radiator. In [52] an approach is employed to enhance the bandwidth of a high-frequency (HF) loop antenna placed on a military platform increasing the bandwidth of the system due to the excitation of the platform modes. In Fig. 2.19(a), the first four
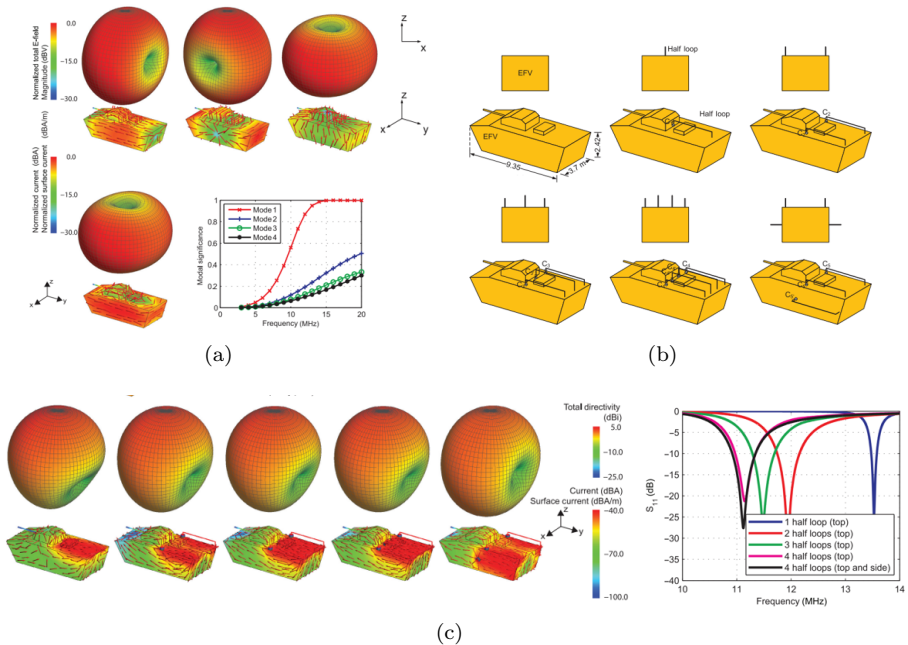
Figure 2.19: a) Rad. Pattern, current distribution, and modal significance of a military platform, b) 6 different feeding configurations using loop antennas, and c) Rad. Patterns, Current distributions, and Return losses of the six configurations [52].

modes of the military platform are depicted with their modal significance. For the platform modes excitation, six different feeding configurations using loop antennas are analyzed (Fig. 2.19(b)). After the analysis (Fig. 2.19(c)), it was stated that the system's bandwidth could be increased as much as ten times compared to the antenna standing alone.

One of the applications which has greatly benefitted from the CMA is the MIMO technology with multiple antenna solutions [55–65] especially for their installation in different size and shape portable devices such as smartphones, smartwatches et al. The modal analysis of the platform permits the installation of multiple antennas, maximizing their radiation performance thanks to the excitation of the platform modes. In addition, the orthogonality properties of the modes permit their excitation, avoiding isolation issues present in such limited scenarios with multiple antennas.

Regarding the excitation of platform modes, an 8-port MIMO array is proposed in [63] operating at the 3.4-3.6 GHz band. With the modal analysis
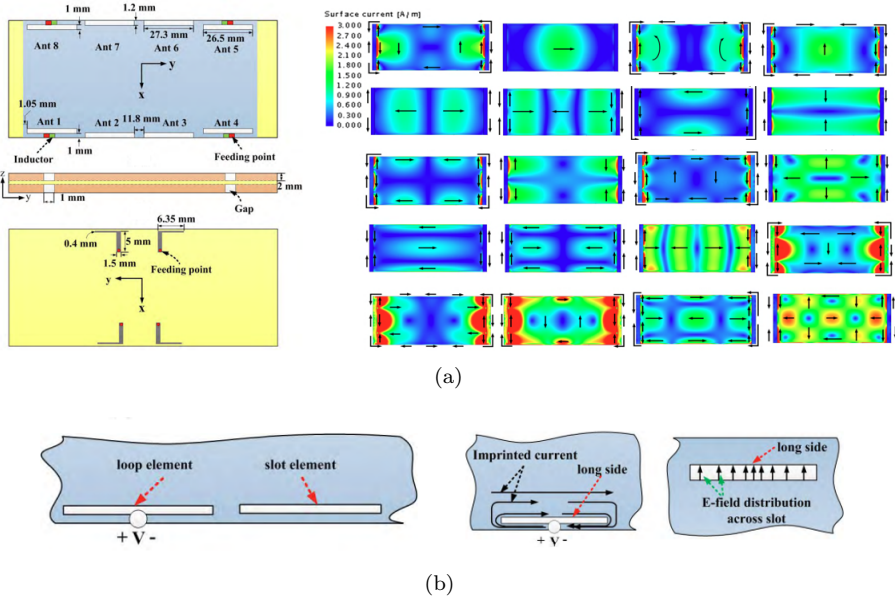
(a)

(b)

Figure 2.20: a) 8-port MIMO array in a mobile platform with inductive coupling elements (loops) and capacitive coupling elements (slots) and the current distribution of the sixteen first modes of the platform b) Loop and slot elements and their current and field distributions [63].

of the mobile platform (Fig. 2.20(a)), eight antennas are strategically placed on the long side of the platform to excite the desired modes. To increase the isolation between ports, two types of excitations are used, such as an inductive coupling element (loop) and a capacitive coupling element (slot), represented in Fig. 2.20(b). For the first time, the MWC is used to check if different antennas are excited in the same mode, either with equiphase or antiphase. It is demonstrated that reinforcing the excitation of antiphase modes increases the isolation and ECC between the antennas.

Another MIMO solution with UWB antennas with pattern diversity for a CMA mobile platform was presented in [56]. Two different antenna elements are optimized to increase their bandwidth and excite different modes to improve their isolation. In Fig. 2.21(a), their characteristic angles show a minimum resonance at about 2.5 GHz. One antenna consists of a compact quarter loop, considered a magnetic source or ICE, and a circular monopole, an electric source or CCE.
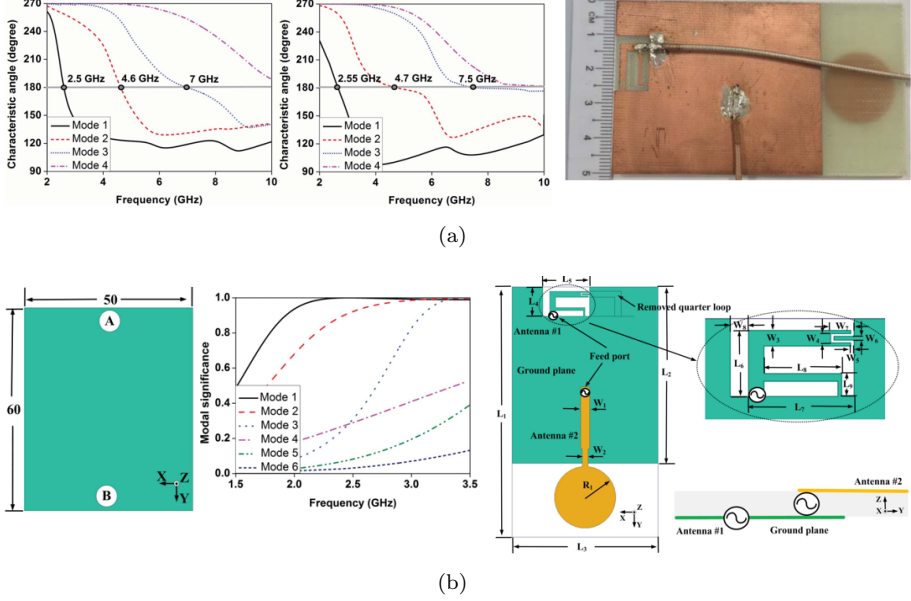
(a)

(b)

Figure 2.21: a) MIMO solution with UWB antennas (right) composed by a compact quarter loop (CA on the left) and circular monopole (CA on the center) b) Modal significance of a 50×60 platform (left) and the proposed design geometry (right) [56].

In addition, the mobile platform is analyzed (Fig. 2.21(b)) with CMA to strategically place the antenna to excite different modes due to the distinct nature of the antennas. Thanks to the other modes that both antennas excite and their orthogonality properties, the isolation between them shows a minimum of 20 dB and an ECC lower than 0.03.

The final design confirms an operating band from 2 to 9.5 GHz (130%) and an efficiency higher than 70%.

CMA has also been applied to excite modes of a smartwatch frame, such as the article presented in [58]. In this article, the frame of the smartwatch is thoroughly analyzed to check the effect of each part on the resonance of each mode. After the analysis, two capacitive feedings (see Fig. 2.22(a)) are used to excite the two fundamental modes, which are degenerated modes.

The excitation of degenerated modes permits equivalent but orthogonal radiation patterns, which show great isolation (30 dB). Fig. 2.22(b) depicts the normalized MWC and the characteristic angle of the structure when Port 1 is fed, where it can be observed that only Mode 1 is excited at 2.4 GHz.
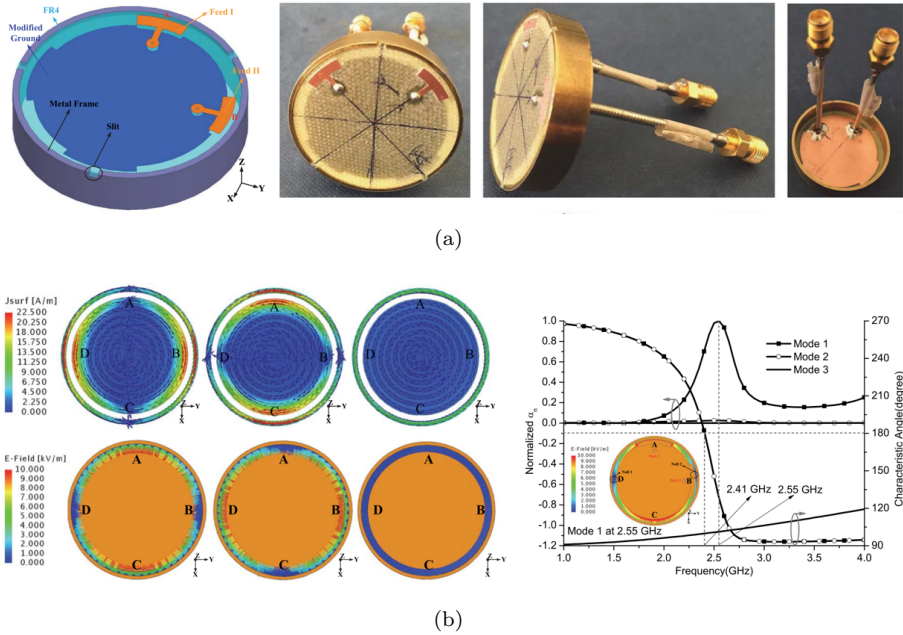
(a)

(b)

Figure 2.22:   a) Geometry of the smartwatch antenna with capacitive feed structure and, b) Current and Electric field distributions of the three first modes of the frame and normalized MWC and the characteristic angle of the structure when Port 1 is fed [58].

On the other hand, when Port 2 is fed, only mode 2 is excited. A two-port MIMO antenna is obtained, operating from 2.4-2.5 GHz for WiFi/Bluetooth applications.

The use of metasurface has also been extended thanks to its unique features, such as the impedance bandwidth enhancement and low profile it can achieve. Multiple solutions have been proposed designed with CMA for Wi-Fi array solutions [66–68], for 5G K/Ka bands arrays [69,70] and even for higher order modes suppression [71].

A metasurface-based patch antenna is presented in [67] with low-profile $(0.06\lambda_0)$ and horizontally polarized (HP) omnidirectional radiation performance. After analyzing three different structures beginning from a square patch antenna, a 4x4 square patches (Fig. 2.23(a) left) array is proposed due to the omnidirectional radiation pattern of its mode J_3 which its current distribution can be observed in Fig. 2.23(b).
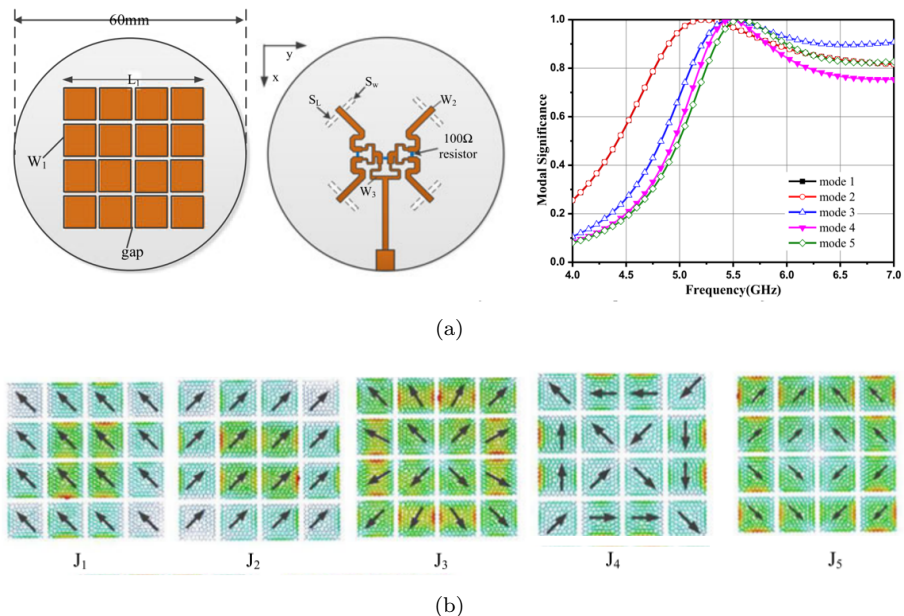
(a)

(b)

Figure 2.23: a) 4x4 square patches metasurface excited by 4 slots and the Modal significance of the first five modes of the metasurface and, b) Current distribution of the first five modes of the metasurface [67].

To excite the J_3 mode and avoid all the other modes, four slots fed with the same amplitude and phase are excited and placed perpendicular to the direction of the currents of mode J_3. Since J_3 is a radial symmetric mode, it is the only mode that will be excited with the four slots fed with the same amplitude and phase. A one to four Wilkinson power divider is used to create the feeding network properly. It is then an omnidirectional pattern antenna obtained working from 5.06 GHz to 6.18 (19.9%) GHz for WiFi applications.

Using characteristic modes results in a beneficial methodology to design arrays because the radiating elements can be optimized independently to the feeding network like the one presented in [66].

A metasurface 2×2 array antenna is proposed in [66] formed by unit cells of a diamond-slotted patch fed by a slot placed beneath the patch (see Fig. 2.24(a)). A feeding network with four symmetric branches is created with microstrip lines to feed the slots properly. It shows an overall size of $1.78\lambda_0$ ×$1.78\lambda_0$ × $0.07\lambda_0$, an impedance bandwidth working at the 5GHz WiFi band operating from 4.85 GHz to 6.21 GHz and a gain of 13-14.5 dBi.
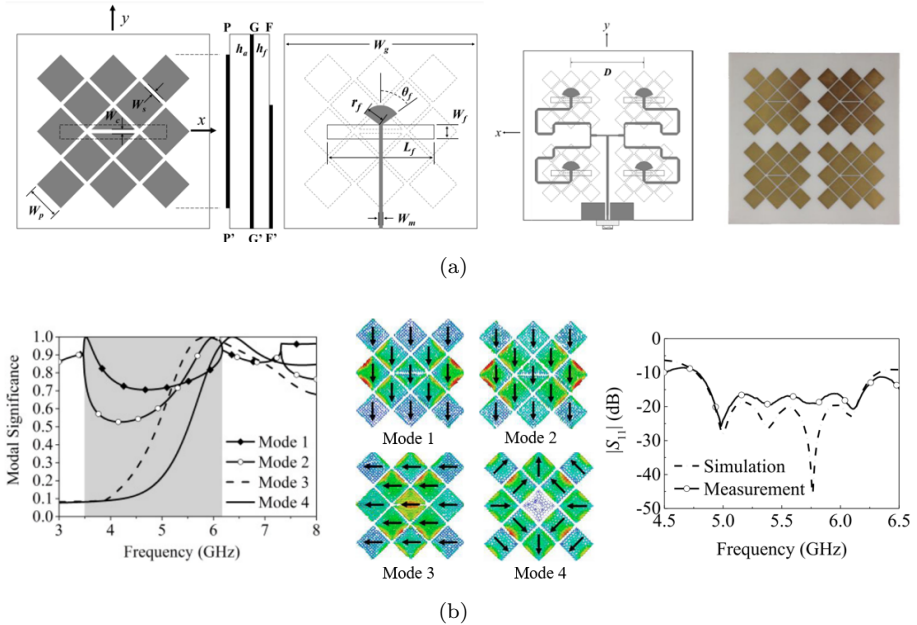
(a)

(b)

Figure 2.24:   a) Metasurface 2×2 array antenna formed by diamond-slotted patch unit cells fed by slots placed beneath and, b) Modal significance, current distribution of the first four modes of the metasurface and return loss of the proposed antenna [66].

CMA is used to analyze the diamond-slotted patch and then add the feeding structure to analyze it as a whole, and the modal significance is detailed in Fig. 2.24(b) left. With the current distribution analysis, it can be demonstrated that only Mode 1 and Mode 2 can be excited, feeding the patch with a slot with its longer side perpendicular to the current flow of these two modes. Mode 1 is a slot mode due to its resonance at the slot length corresponding to $\lambda/2$ of the resonance frequency. On the other hand, Mode 2 is a mode from the metasurface, and it is demonstrated that it can be decomposed in a linear combination of two orthogonal quasi-TM$_{30}$ modes.

In conclusion, the two modes with currents in phase (Mode 1 and 2) are the only modes excited by the slot and with a bandwidth limited by the half-wavelength mode of the slot as the minimum operating frequency, and the Q-TM$_{30}$ mode as the maximum frequency. The antenna has been optimized in shape thanks to the CMA, and the physical insight regarding the excited modes has been explained.
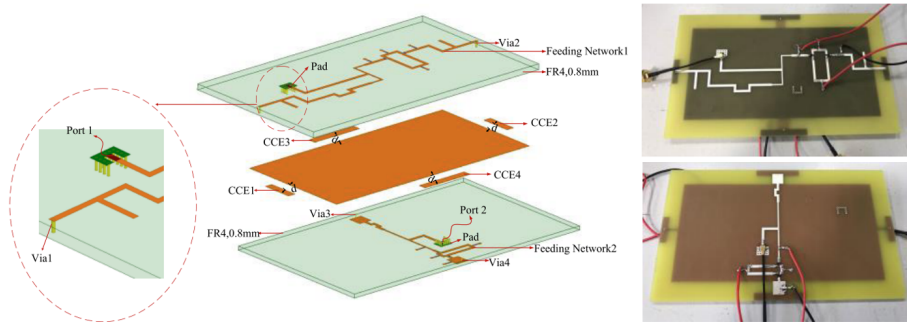
Figure 2.25: Pictures of a pattern reconfigurable two-port MIMO antenna consisting of four CCEs placed in the middle of each side of a rectangular platform fed in pairs using two feeding networks [62].
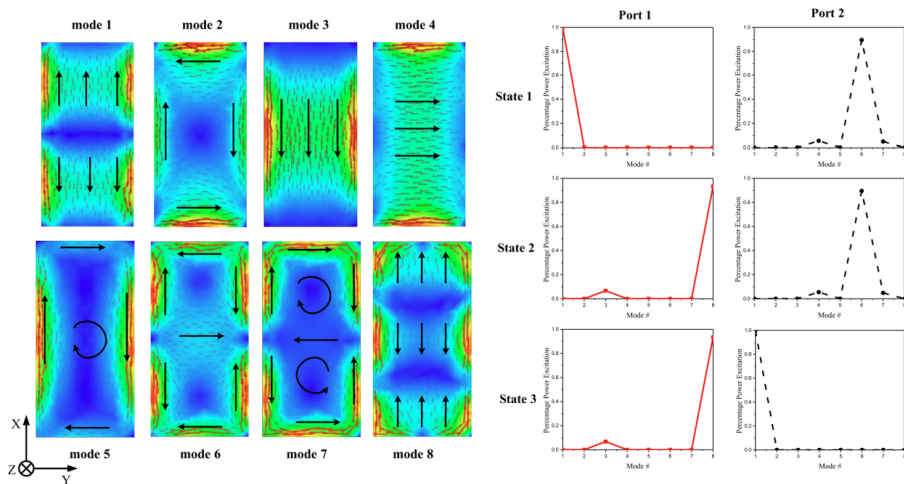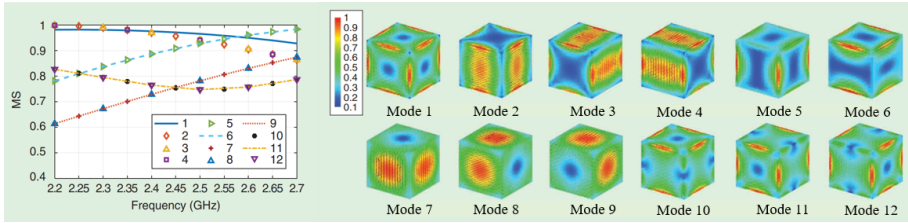

Figure 2.26: Current distribution of the first eight modes of the platform and normalized modal significance depending on the state of the two ports [62].

Another application in which CMA has resulted practical is the design of reconfigurable antennas [62,72–75] to selectively excite different modes depending on the required radiation characteristics.
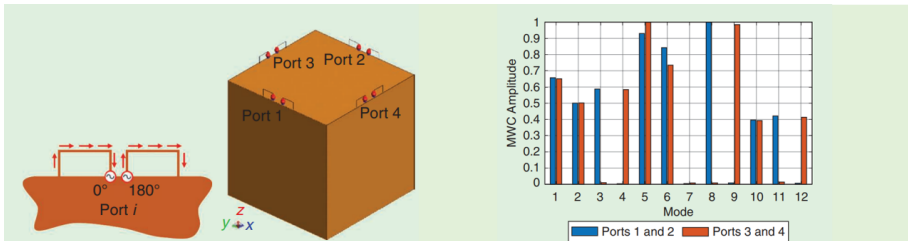
A pattern reconfigurable two-port MIMO antenna is presented in [62] operating at the 2.4 GHz WiFi band. The design consists of four CCEs placed in the middle of each side of a rectangular platform, fed in pairs using two feeding networks (see Fig. 2.25 right). The feeding networks include p-i-n diodes,

(a)

(b)

Figure 2.27: a) Modal significance and current distribution of the first twelve modes of a 1U CubeSat and, b) Picture of the four balanced inductive exciters (non-resonant half-loops) and the MWC Amplitude for Port1-2 and Port 3-4 when they are excited independently [76].

which can be adjusted to selective excite in between three modes (Mode 1, Mode 6, and Mode 8) of the ground plane (see Fig. 2.26 left), obtaining a reconfigurable pattern design with three states.

Three different states and six different radiation patterns are obtained with the control of the four installed switches. Each port excites a different mode depending on the switch's state, as seen in Fig. 2.26 with the normalized modal power contribution. The excitation of different modes permits an ECC lower than 0.02 with an efficiency of between 50-60%.

CMA has also been used for satellite communications [76,77] but especially for the analysis and excitation of antennas placed on nanosatellites to benefit from the radiation properties of the modes of the nanosatellite chassis.

A novel compact radiating system for a 1U CubeSat is presented in [76]. In this article, the characteristic modes of the hosting platform of the CubeSat are exploited to enhance the radiation properties of the whole system. The first 12 modes' modal significance and modal current distribution are depicted in Fig. 2.27(a). Four balanced inductive exciters (non-resonant half-loops) are used as described in Fig. 2.27(b) left to excitation the platform modes. The
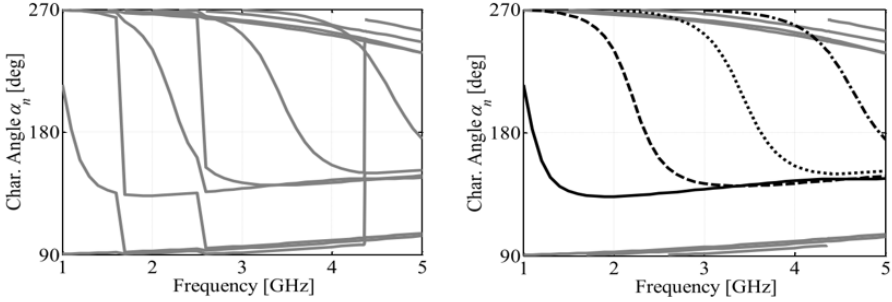
Figure 2.28: Characteristic angle of a square plate of 120 x 20 mm^2 with no tracking technique applied to sort the eigenvalues (left) and with a correlation-based tracking algorithm (right) [78].

MWC is shown in Fig. 2.27(b) right, where the excited modes can be observed when the exciters are fed independently.

The design presents the unique feature of beam scanning in circular and linear polarization at the proposed S-band, thanks to controlling the feedings' phase and amplitude. This allows the excitation of different modes, which provides the desired polarization.

These are the main applications where CMA has been used to design antennas with different radiation characteristics. CMA has not been used only to design antennas. To conclude with the applications where CMA has lately been applied, many efforts have also been made regarding the tracking and computation of characteristic modes.

Characteristic modes are calculated separately on each frequency, and for their correct concatenation, tracking techniques must be used to link the eigenvalues of the same mode. It is vital to have proper tracking techniques that are computationally efficient to get correct results in a reasonable time. In Fig. 2.28 it can be observed the characteristic angle of a square plate of 120 x 20 mm^2 without any tracking technique applied to the eigenvalues sorting (left) and with a correlation-based tracking algorithm on the right. Proper tracking is imperative to represent the eigenvalues through a frequency bandwidth correctly.

Many studies have been proposed [78–84] regarding modal tracking techniques to improve the modal tracking efficiency and precision.

The most used tracking techniques are correlation-based, but multiple new algorithms have been applied to overcome their limitations. A new algorithm to overcome the drawbacks of the correlation-based methods is presented in [78]. In Fig. 2.29(a), the flowsheet of the correlation tracking algorithm is represented along with the characteristic angle of a fractal antenna calculated with

the same algorithm where the degeneration of some modes can be observed. The degeneration appears when two modes have nearly the same eigenvalue and are sorted incorrectly, exchanging their curves as seen in some cases in the analyzed Figure.
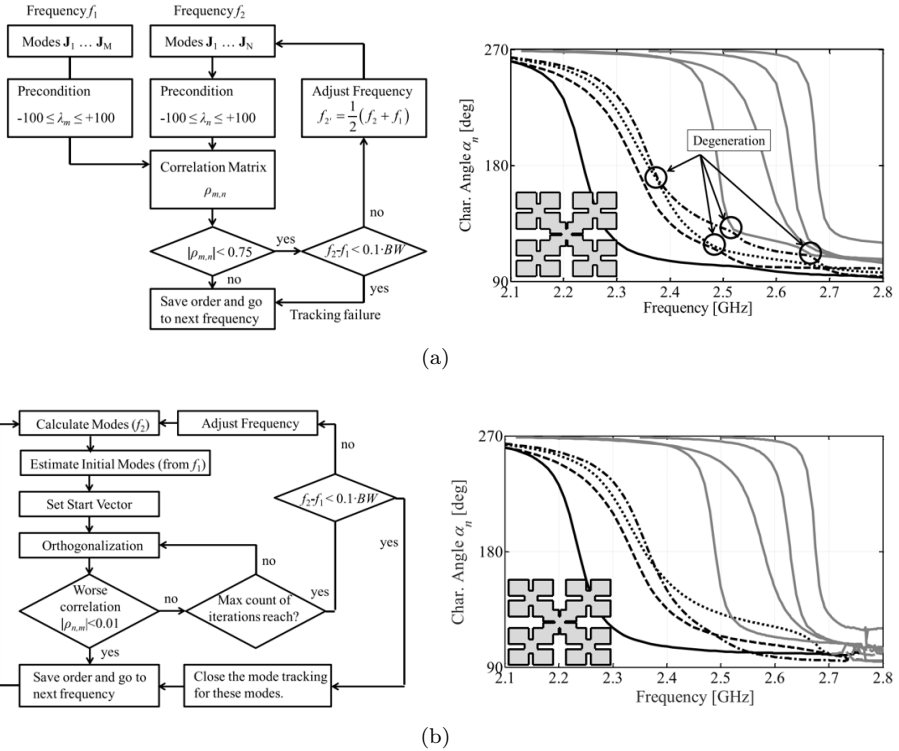

(a)

(b)

Figure 2.29:   a) Flowsheet of the correlation tracking algorithm is represented as long as the characteristic angle of a fractal antenna calculated with the same algorithm and, b) Flowsheet of the orthogonalization-based algorithm [78].

To overcome this problem, the authors present a new orthogonalization-based algorithm whose schematic is represented in Fig. 2.29(b) left and on the right, the characteristic angles of the same fractal antenna are described using the new algorithm. The new approach is an iterative algorithm to find nearly orthogonal eigenvectors from a given starting vector. As seen in Fig. 2.29(b) right, the degeneration of the modes is not present anymore but with

the downside of an increase of convergence time in its computation and could present errors ordering the high-order modes.

Since formulating characteristic modes, they have been linked to using MoM system matrices in their calculation. It has been the most extended procedure to compute the characteristic modes. A new trend is focused on the decomposition of characteristic modes with alternative numerical techniques and different numerical methods that open the limitation of the use of the MoM. Multiple studies [85–89] have been published on this topic lately which opens and enables the use of characteristic modes in different solvers.
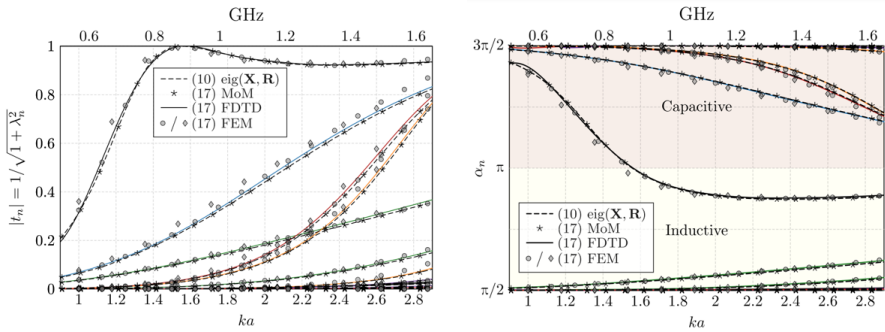

Figure 2.30: Modal significance and the characteristic angle is represented for a rectangular PEC plate of 150×75 mm^2 through Atom directly calculating the eigenvalues from the Z matrix with the Matlab function eig(X,R), with the method of moments (MoM) in FEKO, Finite Difference Time Domain (FDTD) in CST and with Finite Element Method (FEM) in HFSS [89].

A recent article [89] proposes the use of scattering dyadic to define the characteristic mode decomposition, which permits the computation of eigenvalues with different numerical methods and provides the flexibility of their calculation in all full-wave solvers with the only capability of the solution of plane-wave scattering problems. Arbitrary materials and distributions are valid for this method, including lossy materials (with the drawback of losing the modal far-field orthogonality).

In Fig. 2.30, the modal significance and the characteristic angle are represented for a rectangular PEC plate of 150×75 mm^2. For both representations, the eigenvalues have been calculated through Atom directly calculating the eigenvalues from the Z matrix with the Matlab function eig(X,R), with the method of moments (MoM) in FEKO, Finite Difference Time Domain (FDTD) in CST and with Finite Element Method (FEM) in HFSS. All the results are consistent, demonstrating that the new decomposition proposed in the article

is valid. In addition, the authors present the equivalence of the T-matrix and scattering dyadic eigenvalue problems to validate the method analytically.

This chapter has provided a deep study of the mathematical formulation of the TCM, which is required to understand the following chapters properly. In addition, the main applications during the last decades and the state of the art of CMA have been carried out. In the following chapter, CMA will be applied to analyze wideband structures.

Chapter 3

2D Structures: Metallic Plates fed by Wideband Monopoles

This chapter applies CMA to analyze 2D structures such as metallic plates and feed them with wideband (WB) monopoles in different locations. It will be demonstrated which modes from the metallic plates are excited depending on the location of the feeding. The correlation between total radiated fields (plate and monopole) and modal fields (plate) will be introduced.

3.1   Wideband Monopoles

The radiation properties of metallic plates or ground planes have been analyzed in the previous chapter with CMA. Monopole-like antennas require a ground plane to give continuity to the currents and create a virtual dipole or asymmetric dipole. The ground plane must be infinite and orthogonal to the monopole to have a performance quasi-equivalent to a virtual dipole (by applying the theory of images). In practice, monopole solutions do not satisfy this condition and have to be considered asymmetric dipoles where one branch is the monopole and the other the ground plane.

The radiation properties of an asymmetric dipole are affected by both branches, and if broadband behavior is desired, both branches must show broadband potential. Generally, if the ground plane is not size-limited (side $<\lambda/4$), the feeding element (monopole) limits the impedance bandwidth.

In the literature, the wideband bandwidth properties of monopoles with different canonical geometries (Fig. 3.1) have been investigated. Out of the
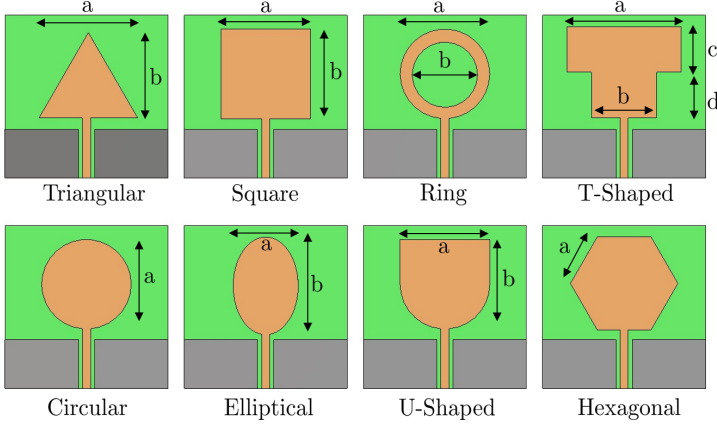
Figure 3.1: Wideband monopoles with different geometries.

canonical geometries, the elliptical [90–93] shape monopole has shown the highest impedance bandwidth ratios such as 12.4:1 from 1.21 GHz to 13 GHz (VSWR<2) presented in [90, 94] or the impressive 21.6:1 bandwidth ratio obtained in [93] with the use of an elliptical monopole with a trapezoidal shape ground plane. In [95], four types of radiators with elliptical shapes were presented for UWB applications ranging from 3.1 GHz to 10.6 GHz. Circular [96, 97] and annular [98, 99] shape monopoles have also shown wideband impedance performance, with a 10.6:1 (S_{11}<-10 dB) bandwidth ratio ranging from 2.7 GHz to 28.8 GHz in [96] and a 10.2:1 (VSWR<2) bandwidth ratio in [97].

Square [100–103] and rectangular [104, 105] shape monopoles present narrower bandwidth than other geometries but with the use of techniques such as bevelling [101] or the use of shorting pins [102], the impedance bandwidth can be enhanced. In [103], a square monopole is trimmed with symmetrical and asymmetrical beveling to enhance its impedance bandwidth up to 2.1 GHz-12.5 GHz (VSWR<2). The T-shape monopoles [106,107] are obtained using notches on the base of square/rectangular shape monopoles. In [107], a notched square monopole on a truncated ground plane is presented ranging from 1.65 GHz to 10.6 GHz (S_{11}<-10 dB).

Triangular [110–112] and bow-tie [113, 114] shape monopoles have been investigated. In [111], a planar triangular monopole is proposed ranging from 4 to 10 GHz (VSWR<3) for UWB applications. In addition, a bow-tie monopole antenna is presented in [114] with 77.1% (1.03-2.31 GHz) impedance bandwidth proposing a novel matching technique with the use of slits and ground plane modification. Additionally, regular polygon shape monopoles were also studied
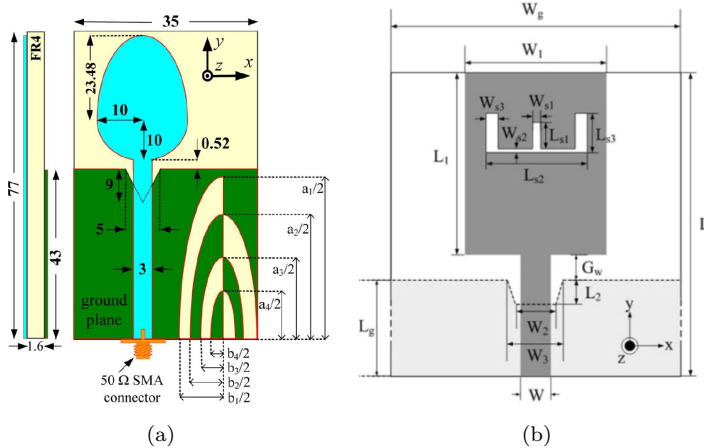
Figure 3.2: a) Compact monopole for super wideband applications [108] and, b) Band-notch function for a printed ultra-wideband monopole [109].

such as pentagonal [115, 116] and hexagonal [117, 118] with a bandwidth ratio of 10:1 (VSWR<2) [115] and 15.3:1 (VSWR<2) [117].

A technique that was also widely used in UWB monopoles was the band-notch function [109, 119–121], which was introduced to overcome the interference created by the monopoles to WLAN applications. This function was able to filter the radiation properties of wideband antennas at specific frequency bands using slots etched in the monopoles. In Fig. 3.2(b) [109], a square monopole antenna is presented with an E-shape slot for notching the 5.2 GHz and 5.8 GHz bands.

After analyzing different UWB monopoles with multiple geometries, it can be stated that they have wideband properties and are an excellent candidate to feed wideband elements such as ground planes or cavities. Another conclusion obtained from the cited papers is that the modification of the connected ground significantly affects the radiation properties of the monopole. An example can be observed in Fig. 3.2(b) with a planar wideband antenna [108], which uses a semi-elliptically fractal-complementary slot in the ground plane to enhance its impedance bandwidth.

The reinterpretation of the monopoles connected to non-infinite ground planes as asymmetric dipoles [122] helps to understand that both branches (monopole and ground plane) must be analyzed and the radiation properties of the design depend on the analysis of both of them.

3.2 Correlation between Total and Modal Fields $\rho_{n,T}$. Square Plate fed by Circular Monopoles

In this section, we introduce the correlation between modal and total fields to analyze which modes of the square plate are excited when we feed it with a circular monopole. We consider the metallic plate as the ground plane of the monopole.

Characteristic modes of metallic plates are well-detailed in the literature and are generally easily calculated by commercial electromagnetic simulators. When the feeding is included to obtain the modal parameters that require the feeding, the calculation of the modes becomes more complex depending on the kind of excitation we choose. Complex feedings require an extremely detailed meshing, time-demanding simulations, and modal tracking issues. Furthermore, some feeding elements include dielectric materials, which complicates the analysis. Commercial simulators do not analyze any lossy material for CMA, a topic still under research.

To address this problem, we analyze the isolated plates with CMA and correlate the radiated fields of each mode (modal fields) with the total radiated fields of the ground plane, including the feeding, which in this case will be a circular monopole. The correlation is then used as a metric to quantify approximately which mode of the ground plane is excited.
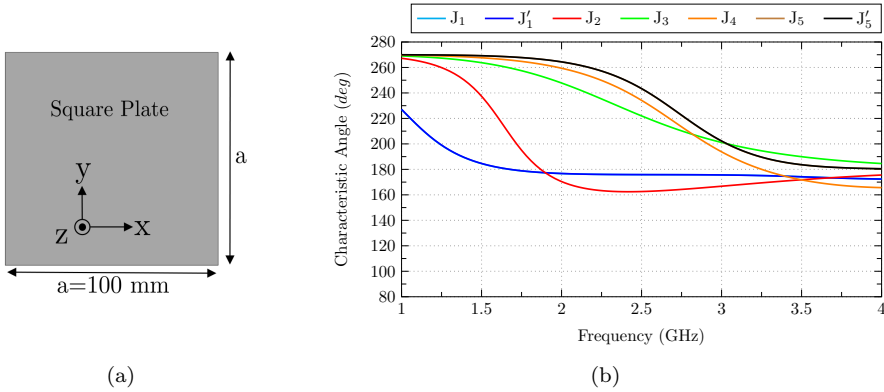

Figure 3.3: a) Geometry of the analyzed square plate and, b) Characteristic angle of modes J_1-J_5 of the plate.

The correlation is detailed in (3.1), where g_n is the radiation pattern associated with mode J_n of the analyzed ground plane, and g_T is the total radiation

pattern (feeding+ground plane). The superscript ^{H} denotes Hermitian and $\Omega = (\theta, \phi)$ is the solid angle.

$$\rho_{n,T} = \frac{\iint\limits_{4\pi} g_n^H(\Omega) g_T(\Omega)\, d\Omega}{\sqrt{\iint\limits_{4\pi} g_n^H(\Omega) g_n(\Omega)\, d\Omega \cdot \iint\limits_{4\pi} g_T^H(\Omega) g_T(\Omega)\, d\Omega}} \qquad (3.1)$$

To demonstrate the methodology, CMA to a $100{\times}100$ mm^2 square plate (Fig. 3.3(a)) is applied between 1 GHz and 4 GHz. A square ground plane is limited at low frequencies depending on the first resonant modes but unlimited at higher frequencies when high-order modes are sequentially appearing.
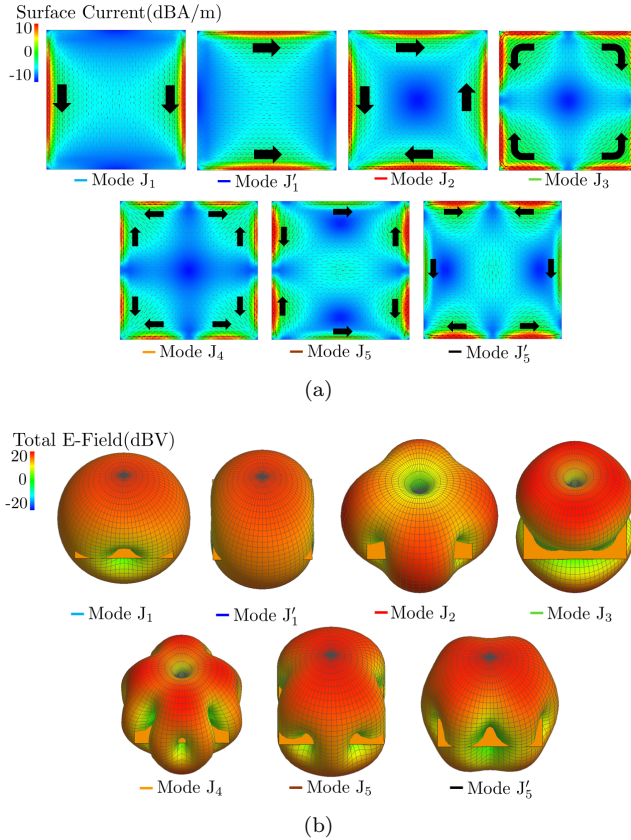

(a)

(b)

Figure 3.4:   a) Current distribution of modes J_1-J_5, b) Radiation patterns of modes J_1-J_5.

For simplicity, the square plane is analyzed between 1 GHz and 4 GHz because, at higher frequencies, the contribution to the radiated power is produced by too many modes. The ground plane is first analyzed and then fed with a wideband monopole. In Fig. 3.3(b), the characteristic angles of the first resonant modes on the analyzed band are depicted.
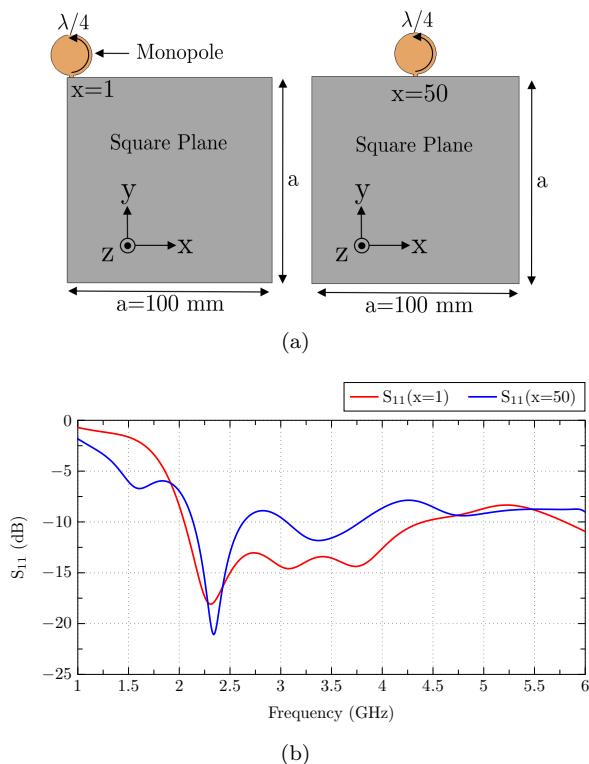

(a)

(b)

Figure 3.5: a) Square plates fed by circular monopoles in x=1 (corner) and
x=50 (middle) and, b) S-parameters of both designs.

To complete the information, each mode's current distribution and radiation pattern are depicted in Fig. 3.4. The fundamental modes are the J_1/J_1' modes, which are the vertical and horizontal modes resonating at f=1.6 GHz for a=$\lambda/2$. The following mode is J_2 (f_r=1.95 GHz), which shows current nulls on the plane's corner and current maximum in the middle of each side. On the contrary, Mode J_3 (f_r=4.5 GHz) presents current maximums in the corners and minimums in the middle of the square plane sides. Mode J_3 resonates at f_r=3.25 GHz and presents current nulls on the corners and the middle of the

four sides. Lastly, modes J_5/J_5' (f_r=4 GHz) show a current null on the corners and the middle of the top and bottom sides.

Once the square ground plane modes are described, we proceed to feed the plane with a circular monopole that is resonant ($\lambda/4$=37.5 mm) at f=2 GHz (Fig. 3.5(a)). Monopoles are considered capacitive feeding and must be placed on a current minimum (E-field maximum) to feed the desired mode properly. We analyze the monopole feeding the square plane in the corner (x=1) and the middle of a side(x=50) to describe which modes are excited.

Without any optimization, it can be observed in the S_{11} of Fig.3.5(b) the wideband capabilities which both designs (x=1 and x=50) show. Both designs are operative from 2 GHz, the monopole's resonance frequency. The impedance bandwidth depends on both the feeding and the fed structures. Both of them should present wideband capabilities to obtain a wideband design. To gather more information about the radiation performance of both designs, a full wave analysis of total fields and currents is performed to get the total radiated fields.

When both total and modal fields are calculated, the correlation introduced above between the total radiation patterns (ground plane + monopole) and the modal radiation patterns (ground plane) is computed.

In the following sections, both designs with the circular monopole in the corner of the ground plane and the middle of a side are further developed.

3.3 Circular Monopole in the corner of a Metallic Plate

The first analyzed design includes the feeding circular monopole in the corner of the a=100 mm square ground plane (Fig. 3.6(a)). The correlation 3.1 is calculated between 1-3 GHz, and it can be observed that only modes with a current null in the corner of the ground plane are excited. As explained above, the monopole is considered a capacitive feeding and excites modes in spots that show a current null. With the correlation is demonstrated that only modes with this current distribution are excited, and the total radiated power is composed by modes J_1/J_1', J_2, J_4 and J_5/J_5' (Fig. 3.7(b)).

In Fig. 3.7(a), the total current and radiation pattern of the monopole and ground plane are depicted with the frequency from 1 GHz to 3 GHz. It can visually check which modes are mainly contributing to the total radiated power, especially by comparing the total (Fig. 3.7(a)) and modal (Fig. 3.7(b)) current distributions and with the calculated correlation (Fig. 3.7(a)). At f=1 GHz, modes J_1/J_1' are excited because they have a current null in the corner and are the only modes close to resonance (Fig. 3.5(b)). Total currents result in a combination of J_1/J_1' with diagonal direction. At f=1.5 GHz, the main contributing mode is J_2 ($\rho_{2,T}$=0.7), and in the total current distribution, it
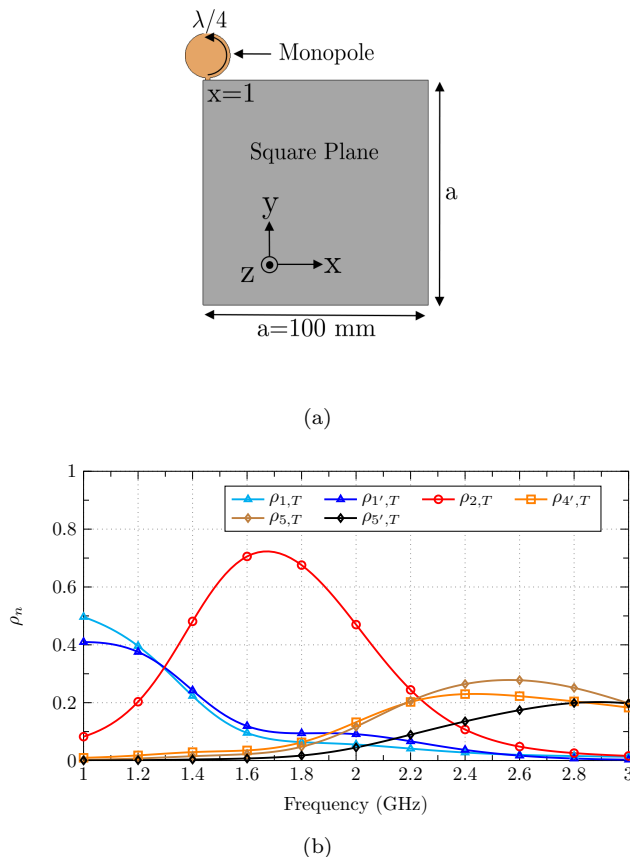
(a)

(b)

Figure 3.6: Monopole in the left corner: a) Picture of the analyzed structure,
and b) Correlation between modal and total fields.

can be observed that the current on the ground plane is similar to the modal
current of J_2. At f=2 GHz the main mode is still Mode J_2 ($\rho_{2,T}$=0.5) but more
modes such as J_4 and J_5 begin to be slightly excited. At f=2.5 GHz, mode J_2 is
no longer excited, and a combination of mode J_4 and modes J_5/J_5' contribute
to the radiated power. From this frequency, it is difficult to visually identify
the contribution of each mode to the total current distribution. In this case,
the correlation is the most suitable figure to consider. Finally, at f=3 GHz, the
same modes are still present.

It has been demonstrated through the correlation that only modes from the
ground plane with current nulls on the corner are excited. In Fig. 3.7(b), they
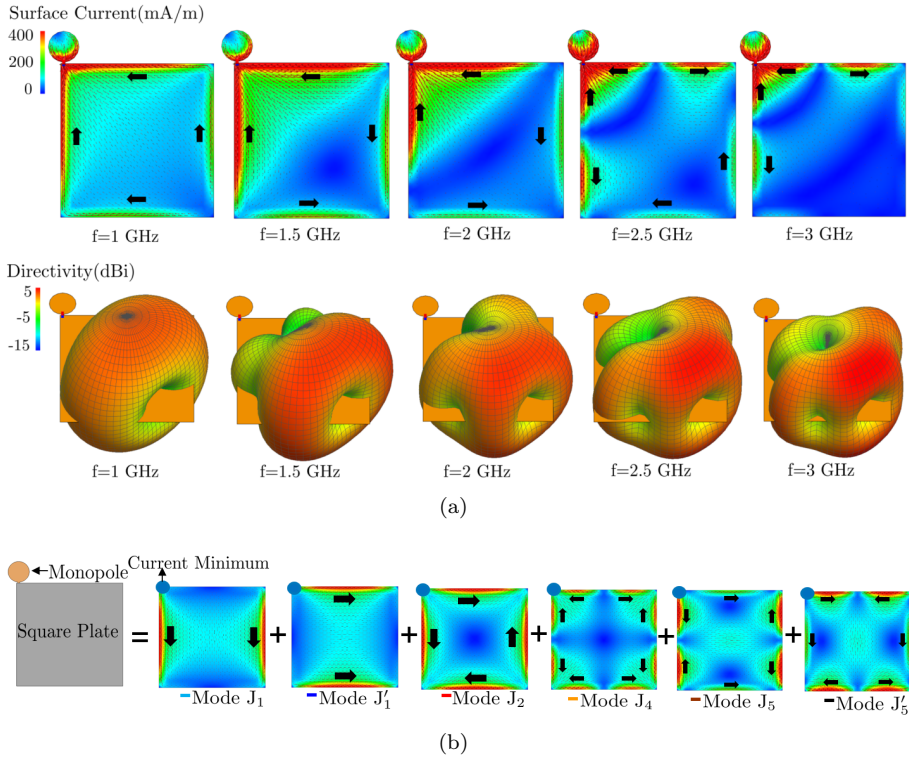
Figure 3.7: Monopole in the left corner: a) Total Current distribution and Total radiated field at different frequencies and b) Excited modes.

are represented together and sequentially excited depending on their resonance frequency. The correlation resulted in a suitable parameter to measure the radiation contribution of the ground plane modes to the total fields of the design of the monopole+ground plane.

3.4 Circular Monopole in the middle of a Metallic Plate Side

The second analyzed design includes the feeding circular monopole in the middle of the square ground plane top side (Fig. 3.8(a)). The correlation 3.1 is also calculated between 1-3 GHz; in this case, only modes with a current null in the middle of the top side of the ground plane are excited. The correlation

indicates that the total radiated power comprises modes J_1, J_3, and J_5' (Fig. 3.7(b)).

(a)

(b)
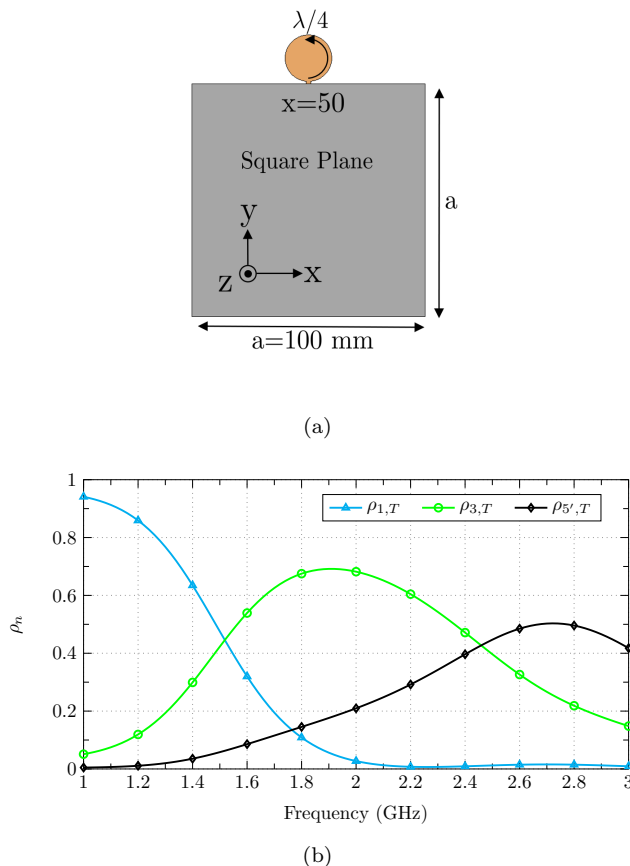
Figure 3.8: Monopole in the middle of top side: a) Picture of the analyzed structure and b) Correlation between modal and total fields.

In Fig. 3.9(a), the total current and radiation pattern of the monopole and ground plane are depicted with the frequency. At f=1 GHz, only mode J_1 is excited with a high level of correlation ($\rho_{1,T}$=0.92). The total current distribution has the same modal distribution as J_1. At f=1.5 GHz, J_1 and J_3 obtain the same correlation level, with a total current distribution that is more similar to that of J_1. At f=2 GHz, the main mode is Mode J_3 ($\rho_{3,T}$=0.65), and the total current distribution becomes similar to the modal of J_3. At f=2.5 GHz, mode J_3 is not the main one, and then mode J_5' becomes relevant with

a total current distribution similar to the modal distribution of J_5'. Finally, at f=3 GHz, mode J_5' becomes. In Fig. 3.9(b), the contributing modes of the ground plane are depicted together—all with a current minimum where the monopole is connected.

(a)

(b)
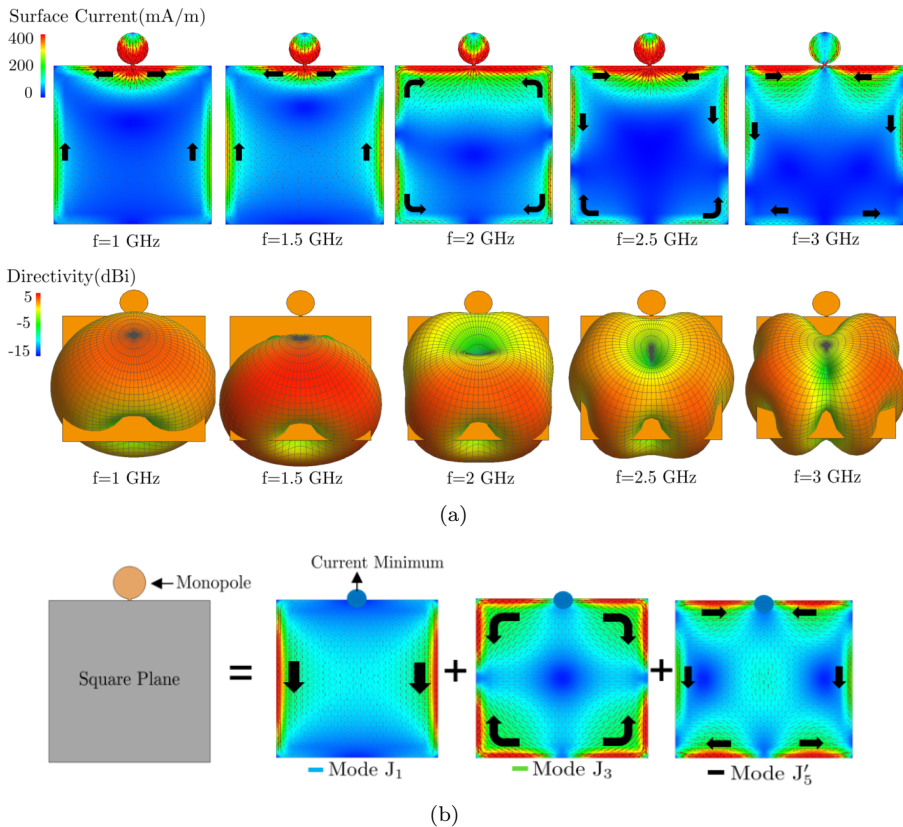
Figure 3.9: Monopole in the middle of top side: a) Total Current distribution and total radiated field at different frequencies and, b) Excited modes.

To conclude this chapter, after the two analyses, it is demonstrated that monopoles must be placed in current minimums to properly excite the desired modes. The methodology of correlating the total radiated fields of the ground plane + feeding with the modal information of the isolated ground plane is more convenient than analyzing the structure, including the monopole, which is more complex.

This methodology will be applied throughout the thesis and will become
especially important when small antennas excite the metallic plates. Small
antennas (especially chip antennas) are complex to analyze and simulate due
to their fine meshing requirements to obtain precise results. Since the main
contribution to the radiated power comes from the connected ground plane, it
will avoid the analysis with CMA of extremely complex setups, including small
antennas, with the benefit of obtaining a proper approximation.

The analyzed 2D structures are a good introduction before the 3D structures
are introduced in the following chapter. So far, bidirectional radiation patterns
have been obtained with the 2D structures. That feature is not attractive for
the main application, which is the design of indoor access point antennas. The
following chapter, 3D cavities are analyzed with CMA to obtain the desired
directional radiation patterns.

Chapter 4

3D Structures: Multiple-fed Cavity-backed Antennas

As introduced in Chapter 1, there is a growing demand for antennas to be installed in 5G indoor base stations or access points covering the new licensed sub-6 GHz bands and also the 2G/3G/4G bands, which are still working. Low profile, high efficiency, unidirectional patterns, easy manufacturing, and low cost are appreciated for their easy and rapid installation in indoor scenarios.

Open cavities have been classically used to back radiating elements and provide unidirectional radiation patterns. This feature fueled the creation of the well-known cavity-backed antennas in many applications requiring unidirectional radiation characteristics. Their geometry allows them to be fed with multiple ports exhibiting symmetric patterns. In addition, cavity-backed antennas can also provide wideband bandwidth performance and highly efficient designs.

This chapter presents a design procedure based on CMA to design cavity-backed antennas, and multiple designs will be given.

4.1 CMA from a Square Plate to an Open Cavity

In Chapter 3, the CMA of 2D structures such as metallic plates have been investigated. This section presents a design procedure combining CMA and

full-wave analysis to design multiple-port cavity-backed antennas beginning
from a square metallic plate, which is already known.

This methodology eases the design process of cavity-backed antennas. It
starts from the CMA of a squared plate with a 100 mm side length and then
reshapes it into an a×a×b cavity, analyzing how the modes change.

CMA will provide a visual insight into finding the optimum height (b) for
impedance bandwidth performance and the optimum feeding configuration.
This information will also determine the minimum operating frequency deter-
mined by the first resonating mode. A complimentary full-wave analysis is also
introduced to obtain additional information regarding the input impedance
and isolation between ports. The characteristic mode analysis helps choose the
type of feeding. Still, it lacks information about the connected port's reference
impedance (50 Ω) because it is calculated without feeding. It is essential to
evaluate the effect of increasing b due to its influence on the input impedance
of the feeding. Different configurations for the feeding are analyzed, including
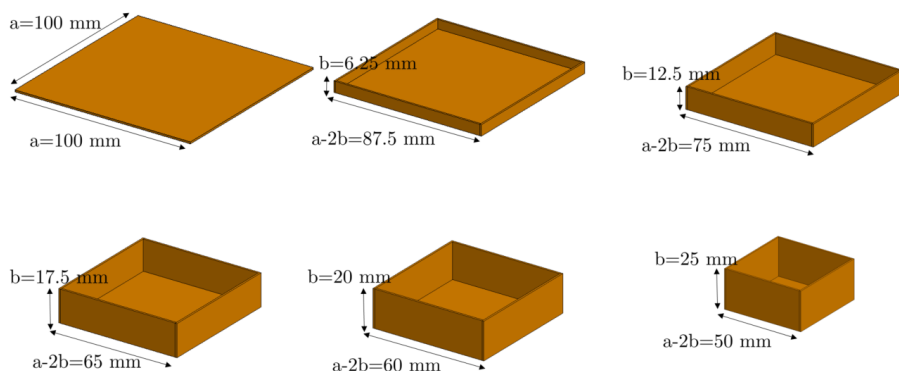multiple wideband monopoles or dipoles.

Figure 4.1:   Analyzed structures starting from an a×a square plate and
reshaping it into a×a×b cavities. Height b is parametric (6.25,12.5,17.5,20
and 25 mm), and length a is obtained with a=100-2b.

The analysis begins with a size variable cavity with a total size of a×a×b
with variable b and length a obtained with a=100-2b. When b=0, the cavity
becomes a square (a×a=100 mm^2) metallic plate, which is a suitable initial
point due to its demonstrated radiation properties and well-studied modes.
When b is increased, length a decreases as observed in Fig. 4.1. The following
values of height b are analyzed: b=0, 6.25, 12.5, 17.5, 20, 25 mm (Fig. 4.1).

This first analysis aims to study the variation of the characteristic modes
of the square plane when it is reshaped to a cavity with parametric b. The
analysis focuses on the shift of the minimum resonance frequency (given by the

first resonant mode) and the viability of a wide-band performance. In addition, the current distribution of all the modes will provide valu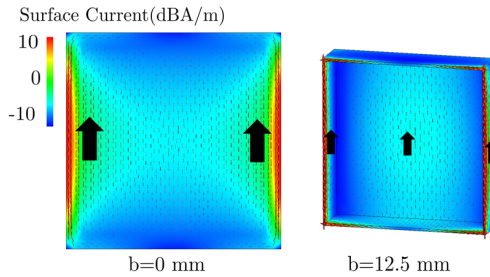able information for choosing the proper excitation. The parametric size cavity's first resonant modes (from J_1 to J_4) are analyzed next.
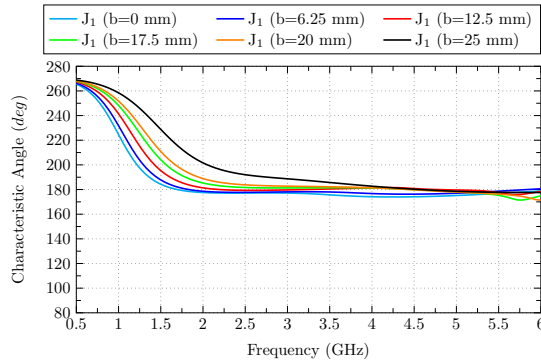
(a)

(b)

Figure 4.2: a) Characteristic angles of Mode J_1 for parametric and, b) Current distribution of Mode J_1 for b=0 and b=12.5.

Fig. 4.2(a) shows the characteristic angles of mode J_1 for parametric b. Fig. 4.2(b) depicts the current distribution for b=0 and b=12.5 cases where it is observed that the current distribution is conserved. Mode J_1 shifts to higher frequencies with b due to the path reduction of the currents flowing through the perimeter of the cavity. When b is increased, the path is shorter. Hence, the resonance frequency is higher. A capacitive effect is also observed due to the capacitive effect of closer metallic walls. The frequency shift is slight for Mode J_1 from b=0 (plane) to b=17.5 mm. Higher values of b would shift a future design to higher frequencies.

(a)

(b)

Figure 4.3: a) Characteristic angles of mode J_2 for parametric and, b)
Current distribution of Mode J_2 for b=0 and b=12.5.

The characteristic angle and the current distribution of Mode J_2 are de-
picted in Fig. 4.3. Mode J_2 is stable in bandwidth because the slope of the
characteristic angle is conserved when b is increased, but not the resonance
frequency. The higher b, the higher the resonant frequency with an additional
capacitive effect observed in the characteristic angle curves with values higher
than 180º. This Mode performs similarly to J_1 but becomes non-resonant when
b exceeds 20 mm. Values of b higher than 20 mm are not recommended.

Regarding Mode J_3, the characteristic angles and the current distributions
are depicted in Fig. 4.4. Mode J_3 shows characteristic angle curves with
a higher slope when b is increased, which is traduced into a lower bandwidth
Mode. The higher b, the higher the resonant frequency because of the reduction
in the path length on the aperture of the cavity when b is increased, and an
additional inductive effect is observed in the characteristic angle curves, which
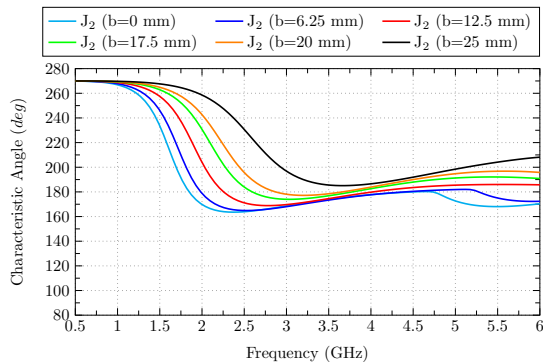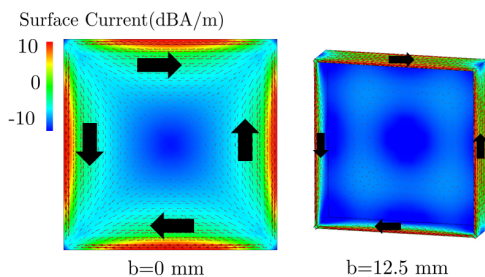displace the curves away from resonance ($\alpha=180$º). The current distribution

(a)

(b)
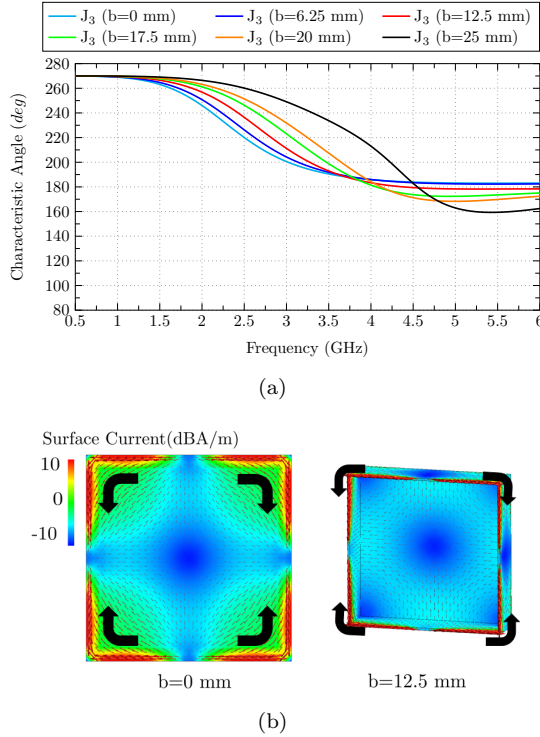
Figure 4.4: Characteristic angles of mode J_3 for parametric and, b) Current distribution of Mode J_3 for b=0 and b=12.5.

of Mode J_3 for b=0 mm and b=12.5 mm is depicted in Fig. 4.4(b) where it can be observed that the current distribution is also conserved.

The last analyzed Mode is J_4. This mode is susceptible to b because it increases the resonance frequency and decreases the bandwidth due to the increase in the slope of the characteristic angle curves. From values higher than b=20 mm, the bandwidth becomes narrow.

After this first analysis, it can be stated that the current distributions of the modes are conserved from a square ground plane when they are reshaped to a cavity. The cavity should remain low profile regarding bandwidth and minimum resonance frequency; otherwise, modes become narrower in bandwidth, and their resonance frequency is shifted to higher frequencies. It is observed that there is a common feature to almost all the modes regarding the current minimum placed in the middle of the bottom and top edge except for mode J_2. A capacitive feeding would be required to excite all the modes with a cur-

(a)

(b)
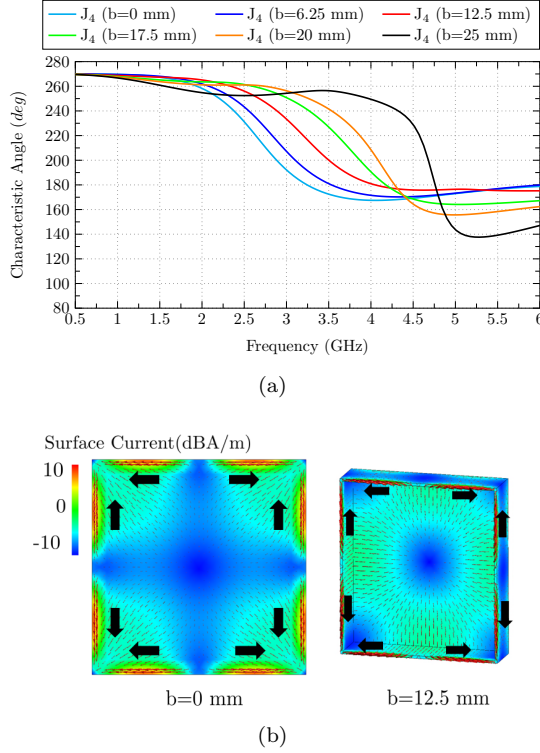
Figure 4.5:   Characteristic angles of mode J_4 for parametric and, b) Current
distribution of Mode J_4 for b=0 and b=12.5.

rent minimum in that position. In such a scenario, a proper solution would be
placing two monopoles in the middle of the upper side and one in the middle of
the bottom. With this setup, a wide-band 2-port antenna could be obtained.
In addition, four ports could be placed because of the existence of degener-
ated modes. In the following sections, the viability of these designs is studied,
considering the coupling effects that could limit their performance.

To add up and summarize the modes of b=17.5 ($65 \times 65 \times 17.5$ mm^3) cavity
(Fig. 4.6(a)), the characteristic angles of the first five resonant modes, including
the degenerated ones, are represented in Fig. 4.6(b). As observed in the square
plane, the cavity also presents wideband performance due to the stability of the
modes, which are close to $\alpha=180°$ even after resonating. In addition, higher
order modes are sequentially appearing, which turns the cavity into a non-
limited upper band design. The first resonant mode (J_1) limits the lowest
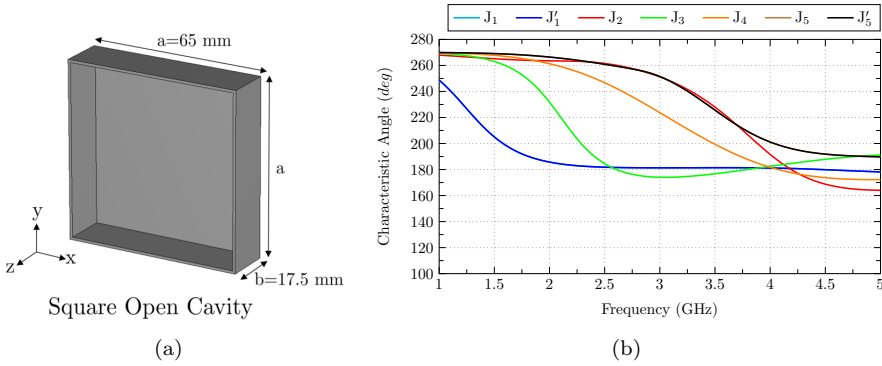
Figure 4.6: a) 65x65x17.5 mm^3 open cavity and b) Characteristic angle of modes J_1-J_5 of the open cavity.

operating frequency, and if it is properly fed, it could be working from around 1.5 GHz.

In Fig. 4.7, the current distribution of the cavity modes is depicted. Analyzing the currents shows identical distributions as in the square plane with slight differences. The main difference can be observed in the radiation patterns due to the current flowing through the walls of the cavities, especially for mode J_5/J_5' in which the current distribution is identical but not the radiation patterns.

As a first conclusion, it can be stated that the current distribution of modes from a square plane is conserved when it is reshaped to a cavity. Regarding modal bandwidth and minimum operating frequency, keeping the cavity as wide and low profile (short b values) as possible is advisable. Once the modes are analyzed, the feeding is studied next. When the feeding is installed, a low value of height b could produce impedance values close to 0 Ω due to current cancellation between the feeding and the cavity. Lastly, another parameter that limits the minimum size of the cavity is the coupling between ports when multiple feeding is addressed. A trade-off between proper matching impedance, coupling, and the cavity modes' minimum resonance frequency and bandwidth has to be evaluated.

Two types of feeding will be analyzed: monopoles placed around the perimeter of the cavity and dipoles in the center. Taking advantage of the analysis introduced in this section, different solutions are proposed to properly excite the cavities' modes in the following sections.
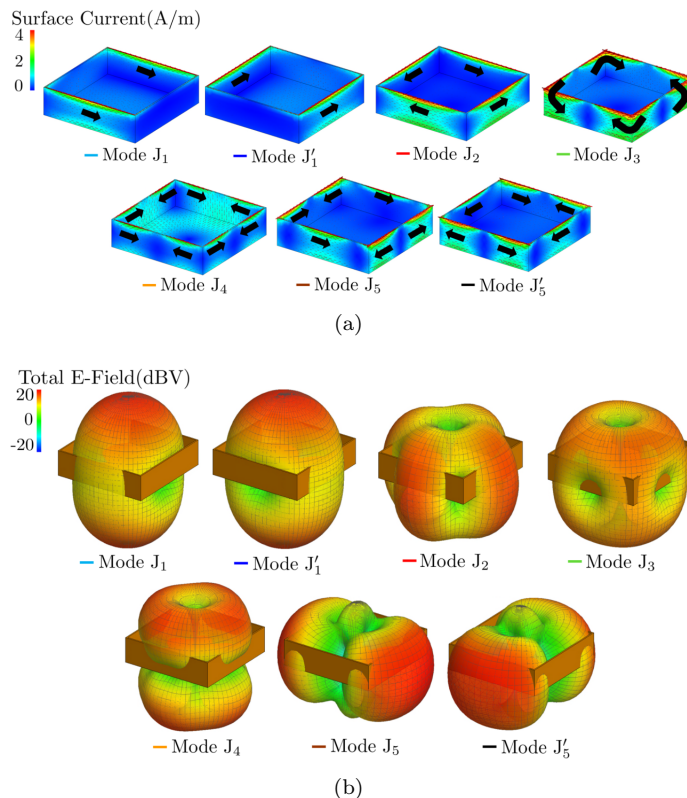
Figure 4.7: a) Current distribution of modes J_1-J_5, b) Radiation patterns of
modes J_1-J_5.

4.2   Cavity-backed Circular Monopole Antennas

In this section, the previously analyzed cavity (a×a×b) is fed by two and
four independent monopoles to obtain multiple-port cavity-backed antennas.
Feeding the cavity with monopoles in the perimeter permits a maximum of 4
independent ports with identical performance. Monopoles must be placed at a
minimum current level, and several modes have a current null in the middle of
each side where the monopole will be installed. In addition, monopoles permit
lower profile designs than dipoles due to their lower input impedance.

In Fig. 4.8(a), the square cavity with the two monopoles is depicted. In
a circular monopole, the currents flow through the contour, then $\frac{\lambda_1}{4}=\frac{2\pi r}{2}=\pi r$
which is depicted in the 4.8(a) obtaining a value of r=7 mm. The cavity presents

Square 2-Port Cavity-backed

(a)

(b)

(c)

Figure 4.8: a) View of the 2-Port Cavity backed antenna, b) S-parameters of Port 1 and, c) S_{21}(dB) for parametric b.

a 65x65x17.5 mm^3 size where the ratio a+2b=λ_1 is respected. The minimum desired operating frequency is f1=3 GHz, then λ_1=100 mm. In the square plate (b=0) the first mode (J_1/J_1') resonates when a=$\lambda/2$, but when the plane is reshaped to a cavity (a×a×b where a+2b=λ_1), the resonance frequency is shifted to higher frequency with b as seen in Fig. 4.2(a). In Fig. 4.7(b), the first Mode resonates at 2.5 GHz. That is one reason to fix the size of the cavity to a+2b=λ_1 and not a+2b=$\lambda_1/2$ which its first mode would resonate higher than 3 GHz after reshaping to the cavity. The second reason is isolation, depicted in Fig. 4.8(c) with parametric height b. For low values of b, the two monopoles are apart and show good isolation values but with poor matching because the monopoles are too close to the base of the cavity. The minimum accepted value for proper isolation between ports is 15 dB, and height b=17.5 mm is the highest value, which still accomplishes the minimum isolation level. Matching and isolation trade-off is optimum for b=17.5 mm, obtaining a design

with an impedance bandwidth ranging from 3.1 GHz to 6.4 GHz with 15 dB minimum isolation between ports (Fig. 4.8(b)).

(a)

(b)
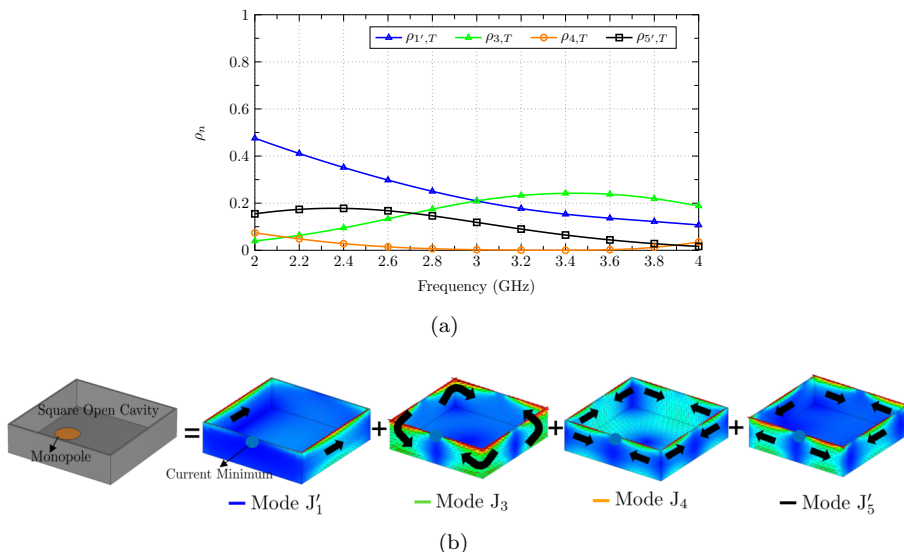
Figure 4.9: a) Correlation between modal and total fields, and b) Excited modes placed together.

To check which modes are excited when the cavity is fed with a monopole in the middle of a side of the cavity, the correlation between the total radiated fields (monopole+cavity) and the radiation patterns of each mode of the cavity is performed between 2 and 4 GHz. The correlation is represented in Fig. 4.9(a), and in Fig. 4.9(b), the contribution modes are placed together. It can be observed that all modes have a current minimum in the spot where the monopole is placed.

This first design demonstrates that a cavity, which is a 3D structure, can be analyzed from a 2D structure like the ground plane with characteristic modes, and a design with wide-band performance can be obtained.

Once the design with two monopoles is analyzed, including two more monopoles is addressed to obtain a 4-port cavity-backed antenna depicted in Fig. 4.10(a) to be operative from f_1=3 GHz. To maintain a minimum level of isolation between ports, the size of the cavity must be increased. The faced ports were previously decoupled in the 2-port design, but when two more monopoles are added, the isolation between contiguous ports is below 15 dB; thus, the separation between them must be increased—the size of the cavity results in a 97x97x20 mm^3, which results in a+2b=1.5λ_1.

Figure 4.10:   a) View of the 4-Port Cavity backed antenna, and b)
S-parameters of Port 1.

The S-parameters of the 4-port cavity-backed design are depicted in Fig.
4.10(b) with isolation between ports always higher than 15 dB and an impedance
bandwidth ranging from 3 GHz to 7.5 GHz.

It can be concluded that the analysis of cavities with CMA starting from
a square plane has been a success. Several constraints must be addressed
depending on the number of monopoles included. In terms of modal bandwidth,
it has been demonstrated that the shorter the cavity, the more bandwidth is
shown in the cavity. In terms of minimum operating frequency, the shorter
the b, the lower the first mode resonance. The second factor that needs to be
addressed is the isolation and the matching when installing the monopoles. It
has been demonstrated that for the 2-port solutions, the cavity must satisfy
$a+2b=\lambda_1$, and for the 4-port cavity, $a+2b=1.5\lambda_1$.

4.3   Cavity-backed Circular Dipoles Antenna

Cavity-backed dipoles are well-known and deeply detailed in the literature.
They are limited in terms of the number of independent ports because only
two dipoles can be perpendicularly installed in the center of the cavity. Dipoles
require higher profile cavities due to their higher input impedance in comparison
to monopoles and also obtain lower impedance bandwidth. As an advantage,
dipole-based solutions obtain higher isolation levels due to their orthogonal
disposition and provide more stable radiation patterns because fewer cavity
modes are excited.

In this section, we analyze a circular dipole backed by a 25x25x50 mm^3
cavity, which satisfies $a+2b=\lambda_1$ for f1=3 GHz (see Fig. 4.11(a)). The cavity

(a)

(b)

(c)

(d)
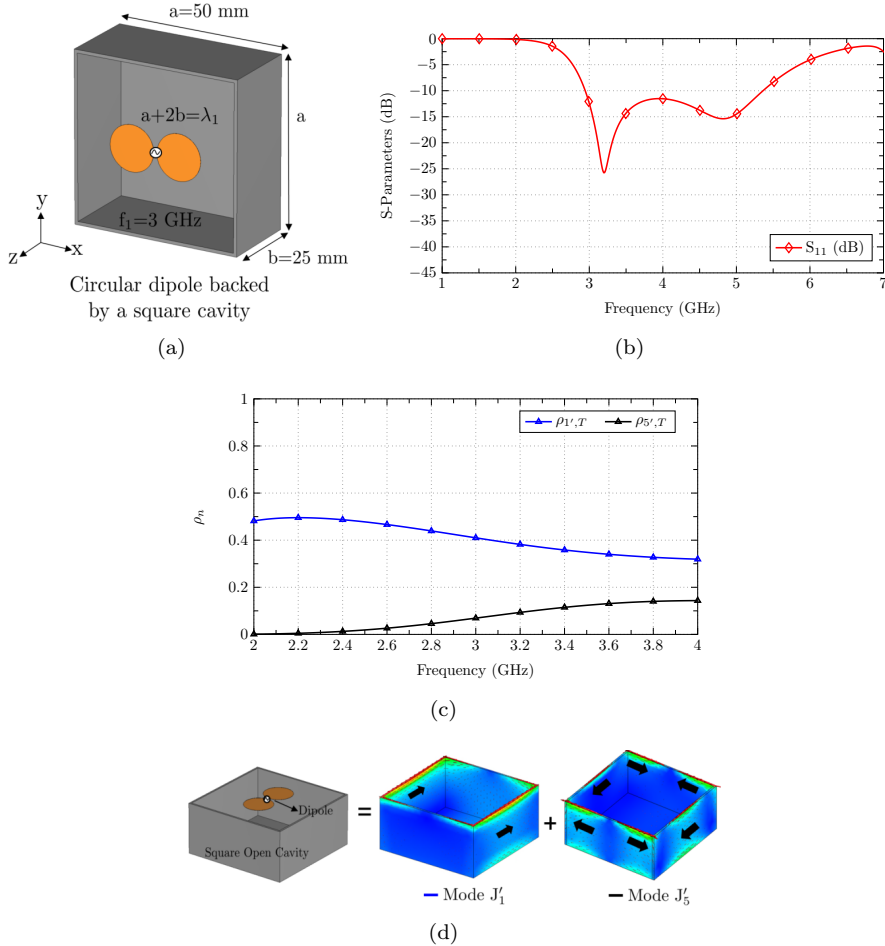
Figure 4.11: a) View of the Square cavity fed by a circular dipole, b) S-parameters of Port 1, c) Correlation between modal and total fields, and d) Excited modes placed together.

must be higher than in the case of the monopole-fed design with b=25 mm. Increasing the cavity height permits proper matching for the dipole with an impedance matching operating from 3 to 5.3 GHz. Bandwidth is limited due to the height of the cavity, which increases the slope of the characteristic angle of the modes and also because fewer modes are excited.

The correlations between total (dipole+cavity) and modal (cavity) radiation patterns are presented in Fig. 4.11(c). Only Mode J_1' and J_5' are excited

because they show a maximum electric field where the dipole is placed with a distribution flowing in the direction of the dipole currents. Fig. 4.11(d) depicts the design's decomposition into the cavity's excited modes.

With this second analysis, the two possibilities of feeding a cavity—a monopole or a dipole—can be compared. Monopoles permit lower profiles, wider bandwidths, and more independent ports. On the other hand, dipoles permit higher isolated designs and more stable radiation patterns.

4.4   Cavity-backed L-shaped Monopoles Antenna

In this section, a 4-port cavity-backed antenna with L-shaped monopoles is presented. It provides four independent unidirectional radiation patterns, with a total efficiency higher than 67%. The antenna presents an excitation with an impedance transformer with L-shaped monopoles, creating a bent-slot effect that decreases the input impedance and permits good matching of the analyzed band.

(a)

(b)

(c)
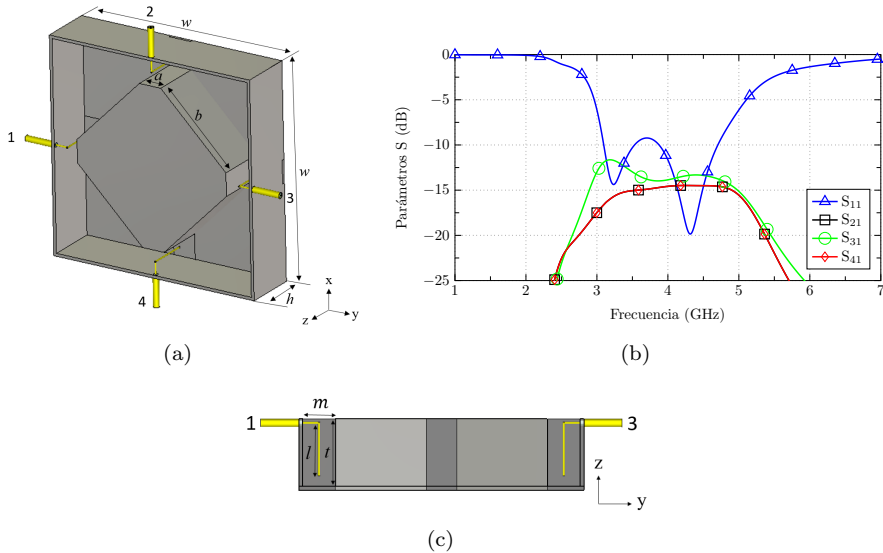
Figure 4.12: a) Picture of the 4-Port Cavity-backed Antenna fed by L-shape Monopoles, b) S-parameters of Port 1, and c) Side view of the proposed design. Dimensions are detailed in Table 4.1.

Fig. 4.12(a) presents the proposed antenna with a 75x75x18.75 mm^3 square cavity including an 8-side center block and 4 L-shape monopoles that feed the

w	h	a	b	l	t	m
75	18.75	8	33.77	14.22	17.75	8.62

Table 4.1: Dimensions of the proposed antenna (unit: mm)

cavity in the middle of the four sides. The center block creates an impedance transformer using the L-shaped monopoles and the cavity which can be reinterpreted as a bent slot.

The S-parameters of Port 1 are depicted in Fig. 4.12(b) presenting an impedance bandwidth ranging from 3 to 5 GHz ($S_{11} <$ -6 dB) and isolation higher than 12 dB. Including the center block permits higher isolation between contiguous ports but increases the coupling between faced ones because it creates a direct bridge where the currents can flow.

Feeding is provided by four 50 Ω coaxial cables located in the middle of each of the four sides of the cavity. A first simulation with direct feeding of the cavities shows a value of the real part of the input impedance between 150-350 Ω (Fig. reffig14). To match the design to 50 Ω, an impedance transformer is used with a 4 to 1 transformation ratio, obtaining the result presented in Fig. 4.14. The value of the real part of the input impedance is close to 50 Ω and permits good matching in the band of interest (3 GHz-5 GHz).
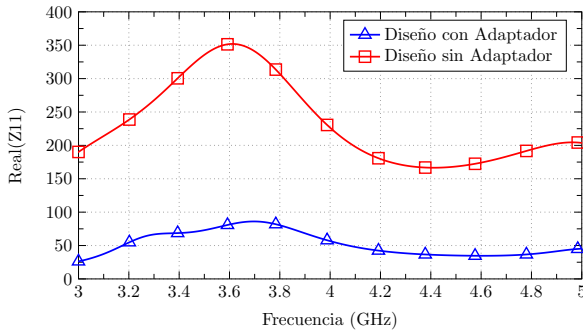
Figure 4.13: $\Re(Z_{11})$ of Port 1 with and without impedance transformer.

The impedance transformer has been realized by extending the inner conductor of the coaxial cable. It has been bent inwards into the cavities between the outer wall and the central block without making metallic contact (capacitive feeding). Using a circuit model with current sources (Fig. 4.14), an even and odd feeding decomposition has been performed to demonstrate the operation of the transformer.

(a)

(b)
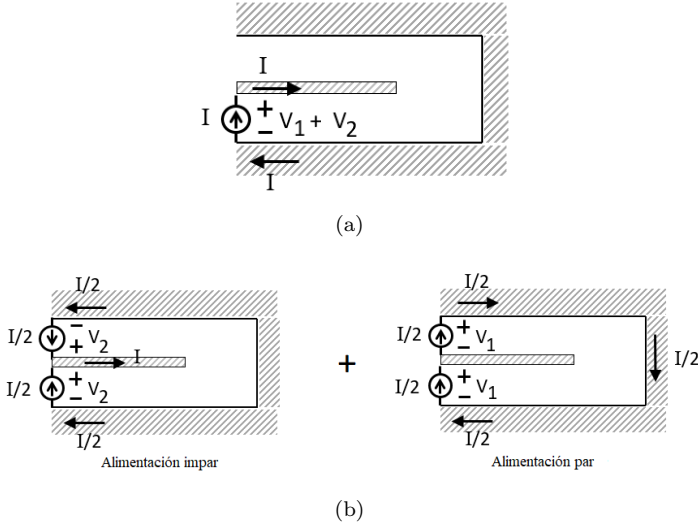
Figure 4.14: a) Impedance transformer b) Even and odd feeding transformer decomposition.

The input impedance of the transformer is defined by Z_t with Z_1 and Z_2 the corresponding impedances of the even and odd feedings.

$$Z_t = \frac{V_1 + V_2}{I} = Z_{even} + Z_{odd} \qquad (4.1)$$

The even feeding is equivalent to feeding the slot, as seen in Fig. 4.15(a). With this equivalence, the Z_{11} impedance is obtained:

$$Z_{slot} = \frac{2V_1}{\frac{I}{2}} \qquad (4.2)$$

$$Z_{even} = \frac{Z_{slot}}{4} \qquad (4.3)$$

The image theory can simplify the odd feeding, becoming an open-ended transmission line (Fig. 4.15(b)).

$$\frac{V_2}{\frac{I}{2}} = -jZ_0 \cot(\beta l) \qquad (4.4)$$

$$Z_{odd} = -j\frac{Z_0}{2} \cot(\beta l) \qquad (4.5)$$

Finally, the input impedance of the transformer is obtained:

(a)

(b)
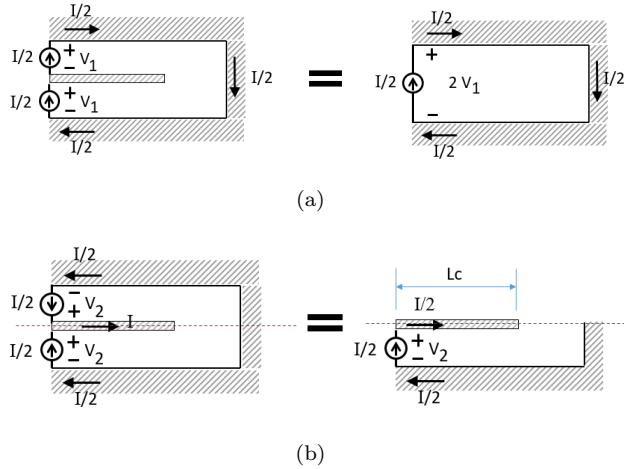
Figure 4.15: a) Even feeding, b) Odd feeding.

$$Z_t = \frac{Z_{slot}}{4} - j\frac{Z_0}{2}\cot(\beta l) \tag{4.6}$$

In Fig. 4.16, the directivity and total efficiency with the frequency are represented. The directivity present values are always higher than 7.35 dBi, and the total efficiency has an average value of 80% and a minimum value of 67%.
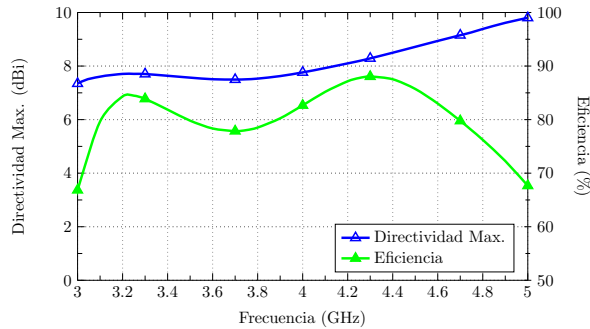
Figure 4.16: Directivity and total efficiency.

In Fig. 4.17 the radiation pattern at plane $\phi = 90°$ is represented for port 1 and 3 at 3 GHz(Fig. 4.17(a)) and 5 GHz(Fig. 4.17(b)). At low frequencies (3 GHz), the radiation pattern is broadside, pointing to $\theta = 0°$, but at higher

Figure 4.17: Port 1 and Port 3 radiation patterns at: a) f=3 GHz b) f=5 GHz

frequencies (5 GHz), the main lobe tilts to $\theta = 30°$. In both figures, the symmetry of the ports can be observed.

This design presents a novel feeding with a transformer and permits the decoupling of contiguous ports by using an isolating block in the center of the cavity. If the center block is big, the coupling between faced ports must be considered due to the current flowing directly through the block. This issue will be deeply analyzed in the next chapter.

4.5 Cavity-backed Crossed-Dipoles Antenna

In this section, the previous concept of a cavity-backed dipole antenna is further developed to obtain an eight-port wideband MIMO antenna composed of an aggregation of 4 unit cells. The overall view of the complete design is shown in Fig. 4.18 with a total size of 220×220×28 mm³ (2.42λ×2.42λ×0.3λ, at central frequency f=f_c=3.3 GHz) and dimensions are provided in Table 4.2. The unit cell has been designed with two orthogonal I-shaped wideband dipoles providing two orthogonal polarizations with highly isolated ports.

The feeding of the two dipoles is realized using two coaxial cables coming through the center of the bottom of the cavity and connected to the dipoles. The two dipoles are separated by 1.5 mm to properly feed them (Fig. 4.18). The 2×2 disposition provides eight independent radiation patterns for MIMO applications. Still, the geometry of this design supports an easy escalation to a massive MIMO system with an N×N replication of the unit cell. A cross-shaped block has been added to increase the isolation between unit cells.
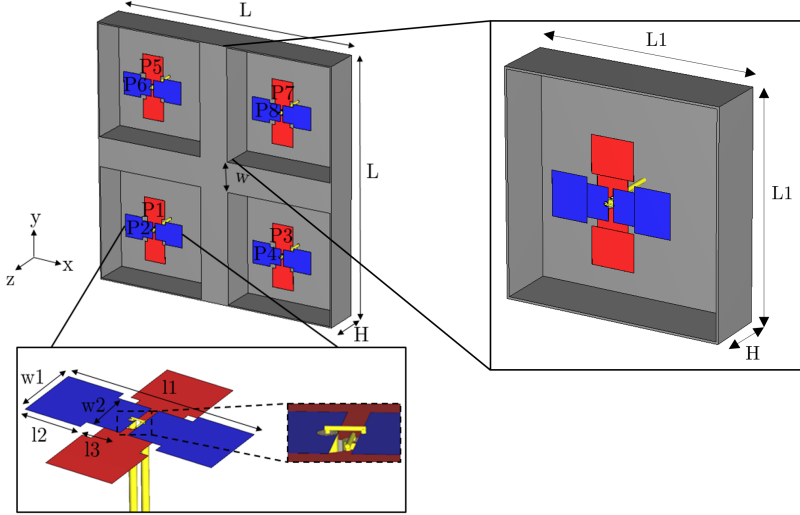
Figure 4.18: Geometry of the proposed antenna.

L	H	l1	l2	l3	w	w1	w2
220	28	55	16.5	10	25	19	15

Table 4.2: Dimensions of the proposed antenna (unit: mm)

Fig. 4.19 shows the S-parameters of the antenna. Due to the symmetry, only the S-parameters of P1 and P2 are shown. Results show an impedance bandwidth (S_{nn} <-10 dB, for n=1,2...8) of 97% ranging from 1.8 to 5 GHz. The isolation is always higher than 21.5 dB thanks to the orthogonal polarization and the isolating block between unit cells. Higher isolation is one of the main upsides of using crossed-dipole solutions, which is why there are so many standard solutions. As a downside, obtaining a design with a lower profile and a higher number of ports is possible if a monopole-based solution is used.

Fig. 4.20 depicts the simulated radiation patterns in the XZ plane (ϕ=0°) and the YZ plane (ϕ=90°) at 1.8 GHz (Fig. 4.20(a)),and 5 GHz (Fig. 4.20(b)). The antenna has a unidirectional pattern at the whole operating band.

An eight-port MIMO antenna is proposed for its installation in a 5G sub-6 GHz base station. The antenna comprises a 2×2 aggregation, defining as a unit cell, a cavity-backed antenna with crossed dipoles. The geometry of the unit cell permits scaling the design to an N×N aggregation for a massive MIMO system application. Results confirm a wideband behavior between 1.8-5 GHz, isolation higher than 21.5 dB, unidirectional radiation patterns, and high
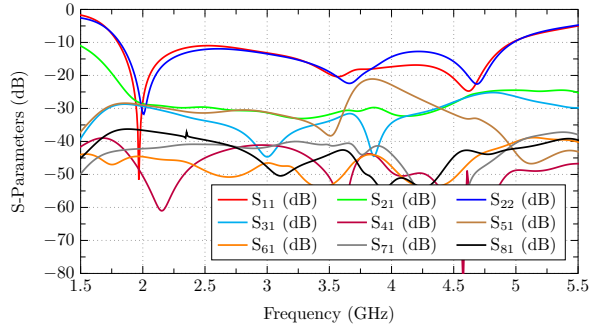
Figure 4.19:   S-Parameters of Port P1 (S_{22} also added).
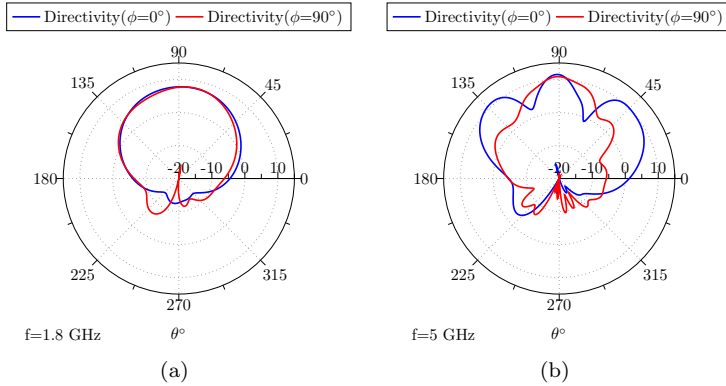
Figure 4.20: Simulated radiation pattern when Port P1 is excited. Plane $\phi = 0°$ (blue) and $\phi = 90°$ (red) at: a) f=1.8 GHz, and b) 5 GHz.

efficiency (higher than 87%). The analysis confirms that this antenna can be installed in 5G indoor access points.

This chapter presents a design procedure based on CMA to design cavity-backed antennas starting from the modes of a square plate and checking the modes conservation when it is reshaped to an open cavity. The main conclusions obtained are that in terms of modal bandwidth, the shorter the cavity is, the more modal bandwidth is shown, and also, in terms of minimum operating frequency, the shorter is b, the lower the first mode resonance. Isolation and matching limit the minimum height of the cavity so as not to have current cancelations and coupling. The height of the cavity is generally about $\lambda_c/4$ at the central frequency f_c. It has been demonstrated that for the 2-port solutions,

79

the cavity must satisfy a+2b=λ_1 and for the 4-port solutions, a+2b=1.5λ_1 for the minimum operating frequency f_1.

With the proposed procedure, multiple antennas have been successfully designed, showing unidirectional radiation patterns with high efficiency, high isolation, and multiple ports. These features make them suitable candidates for installation as antennas for indoor base stations.

In the next chapter, novel methodologies based on CMA will be introduced to overcome some limitations experienced in the design of previously proposed designs, such as the increase of isolation between ports in monopole-based cavity-backed designs and the reduction of simulation times of designs with a high number of ports, which become complex and time-demanding.

Chapter 5

Novel Methodologies based on CMA

In the previous chapter, multiple cavity-backed antennas were proposed using a design procedure based on CMA. Certain limitations in cavity-backed designs have been spotted. They are the isolation between ports, which limits the miniaturization of the designs, and the complex and time-demanding simulations of these kinds of solutions when the number of ports increases.

This chapter presents two CMA-based methodologies to address the two main limitations found in the previous chapter's designs. The first investigates the nature of the coupling in cavity-backed monopole antennas. The first introduces a solution, and the second presents a methodology that decreases the simulation time of cavity-backed designs with revolution symmetry.

5.1 Decoupling Methodology: 4-Port Cavity-backed antenna with X-shape Isolating Block

The isolation between ports is critical, especially when multiple-port solutions are installed in limited-space scenarios. Some of the techniques used for increasing isolation are based on using a decoupling element [123], a neutralization line [124], orthogonal polarizations [125]- [129], decoupling networks [130] and self-isolated/self-decoupled [131]- [133] antennas.

In this section, a four-port wide-band cavity-backed antenna is designed for sub-6 GHz 5G indoor access point applications using a decoupling methodology based on CMA. The design consists of 4 T-shaped monopoles arranged in an orthogonal and symmetric configuration. An X-shaped isolating block is included at the center of the cavity to increase the isolation between ports. The

design provides four independent unidirectional radiation patterns with high efficiency, MIMO capability, and wide-band impedance bandwidth. Due to the presence of the isolating block, it is not necessary to use differential feeding to isolate the ports, which would decrease the number of independent ports. Thus, hybrid couplers or baluns are not required here, turning the design into an easy-manufacturing, low-cost solution. It is appropriate to install it as an indoor MIMO access point antenna.

The novelty of the proposed methodology lies in the CMA-based methods used to obtain a four-port wide-band design by exciting clusters of orthogonal modes and identifying which contribute to the coupling between ports. This information introduces a proper isolating element (isolating block) to fade the non-desired modes. As a result of the inclusion of an isolating block, the coupling between ports is reduced to the minimum required for base station indoor applications, obtaining a four-port decoupled design that improves the performance of some antennas proposed in recent publications like [26]. Unlike the referenced designs based on characteristic modes, which try to excite a single mode per independent port, either using direct feeding or differential feeding, in the proposed design, each independent port excites a cluster of modes, providing the antenna's wide-band behavior. In addition, all the referenced designs are not 3D but planar designs based on simple structures. In the proposed design, characteristic modes are applied for the first time for analyzing an open cavity fed by monopoles, which is a 3D structure that involves high complexity.

Initial design

Our initial approach to designing a wide-band and unidirectional structure is based on combining wide-band elements. As shown in Fig. 5.1(b), the first element is a squared cavity that may exhibit unidirectional and wide-band behavior if properly excited. Taking advantage of the symmetry of this cavity, four independent feeding elements are placed in a symmetric and orthogonal arrangement in the middle of the four edges at the top aperture of the cavity (see Fig. 5.1(b)). This design is based on the previous chapter's cavity-backed monopole antenna but with a reduction in the size of the cavity, which introduces higher coupling between ports.

A wide-band excitation is necessary to attain a wide-band operation of the cavity. Therefore, T-shaped planar monopoles (shown in Fig. 5.1(a)) have been chosen for the design since they are easy to construct and present large impedance bandwidth.

The minimum operating frequency is determined by the length l_m (Fig. 5.1(a)) of the monopoles, since $l_m = \lambda/4$ at $f=f_{min}$. In addition, a minimum separation of $\lambda/2$ ($f=f_{min}$) is required between feedings to guarantee minimum
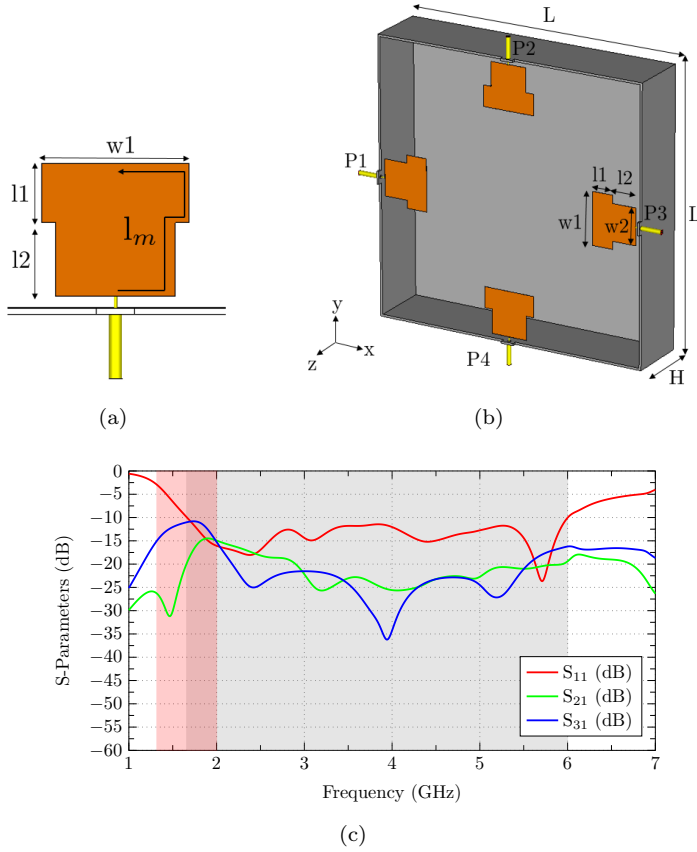
Figure 5.1: a) T-shaped monopole; b) Initial design with the squared cavity; c) S-Parameters of the initial design, where $S_{21}=S_{41}$ and $S_{31}=S_{42}$. The red area highlights the band with high coupling levels (1.35 to 2 GHz), whereas the grey area shows the operating bandwidth (1.55 to 6 GHz). Dimensions are detailed in Table 5.1.

L	H	w2	w2	l1	l2
130.5	29.2	24	18.5	9.5	11.5

Table 5.1: Dimensions of the initial design (unit: mm)

coupling. Four feedings (monopoles) have been incorporated, resulting in a minimum square cavity aperture perimeter of 2λ.

Considering these requirements, the antenna dimensions have been optimized for the sub-6 GHz 5G bands. The final dimensions of the structure are summarized in Table 5.1, resulting in an antenna with a total electrical size of $0.68\lambda \times 0.68\lambda \times 0.15\lambda$ (at $f = f_{min}$).

Fig. 5.1(c) shows the simulated S-parameters of this initial antenna. As observed, this cavity is a promising four-port wide-band solution with the drawback of low isolation between ports, especially between adjacent ports P1 and P2 at 1.35-2 GHz (see red area and S_{21} in Fig. 5.1(c)). This isolation is insufficient for installing the antenna in an indoor base station. Consequently, a modal analysis using CMA will be performed next to understand why there is a high coupling between ports and overcome the problem. Notice that the minimum matched frequency is f_{min}=1.55 GHz. Hence, the analysis will focus on 1.55-2 GHz, the band with coupling issues in the operating impedance bandwidth.

Modal Analysis of the open cavity

The electromagnetic analysis of a closed square cavity is well-known and described in the electromagnetic theory with field cavity modes. However, the information in an open cavity is not detailed, and the feeding elements would not be considered in a cavity modes analysis. For the proper understanding, we propose using characteristic modes analysis, an appropriate approach to analyzing an open cavity, including the four monopoles.

Figure 5.2: Characteristic angle of the initial design (solid curves) and final design (dashed curves).

Due to the complexity of the structure, the modal analysis of the 3D structure is limited to the frequency range from 1.1 to 2.1 GHz, considering only the lowest-order characteristic modes and including the band from 1.55 to 2 GHz, which has coupling issues. Nevertheless, identifying the first resonant modes at low frequencies helps to understand the antenna's behavior at higher frequencies.

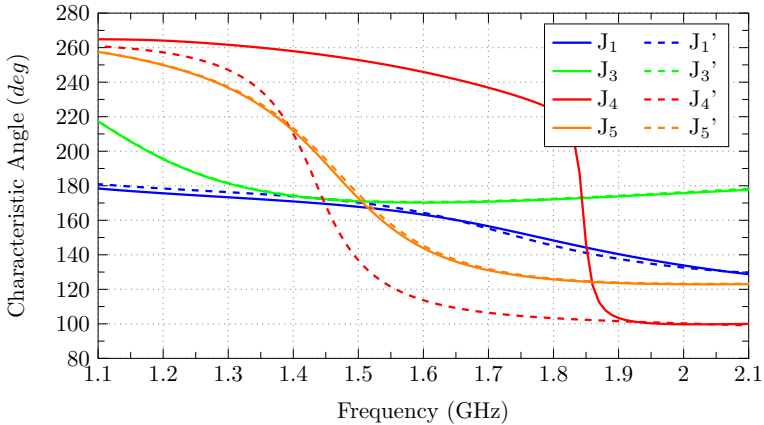Fig. 5.2 depicts the characteristic angle variation with frequency for the first resonant modes (J_n) of the initial design (solid lines) described in Fig. 5.1, which dimensions correspond with those of Table 5.1. Since J_1 and J_2 are degenerated modes, only the characteristic angle of J_1 is presented. As observed, all the analyzed modes resonate below 2 GHz.

Fig. 5.3 shows the current and electric near-field distribution associated with each mode at resonance. J_1 (Fig. 5.3(a)) and J_2 (Fig. 5.3(c)) are the horizontal and vertical fundamental modes, J_3 (Fig. 5.3(e)) is a mode with current nulls in the corners of the cavity and with current maximum at the center of the outer walls of the cavity. As observed, its electric field distribution E_3 (Fig. 5.3(f)) has a maximum at the corner of the cavities and a null at the center. J_4 (Fig. 5.3(g)) is a radial mode, in which the currents flow from the center of the cavity to the four monopoles and E_4 (Fig. 5.3(h)) has a maximum in the center of the cavity, with perpendicular direction. J_5 (Fig. 5.3(i)) has a distribution similar to that of J_3, but in this case, the current nulls are in the center of the outer walls and not in the corners. E_5 exhibits a maximum where the monopoles are located and a minimum in the center of the cavity. Regarding the electric field distribution of the modes, as can be observed, all of them have a TE distribution except E_4, which has a TM field distribution.

Since capacitive feeding is used in the proposed design, only modes with a maximum electric field at the feeding position will couple to the excitation. Fig. 5.4(a) and Fig. 5.4(b) present the Modal Weighting Coefficient (MWC) and the far-field power contribution obtained when port P1 is excited, respectively. It should be noted that both parameters depend on the excitation, but the MWC does not consider the port impedance matching. From these two figures, it can be seen that when port P1 (or port P3) is active, only modes J_1, J_4, and J_5 are excited. Due to the symmetry, when port P2 (or port P4) is active, only modes J_2, J_4, and J_5 will contribute to the total radiated power. Mode J_3 is not excited because it has a current maximum and minimum electric field at the feeding locations, so it does not couple with the feeding monopoles.

It is also observed that below 1.8 GHz, there is no dominant mode, but once mode J_4 resonates (at 1.84 GHz), it becomes dominant, contributing significantly to the total radiated power. In Fig. 5.1(c), it is detailed that the maximum coupling between ports P1 and P2 occurs exactly when mode J_4 resonates. These results reveal that the low isolation between adjacent ports from 1.55 to 2 GHz is due to the excitation of the radial current mode J_4.
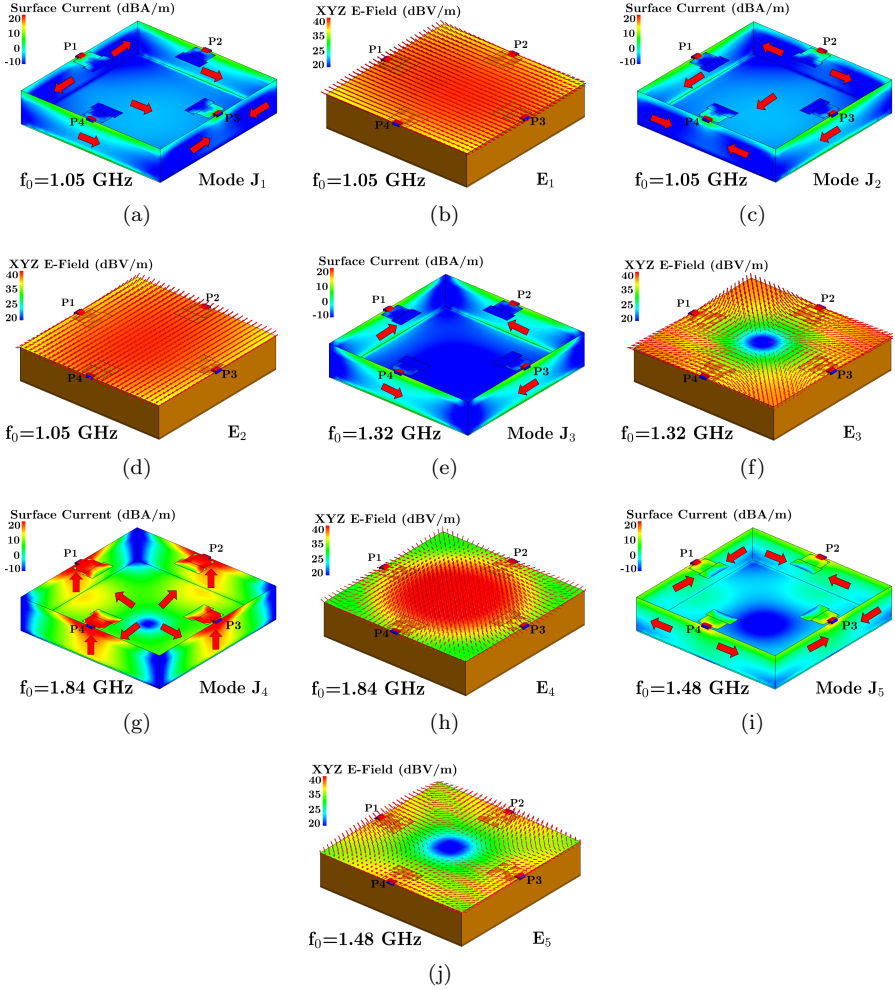
Figure 5.3: Instantaneous magnitude of the modal current distribution J_n and modal field distribution E_n at modal resonance f_0 of the initial design: a) J_1; b) E_1; c) J_2; d) E_2; e) J_3; f) E_3; g) J_4; h) E_4; i) J_5 and j) E_5.

The following subsection details a novel methodology based on CMA that improves the isolation between ports of this initial design.
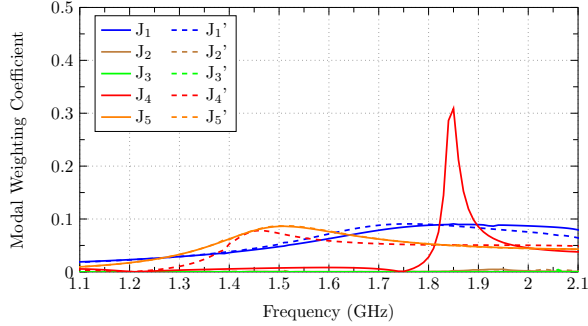
(a)
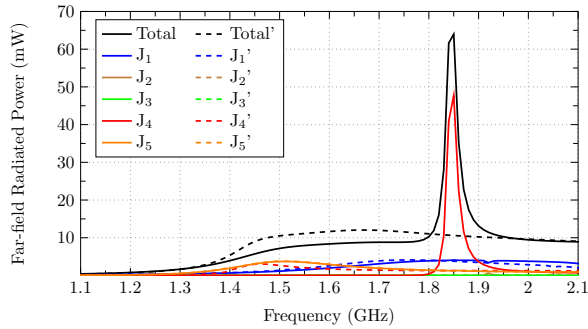
(b)

Figure 5.4: a) Modal Weighting Coefficient of the initial design (solid curves) and final design (dashed curves), and b) Far-field power contribution of the initial design (solid curves) and final design (dashed curves).

Decoupling Methodology

The initial design presents low isolation between adjacent ports in the frequency range between 1.55 and 2 GHz. At this stage, a full-wave analysis does not provide clear information about the coupling because the total currents and total fields combine several modes, so it is difficult to identify the reason for the coupling. In the previous subsection, CMA has been applied to determine the modes of the square cavity that are excited when one of the feeding monopoles is activated. This section aims to use CMA to identify which modes are causing the coupling between ports already observed. The modal analysis reveals that a decoupling structure placed in the center of the cavity is a good solution for fading the non-desired modes.
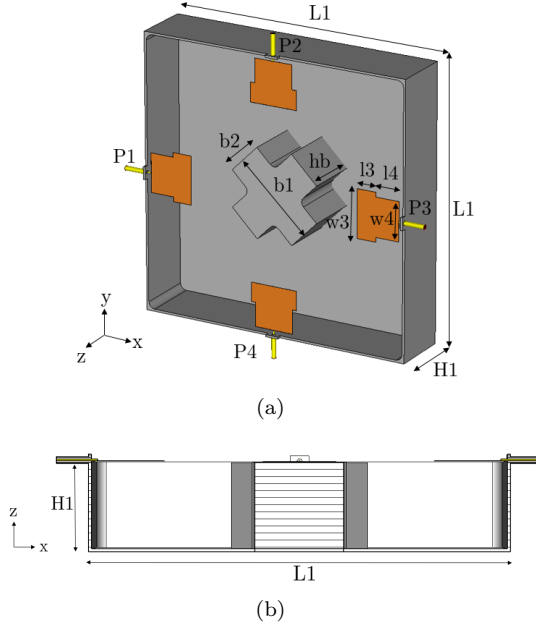
Figure 5.5: a) The overall view of the antenna includes the four monopoles colored orange and the square open cavity with the X-shaped block colored grey, and b) the Side view of the design (XZ-plane). Dimensions are detailed in Table 5.2.

As demonstrated before, the far-field radiated power from 1.55 to 2 GHz obtained when port P1 is excited is mainly produced by modes J_1 and J_4 (Fig 5.4(b)). The current distribution of Mode J_1 (Fig. 5.3(a)) shows that the currents associated with this mode flow from port P1 to port P3. Since this current flow is orthogonal to ports P2 and P4, it can be concluded that mode J_1 is not responsible for the high coupling observed between adjacent ports.

L1	H1	w3	w4	l3	l4	b1	b2	hb
129.5	28.2	23.15	18.7	9.3	11.5	42.6	17.8	26.6

Table 5.2: Dimensions of the final design (unit: mm)

In contrast, mode J_4 has maximum contribution to radiation at the frequency in which the coupling between ports P1 and P2 is maximum (Fig 5.1(c)). Moreover, the current distribution of mode J_4 (Fig. 5.3(g) shows that this mode has minimum current at the center of the cavity, and the currents flow radially

towards the four monopoles. The current intensity associated with mode J_4 is high inside the cavity, and all the ports have intense induced currents, which cause coupling between ports.

Therefore, the modal analysis reveals that mode J_4 is responsible for the high coupling between adjacent ports at these frequencies.
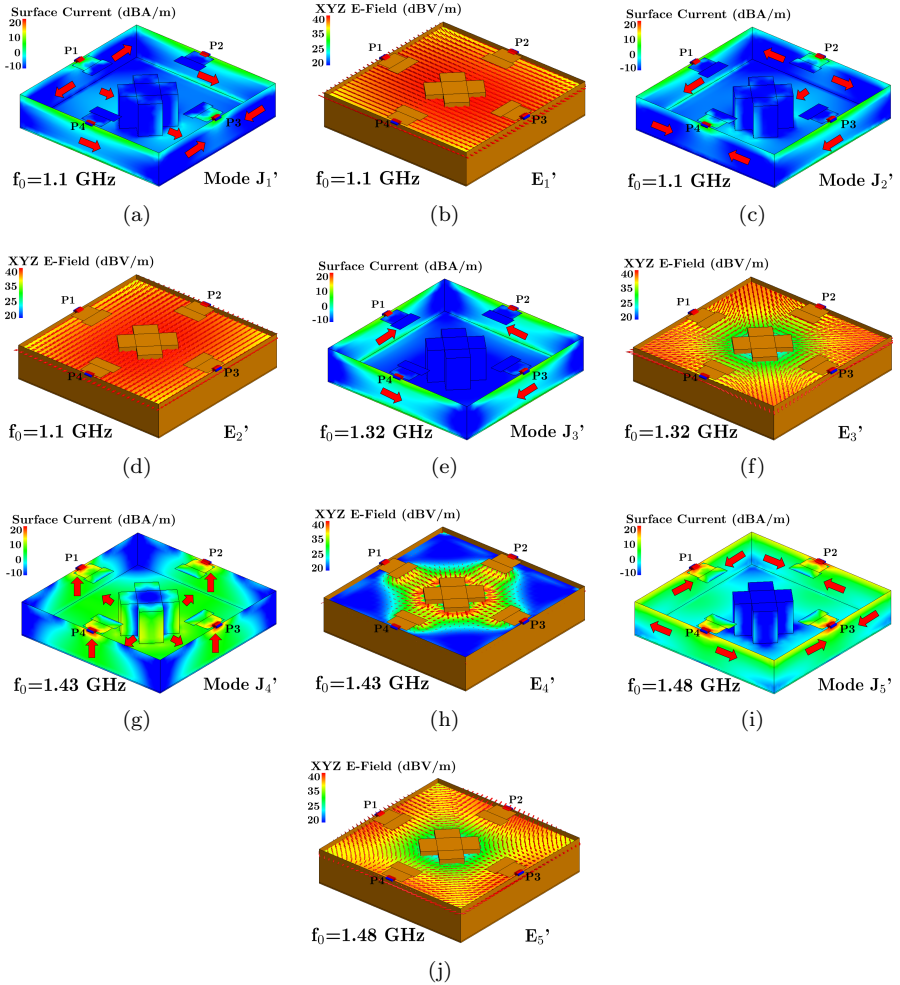
Figure 5.6: Modal current distribution J_n' and modal field distribution E_n' of the initial design at modal resonance f_0' . Instantaneous magnitude: a) J_1', b) E_1', c) J_2', d) E_2', e) J_3', f) E_3', g) J'_4, h) E_4', i) J_5' and j) E_5'.

As seen in Fig. 5.3(h), the electric field flows in the z-axis direction and exhibits a maximum in the center of the cavity. Mode J_4 has no variation in the z-axis, and the maximum magnitude is settled in the center. The solution taken to mitigate this mode is to place a metallic block in the center of the cavity. A metallic block placed in the center cancels the electric field in z-direction, changing the boundary conditions of the cavity. The final design is described in Fig. 5.5, and its dimensions are detailed in Table 5.2. The electric field distribution E_4 of mode J_4 cannot exist in this new scenario.

Different block shapes have been analyzed in the following subsection. All of them vanish mode J_4, but some geometries impact the other modes differently. The goal is to fade mode J_4 and not disturb the other modes. The chosen geometry is the X-shaped block, which will be justified in the following section.

To verify this effect, the modal analysis of the final design, including the isolating block, is presented in Fig. 5.6. The notation of J_n and J_n' represents the modes of the initial design without the isolating block (J_n) and the modes of the final design with the isolating block (J_n'). As observed in Fig. 5.5, the characteristic currents and characteristic electric fields have an identical distribution of those in Fig. 5.3 (structure without block), except for mode J_4'.

In Fig. 5.7 the characteristic angle and the far-field radiated power are depicted for the initial design (without block) and for the final block (with block), at the analyzed band with coupling issues (1.55-2 GHz). The inclusion of the block does not distort modes J_1, J_2 and J_3 (see J_1', J_2' and J_3' in Fig. 5.7(a)). However, J_4 is shifted to lower frequencies (see J_4'), and the peak power at 1.85 GHz fades due to the presence of the isolating block, as desired. As mentioned above, the mode J_4 vanishes due to the inclusion of the isolating block. However, it still appears at the characteristic angle representation (J_4'), resonating at 1.45 GHz and having some power contribution at resonance. The reason behind this phenomenon can be explained by the mode J_4' field representation. Fig. 5.6(h) illustrates the modal electric field distribution of mode J_4' at the aperture. Its electric field distribution has no component in the z-axis, showing a TEM-like field distribution.

In conclusion, the mode J_4 is responsible for the coupling in the initial design. To improve the behavior, an isolating block is used to vanish mode J_4, and a new J_4 mode appears when the final design modes are computed. J_4' mode represents a new mode created by including the inner block. The new J_4' mode does not impact the coupling because its electric and magnetic fields are maximum in the center of the cavity surrounding the isolating block.
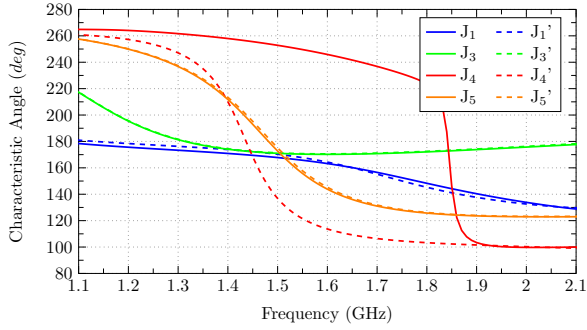
(a)
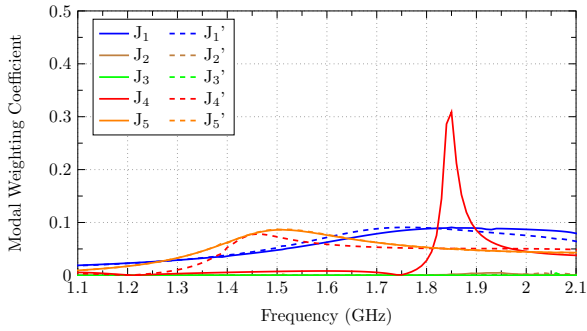
(b)
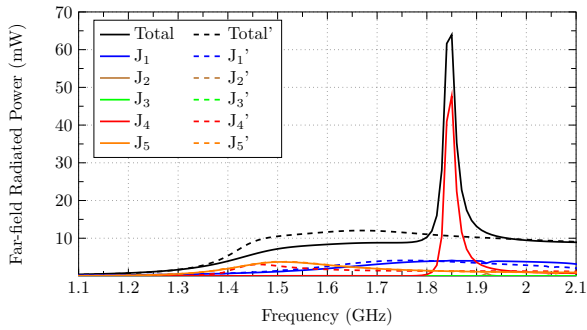
(c)

Figure 5.7: Initial design (solid curves), Proposed design (dashed curves): a) Characteristic angle, b) Modal Weighting Coefficient, and c) Far-field power contribution.

Isolating Block Geometries

In this subsection, a comparison of four different isolating-block geometries is presented in terms of coupling and matching. Figure 5.8 shows the four geometries: circular, rhombus, square, and X-shaped blocks.

As stated in the previous section, the goal of the isolating block is to vanish mode J_4' to increase the isolation between ports and not distort the modes contributing to the antenna's wide-band performance.
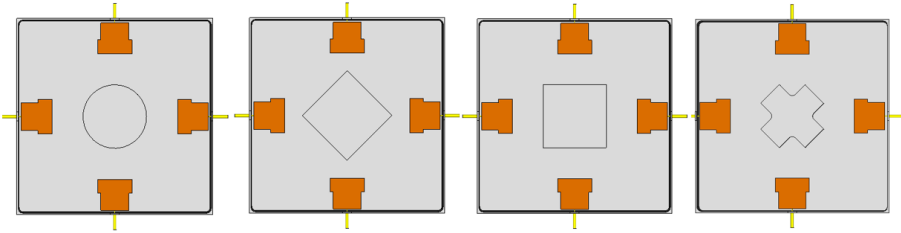
Figure 5.8: The four analyzed designs with different isolating-block geometries: circular, rhombus, square, and X-shaped.

Fig. 5.9(a) depicts the S_{11} parameter of all the geometries. The X-shaped geometry has excellent behavior with S_{11} <-10 dB in a wide range of frequencies. The circular geometry has matching issues between 5 and 5.4 GHz, the square geometry at 3.5 GHz and 3.9 GHz, and the rhombus geometry at 5 GHz.

The coupling between ports P1 and P2 can be determined by the S_{21} parameter depicted in Fig. 5.9(b). X-shaped and square block geometries perform well with coupling lower than S_{21} <-15 dB in the analyzed frequency range. The circular case has coupling issues at 3.3 GHz and the rhombus between 4.4-4.7 GHz.

The last analyzed parameter in Fig. 5.9(c) is the coupling between ports P1 and P3 (S_{31}). X-shaped and circular block geometries present coupling levels lower than S_{31} <-15 dB. The rhombus has coupling issues at 4.4-5.3 GHz and the square at 3.9 GHz.

	Circular	Rhombus	Square	X-Shaped
S_{11} <-10 dB	✗	✗	✗	✓
S_{21} <-15 dB	✗	✗	✓	✓
S_{31} <-15 dB	✓	✗	✗	✓

Table 5.3: Comparison table between isolating block geometries.
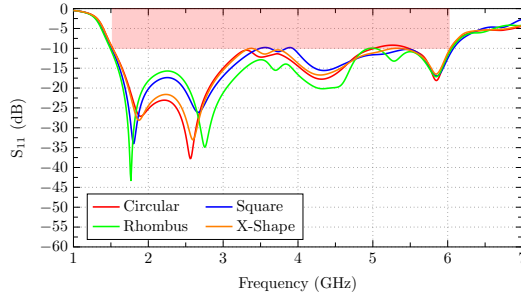
(a)
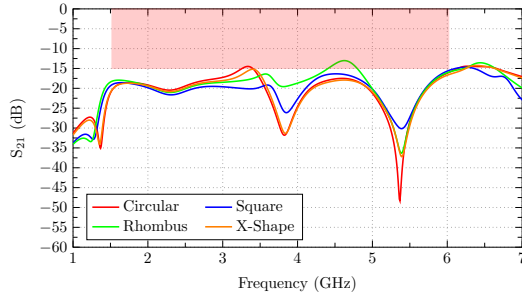
(b)
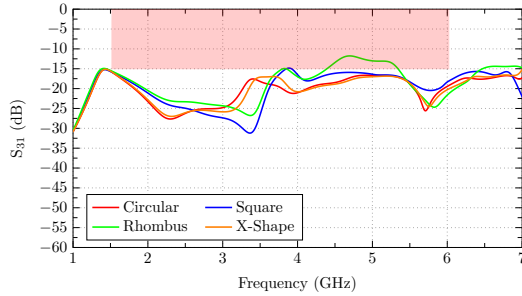
(c)

Figure 5.9: a) S_{11} of the four analyzed designs, b) S_{21} of the four analyzed designs and c) S_{31} of the four analyzed designs. Red area (values in the impedance bandwidth from 1.55 to 6 GHz in which minimum matching(S_{11}) or coupling (S_{21}, S_{31}) is not satisfied)

Table 5.3 summarizes the results obtained in the analysis. The X-shaped geometry is the most suitable due to the results obtained throughout the band.

The physical reason behind these results can be addressed with the size and geometry of the X-shaped block. The X-shaped block has a geometry that can vanish mode J_4 with a lower size than the rest of the blocks, hence, it is more innocuous to the rest of the modes which flow through the edges of the cavity. It does not interfere with matching or induce coupling due to its lower size. In addition, the X-shaped block does not have parallel sides to the monopoles, which would cause more coupling.

Final Design. Results and Fabrication

The final design includes an X-shaped isolating block and a Rogers R04003C PCB (ϵ_r=3.55, $\tan \delta$=0.0027 and thickness t=0.6 mm) containing the four monopoles (Fig. 5.10(a)) which leans on top of the cavity. The PCB is proposed to support the four monopoles that facilitate the fabrication process with negligible impact on the operation frequency. The PCB is included in all the measured and simulated results of the final design.

(a)

(b)

(c)

(d)
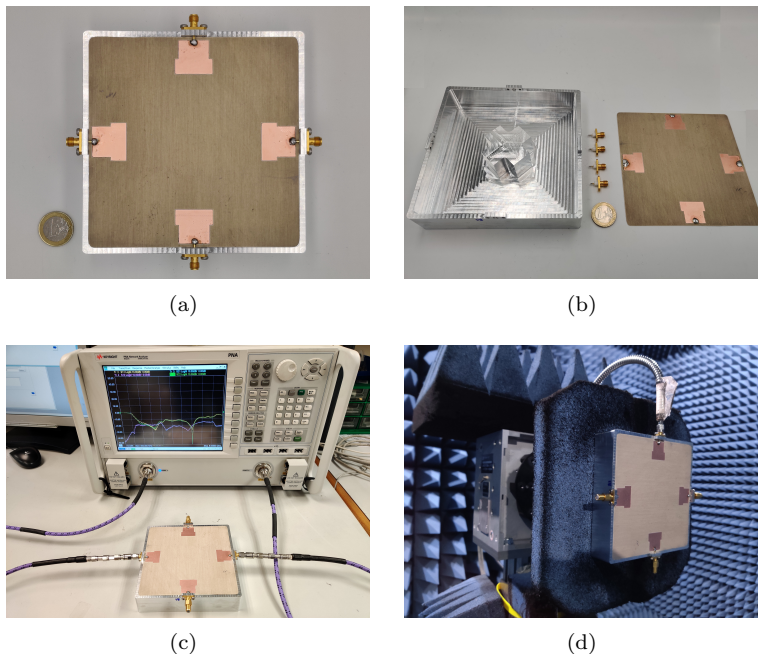
Figure 5.10: a) Fabricated Antenna b) Dissembled antenna c) Antenna set-up for the measurement with the network analyzer and, d) Antenna set-up for the measurement in the anechoic chamber.

The cavity and the isolating block have been milled from an aluminum piece, and the PCB has been placed on top. Lastly, four coaxial ports have been attached to each side of the cavity, welding the inner conductor to each monopole. In Fig. 5.10(b), the final design is disassembled to correctly identify all the components included in the design. The antenna has been measured with a network analyzer (Fig. 5.10(c)) and in an anechoic chamber (Fig. 5.10(d)). All the results are detailed below.
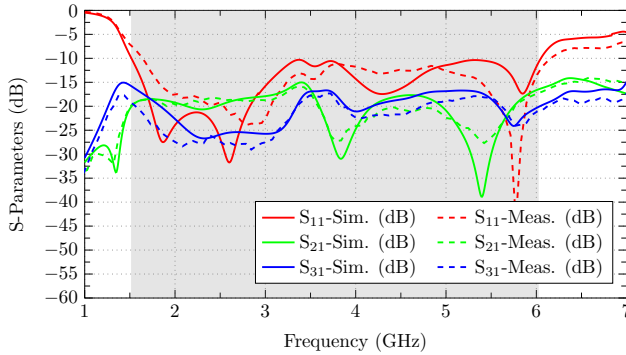
Figure 5.11: S-parameters of the final design. Due to the design symmetry, $S_{21}=S_{41}$.

Fig.5.11 presents the simulated (solid curves) and measured (dashed curves) S-parameters of the final design. Results confirm the wide-band behavior, with good matching from 1.55 GHz to 6 GHz with a slight difference between simulated and measured S_{11} due to fabrication tolerances. Regarding the measured isolation, it is higher than 16 dB through the band (see S_{21} and S_{31}). Measured isolation is slightly higher than simulated. Unlike the initial design (Fig. 5.1(b)), the desired minimum isolation level between ports of 15 dB is achieved.

Fig. 5.12 depicts measured and simulated radiation patterns in XZ plane ($\theta=0°$) and YZ plane ($\theta=90°$) at 1.5 GHz (Fig. 5.12(a)), 3 GHz (Fig. 5.12(b)), 4.5 GHz (Fig. 5.12(c)) and 6 GHz (Fig. 5.12(d)). At low frequencies, the radiation pattern presents a single lobe and side lobes appear as the frequency increases. The antenna has a unidirectional radiation pattern at the whole operating band, and there is good agreement between simulated and measured results.

In Fig. 5.13, the simulated and measured total efficiency curves are represented. Total efficiency values are higher than 84% for simulated results and 81% for measured results. The total efficiency (ϵ_t) is calculated as $\epsilon_t=G_r/D$ where G_r is the realized Gain and D the Directivity.
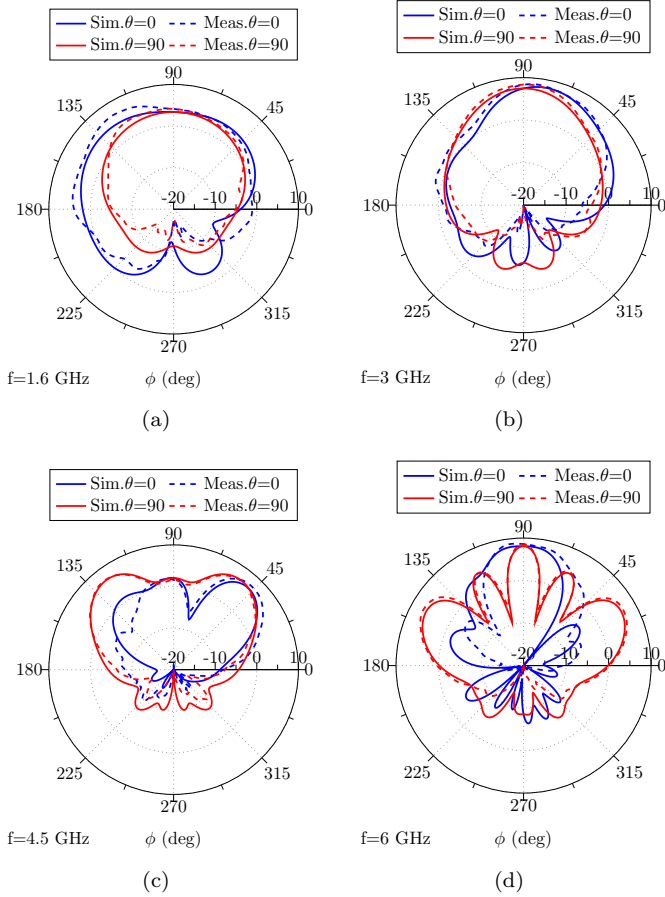
Figure 5.12: Simulated (solid) and Measured (dashed) radiation pattern when Port P3 is excited. Plane $\theta = 0°$ (blue) and $\theta = 90°$ (red) at: a) f=1.6 GHz, b) 3 GHz, c) 4.5 GHz, and d) 6 GHz.

To sum up, Table 5.4 compares the features of the most relevant recent publications of indoor base station antennas and the proposed design, highlighting the impedance bandwidth, the size, the isolation, the number of independent ports, and the total efficiency.

This section presents a four-port wide-band antenna with unidirectional and independent radiation patterns for MIMO indoor base station applications. Measurements and simulations show impedance bandwidth ($S_{11} < $ -10 dB) of 118 % (1.55-6 GHz), total efficiency higher than 84%, isolation between
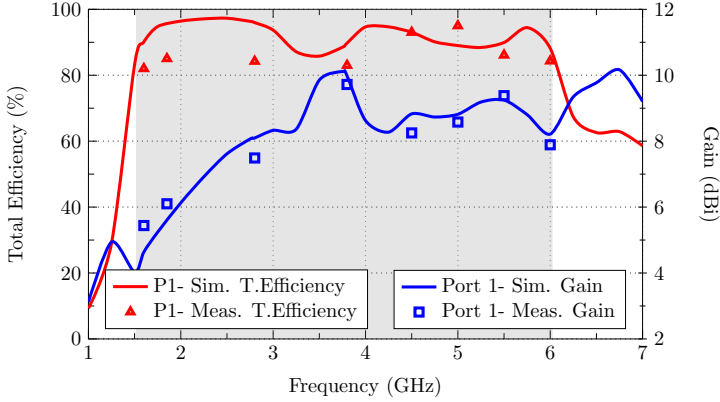
Figure 5.13: Total Efficiency (red-left axis) and Gain (blue-right axis) of port P1. The grey area (operating band 1.55-6 GHz).

ports higher than 16 dB, providing compatibility with a 4×4 MIMO system. The antenna has dimensions of 129.5×129.5×28.2 mm^3 and provides four independent ports in such a limited space due to the use of an isolating block that increases from 10.5 dB to 16 dB the isolation between adjacent ports. Furthermore, the design does not need differential feeding, which requires using hybrid couplers or baluns to obtain independent patterns and limits the number of independent ports. This feature makes this antenna easy to manufacture and a reasonable, low-cost solution.

For the design of the isolating block, a novel methodology based on CMA has been used to identify the nature of the coupling between ports. Decomposing the total currents and fields into modal currents and modal fields has provided valuable information to determine the mode (J_4) contributing to the coupling.

Ref.	BW (GHz)	BW (%)	Size (mm^3)	Is. (dB)	Ports
[134]	0.70-0.96/1.7-3/3.3-3.8	31 55.3 14	220×220×100	19	2
[22]	3.14-3.8/4.4-5	19.8 13.2	79.6×79.6×10	20	2
[23]	1.68-4.15	84.73	180×180×2.7	30	3
[135]	0.8-0.96 1.7-2.7	22 71.8	220×220×42	18	2
[26]	3.3-5	41	150×150×10	16.5	4
Prop.	**1.55-6**	**118**	**129.5×129.5×28.2**	**16**	**4**

Table 5.4: Comparison Table

The antenna has been fabricated, milling the cavity in an aluminum block and placing a Rogers PCB on top of the cavity, exhibiting good agreement between simulated and measured results. The proposed design is a proper candidate to be installed as a sub-6 GHz 5G indoor base station antenna because of its simple structure, compact size, and wide impedance bandwidth. Moreover, MIMO operation is also possible with the proposed design, as it includes four well-isolated ports with independent radiation patterns.

5.1.1 MIMO Channel

One of the most relevant features of 5G indoor base stations is that they are compatible with multiple-input multiple-output (MIMO) technology, which is crucial to providing high data rates. To ensure that the introduced 4-port cavity-backed monopole antenna is compatible with the MIMO system, we introduce the main parameters that must be calculated to check if the design would perform adequately in a real MIMO system environment.

In this section, the effect of the propagation channel is studied with the evaluation of the proposed antenna in a 4×4 MIMO system. The first analysis addresses the channel capacity calculation in mutual coupling, as proposed in [136]. The second analysis studies the envelope correlation coefficient (ECC) in different propagation conditions modeled by several angular distributions (uniform, Gaussian, and Laplacian).

Channel Capacity

Mutual coupling degrades the performance of a MIMO system [136], and one of the main concerns was to increase the isolation between ports of the initial design, especially at low frequencies. To quantify the improvement regarding the propagation channel when the isolation is increased, the channel capacity is calculated for the initial and final design at 1.8 GHz (the lowest isolation level for the initial design). It will quantify the effect of adding the x-shape block and its benefit.

For the calculation, the procedure detailed in [136] is followed. Still, in this case, four uncorrelated antennas are settled as transmitting antennas, and the four receiving antennas are those of the proposed design. The receiver is assumed to have perfect channel state information (CSI), but the transmitter does not. Furthermore, the analysis is calculated in an isotropic scattering environment. With these assumptions, the ergodic capacity can be calculated using (5.1) [136], where I is the 4×4 identity matrix, $\overline{\gamma}_0$ the reference SNR, R the correlation matrix of receive antenna and H_w the spatially white MIMO channel with independent and identically distributed (i.i.d) complex Gaussian entries. H_w^H denotes hermitian of H_w.
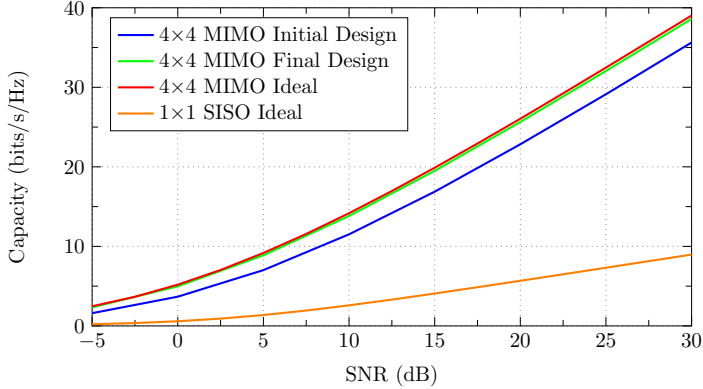
Figure 5.14: Channel Capacity.

$$C = E \left\{ \log_2 \left[\det \left(\mathrm{I} + \frac{\overline{\gamma}_0}{2} \mathrm{R} \mathrm{H}_w \mathrm{H}_w^H \right) \right] \right\} \tag{5.1}$$

Fig. 6.12 represents the capacity calculated for 100000 simulated channel realizations of a 4×4 MIMO system, setting as receiving antennas the initial design (blue curve), the final design (green curve), and an ideal receiver (red curve). In addition, the capacity of an ideal 1×1 SISO system (orange curve) is calculated for comparison. The results show an average 3 b/s/Hz increase between the initial and final designs. The final design provides results close to the ideal 4×4 MIMO system. It can also be observed that the 4×4 MIMO capacities are on average four times higher than the ideal 1×1 SISO system capacities.

Envelope Correlation Coefficient (ECC)

The envelope correlation coefficient (ECC) has become a standard parameter for measuring the performance of an antenna in a MIMO system. This parameter takes into account both the propagation conditions and the radiation pattern of the antenna and can be defined as (5.2) [136]. Generally, it is considered a low correlation level when the ECC is lower than 0.5 [126].

$$\rho = \frac{\iint\limits_{4\pi} g_1^H(\Omega) P a(\Omega) g_2(\Omega) \, d\Omega}{\sqrt{\iint\limits_{4\pi} g_1^H(\Omega) P a(\Omega) g_1(\Omega) \, d\Omega \cdot \iint\limits_{4\pi} g_2^H(\Omega) P a(\Omega) g_2(\Omega) \, d\Omega}} \tag{5.2}$$

Regarding equation (5.2), $g_1(\Omega)$ and $g_2(\Omega)$ describes the two analyzed radiation patterns, where the superscript ^{H} denotes Hermitian, $\Omega = (\theta, \phi)$ is the solid

angle of arrival and Pa(Ω) denotes the dyadic power angular spectrum of the incident field which is described by different angular distributions [137]. Usually, the ECC is calculated in ideal scenarios with isotropic scattering. Hence Pa(θ,ϕ) is assumed to be described by a uniform distribution (Pa(θ,ϕ)=1).

This section considers different Pa(θ,ϕ) to simulate different propagation conditions. The analyzed distributions are depicted in Fig. 5.16(a) including uniform (Pa(θ,ϕ)=1), Gaussian (5.3)(5.4) and Laplace (5.5)(5.6) distributions. For their comparison and simplicity, all the distributions exhibit their maximum at $\phi^\circ = 90^\circ$ and $\theta^\circ = 90^\circ$.
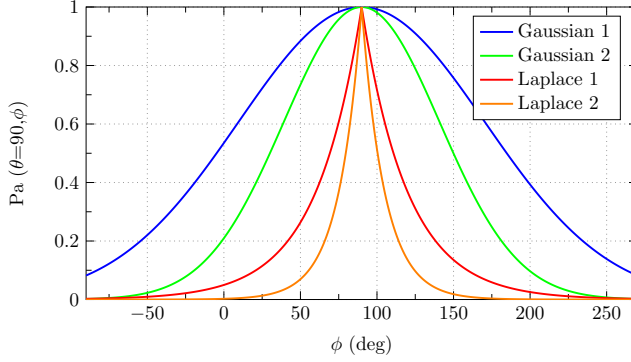
Figure 5.15: a) Analyzed angular distributions: Gaussian 1 (5.3), Gaussian 2 (5.4), Laplace 1 (5.5) and Laplace 2 (5.6) . b) ECC between P1 and P2 and c) ECC between P1 and P3.

$$Pa(\theta,\phi) = e^{(-(\theta-\pi/2)/(\pi/10)-(\phi-\pi/2)/(\pi/5))/10} \tag{5.3}$$

$$Pa(\theta,\phi) = e^{(-(\theta-\pi/2)/(\pi/10)-(\phi-\pi/2))/(\pi/5))/4} \tag{5.4}$$

$$Pa(\theta,\phi) = e^{-|\theta-\pi/2|/(\pi/8)-|\phi-\pi/2|/(\pi/4)} \tag{5.5}$$

$$Pa(\theta,\phi) = e^{-|\theta-\pi/2|/(\pi/16)-|\phi-\pi/2|/(\pi/8)} \tag{5.6}$$

In addition, the ECC is also calculated with an approximation using the S-parameters of the antenna (5.7) [138] under the assumption of an isotropic scattering scenario.

$$\rho = \frac{|S_{11}^* S_{12} + S_{21}^* S_{22}|^2}{(1 - (|S_{11}|^2 + |S_{21}|^2))(1 - (|S_{22}|^2 + |S_{12}|^2))} \tag{5.7}$$

(a)

(b)
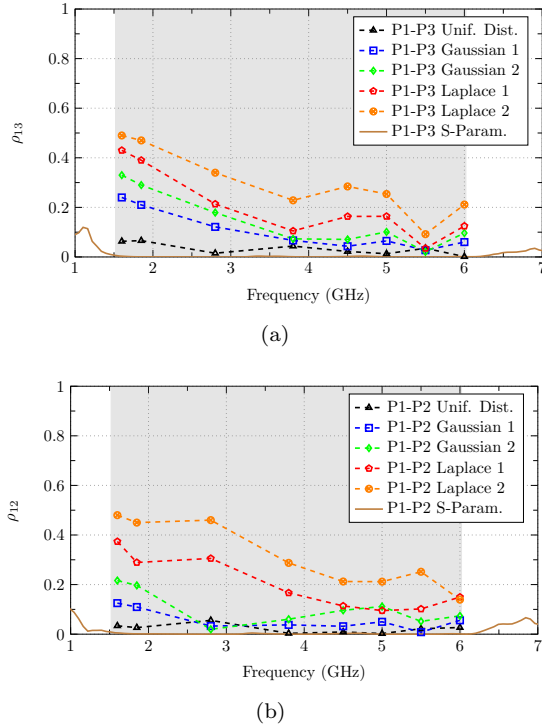
Figure 5.16: a) Analyzed angular distributions: Gaussian 1 (5.3), Gaussian 2 (5.4), Laplace 1 (5.5) and Laplace 2 (5.6) . b) ECC between P1 and P2 and c) ECC between P1 and P3.

Fig. 5.16(b) depicts the results of the ECC between P1 and P2 calculated with (5.2) using the 3D measured radiation patterns and the distributions represented in Fig. 5.16(a). Furthermore, the ECC is calculated with the measured S-parameters (5.7) and also added in Fig. 5.16(b). Fig. 5.15 represents the same analysis for P1 and P3. All the obtained correlation coefficients show an ECC<0.5. The best performance is obtained with the uniform distribution, followed by the Gaussian, and the most complex scenario is the one modeled with the Laplace distribution. It can be observed that the narrower the distribution is, the higher the higher the correlation coefficient is.

Due to the antenna's symmetry, the analysis of the ECC between P1-P2 and P1-P3 is enough to confirm uncorrelated radiation patterns and the proposed 4-port antenna's good performance in different simulated propagation conditions.

After analyzing the channel capacity and the ECC results, the proposed antenna is compatible and a good candidate for use in $4 times 4$ MIMO system applications.

5.2   Sector Unit Cell Methodology

A novel methodology based on the sectorization of multiple-port cavities with azimuthal symmetry into sector unit cells is presented to design 5G multiple-input multiple-output (MIMO) sub-6 GHz antennas. The methodology divides an N-port cavity antenna into N unit cells and predicts the performance of the N-port design with the analysis of two adjacent cells. This approximation reduces the time and complexity of the cavity antenna simulation with many ports. For the theoretical justification, cavity mode analysis of a closed cavity and characteristic modes analysis of open and sector cavities is addressed. This section presents five different cavity designs with circular, square, hexagonal, octagonal, and saw-tooth geometries with the proposed methodology. In addition, the fabrication of the 4-port circular shape design and its MIMO performance are also studied. Results show an impedance bandwidth of 130% (1.27-6 GHz) and an envelope correlation coefficient (ECC) lower than 0.1.

The tendency to increase the number of ports has led to complex designs with time and memory-consuming simulations. In array applications, Floquet theory proposes a methodology that studies the behavior of a periodic structure with a Cartesian coordinates system-based symmetry, analyzing only a unit cell, simplifying the simulation process. Recent articles apply Floquet theory for the design of arrays [139], reflect-arrays [140]- [141] and meta-surfaces [142]. This section proposes a novel methodology based on polar coordinate system symmetry that benefits from the field distributions' azimuth periodicity. Cavity and characteristic modes are used to analyze a closed and open circular coaxial cavity and different angle sectors. Characteristic modes analysis is introduced to study open cavities, which the classical theory of cavity modes can not analyze.

The proposed methodology guarantees that the analysis of two adjacent cells is enough to predict the performance of an N-cell antenna, simplify the designing process, and reduce the time of simulations. The decrease factor is essential for designs with more ports, converting the proposed methodology into a proper candidate for simplifying the design of MIMO antennas. The novelty of this section leans on the proposed methodology, which has been successfully applied for the design of a 4-port circular open cavity, a 4-port square open cavity, a 6-port hexagonal open cavity, an 8-port octagonal open cavity, and an 8-port teeth-saw open cavity. For the octagonal design, using the proposed methodology reduces their simulation time by 26. The 4-port circular open-

cavity has been fabricated to demonstrate the viability of the methodology, and a MIMO compatibility study has also been provided with the calculation of the channel capacity and the envelope correlation coefficient (ECC).

Coaxial Cavities Analysis

This subsection addresses the analysis of a closed coaxial cavity, an open cavity, and 1/2, 1/4, 1/6, and 1/8 open cavity sectors. Fig. 5.17(a) shows the coaxial closed cavity, which will be denominated as the coaxial cavity. Fig. 5.18 presents the open coaxial cavity and its sectors. For the sake of comparison, they all have dimensions of r1=108.5 mm, r2=43.8 mm, and h1=34.2 mm, and the only difference is that the closed cavity has a top cover enclosing the structure, and the open cavity does not.

Closed cavities are described in the electromagnetic literature through the use of cavity modes, and the electric and magnetic fields have been derived for canonical geometries [143] including the coaxial cavity, which is analytically described in [144]. On the contrary, open cavities are not analytically described, so we propose using characteristic mode analysis to analyze open cavities and sectors.

The first five modes of the coaxial cavity represented in Fig. 5.17(a) are analyzed. In cavity resonators, a three-symbol subscript (mnp) is required to describe both transverse (mn) and longitudinal (p) variations. In this case, the z-axis defines the longitudinal variation and has been settled as the direction of propagation.

The analysis aims to check the azimuthal periodicity and symmetry of the first modes by dividing the whole cavity into several sectors. The sector subdivision would simplify the analysis and simulation of a multiple-fed cavity-based design and provide valuable information about the number of independent ports and the required type of excitation.

Fig. 5.17 depicts the analyzed coaxial cavity with r1=108.5 mm, r2=43.8 mm and h1=34.2 mm and the electric field distribution of the first resonant modes of the cavity: Modes TM_{010}, TM_{110}, TM_{210}, TM_{310} and TM_{410}. The azimuth variation of the electric fields, except TM_{010} (which has no variation), has a sinusoidal behavior defined by $\sin(\phi)$-TM_{110}, $\sin(2\phi)$-TM_{210}, $\sin(3\phi)$-TM_{310} and $\sin(4\phi)$-TM_{410}. The radial variation is equivalent in all of them.

With an inspection of the field distributions, division into N sectors can be observed depending on the azimuth variations of the electric field. For Mode TM_{110} two sectors are obtained, for mode TM_{210} four sectors, for mode TM_{310} six sectors and for TM_{410} eight sectors. The coaxial cavity could be segmented into N sectors, cutting the cavity through the maximums of the electric field (colored in red) and applying a condition of open-circuit. All the field distributions of the modes are present if one of the N sectors is analyzed
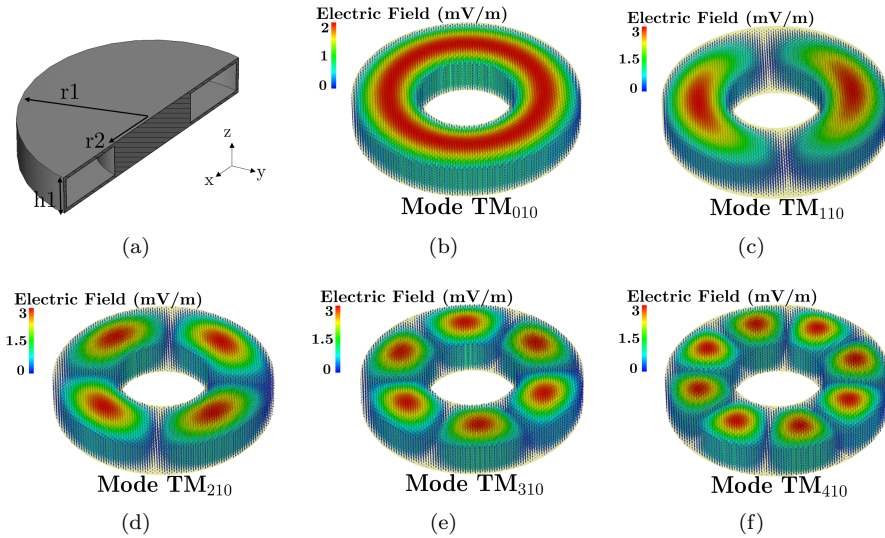
Figure 5.17: a) Section View of the coaxial cavity. Electric Field distribution of b) Mode TM$_{010}$ c) Mode TM$_{110}$ d) Mode TM$_{210}$ e) Mode TM$_{310}$ and f) Mode TM$_{410}$.

independently. This strategy would simplify the design process for multiple-port open cavities, whose simulation is time-demanding, especially when N is high. Since cavity modes cannot describe open cavities, we use CMA to deal with that issue in the following section.

CMA of an Open Cavity and its Sector Subdivision

Open cavities have different boundary conditions than closed cavities, and the available literature does not provide detailed information regarding modes. We propose using characteristic modes analysis, a proper approach for analyzing an open coaxial cavity.

This subsection addresses the characteristic modes analysis of an open coaxial cavity and its 1/2, 1/4, 1/6, and 1/8 sectors. Open coaxial cavity and sectors have equivalent r1, r2, and h1 (as depicted in Fig. 5.18). The open coaxial cavity has equivalent dimensions to the closed cavity analyzed in the previous subsection but without the top cover enclosing the cavity. The decision to analyze sectors with different sizes responds to the fact that N excitations will feed the open cavity and be divided into N identical subdivisions or unit cells. The cavity then can be reinterpreted as a unit cell replicated N times with azimuthal
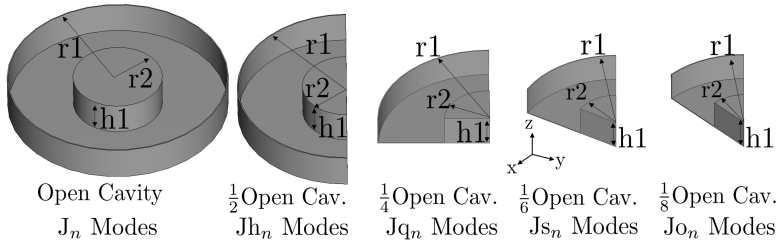
Figure 5.18: Open cavity and its 1/2, 1/4, 1/6 and 1/8 sectors picture.

periodicity. Commercial electromagnetic simulators can analyze unit cells with periodic boundaries when Cartesian axes of symmetry are used but not when boundary conditions with azimuthal periodicity are needed. Since the desired periodicity conditions cannot be simulated, open boundary conditions are set along the symmetry planes, which cut the open cavity into sectors. This subsection analyzes which modes are still present and which are filtered when the open cavity is reduced to different angle sectors. For the modes labeling, J_n will refer to the modes of the open cavity, Jh_n to the 1/2 open cavity, Jq_n to the 1/4 of the open cavity, Js_n to the 1/6 of the cavity, and finally Jo_n to the 1/8 of the open cavity.

Fig. 5.19(a) and Fig. 5.19(b) represent the characteristic angle of the five first resonant modes between 0.5-4.5 GHz of the open coaxial cavity and the equivalent modes after sectorization. The open coaxial cavity modes are denoted by J_n, the 1/2 sector modes by Jh_n, the 1/4 sector modes by Jq_n, the 1/6 sector modes by Js_n and the 1/8 sector modes by Jo_n. For their easier inspection, modes from J_0 to J_2 are represented in Fig. 5.19(a) and from J_3 to J_4 in Fig. 5.19(b). A shift in the characteristic angle of the sectors' modes is observed due to the inductive effect of currents flowing around their perimeter. Also, some modes vanish due to the modification of the structure. Generally, the behavior of the sectors' conserved modes is similar to the original modes of the cavity.

In Fig. 5.20, the modal electric field distribution at the corresponding resonance of the five first resonant modes of the open coaxial cavity and the equivalent modes of the 1/2, 1/4, 1/6, and 1/8 sectors is represented in z=h1=34.2 mm plane. Two kinds of modes are observed in Fig 5.20; mode J_0 presents an electric field distribution with only radial variation. The other modes have radial and azimuth variations in their associated radiated field. Since the electric field distribution of radial modes, like J_0, is constant in azimuth variation, these modes are always present in the cavity and all the analyzed sectors. Modes with azimuth variation (J_1-J_4) exhibit sinusoidal field distribution along the perimeter of the cavity. They risk vanishing if specific boundary conditions
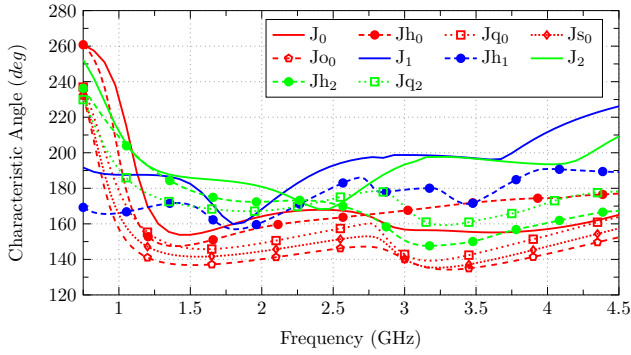
(a)
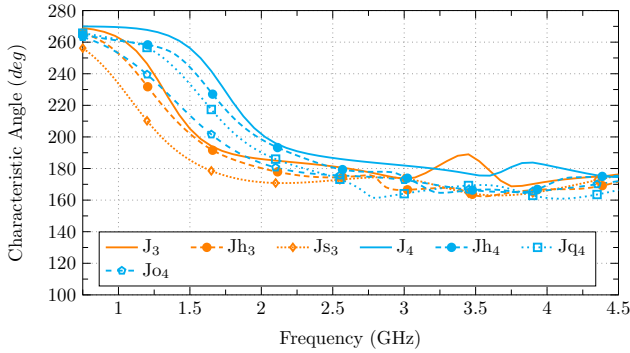
(b)

Figure 5.19: Open cavity and its $1/2$, $1/4$, $1/6$ and $1/8$ sectors: a) Characteristic angles from mode J_0 to mode J_2 and b) Characteristic angles of mode J_3 and J_4.

are unsatisfied when the open cavity is reduced to a sector. Since an open circuit boundary condition is set through the lines of symmetry when sectors are created, modes must exhibit maximum field distribution where the cavity is cut. Lines of symmetry that satisfy the previously specified conditions are depicted in black dashed lines in Fig. 5.20. If the cavity is split through the dashed lines, the mode will still be present in the created sector.

According to this analysis, it can be stated that modes with only radial variation will always be present when sectorization is applied. On the contrary, azimuthal variation modes are filtered depending on the sector's size. For the $1/2$ sector, all the modes are present except for the degenerated modes.
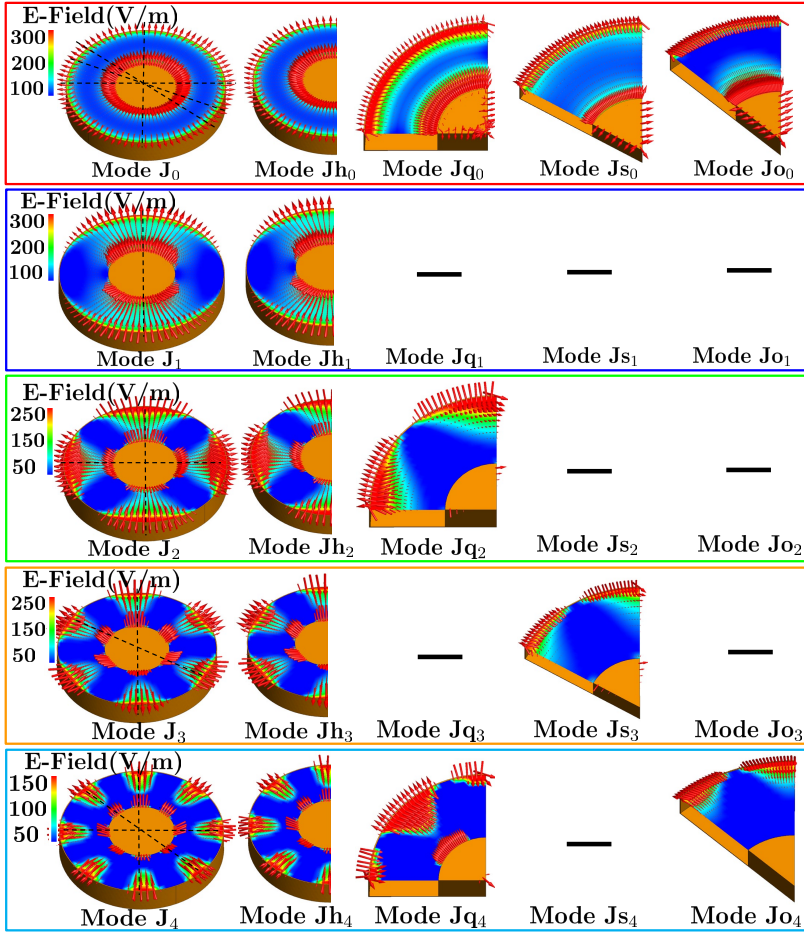
Figure 5.20: Modal field distribution at z=h plane of the open cavity and its 1/2, 1/4, 1/6 and 1/8 sectors from mode J_0 to mode J_4.

For the 1/4 sector, modes with $\sin(2n\phi)$ variation (n=1,2,3...) are present. 1/6 sector conserves $\sin(3n\phi)$variation modes and 1/8 sector presents $\sin(4n\phi)$ variation modes. In conclusion, azimuthal variation modes will be present when sectorization of 1/N sector is applied if an electric field distribution of $\sin(\frac{N}{2}n\phi)$ for n=0,1,2... is satisfied in the cavity. In Table 5.5, a summary of the conserved modes and their resonance frequency are depicted.

	J_0	J_1	J_2	J_3	J_4
Cav.	1.2 GHz	1.52 GHz	2.05 GHz	2.55 GHz	3.25 GHz
1/2 Sec.	1.05 GHz	0.65 GHz	1.48 GHz	2.05 GHz	2.5 GHz
1/4 Sec.	1 GHz	✗	1.2 GHz	✗	2.3 GHz
1/6 Sec.	0.9 GHz	✗	✗	1.6 GHz	✗
1/8 Sec.	0.88 GHz	✗	✗	✗	2.15 GHz

Table 5.5: Resonance frequency of the Modes.

CMA of Sectors with Equivalent Arc Length

In the previous analysis, the open cavity has been reduced to different angle sectors with constant r1 and r2 dimensions. The analysis proposed in this subsection studies the 1/2, 1/4, 1/6, and 1/8 sectors with equivalent arc length (d1) and height (h1) of open cavities with different dimensions (different r1 and r2) as represented in Fig. 5.21.
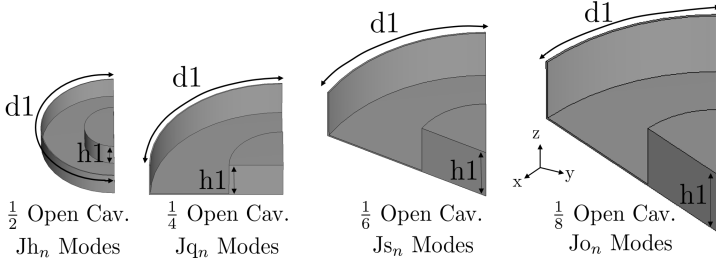
Figure 5.21: View of 1/2, 1/4, 1/6, and 1/8 sectors with equivalent arc length d1.

The motivation of the analysis responds to the fact of the future inclusion of feeding in the center of the arc (d1) of each sector (sector unit cell), creating an N-port design if the sector unit cell is replicated N times. Distance d1 should guarantee a minimum distance between ports to avoid coupling ($\lambda/2$ at f_{min} approximately) and define the resonance frequency of the azimuthal modes. If distance d1 between ports is respected, the size of the perimeter of the cavity will be determined by N×d1. The higher N is, the higher the cavity size is, and the first modes will resonate at lower frequencies. The operating bandwidth will not be defined by the first resonating modes of the cavity but by the bandwidth of the excitation. The excited modes of high N cavities will be higher-order modes of the cavity because the first modes are far from the frequency at which the feeding is operative.

In this study 1/2 (N=2), 1/4(N=4), 1/6(N=6) and 1/8(N=8) sectors of Fig. 5.21 with equivalent d1 are analyzed. The first two azimuthal resonating modes
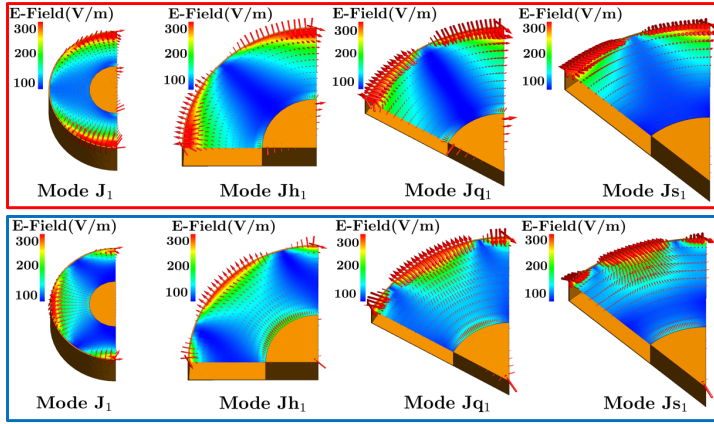
(a)
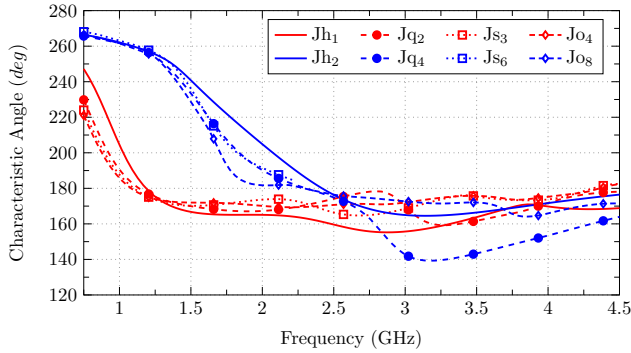
(b)

Figure 5.22: a) Modal field distribution at z=h plane of the first two resonant modes of the analyzed sectors, and b) Characteristic angle of analyzed sectors.

of the sectors are studied by representing the field distribution at resonance (Fig. 5.22(a)) and the characteristic angles (Fig. 5.22(b)). It can be observed that modes are resonant at approximately the same frequency (because d1 is equivalent), but modes come from different order modes of the complete cavity. It is then confirmed that if the cavity is scaled up with N×d1, there is always an excited mode that comes from a different order mode of the complete cavity, depending on N. The cavity size will not matter because d1 is respected, and the first modes (for high values of N) resonate at a frequency out of the bandwidth

in which the feeding is operative. The study confirms the conservation of the modes if d1 is respected.

Applying the Sector Unit Cell Methodology

The information obtained from the previous analysis is gathered and used in a certain design with azimuthal symmetry to apply the sector unit cell methodology. This methodology predicts the performance of an N-port cavity-backed antenna by analyzing only two of the N unit cells in which the antenna is divided.

In previous subsections, the modes of the coaxial open cavity and different angle sectors have been obtained. It has been demonstrated that radial modes are always present in both designs, but azimuth modes are filtered if certain boundary conditions are not satisfied when sectorization is applied.

Taking advantage of the information obtained regarding the conservation of the modes, we propose feeding an open cavity by N excitations arranged symmetrically and dividing the whole design into N sector unit cells. The new subdivision is called the sector unit cell and is composed of a sector of the cavity fed in the center of the arc length by a T-shaped monopole.

The methodology aims to simplify the analysis of the N-port design to the study of only a sector unit cell for impedance matching information and two adjacent unit cells for the study of isolation. In previous articles, coaxial cavities have been used due to their capacity to isolate faced ports exhibiting their minimum isolation level between contiguous ports. This feature guarantees that all design ports are isolated if two contiguous ports are decoupled. Sector unit cell methodology benefits from this feature and only ensures a good isolation performance by analyzing two contiguous unit cells.

The methodology leans on the fact that a minimum distance d1 (arc length of the unit cell) should be close to $\lambda/2$ at f_{min} to guarantee minimum isolation between adjacent ports. Since the perimeter of the cavity is obtained with N×d1, modes of the cavity from different orders but with the same field variation at the unit cell are excited. The excitation consists of a wideband T-shaped monopole whose f_{min} is set by the $\lambda/4$ path between the short (coaxial feeding point) and the open circuit (top edge of the monopole). The height of the cavity will be optimized due to its effect on the input impedance of the monopoles. Its value will always be constrained by a minimum of $\lambda/4$ and a maximum of $\lambda/2$ at the central frequency of the operating bandwidth.

In the following sections, two different cavity geometries are studied using the sector unit cell methodology, a first subsection for designing circular cavities and a second for designing regular polygon geometry cavities. For demonstration, a wideband 4-port circular coaxial cavity, a 4-port square coaxial cavity, a 6-port hexagonal coaxial cavity, and an 8-port octagonal coaxial cavity will be

designed using the proposed methodology. This design method decreases the time and complexity of the design and simulation of multiple-fed open cavity solutions, especially when the number of ports is high. The following sections will be demonstrated.

5.3 4-Port Circular Cavity-backed Monopole Antenna with the Sector Unit Cell Methodology

This section uses the sector unit cell methodology to design a 4-port circular cavity-backed monopole antenna. The four monopoles are placed in a symmetric and orthogonal fashion around the perimeter of the cavity. The number of unit cells is N=4, composed of a quarter of the cavity and a T-shaped monopole.

The methodology is summarized in Fig. 5.23(a). The first stage of the methodology is based on the optimization of the dimensions of the unit cell in terms of matching. In the second stage, two unit cells are analyzed, and the dimensions are slightly modified, if needed, to guarantee a minimum isolation level of 15 dB. Finally, in the third stage, the whole design with all unit cells is simulated to ensure the correct performance of the antenna. The optimized dimensions of the design are detailed in table 5.6, resulting in a cavity with a height h=λ/7 for f$_{min}$ and a distance between ports higher than d1=λ/2 to guarantee 15 dB of isolation level.

In Fig. 5.23(b), the S-parameters computed for the three stages are depicted, including the reflection coefficient (S$_{11}$(dB)) and the coupling between contiguous unit cells (S$_{21}$(dB)). Solid lines represent the coaxial open cavity design results, densely dashed curves of the Unit Cell, and dashed curves of the two adjacent cells. The reflection coefficient is slightly shifted to lower frequencies for the two unit cells and coaxial open cavity design due to the broader area where the currents can flow. Isolation is not in good agreement between 1-1.5 GHz, but the coupling level is not critical in this band. The S-parameters represented in Fig. 5.23(b) show highly correlated results of matching and isolation between the unit cells and the complete design, confirming the reliability of the methodology of designing N-port antennas with the analysis of sector unit cells.

r1	r2	r3	r4	h1	w1	w2	w3
107.5	44	5.7	2	33	11.2	23.1	2.9

Table 5.6: Dimensions of the circular 4P cavity design (unit: mm)

(a)

(b)
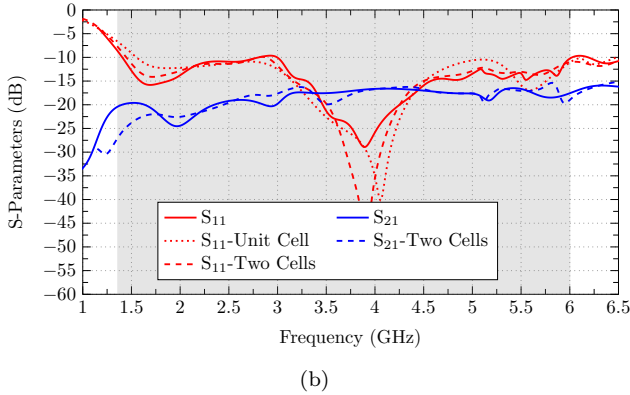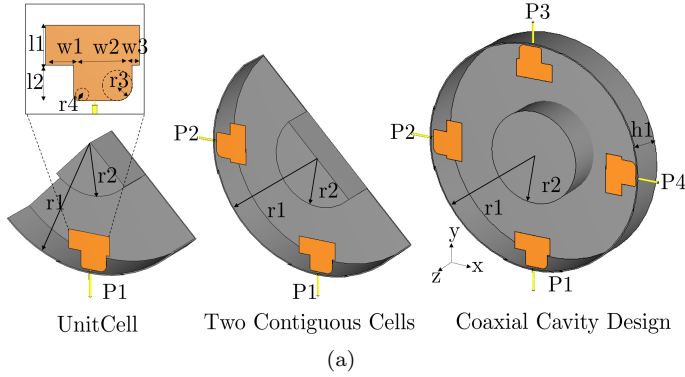
Figure 5.23: Unit cell, two contiguous cells, and the open coaxial cavity antenna: a) Overall view (dimensions in Table 5.6) and b) S-parameters.

The fabrication and MIMO performance of the 4-port coaxial antenna are presented next to prove the methodology's accuracy.

Results and Fabrication

The 4-port coaxial circular cavity antenna has been fabricated using a Rogers R04003C PCB (ϵ_r=3.55, tan δ=0.0027 and thickness t=0.6 mm) for supporting the four T-shaped monopoles (Fig. 5.24(a)) on the aperture of the cavity. The cavity has been milled from a solid aluminum cylinder. Four coaxial ports have been screwed and welded to the four monopoles.

Fig. 5.24(b) depicts the disassembled design for its correct inspection. The simulated (solid curves) and the measured (dashed curves) of the S-Parameters

(a)

(b)

(c)
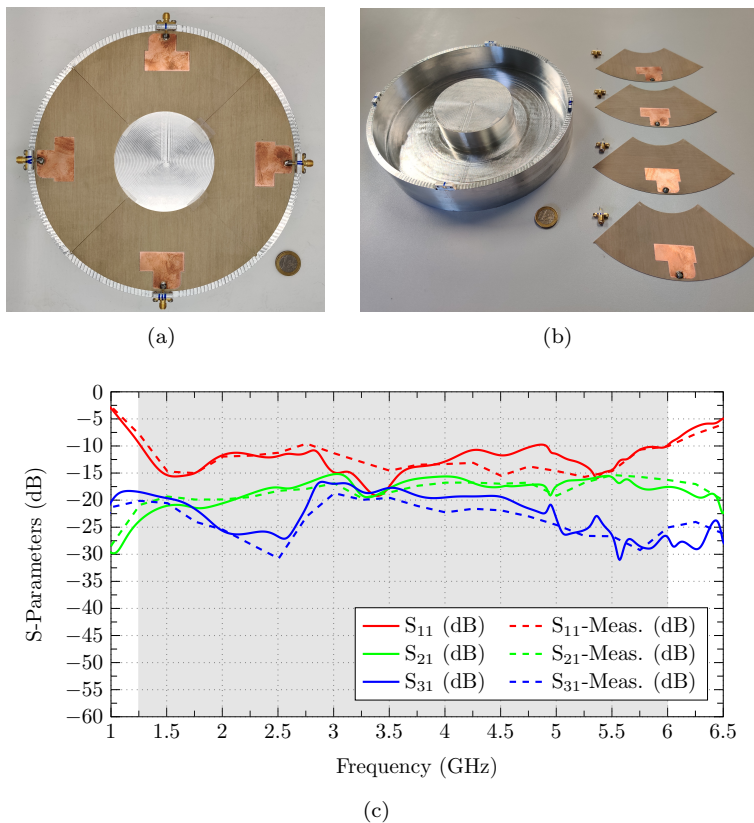
Figure 5.24: a) Front view of the Fabricated Antenna b) Dissembled antenna and, c) S-parameters.

are represented in Fig.5.24(c) with an impedance bandwidth ranging from 1.25 GHz to 6 GHz. The isolation is higher than 15 dB in the band (S_{21}(dB)=S_{41}(dB) and S_{31} in Fig.5.24(c)). Both are obtained using the Rogers PCB represented in Fig. 5.24(c). The S-parameters slightly differ from the results of Fig. 5.24(b) due to the inclusion of the Rogers PCB. In addition, the total simulated and measured efficiency and gain are represented in Fig. 5.25 with a good agreement between simulated and measured results. Results show a measured efficiency higher than 82% and an average peak gain of 8 dBi.

Regarding the radiation patterns, Fig. 5.26 depicts measured and simulated patterns in XZ plane (ϕ=0°) and YZ plane (ϕ=90°) at 1.5 GHz (Fig. 5.26(a)), 3 GHz (Fig. 5.26(b)), 4.5 GHz (Fig. 5.26(c)) and 6 GHz (Fig. 5.26(d)).
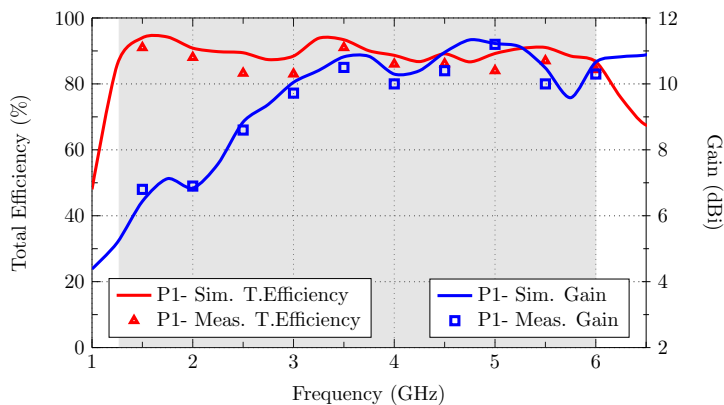
Figure 5.25: Total efficiency and Gain of Port1.

When the frequency is low, the radiation pattern comprises a single lobe. The radiation pattern is slightly disturbed when the frequency increases and side lobes appear. The antenna keeps a unidirectional radiation pattern in all the operating bands.

This first design presents a novel methodology based on the subdivision of an N-port cavity with radial symmetry into N sector unit cells for N-port MIMO antenna designs for 5G/Wi-Fi indoor access point applications. It can be concluded that the methodology simplifies the design and simulation process thanks to the approach based on the analysis of two contiguous cells. With the study of two contiguous cells, the performance of the N-port antenna can be predicted. For the physical insight justification of the methodology, a complementary cavity mode analysis of a close circular coaxial cavity and a characteristic mode analysis of a coaxial circular open cavity and its unit cell (1/4 of the open cavity) have been addressed. The study has demonstrated which modes are filtered due to the simplification of the cavity to the unit cell and which others remain. Radial and feeding modes are present, and modes with azimuth variation are filtered if a particular symmetry condition is not fulfilled. In the next section, the methodology is applied to design cavities with polygonal geometry which can afford a higher number of ports, hence the time saved in the design and simulation is highly decreased.

Figure 5.26: Simulated (solid) and Measured (dashed) radiation pattern of P1. Plane $\phi = 0°$ (blue) and $\phi = 90°$ (red) at: a) f=1.5 GHz, b) 3 GHz, c) 4.5 GHz, and d) 6 GHz.

5.4 Regular Polygons Cavity-backed Monopoles with the Sector Unit Cell Methodology

This section applies the Unit Cell Methodology to design coaxial cavities with regular polygon geometry. A feeding is connected in the center of each face of the polygon; hence, the number of ports N of the designs is equal to the number of faces of the polygon. A design with four ports has a square shape, six ports hexagonal, eight ports octagonal, and so on. The distance d1, which

describes the arc sector of the unit cell of the circular design and the distance between ports in these designs, is described more intuitively by the side length (Lx) of the regular polygon shape.
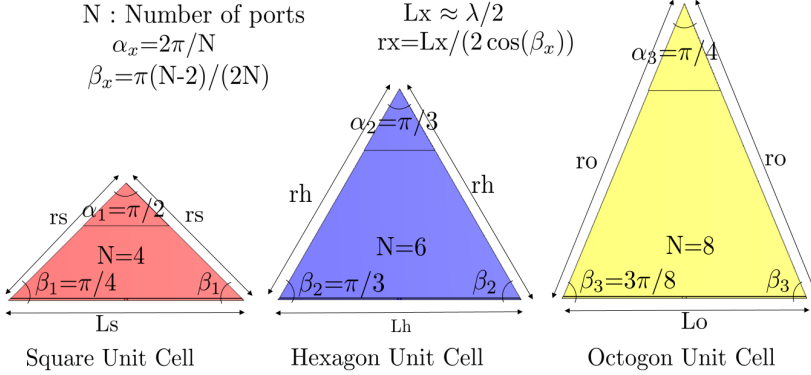
Figure 5.27: Unit cell equations and the obtained angles and dimensions for a square(N=4), hexagonal (N=6), and octagonal (N=8) open cavity designs unit cells.

A systematic design process is presented for optimizing the unit cell of an N port design with regular polygon geometry. The equations detailed in Fig. 5.27 are meant to be used with any regular polygon geometry unit cells. The distance between ports must be close to $\lambda/2$ at f_{min} to guarantee a minimum isolation level of 15 dB, hence $L_x \approx \lambda/2$. The angles β_x of the base of the unit cell increase with N, and it is defined by $\beta_x=\pi(N-2)/(2N)$. The top angle α_x decreases with N, defined by $\alpha_x=2\pi/N$. In Fig. 5.27, the unit cell of an N=4 (square cavity-red), N=6 (hexagonal cavity-blue), and N=8 (octagonal-yellow) cavities are obtained with the use of the proposed equations.

With this information, optimizing a unit cell of an N-port regular polygon geometry is simple and fast, no matter the number of N. This process limits the simulation and optimization process of the whole design to optimizing a unit cell and checking the isolation with a contiguous cell.

To check the viability of the methodology, three examples are presented in Fig. 5.28 with square (N=4), hexagonal (N=6), and octagonal (N=8) geometries. The three-unit cells have been optimized in terms of matching (S_{11}(dB)) at the first stage, including the monopole. Then, for isolation purposes, two contiguous unit cells have been analyzed. After these two studies, the whole design is simulated to check the correlation between the unit cell approximation and the entire design performance. The S-parameters of the three stages are represented for the three geometries, and only S_{11}(dB) and S_{21}(dB) are
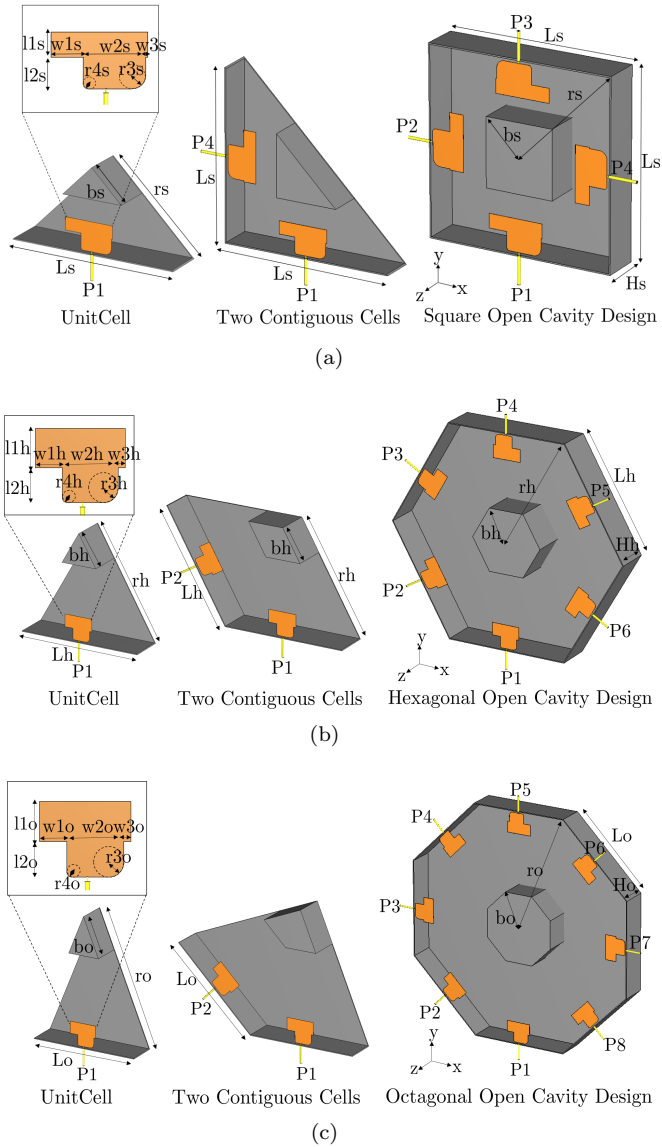
Figure 5.28: Scheme of the sector unit cell methodology for: a) square cavity-backed design, b) hexagonal cavity-backed design, and c) octagonal cavity-backed design.
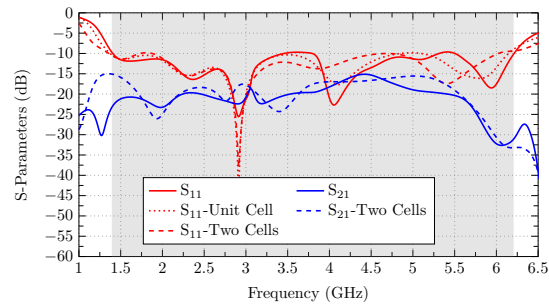
(a)
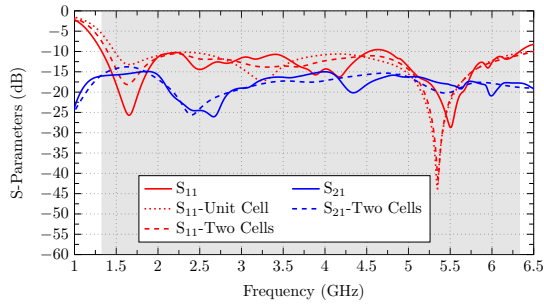
(b)
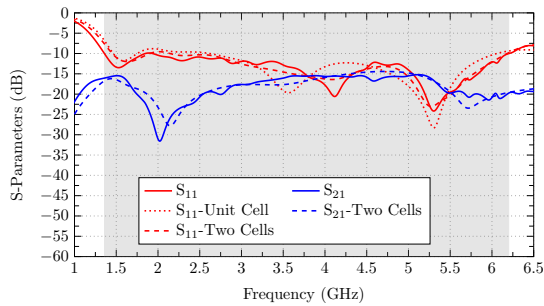
(c)

Figure 5.29: S-parameters of the unit cell, two contiguous cells, and complete design of a) square open cavity design, b) hexagonal open cavity design, and c) octagonal open cavity design.

described due to the symmetry of the design and also because contiguous ports show the lowest isolation levels (See Fig. 5.29).

118

	Lx	rx	Hx	bx	r3x	r4x	w1x	w2x	w3x
Square	138	97.5	28.5	36	5.8	2	13.7	26.6	0.9
Hex.	136.5	136.5	38.4	40	5	1.6	9.6	19.8	2.5
Oct.	129.7	168.5	40	50	5.1	1.7	10	20.6	2.6

Table 5.7: Dimensions of the initial design (unit: *mm*)

Results present a 4-port square open cavity, a 6-port hexagonal open cavity, and an 8-port octagonal open cavity with an impedance bandwidth of 126% (1.4-6.2 GHz), 130% (1.33-6.33 GHz) and 128% (1.36-6.2 GHz), respectively, with isolation always higher than 15 dB. Highly correlated results between the unit cell and the whole design confirm the viability of the methodology. Additionally, simulated total efficiency and gain are represented in Fig. 5.30, obtaining results higher than 82% of total efficiency.
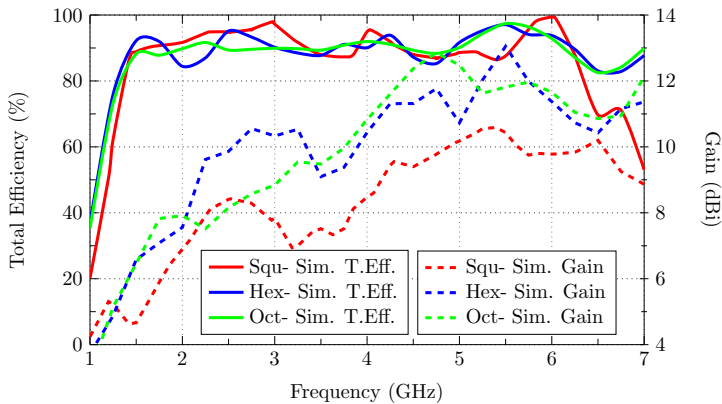
Figure 5.30: a) Simulated total efficiency and simulated gain of the square, hexagonal, and octagonal designs.

5.5   8-Port Saw-tooth Design with X-axis replication

All the designs analyzed so far are based on the unit cell methodology with the azimuth replication of a unit cell, creating closed cavity designs with canonical shapes. In this section, it is explored another way of designing cavity-based structures with the replication of the unit cell through the x-axis, obtaining a saw-tooth (linear array disposition) antenna (Fig 5.31).
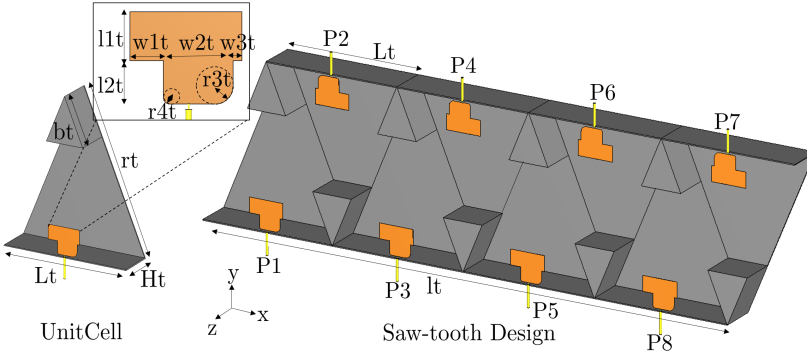
Figure 5.31: Scheme of the sector unit cell methodology for x-axis replication for the saw-tooth design. Dimension in Table 5.8.

Table 5.8: Dimensions of the saw-tooth design (unit: mm)

lt	Lt	rt	Ht	bt	r3t	r4t	w1t	w2t	w3t
555.5	138.8	180.45	35.9	50	5.1	1.7	9.5	22.3	1.5

In this case, the obtained design is not symmetric and involves more complexity than the previous ones. The methodology has been only used for the matching information prediction (S_{11}(dB) dotted curve of Fig 5.32(a)). The unit cell was obtained from the octagonal open coaxial design and slightly modified due to isolation problems in the saw-tooth design disposition. The separation between contiguous has increased because the coupling between contiguous cells experienced higher coupling values when replicated through the x-axis. Fig 5.32(a) shows the S-parameters of the saw-tooth design with an impedance bandwidth of 129% (1.46-6.85 GHz) and isolation higher than 15dB. Furthermore, simulated gain and total efficiency are represented in Fig 5.32(b) with an average 8 dBi gain and a total efficiency higher than 82%.

It is demonstrated that further distribution with different geometries can also be obtained with the replication of the unit cell, but only matching can be predicted. Isolation must be checked in the complete design due to the structure's lack of symmetry. This method of replication of the unit cells offers a new disposition, which increases the flexibility of this methodology's use.

This section presents a novel methodology based on the subdivision of an N-port cavity with radial symmetry into N sector unit cells for N-port MIMO antenna designs for 5G/Wi-Fi indoor access point applications. The methodology simplifies the design and simulation process thanks to the approach based on the analysis of two contiguous cells. With the study of two contiguous cells,

(a)

(b)
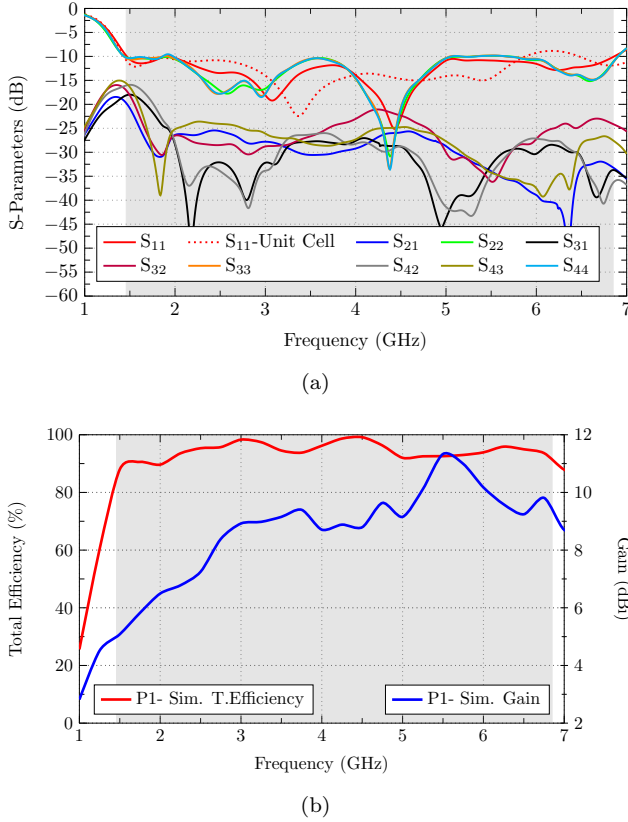
Figure 5.32: a) S-parameters of the unit cell, two contiguous cells, and complete design, and b) Port 1 simulated total efficiency and gain of the complete design.

the performance of the N-port antenna can be predicted. For the physical insight justification of the methodology, a complementary cavity mode analysis of a close circular coaxial cavity and a characteristic mode analysis of a coaxial circular open cavity and its unit cell (1/4 of the open cavity) have been addressed. The study has demonstrated which modes are filtered due to the simplification of the cavity to the unit cell and which others remain. Radial and feeding modes are present, and modes with azimuth variation are filtered if a particular symmetry condition is not fulfilled.

Five designs of N-port open cavities with circular (N=4), square (N=4), hexagonal (N=6), octagonal (N=8), and teeth-saw (N=8) shapes have been

Ref.	BW (GHz)	BW (%)	Size (mm^3)	Is.(dB)	N-Ports
[134]	0.7-0.96/1.7-3/3.3-3.8	31/55.3/14	220×220×100	19	2
[22]	3.14-3.83/4.4-5.02	19.8/13.2	79.6×79.6×10	20	2
[145]	1.55-2.75/3.3-3.8	55.8/14	150×150×48	30	2
[135]	0.8-0.96/1.7-2.7	22/71.8	220×220×42	18	2
[146]	3.5-5.1	37	27.2×27.2×17	18	2
[23]	1.68-4.15	84.73	159.5×159.5×2.7	30	3
[24]	3.3-4.2	24	70×70×11.5	15	3
[25]	3.3-4.5	31	100×100×10	15	4
[26]	3.3-5	41	133×133×10	16.5	4
[27]	3.1-7.2	80	195×195×14	20	6
Sq.	**1.4-6.2**	**126**	**138×138×28.5**	**15**	**4**
Hex.	**1.33-6.33**	**130**	**219.5×219.5×38.4**	**15**	**6**
Oct.	**1.36-6.2**	**128**	**284×284×28.2**	**15**	**8**
Saw	**1.46-6.85**	**129**	**555.5×166.6×35.9**	**15.1**	**8**
Ci.	**1.27-6**	**130**	**190.5×190.5×33**	**15**	**4**

Table 5.9: Comparison Table

successfully designed using the proposed methodology. The matching and isolation correlation between the unit cell approximation and the complete design has been confirmed to be high, and the slight differences are due to the filtered modes when the reduction to a unit cell is applied.

The fabrication of the circular coaxial design with four ports has also been presented. Measurements and simulations exhibit good agreement with an impedance bandwidth (S_{11}(dB)<-10 dB) of 130% (1.27-6 GHz), isolation between ports higher than 15 dB. The channel capacity and ECC<0.1 have also been calculated, providing compatibility with a 4×4 MIMO system.

Simulated results of the square, hexagonal, octagonal and saw-tooth designs show an impedance bandwidth (S_{11}(dB)<-10 dB) of 126% (1.4-6.2 GHz), 130% (1.33-6.33 GHz), 128% (1.36-6.2 GHz) and 129% (1.46-6.85 GHz) respectively. Isolation between ports is always higher than 15 dB because the minimum distance between ports of $\lambda/2$ is always respected. Additionally, Table 5.9 compares the features of the most relevant recent publications of MIMO access point antennas and the proposed designs, highlighting the impedance bandwidth, the size, the isolation, the number of independent ports, and the total efficiency.

The proposed sector unit cell methodology introduces a significant simplification of the simulation and design process and a systematic strategy for designing complex and time-demanding cavity-based designs with a high number of ports. As a reference, the simulation of the 8-port octagonal design takes

4h 0m 14s, the simulation of two unit cells 8m 57s and a unit cell 4m 6s in a computer with 16 GB of RAM and an Intel Core i7-8700 CPU. It then justified the benefits of using the unit cell approximation methodology.

In addition, in this chapter, a four-port wide-band antenna with unidirectional and independent radiation patterns has also been designed and fabricated for MIMO indoor base station applications with a methodology to isolate the ports with CMA using an x-shaped isolating block. Measurements and simulations showed an impedance bandwidth (S_{11} < -10 dB) of 118 % (1.55-6 GHz), total efficiency higher than 84%, isolation between ports higher than 16 dB, and ECC lower than 0.5 in different propagation conditions, providing compatibility with a 4×4 MIMO system with a deep study of channel parameters. For the design of the isolating block, a novel methodology based on CMA has been used to identify the nature of the coupling between ports. Decomposing the total currents and fields into modal currents and modal fields has provided valuable information to determine the mode (J_4) contributing to the coupling.

As a main conclusion, CMA has been successfully applied to ease and simplify the design process of cavity-backed antennas, providing a visual insight into their physical operating principle. Two novel methodologies have been presented to isolate and decrease cavity-backed antennas' design and simulation time.

Chapter 6

Small Antennas

In the last decade, the interest in small antennas has increased due to the integration of antennas in all kinds of devices for IoT applications, even in extremely size-limited ones that require highly miniaturized antennas. Sometimes, the wavelength of the frequency band that the antenna is working at has a similar length to the device size. That brings miniaturization and integration challenges, which antenna designers have been dealing with. The low 5G/IoT frequency bands (0.7-1 GHz) have a wavelength between λ=428 mm and λ=300 mm, which complicates and challenges a resonant antenna's integration in a size-limited device. Small antennas and miniaturization techniques are the only solutions that can provide connection in these bands.

The terms "Small antennas" or "ESA" were first described by Wheeler and Chu as electrically small antennas compared to the frequency bands where they operate. By definition, they satisfy $ka < 1$ (where k is the wave number and a is the smallest radius of a sphere containing the antenna).

The size limitation affects the antenna's radiation properties and sets a trade-off between size and performance. Radiation efficiency, impedance matching, and frequency bandwidth are the main attributes studied to establish their fundamental limitations. Antenna designers must consider these limitations and achieve a compromise between the dimension of the antenna and its performance. Antenna miniaturization techniques [33] permit the installation of antennas in such limited scenarios.

6.1 Fundamental limits

The theoretical limits concerning small antennas were introduced by the work of Wheeler [34] and Chu [147] about eight decades ago, and they are still in use. Wheeler's work was a pioneer in introducing the small antenna concept.

He stated that small antennas are the ones that can be enclosed in a sphere with a radius of a=1/k, and the radiation properties are significantly degraded when this limit is crossed. Chu was the first to derive the minimum quality factor Q through spherical modes, which a small antenna can obtain.

The quality factor (Q) is used to quantify the bandwidth of an antenna. The ratio between the stored energy and the radiated power of an antenna defines it.

$$Q = \begin{cases} \frac{2wW_e}{P_R} & \text{, if We} > \text{Wm} \\ \frac{2wW_m}{P_R} & \text{, if We} < \text{Wm} \end{cases} \tag{6.1}$$

where W_e/W_m is the time-averaged stored electric/magnetic energy densities and P_R is the radiated power.

Their work established a trade-off between size, bandwidth, and efficiency and set the upper limit for the performance of small antennas. Collin and Rothschild [148] continued the work of Chu and derived the minimum Q expression for linearly polarized antennas (6.2).

$$Q = \frac{1}{ka} + \frac{1}{(ka)^3} \tag{6.2}$$

McLean [149] confirmed Collin and Rothschild's work and also introduced the minimum Q for circularly polarized antennas (6.3) involving TE and TM modes together.

$$Q = \frac{1}{ka} + \frac{1}{2(ka)^3} \tag{6.3}$$

Many other studies have provided several approximations for the calculation of minimum Q, such as Fante [150], Hansen [35]- [151] or Pozar [152]. Still, most of them confirmed the definitions of (6.2) and (6.3), which are generally accepted expressions.

All the authors agreed that the size reduction comes with a reduction in bandwidth and efficiency. Furthermore, the analyzed small antennas that have obtained the highest performance are those with the lowest permittivity, have an aspect ratio close to unity, and which fields fill the enclosing sphere with the greatest uniformity [153].

The bandwidth is one of the most important parameters for antenna designers. Even though most of the efforts focused on the Q factor analysis, the relation between Q and bandwidth has also been discussed [148, 154–157]. Geyi [156] stated that antennas with Q≫1 present a bandwidth equivalent to 1/Q. Yaghjian and Best [157] presented an expression with the relation between Q and B, which is detailed in (6.4). Antennas with Q close to 1 are considered wideband antennas, and authors disagree on a common expression. In the case of small antennas, Q≫1 is always accomplished, and the expression introduced by Yaghjian and Best (6.4) is commonly used.

$$B \approx \frac{1}{Q}(\frac{s-1}{\sqrt{s}}) \tag{6.4}$$

where s is the Voltage Standing Wave Ratio (VSWR).

6.2 Miniaturization techniques

Miniaturization techniques emerge as the unique solution for installing an antenna in a physically limited scenario. As explained in the previous section, miniaturization degrades an antenna's radiation properties, but the key point is to reduce the antenna's size with the minimum reduction of bandwidth and efficiency.

Over the last decades, extensive research has been conducted on different miniaturization techniques to explore their benefits and drawbacks, and this section reviews the most relevant strategies and publications.

Geometry miniaturization

Geometry miniaturization is one of the most relevant techniques for reducing the size of an antenna because it only requires bending, cutting, or moving some parts of its structure.

In Fig. 6.1 the three most relevant miniaturized designs constructed from a wire monopole antenna (Fig. 6.1(a)) are depicted. Fig. 6.1(b) represents the inverted L antenna (ILA), which is a monopole antenna that has been bent, resulting in a section perpendicular to the ground plane (h) and a second section (l) connected to the first one, which is placed in parallel to the ground plane. The distance h significantly affects the input impedance of the antenna, and it can be optimized to match the antenna. The distance of section l to the ground plane may produce current cancellation and a capacitive effect, increasing the antenna's Q. This antenna is suitable when a monopole is required and not a large space on the ground plane is provided.

Fig. 6.1(c) details one of the most miniaturized antenna, the inverted F antenna (IFA). The IFA antenna is constructed by bending the upper section until parallel to the ground plane (like the IFA) and short-circuiting the monopole base to the ground plane. The reason this antenna is so common is the type of feeding. The antenna feeding can be placed with a variable distance (d) to section h (Fig. 6.1(c)). The shorter is d, the lower is $\Re(Z_{11})$ because it approaches the short circuit. On the contrary, $\Re(Z_{11})$ increases when d increases because it moves towards an open circuit. The fact that the $\Re(Z_{11})$ can be controlled easily with the feeding displacement explains why this antenna is so standard and widely used.
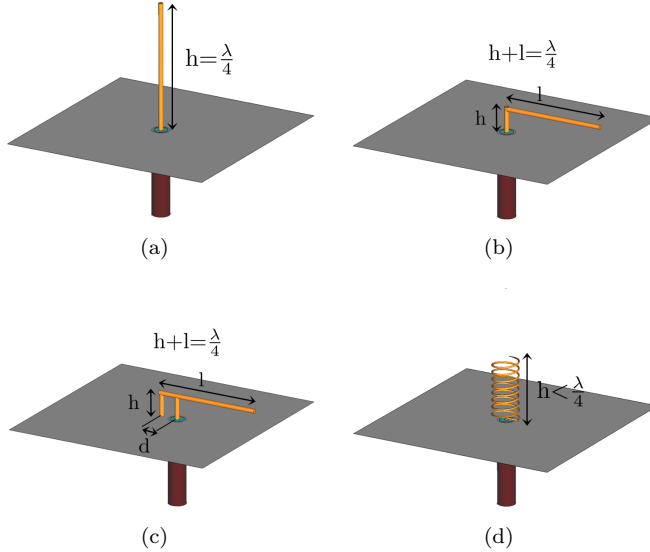
Figure 6.1: a) Monopole antenna, b) Inverted L antenna (ILA), c) Inverted F antenna (IFA) and, d) Helix antenna.

The helix antenna is the last antenna, detailed in Fig. 6.1(d). The helix antenna is constructed by coiling the whole wire monopole to decrease the total height of the structure $(h < \frac{\lambda}{4})$. This solution is suitable when a high and thin space is disposed of for the antenna, contrary to IFA or ILA, which require a short but wide volume to be installed. This antenna was famous for its installation in handy mobile phones in the 90s.

Equivalent techniques are also applied in printed circuit board (PCB) technology (Fig. 6.2). Regarding geometry optimization, the meandered technique is the most used solution. In Fig. 6.2(c), a meandered ILA is depicted, and the antenna's electric length is reduced with up-down meanders. Meandering is an effective solution for decreasing the antenna length. Still, it comes with high current cancellation, and the meanders create an inductive effect that increases the Q factor of the antenna.

Regarding planar solutions, the planar inverted F antenna (PIFA) is used thanks to its mechanical consistency and the matching control that the feeding positioning enables. In Fig. 6.3(b), a technique to increase the electric length of the PIFA is applied using two notches, which force the currents to flow through a longer path (especially the currents on the edges). Another technique is shown in Fig. 6.3(c) with a corrugation technique. It is an equivalent solution of meandering but in 3D. The corrugation of the PIFA reduces the
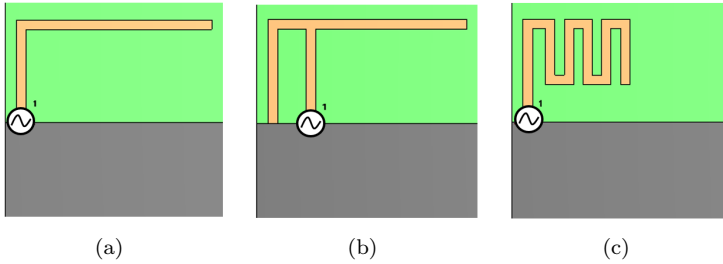
Figure 6.2: PCB solutions: a) Inverted L antenna (ILA), b) Inverted F antenna (IFA), c) Inverted L meandered antenna.

length of l thanks to the concatenation of grooves and ridges. Identically as in the meandered solutions, current cancellation and reactive effects are induced, increasing the Q and decreasing the bandwidth and efficiency.
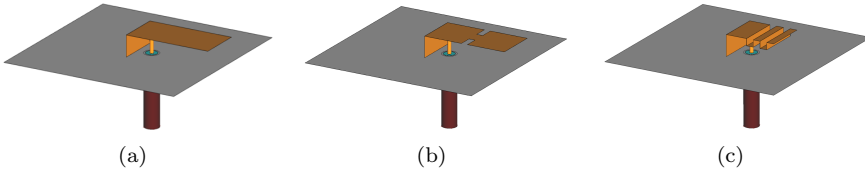
Figure 6.3: a) Planar inverted F antenna (PIFA), b) Meandered planar inverted F antenna (PIFA), and c) Vertical meandered planar inverted F antenna (PIFA).

Antenna loading

Loading antennas with lumped elements is also a standard solution for miniaturization. With the inclusion of reactive elements, it is possible to change the input impedance of the antenna and tune it to match the antenna at the desired frequency. The inclusion of one or various reactive elements enables the possibility of reducing the size of the antenna and compensating the impedance shift. Reactive elements store energy, thus increasing Q and consequently decreasing the antenna bandwidth.

In Fig. 6.4, different loaded monopoles are depicted. The first one is the ILA (Fig. 6.4(a)), which can be considered a loaded monopole because the proximity of the second section to the ground plane creates a capacitive effect controlled by the height of the first section. In Fig. 6.4(b), a step further is observed,
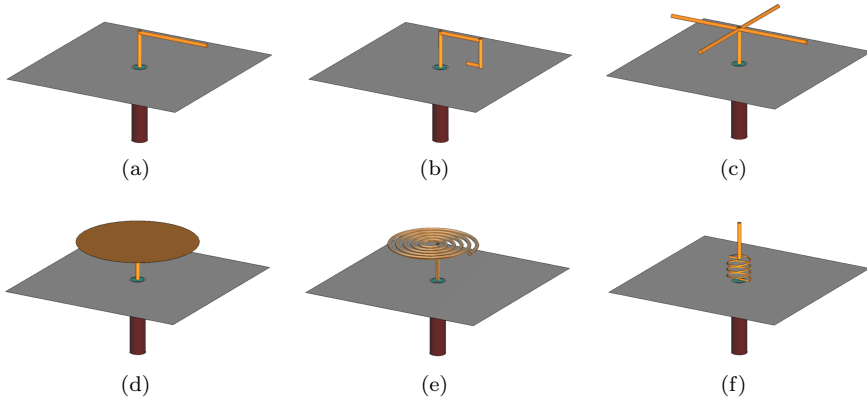
Figure 6.4: Loaded monopoles with different techniques and geometries.

where the ILA is bent two more times to produce a high capacitive effect on the last section to tune with its distance to the ground plane the resonance of the antenna. A modification of the ILA with four symmetrical and orthogonal sections is depicted in Fig. 6.4(c), resulting in an easier matching thanks to its symmetry. A capacitor plate-loaded antenna is detailed in Fig. 6.4(d), showing an input with four times more radiation resistance than an antenna with the same height without a top plate. In Fig. 6.4(e), a self-resonant antenna with a coil at the top is presented. Lastly, in Fig. 6.4(f), a short monopole loaded with a coil is depicted.

Another technique is loading antennas with discrete elements such as capacitors and inductors. These are placed either in series or parallel to miniaturize the antenna. Reactive elements allow the antenna to be tuned to lower frequencies; hence, the antenna can be shortened to compensate for the frequency shift produced by the discrete element.

In Fig. 6.5(a), an ILA and an IFA are depicted with either a capacitor C1=0.1 pF or inductor L1=1 nH in series or parallel depending on the position of the switch. All the cases are studied to check if the antenna's resonance is shifted to higher or lower frequencies. It can be observed in Fig. 6.5(b) that for the ILA, to tune the antenna to lower frequencies or miniaturize, an inductor in series or a capacitor in parallel must be used. The inductor in parallel and capacitor in series tune the antenna to higher frequencies. For the IFA, the same criteria must be followed, which can be observed in Fig. 6.5(c).

The input impedance with $\Re(Z_{11})$ and $\Im(Z_{11})$ is depicted for the cases in which the antenna can be miniaturized. It can be observed the resonance shifts
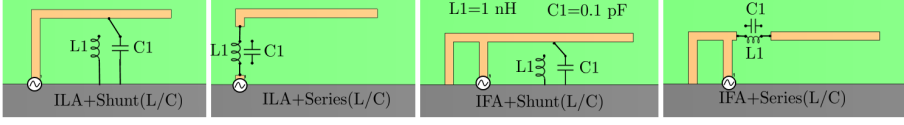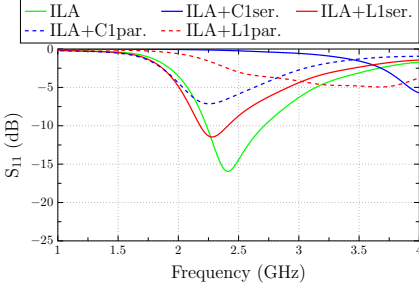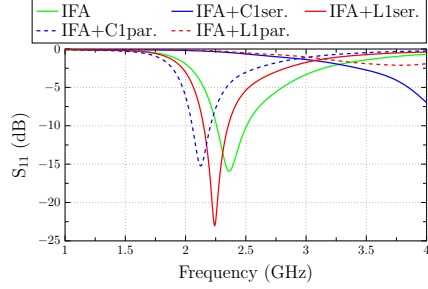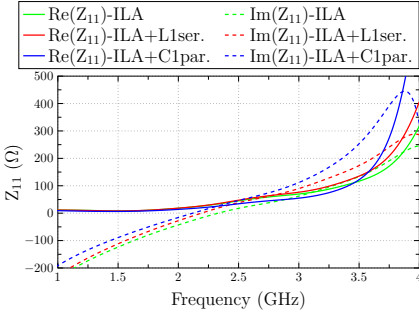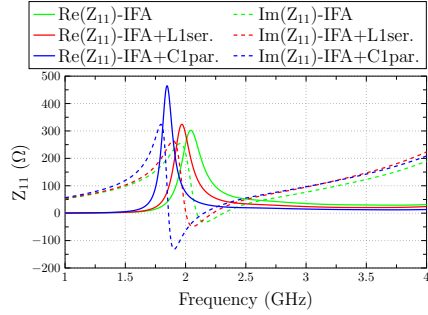
Figure 6.5: a) ILA and an IFA with either a capacitor C1=0.1 pF or an inductor L1=1 nH in series or parallel, b) S_{11} of the ILA for all the cases, c) S_{11} of the IFA for all the cases, d) $\Re(Z_{11})$ of the ILA, and e) $\Re(Z_{11})$ of the IFA.

to lower frequencies for the ILA (Fig. 6.5(d)) and for the IFA (Fig. 6.5(e)) when L1 is connected in series or C1 in parallel.

Material loading

Material loading enables the possibility of reducing the size of the antenna, surrounding the antenna with a material with different dielectric or magnetic

properties. The electric length of an antenna is related to the wavelength in the medium, which decreases when either the electric or magnetic permittivity is increased. The relation between the real length of the antenna surrounded by a material and the initial length l_0 is described by eq. (6.5).

$$l = \frac{l_0}{\sqrt{\epsilon_e \mu_e}} \tag{6.5}$$

where ϵ_e and μ_e are the effective electric permittivity and the effective magnetic permeability, they both depend on the size and shape of the dielectric material, and their maximum value is ϵ_r and μ_r which are the relative permittivity and permeability. Effective and relative values are equivalent when an infinite dielectric material surrounds the antenna. In Fig. 6.6, a comparison between the length of an ILA in free space, coated with a dielectric and surrounded by an infinite dielectric volume.
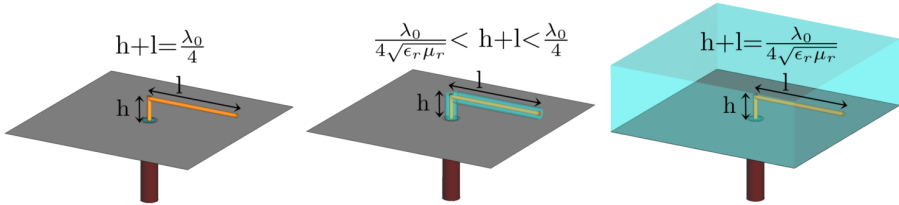
Figure 6.6: Image of a wire ILA in free space, coated with a dielectric and surrounded by an infinite dielectric volume.

Material loading is a common solution, and it is widely used in commercial, low-cost PCB FR4-based solutions. Solutions with antennas embedded in ceramic materials that highly miniaturize the antennas due to their high electric permittivity value are also available.

Material loading is also undesired and a problematic issue in many in-case solutions. The antennas are surrounded by many plastic covers and pieces or even totally embedded in dielectric materials to give mechanical consistency, which detunes and increases the antenna's total losses.

Adding any dielectric material surrounding the antenna increases the Q, reducing the BW due to the concentration of the electric field in high-permittivity regions. This makes propagating the wave more difficult than in free space. In addition, high-permittivity materials also come with higher losses.

6.3 Ceramic Chip antennas

Ceramic antennas were introduced two decades ago to overcome the miniaturization limitations that the current solutions were facing. Thanks to the

ceramic substrates' high electric permittivity and low losses, antennas can be highly miniaturized (6.5), and in the last two decades, many designs have been proposed to integrate them into size-limited devices.

They emerged in parallel with PCB-based solutions, which are limited in miniaturization and require a larger area free of metal (clearance area) to be installed, and their sensitivity and difficulty to adapt when any change in the PCB is produced. On the other hand, chip antennas are more complicated to design and fabricate and more expensive if not fabricated in mass production. PCB-based solutions and chip antennas are the two main alternatives that IoT antenna designers still consider.

In the 90s, whip/helical antennas were widely used in mobile handsets, and a promising built-in solution was the PIFA antenna, which was widely used. PIFA antennas were limited in size to $\lambda/8$ when capacitively loaded [92].

(a)   (b)
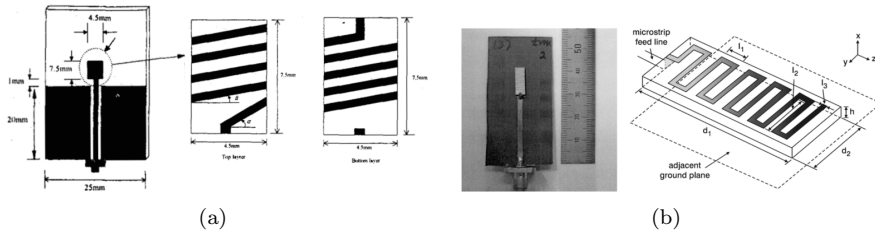
Figure 6.7: a) Ceramic chip antenna for PCS phone [158] and, b) Ceramic Chip antenna using meander conductor lines [159].

Using internal antennas became a hot issue in the 2000s, and ceramic chip antennas permitted highly miniaturized internal solutions. Many papers and patents [160–163] were presented in the early decade of the 2000s, and especially many designs for mobile communication system applications. Several chip antennas for the IMT-2000 band (1920-2170 MHz) were presented in [158,159,164] with a helical solution [158] (Fig. 6.7(a)), a meander conductor line on alumina dielectric [159] (Fig. 6.7(b)) or with two separate strip lines [164]. In addition, a dual-band antenna for the 900/1800 MHz band was presented in [165] fabricated in LTCC technology.

Another band that received significant attention was the 2.45 GHz band which was used for short-link applications such as WLAN [166,168–170], Bluetooth [171, 172], or sensors [167, 173] applications. Fig. 6.8 depicts two representative chip antennas. The first one is a monopole chip antenna [166] mounted on a foam base for WLAN applications, and the second one [167] is a ceramic (alumina, ϵ_r=7.7) dielectric antenna using the advanced meander line technique for 2.4/5.8-GHz dual ISM-band applications.

(a)   (b)
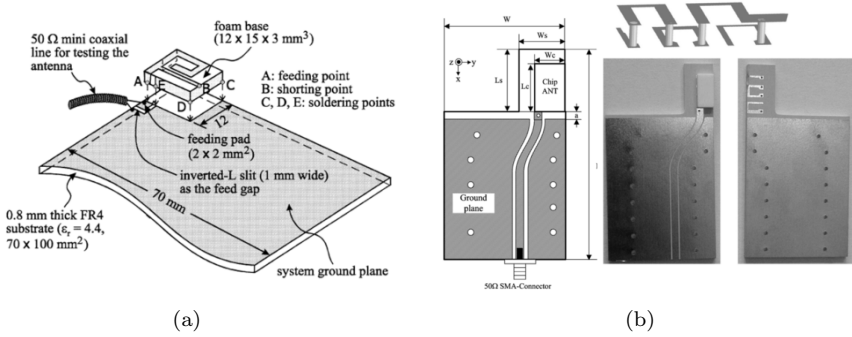
Figure 6.8: a) Monopole chip antenna for WLAN applications [166] and, b)
Meandered Chip antenna for dual ism-band (2.4/5.8 GHz) [167].

Ceramic chip antennas were also introduced for ultra-wideband (UWB)
applications in [174–178]. These antennas were used for short-range, high-speed
wireless communications for handheld devices. In Fig., 6.9(a), a multilayer
ceramic chip antenna [174] is proposed with two helical conductors embedded
in a ceramic material (ϵ_r=7.8) with an impedance bandwidth of 7.5 GHz (3.1-
10.6). In Fig., 6.9(b), a slotted patch antenna [175] working from 2.215 to
2.947 GHz is studied and fabricated in LTCC (Ferro, ϵ_r=5.9 and tan δ=0.002)
technology.

From 2010, the demand for UWB chip antennas [179–182] increased due
to the communication industry expansion and the approbation by the Federal
Communications Commission (FCC) the operation of UWB systems within 3.1-
10.6 GHz bands which were divided into six band groups. In [179] a 6×2.4×4
mm^3 ceramic (ϵ_r=7.5) PIFA antenna (Fig. 6.10(a)) is presented for UWB
bands covering groups 3 and 6 (6.3-9 GHz) and for Group 1 (3.1-4.8 GHz)
a dual-PIFA ceramic (ϵ_r=7.5) antenna (Fig. 6.10(b)) is presented in [180]
in a volume of 17.5×6×3 mm^3. Two LTCC solutions with monopoles were
presented in [181, 182] working at 3.6-10.6 GHz band [181] and at 2.85-11 GHz
with a 17×10×1 mm^3 volume.

The creation of the new long-term evolution (LTE) standard which sup-
posed the evolution of the 3G to the intermediate system 3.9G (previous to 4G)
also created the need for the design of in-case chip antennas [183–188] to pro-
vide connection to the LTE bands (LTE700/2300/2500) and the wireless wide
area network (WWAN) which included the previous 2G/3G (GSM/UMTS)
bands. An IFA with multi-branch strips fabricated on both sides of a ceramic
substrate with a 97×11.2×0.5 mm^3 volume is presented in [185] with four op-
erating bands 646–983 MHz, 1503–1589 MHz, 1696–2963 MHz, and 3396–3646

(a) (b)
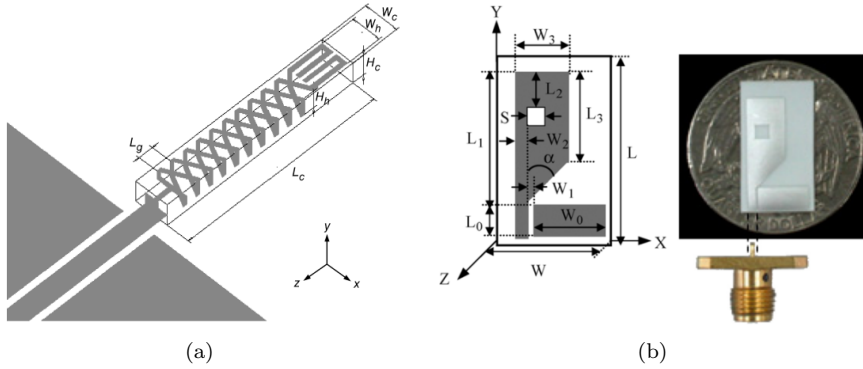
Figure 6.9: a) A broadband multilayer chip antenna with helical conductor [174] and, b) Ceramic chip antenna of a slotted patch antenna for UWB [175].

(a) (b)
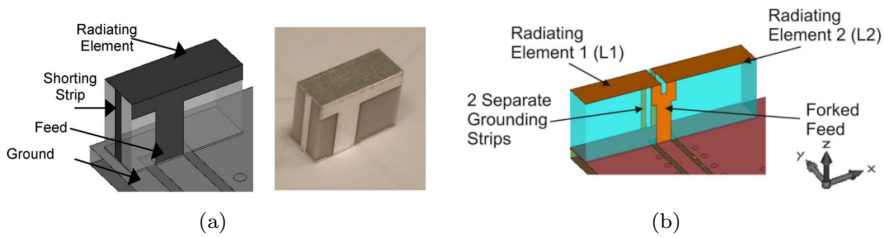
Figure 6.10: a) Miniaturized Ceramic PIFA [179], b) Dual-PIFA chip antenna for group 1 UWB [180].

MHz for the LTE, WWAN, GPS, WiMAX (2.3/2.5/3.5 GHz) and WLAN (2.4 GHz) systems. A ceramic (Cerabrid, ϵ_r=6.45, $\tan\delta$=0.0011) chip antenna for LTE MIMO systems is analyzed in [183] with a size of $35\times11\times5$ mm^3 (Fig. 6.11(a)). Another chip antenna for LTE was presented in [184] using a base of foam except a ceramic material presenting a volume of $35\times15\times3$ mm^3. The same strategy was followed in [188] using an economic fabrication method using a multilayer PCB process with a permittivity between 3 and 3.6. The antenna uses a folded meander line and two loading patches presenting a total size of $3.2\times1.6\times0.83$ mm^3.

In the first decade after 2000, many papers with different solutions concerning ceramic chip antennas for sub-6 GHz applications were proposed (most relevant publications cited above). After 2010, a decrease in relevant publications was observed, and from 2015 until now, the interest in chip antennas

(a)   (b)
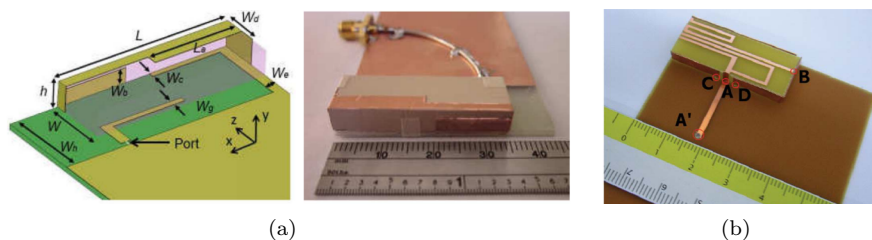
Figure 6.11: a) Ceramic Based Small LTE MIMO Handset Antenna [183] and, b) Miniature Ceramic PIFA [184].

has become almost exclusive to commercial purposes. Due to the increase in handheld devices and the creation of new IoT applications, a wide variety of miniaturized antenna solutions are required for size-limited devices. Another reason behind chip antenna commercialization is the fact that the radiation properties of small antennas are highly affected by the scenario in which they are installed, and they require a customized analysis.

Figure 6.12: Ceramic chip antenna for different bands and applications from Taoglas [189].

Several companies such as Taoglas [189], Würth Elektronik [190], Johanson [191], Yageo [192], Antenova [193] or Ignion [194] have covered the commercial need for chip antennas. Nowadays, they offer an extensive catalog with ceramic chip antennas for different bands and applications like the ones from Taoglas represented in Fig. 6.12. In the following figures, the most relevant commercial solutions are analyzed with solutions for Bluetooth/ZigBee (2.4 GHz), Wi-Fi(2.4/5.5 GHz), ISM (400,783,868,915 MHz), WiMAX (2.5/2.6 GHz), GPS/Glonass/Galileo (1.227/1.575-1.602 GHz) and Cellular Communication, 4G/LTE/5G. Multiple solutions are offered in Fig. 6.12. Still, the

design process and the chip antennas' internal composition are confidential and not detailed due to commercial interests.
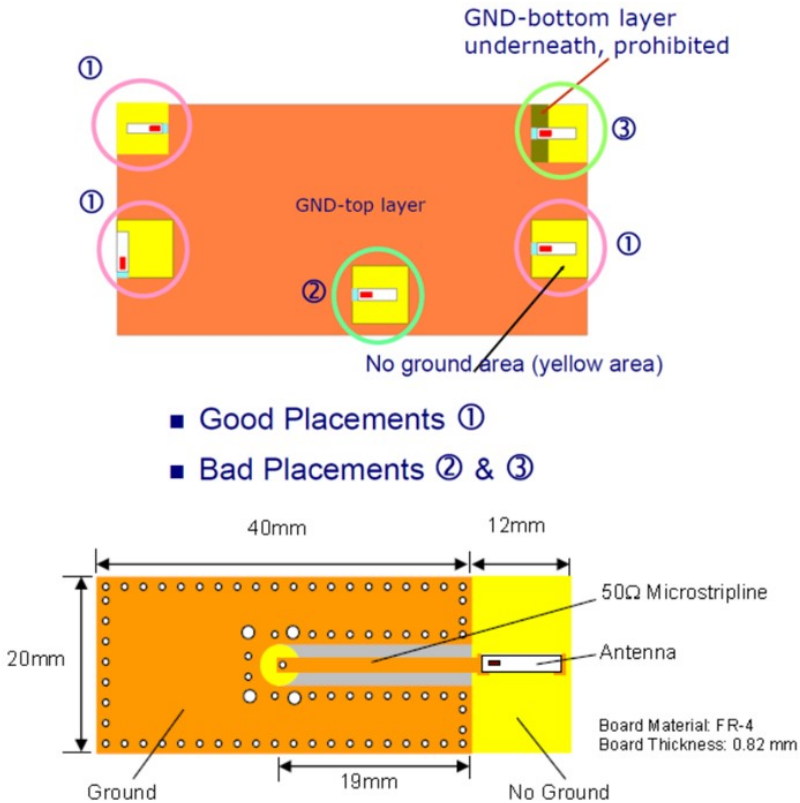
Figure 6.13: Guidelines to properly install a Johanson [191] chip antenna in a PCB.

Ceramic chip antenna manufacturers provide guidelines in the datasheet for installing the antenna properly. The antenna's performance is greatly affected by the location of the antenna on the connected ground plane; hence, it is of great importance to follow the manufacturer's tips (Fig. 6.13). In the following subsection, a deep analysis of the effect of the size/shape of the ground plane and the location of the antenna is analyzed to quantify the analysis.

6.4   Ground Plane effect and CMA

As the previous section shows, ceramic chip antenna manufacturers provide appropriate placement guidelines in different scenarios. The reason behind this fact is the importance of the contribution of the connected ground plane to the chip antennas and their sensibility to the surrounding scenario. It has been demonstrated that a high percentage of the total radiated power contribution of the antenna is produced by the ground plane [195]. That is why it is necessary to pay attention to the size and shape of the ground plane and the location of the antenna in order not to degrade the radiation properties of the whole set-up.

During the last decades, the research about the radiation properties of the connected ground planes or chassis to ESAs has increased [195–201]. In early designs (90s decade) of compact integrated antennas for mobile phones, the effort focused on the optimization of the geometry of resonant antennas and the radiation properties of the connected chassis was underestimated. At the end of the '90s decade, some miniaturized antennas broke some fundamental limitations regarding bandwidth incentives and the consideration of the connected ground plane as a radiating element. It was demonstrated that the ground plane increases the adequate size of the antenna, and it has a solid contribution to the total radiated power [31, 92, 195, 202]. In [195, 196], it was reported that about 10% at 900 MHz and 50% at 1800 MHz of the total radiated power was produced by a PIFA and the rest from the chassis. It was stated that resonant antennas, especially at low frequencies (about 1 GHz), could be considered as matching circuits and coupling elements [198] to the main radiator, which was the chassis. This feature permitted low-profile designs that pursued the maximum coupling between the antenna and the chassis to enhance the matching bandwidth.

The new scenario of taking into consideration the radiation properties of the connected ground planes triggered new techniques to increase the impedance bandwidth, such as the slotted ground planes [195, 200, 204, 205] or the use of parasitic elements [206].

One of the most relevant research for understanding the radiation performance of ground planes was applying characteristic mode analysis [207–209] to the analysis of connected planes. The theory of characteristic modes (TCM) [38]- [39] is widely used for the study of metallic structures. The use of characteristic modes analysis presented the current distribution of the first modes of ground planes corresponding to natural resonances of the structure. It provided a significant advance in getting information about properly feeding the structure to excite the desired modes and enhance the radiation properties. In chapter 2, the theory of characteristic modes and its application is deeply detailed.
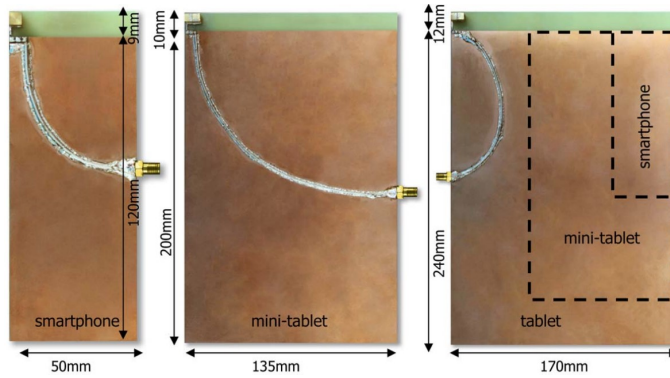
(a)
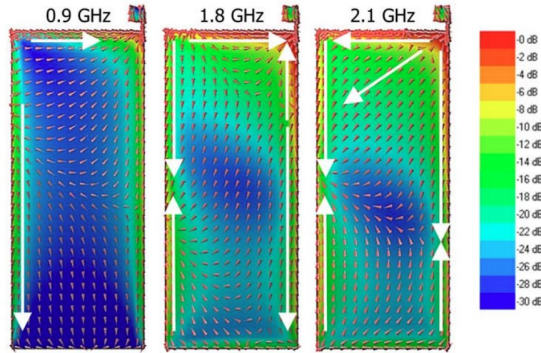
(b)

Figure 6.14: a) Antenna boosters on different size ground planes and, b) Current distribution on the analyzed ground plane [203].

With the use of CMA and the fact that small antennas can be used as matching elements to excite ground plane modes, the concept of antenna booster was introduced in [201, 203] (See Fig. 6.14). It consists of non-resonant elements with a very high-quality factor (Q) strategically placed on a ground plane to correctly excite the desired ground plane (chassis) modes. Antenna boosters [210] require a matching circuit to tune the antenna to the desired frequency and a clearance area to ensure its correct performance.

After decades of research, it can be stated that the size of the ground plane and the antenna positioning are crucial for proper radiation performance. The ground plane must be considered to calculate the antenna's effective size. It is then essential to define the radius (a) of the sphere enclosing the "effective"

antenna (antenna including the ground plane) to calculate the fundamental limits.
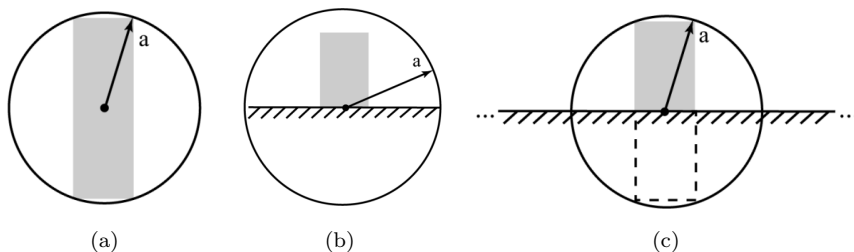
Figure 6.15: The method for determining the radius (a) of the smallest enclosing sphere of: a) Antennas without a ground plane, b) Antennas on a small ground plane with less than $\lambda/4$ radius, or closer than $\lambda/4$ from an edge, and c) Antennas on an electrically large (or infinite) ground plane [153].

In [153], Daniel F.Sievenpiper presented a method for determining the radius (a) of the smallest enclosing sphere detailed in Fig. 6.15. In Fig. 6.15(a), the calculation of the radius of the sphere of an antenna without a ground plane is depicted. In Fig. 6.15(b), the radius is calculated considering the whole ground plane when it is smaller than $\lambda/4$ or the antenna is closer than $\lambda/4$ of an edge. Finally, when the antenna is located in an infinite ground plane, the theory of images is applied, and the antenna has a size of double its volume, so the radius is duplicated.

In most integrated solutions, the ESA is located close to any of the borders, and the whole ground plane should be considered for the calculation of the radius a. This aspect should be clarified to the companies because the ground plane boosts the radiation properties of the measured antenna. The measured results may be misleading if the size and location of the antenna are not detailed, and the final user may think that the antenna itself could present such results without considering the ground plane effect. Generally, most manufacturers detail the set-up conditions where the antenna is measured, but in some cases, they do not. In addition, they provide guidelines for the optimum position of the antenna in a PCB, but in general, there is no deep study or justification for it.

In this section and the following, we provide a deep analysis using characteristic modes analysis to understand the radiation performance of a small antenna located in different positions on different-sized ground planes.

6.5 Low-Temperature Co-fired Ceramic (LTCC)

LTCC (Low-Temperature Co-fired Ceramics) is a multilayer fabrication process that manufactures RF devices from ceramic substrates (Glass ceramic sheets), which are co-fired with metal conductors at low temperatures (below 1000°). LTCC permits the fabrication of antenna and integrated circuits (ICs), including embedded components that can be packaged together, enabling a high degree of freedom to design and miniaturize. LTCC allows designing independent antennas or RF devices or a combination of them, like antennas in package (AiP), which include RF integrated circuits and systems on package (SoP) that integrate different ICs in the same chip. In the following list, the advantages of using LTCC technology are enumerated:

- Good electric and thermal conductivity

- Low electric permittivity tolerances

- High-frequency stability

- High degree of miniaturization

- 3D integration with cavities or RLC components

- Low-cost production at medium-large scale

- Long-lasting Hermetic designs. Robust against mechanical and thermal stress

- Packaging solutions (AiP or SoP)

LTCC devices are composed of dielectric sheets or tapes, screen-printed conductors, embedded components (resistors, capacitors, inductors), and vias for the interconnection of the layers. The multiple layers are stacked in a specific order and laminated together, obtaining hermetic and monolithic structures.

The process flow of LTCC fabrication is depicted in Fig. 6.16 in 7 steps:

1. Blanking: The LTCC ceramic sheets are blanked with the coupon size.

2. Vias/cavities forming: Via holes and cavities are mechanically punched.

3. Via filling: Using a vacuum pump, via holes are filled with paste with a print nest.

4. Conductors/passives printing: Deposition of Conductors and passives elements using screen printing techniques.

5. Stacking and Lamination: Layers are stacked. The stack-up is laminated using a press to avoid de-lamination.

6. Co-firing: The previously laminated coupon is introduced in a sintering oven at 850° C. During the firing process, the coupon shrinks.

7. Device singulation and back-end processing: A saw separates different devices added in the same coupon. Back-end processing, such as connectorization or wire bonding, can be done at this stage.
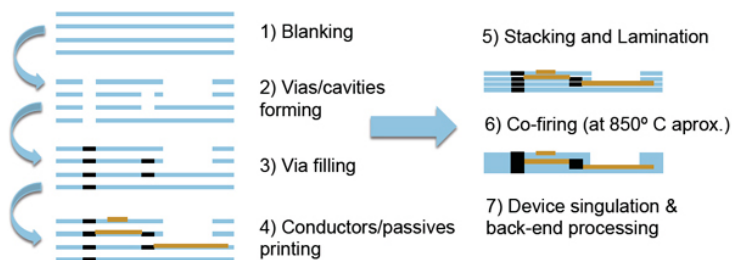
Figure 6.16: Process flow of the fabrication process in LTCC.

LTCC has been used for decades to fabricate ceramic chip antennas and RF devices. Currently, they are extended solutions fabricated in LTCC for commercial purposes. The tendency of research about LTCC antennas in recent years has focused on high frequencies (mm-wave frequencies and above) due to the excellent performance of LTCC at those frequencies compared to other fabrication processes. Multiple designs have been proposed in recent years for mm-wave arrays [211–217] at Ka-band (26.5-31 GHz), for arrays [218–221] in 5G base stations working at the 60 GHz license-free band, and for W-band (60–100 GHz) arrays [222–224].

In this thesis, we focus on the design of several antennas for IoT devices working at sub-6 GHz bands. For their fabrication, we have taken into consideration the fabrication limitation of tolerances of the laboratory for high-frequency LTCC circuits (LCAF) [225] of the Universitat Politècnica de València (UPV). The main area of the laboratory is a clean room comprising Class 10.000 (ISO 7) and Class 1.000 (ISO 6) zones. In Fig. 6.17, a picture of the laboratory where the Aurel 900AV Screen/Stencil Printer is observed on the right and the KMS Laboratory Puncher on the left.

Figure 6.17: Laboratory for high frequency LTCC circuits (LCAF) [225] of the Universitat Politècnica de València (UPV).

6.6 Classic Chip Antenna Solutions. Parametric Study

In this section, a classical solution, including a chip antenna, is presented. Most chip antenna solutions require a clearance area and are accompanied by guidelines for their installation. To gather more information, we analyze a typical design based on a loaded monopole antenna with different parametric studies to provide a deeper insight into the radiation mechanisms of chip antennas. The size of the connected ground plane, the antenna position, and the clearance area size are analyzed using radiation efficiency as the figure of merit.

The loaded monopole comprises a chip antenna (load) connected to a terminal line. The chip antenna resonates at 1.4 GHz, but by connecting the terminal line in series, the antenna can be tuned at lower frequencies, modifying the length of the line. In this analysis, the design has been tuned at 868 MHz (European ISM Band), but it could be tuned for any sub-1 GHz 5G band or 915 MHz ISM band (USA). Loading the design with a coil permits the shortening of the effective length of the antenna, maintaining the resonance frequency due to the series inductance, which compensates for the capacitive behavior of a monopole before resonance. In Fig. 6.18(a), the two top and bottom-loaded antennas are depicted. For miniaturized purposes, we use the base-loaded monopole. The evaluation board we use for the parametric study is shown in Fig. 6.18(b), which consists of an a×b FR4 PCB with a clearance area with a1×b1 size.

The chip antenna consists of a coil embedded in a ceramic substrate ($\epsilon_r = 7.1$ and $\tan\delta = 0.0009$) fabricated in LTCC technology with a dimension of
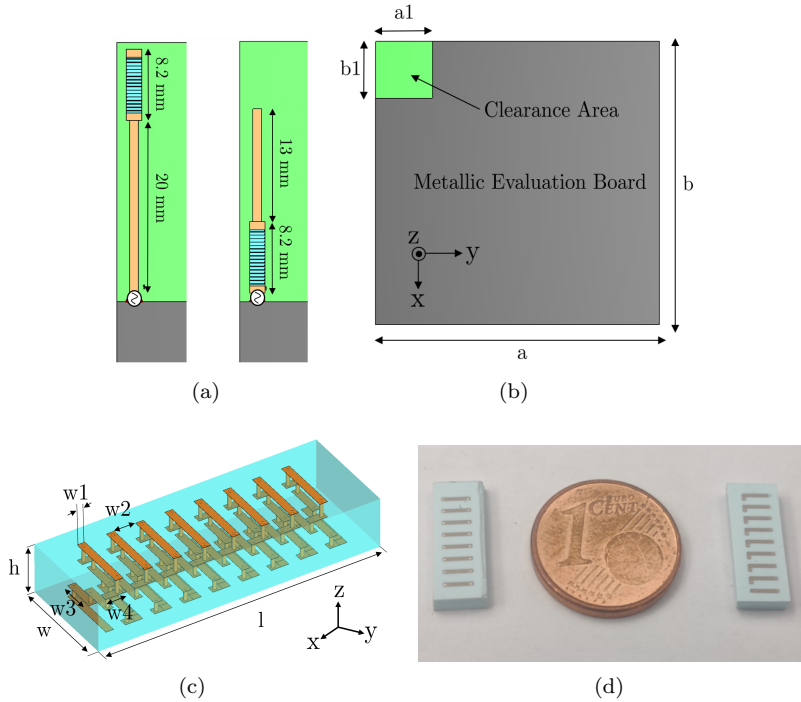
Figure 6.18: a) Antennas with equivalent resonance frequency. Top: Base-loaded monopole antenna. Bottom: Top loaded monopole antenna, b) PCB used for the study with a size of a×b, c) 3D View of the chip antenna, and d) Picture of the fabricated LTCC chip antenna.

8.22×1.8×0.6 mm and 13 mm the connected line. The simulated and fabricated models are depicted in Fig 6.18(c) and Fig. 6.18(d).

The following subsections analyze the antenna position, the ground plane's size, and the clearance area's importance. They also calculate the radiation efficiency for different cases.

Antenna position

The first study analyzes the effect of shifting an antenna around the perimeter of the ground plane. The configuration with the chip antenna perpendicular to the terminal line, resonating at 868 MHz, has been used.

In Fig.6.19(a), the effect of shifting an antenna from the top-left corner (y=0) to the center of the left side of the PCB is depicted. Several positions

(a)

(b)
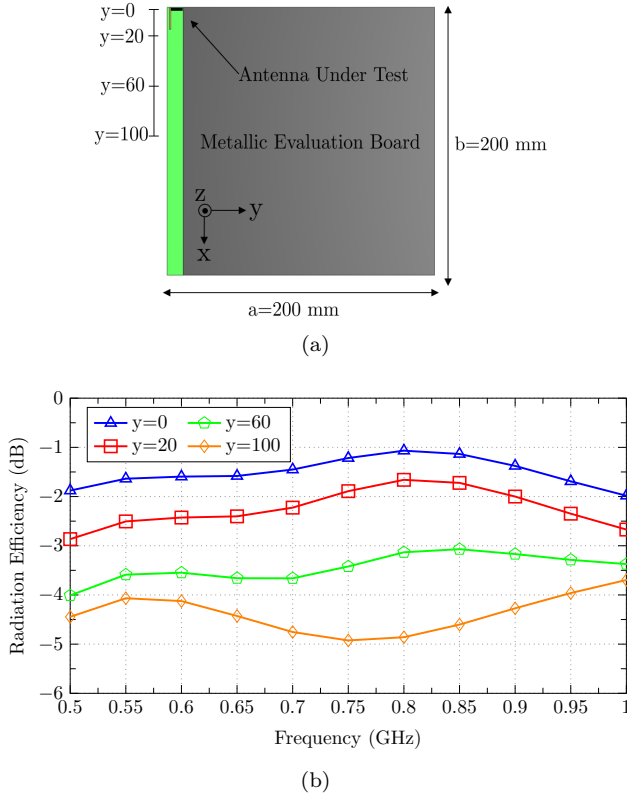
Figure 6.19: a) Antenna in position y=0 mm and y=100 mm. b) Radiation
Efficiency as a function of the antenna's position.

have been analyzed, moving down the antenna from position y=0 mm to y=100
mm.

Fig. 6.19(b) shows the radiation efficiency obtained for each position. The
results show a reduction of efficiency with the variable y, with a minimum
obtained when the antenna is at the center of the clearance area (y=100 mm).
The first conclusion is that placing an antenna at the corner of a squared PCB
has higher radiating performance than placing it in the middle of the external
sides.

Size of the ground plane

The second analysis is based on the effect of reducing the size of the ground
plane in terms of radiation efficiency. This study uses the same antenna config-

uration as in the previous section. The antenna is fixed on the top-left corner, and the clearance area is fixed to $10 \times b$ mm^2. The dimension of the squared PCB has been reduced from a=b=200 mm to a=b=50 mm (Fig. 6.20(a)).

(a)

(b)
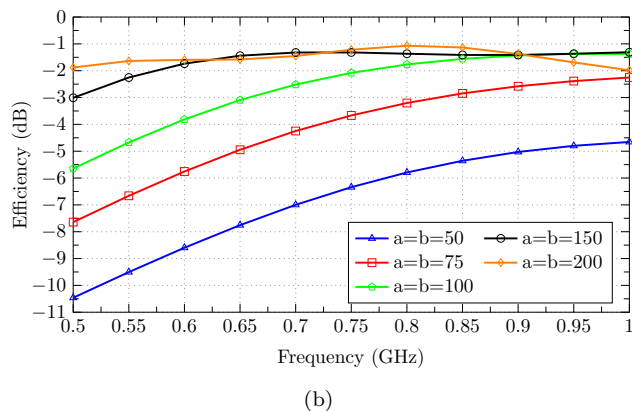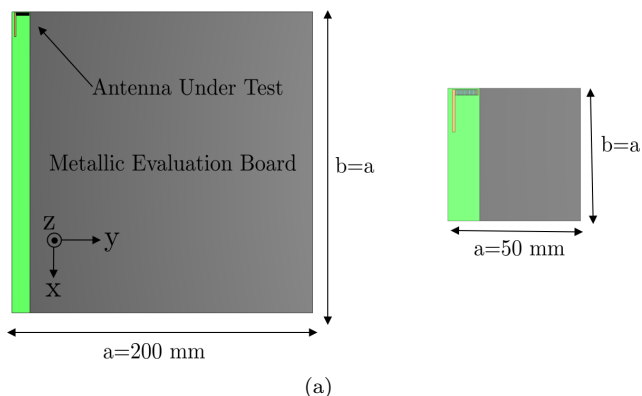
Figure 6.20: a) PCB with a size of a=b=200 mm and a=b=50 mm, and b) Radiation Efficiency depending on the size of the PCB.

Fig. 6.20(b) shows a reduction of radiation efficiency for smaller ground planes. From a=b=100 mm, the efficiency begins to saturate, and the increase is insignificant with the size. The loss of radiation efficiency between 100 mm^2 PCB and 50 mm^2 PCB is 3dB. Regarding input impedance, the value of the Re(Z_{11}) increases with the size of the ground plane. A matching circuit must be added for small ground planes to raise the Re(Z_{11}).

As a general recommendation, in a squared PCB with an antenna at the corner, a PCB with a size greater than $\lambda/4 \times \lambda/4$ must be used in order not to limit the radiation efficiency.

Clearance area reduction

The third analysis is based on the clearance area where the antenna is installed. This area must not only be considered a place where the antenna fits but also an area where the distance between the antenna and the ground plane must be respected. If the minimum distance is not respected, the antenna's performance may decrease due to the cancellations produced by the currents flowing in the surrounding ground plane.
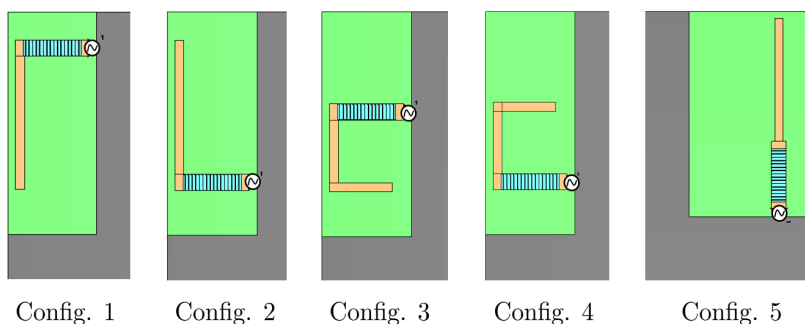
Figure 6.21: Configurations used for the study of the clearance

Five configurations have been studied (see Fig. 6.21), all resonating at 868 MHz. Configurations 1 and 2 connect the antenna to the terminal line perpendicularly, with the difference in config. 1, the terminal line is the closest element to the a1 wall (see Fig. 6.21), and in config. 2, the closest element is the antenna.

Configurations 3 and 4 are a more compact solution with the terminal line in L shape. The last configuration (config. 5) represents an ideal disposition with the antenna and the terminal line connected in the same direction.

Unfortunately, configuration 5 is not typical due to the clearance needed. Still, it is the proper configuration to check the cancellation between the antenna+terminal line with the parallel bottom ground plane wall a1 (see Fig. 6.21). The antenna is fixed for this study, and the clearance area (a1×b1) has been reduced from 25×200 mm to 25×20 mm. The worst scenario is represented when the parallel wall is at a distance of d1=1 mm from the antenna when the clearance is 25×20 mm. Fig. 6.22 represents the increase in radiation efficiency by separating the parallel wall (d1).

The analysis shows a reduction of radiation efficiency with the wall's approach, especially when the ground plane is closer than 25 mm. Due to this factor, it is recommended that this distance be respected for the antenna's proper performance.
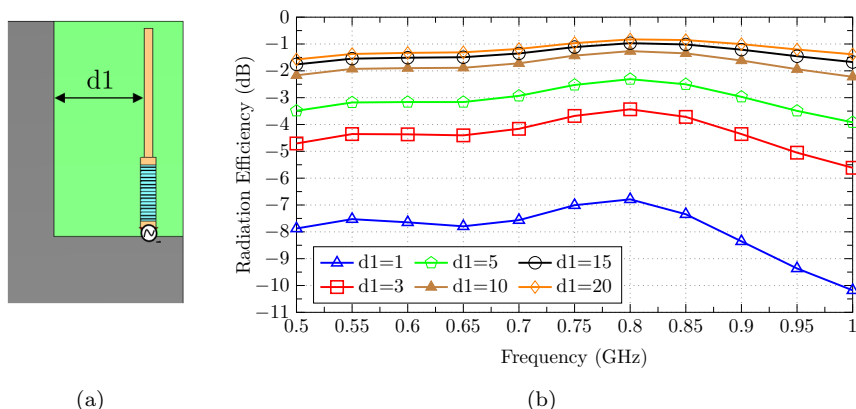
Figure 6.22: a) PCB with the antenna config. 5 was used to reduce the clearance area, and b) Radiation efficiency with parametric d1, which is the distance between the antenna and the parallel ground plane.

Config. 1 and config. 2 are based on a more realistic configuration with the antenna perpendicular to the terminal line. Two configurations have been designed to check whether placing the chip antenna or the terminal line close to the bottom ground plane wall (a1) is better. As in the previous study, a parametric analysis has been made to increase the distance between the antenna and the wall (a1).

In Fig. 6.23(b), the configuration with the antenna close to the bottom part shows a worse radiation efficiency than the configuration with the antenna in the top part. Hence, placing the chip antenna far away from the parallel wall is recommended for this configuration, as in the config. 1.

Config. 3 and config. 4 represents a configuration with a bent L terminal line. It is a realistic solution in a scenario where the clearance area is limited. In this case, the terminal line is parallel with the ground plane wall(a1); hence, the current cancellation may increase. To check which configuration, 4 or 5, is more robust to current cancellation, the clearance area has been increased a distance d1 and d2(Fig. 6.24(a) a)).

The results in Fig. 6.24(b) show that when the ground plane is close, the placement of the terminal line on the bottom (config. 3) obtains worse results than config. 4. In conclusion, when the clearance area is minimal, and an L

(a)   (b)
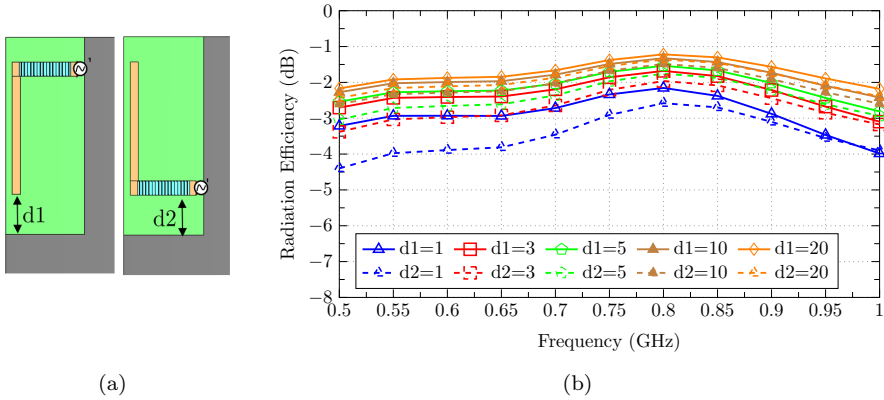
Figure 6.23: a) PCB with the antenna config. 1 and 2 were used to study the reduction of the clearance area. b) Radiation efficiency depends on the distance d1 between the antenna with config. 1/config. 2 and the ground plane wall a1.

(a)   (b)
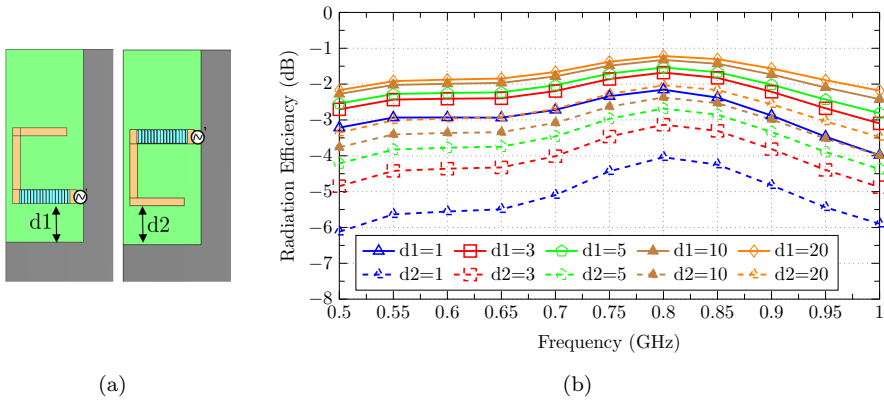
Figure 6.24: a) PCB with the antenna config. 3 and 4 were used to study the reduction of the clearance area. b) Radiation efficiency depends on the distance d1 between the antenna with config. 3/config. 4 and the ground plane wall a1.

terminal line must be included, placing the antenna qw in config is better. 4 with the antenna on the bottom part. Suppose the distance from the antenna

or terminal line to the ground plane is greater than 10 mm. In that case, both solutions have no difference, but switching to config. 1 or 2 is advisable.

To conclude with this chapter, the study confirms the vital role that the ground plane plays in the radiation properties of small antennas. The size of the ground plane, the positioning of the antenna, and the clearance area strongly impact the radiation characteristics of the whole setup. Several points must be respected to ensure good radiation performance for an antenna requiring a clearance area. The corners are the optimum location for this kind of chip antenna in a squared PCB. The size of the ground plane is recommended to be greater than $\lambda/4$ x $\lambda/4$ so that the antenna is not detuned and the radiation efficiency is not decreased. A minimum distance of 10 mm must be left between the surrounding walls and all the radiation elements to avoid current cancellations.

Chapter 7

On-Ground LTCC Chip Antennas

After analyzing all the miniaturization techniques and presenting the latest advances in chip antenna solutions, this chapter presents the design and fabrication of a new kind of chip antenna and a novel methodology based on CMA to install the antennas properly.

This chapter presents LTCC miniaturized antennas that do not require a clearance area and can be placed straight on a ground plane to be installed. The antennas will be used to analyze the degradation of the radiating performance of the device (antenna+ground plane) depending on the size of the ground plane and the position of the antenna positioning.

7.1   Design Process of the On-Ground Antennas

This section uses the 2.4 GHz on-ground chip antenna to present the design process followed by all the antennas in this chapter before they were fabricated in LTCC.

Miniaturization is obtained using a high permittivity ceramic substrate and includes four ridges and three grooves to increase the electric length of the antenna and reduce its size. The design process for the proposed antenna is depicted in Fig. 7.1(a).

The first analyzed antenna is a capacitively-fed PIFA of 4 mm height (Design 1 of Fig. 7.1(a)). PIFA antennas are low-profile and can be placed on a ground plane without a clearance area. In addition, feeding the antenna at the furthest point from the short circuit simplifies the future fabrication of a chip antenna, which will be welded to a PCB. The first size reduction applied to the
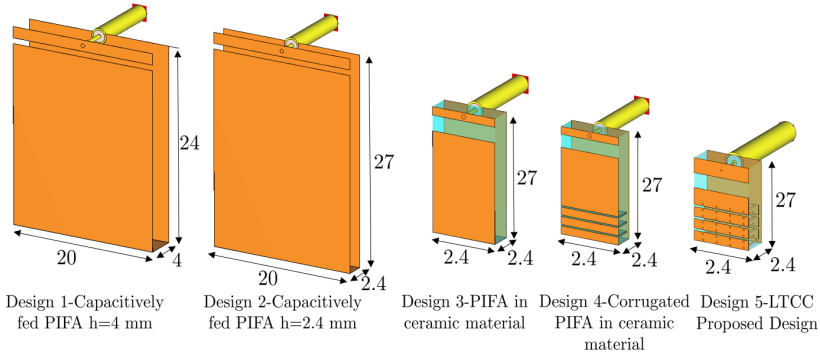
(a)
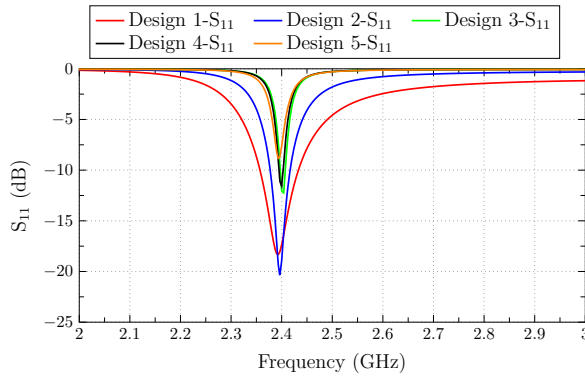
(b)

Figure 7.1: a) Miniaturization process for obtaining the proposed antenna (from Design 1 to the proposed design (Design 5)) with dimensions in mm, b) Reflection coefficients (S_{11}) from Design 1 to Design 5.

PIFA antenna is its height reduction to 2.4 mm (Design 2 of Fig. 7.1(a)), which comes with a reduction of impedance bandwidth (see Fig. 7.1(b)). The following step to compact the low-profile PIFA is to embed the antenna in a ceramic substrate (Design 3 of Fig. 7.1(a)). As observed, the size of the PIFA antenna is considerably reduced thanks to a high-permittivity substrate. Although the resonance frequency is preserved, the impedance bandwidth is decreased in this case.

To further reduce the size of Design 3, the antenna is corrugated to increase its electrical length (Design 4 of Fig. 7.1(a)), and lastly, in Design 5 (final design), the vertical walls created by the groove of Design 3 are replaced by
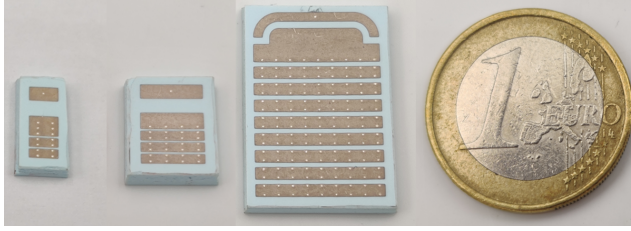
Figure 7.2: Picture of the 868 MHz, 2.4 GHz, and 3.6 GHz on-ground LTCC chip antennas.

vias, creating an additional reactive effect which shifts the resonance to lower frequencies and permits the significantly reduced size of the proposed design. LTCC technology was used to fabricate the antenna, including many vias in spurs with limited space. The last design accounts for the restrictions of the LTCC fabrication process, where the vias must be meandered because no more than four layers with vias at the same point can be stacked. Otherwise, bulge effects may appear.

In Fig. 7.1(b), it can be observed that the impedance bandwidth decreases with the antenna miniaturization, mainly when the antenna height is reduced and when a high-permittivity substrate is used. The height reduction decreases $\Re(Z_{11})$ close to 0 Ω except for a sudden high-impedance peak at the frequency where the antenna anti-resonates. The imaginary part also shows a high slope change at the anti-resonance frequency. This behavior produces a decrease in the impedance bandwidth when the antenna height is reduced. In addition, the high-permittivity substrate permits the size reduction of the antenna, increasing its stored energy (Q-factor) and decreasing its impedance bandwidth. The extreme miniaturization and the low-profile characteristics of the antenna, which can be placed straightforwardly on a ground plane with no clearance area, produce the antenna's narrow bandwidth and low-efficiency features.

This LTCC 2.4 GHz design will be further detailed in the following section. In this chapter, three LTCC antennas will be presented using a similar design process. They are depicted together in Fig. 7.2.

7.2   LTCC 868 MHz On-Ground Chip Antenna

The proposed low-profile antenna is a corrugated (accordion-like) planar inverted-F antenna (PIFA) embedded in a ceramic substrate. For its design, eight grooves/ridges with an accordion shape have been created for the miniaturization of the antenna. This low-profile solution does not need clearance to be installed; it just needs a ground plane to be placed on. Bandwidth is compro-
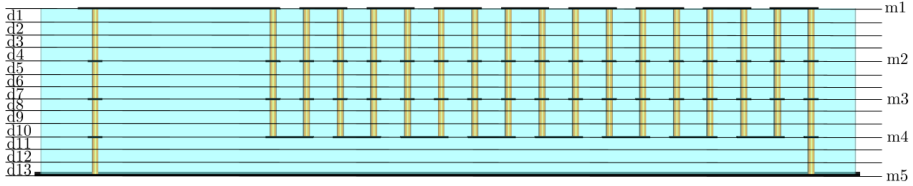
Figure 7.3: Side view of the proposed antenna with the LTCC dielectric ceramic layers (d1-d13) and the metallic layers (m1-m5).

mised due to its extreme miniaturization and the absence of clearance. Still, this antenna can be installed in size-limited clearance-less devices, and it shows high stability to frequency detuning when the antenna is reallocated at any position on the ground plane.

The antenna has been designed for fabrication using LTCC (low-temperature co-fired ceramics) technology. LTCC is a fabrication process based on stacking multiple glass-ceramics sheet layers. Metallic sheets are included between the ceramic layers, and their interconnection is ensured with vias.

The proposed design has been manufactured with the DuPont GreenTape 9k7 (ϵ_r=7.1, $\tan\delta$=0.0009) low-loss glass ceramic dielectric tape, silver sheets, and silver vias. In Fig. 7.3, a side view picture of the antenna is depicted, detailing the 13 ceramic layers (d1-d13), the five metallic layers (m1-m5), and the vias. Fig. 7.4 depicts a picture of the fabricated antenna.

Figure 7.4: Front view of the fabricated LTCC 868 MHz on-ground chip antenna.

Fig. 7.5(a) shows the geometry of the proposed antenna, where dimensions are provided in Table I. The ceramic layers have either 112 μm or 224 μm thickness, and to avoid bulge effects and ensure proper metallic contact between layers, a maximum of four layers with vias at the same position are allowed. Vertical meandered paths with vias are used to cope with this limitation, as observed in the bottom images of Fig. 7.3.

(a)

(b)
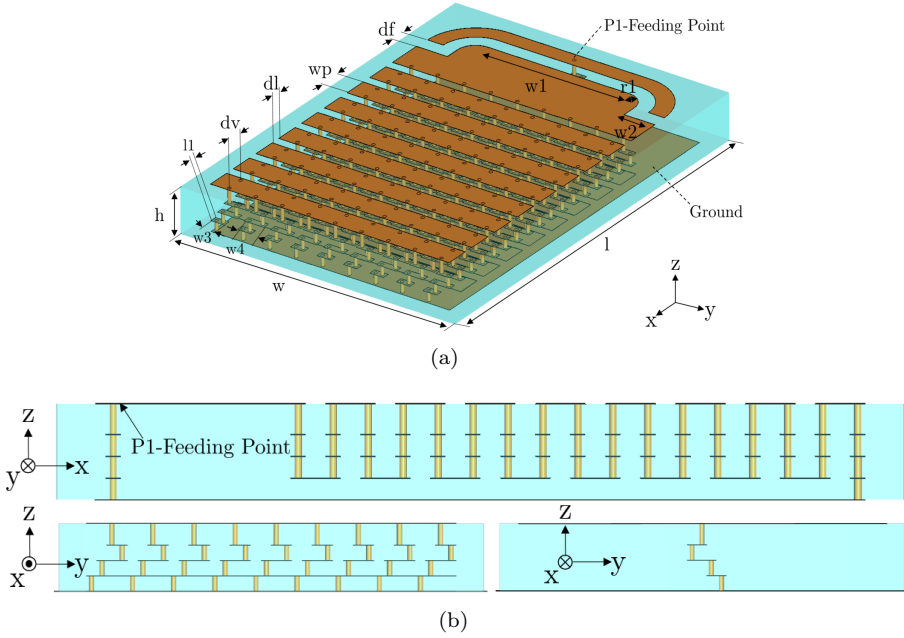
Figure 7.5: a) Overall view of the proposed antenna, and b) Side views of the proposed antenna. Dimensions are detailed in Table 7.2.

l	w	h	dv	dl	wp	df	l1	w1	w2	w3	w4	r1
21.85	15.5	2.45	0.9	0.52	1.28	0.75	0.38	8	1.75	0.76	1.12	1

Table 7.1: Dimensions of the proposed chip antenna (unit: mm)

The antenna is capacitively fed at the furthest point with a feeding line. The feeding point can be found on the back side of the antenna (right on Fig. 7.5(b)). The antenna is meant to be placed on a PCB ground plane and fed from below. Fig. 7.5(b) (bottom right) details the connection with vias from the lower and upper feeding points.

The proposed antenna is evaluated to quantify the difference between its performance on different positions at ground planes of various sizes in terms of matching and total efficiency. In addition, the study of the excitation of different characteristic modes of the ground plane depending on the antenna's position is implemented to justify the results.

To obtain more information about the contribution of the ground plane to the total radiated power, the characteristic modes analysis (CMA) of the

155

isolated ground plane is performed. The radiation patterns of each mode of the ground plane are compared to the total radiation pattern of the antenna+ground plane for different antenna positions. The comparison is realized with the use of the correlation detailed in (7.1), which is an equivalent correlation to the one introduced in 3.1 from Chapter 3.

$$\rho_{n,T(x,y)} = \frac{\iint\limits_{4\pi} g_n^H(\Omega) g_{T(x,y)}(\Omega)\, d\Omega}{\sqrt{\iint\limits_{4\pi} g_n^H(\Omega) g_n(\Omega)\, d\Omega \cdot \iint\limits_{4\pi} g_{T(x,y)}^H(\Omega) g_{T(x,y)}(\Omega)\, d\Omega}} \tag{7.1}$$

The upside of using the correlation between the total and modal fields is avoiding calculating characteristic modes of such a complex structure as the proposed antenna, which includes a lossy dielectric material (the theoretical background of TCM is well-established for lossless structures). Such an analysis is problematic due to its narrow-band resonant behavior, which would require high-frequency resolution calculation for proper modal tracking and modal crossing avoidance. On the other hand, calculating characteristic modes of a square ground plane is simple and deeply studied in the literature. With the correlation, it is possible to establish how similar the total radiated fields are to the modal radiated fields and then use this metric to know approximately which mode of the ground plane is excited.
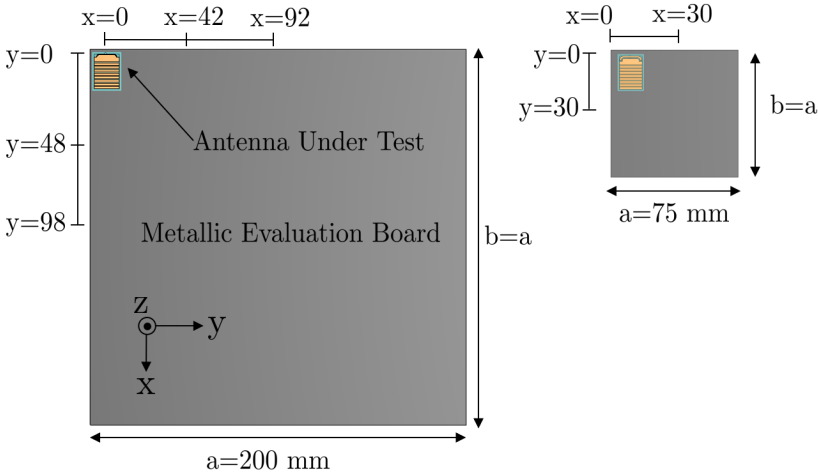
Figure 7.6: Evaluated 200x200 mm^2 and 75x75 mm^2 ground planes with the antenna installed in different locations.

In the following subsections, the proposed antenna installed in a square (with a side length a) electrically large (a=200 mm > $\lambda/2$) and a square electrically small (a=75 mm < $\lambda/4$) ground plane is analyzed.

Study of an Electrically Large Ground Plane (a > $\lambda/2$).

The first study consists of analyzing an a=200 mm square ground plane with the proposed antenna located at four different positions of the ground plane: top-left corner P1(x,y)=(0,0), top-middle P2(x,y)=(92,0), left-middle P3(x,y)=(0,92) and center P4(x,y)=(92,92). Fig. 7.6 left shows the setup with all the considered positions of the antenna in the a=b=200 mm ground plane.

The initial step for the study is the calculation of the first resonant modes of the isolated ground plane. In Fig. 7.7(a) and Fig. 7.7(b) the modal field distributions and characteristic angles of modes J_1-J_4 are depicted.
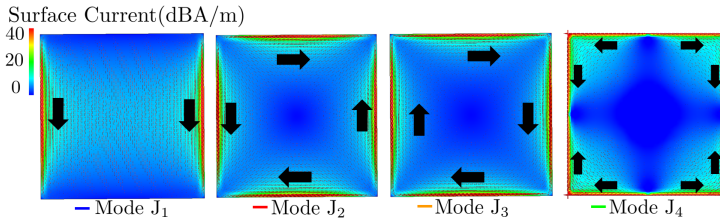
(a)
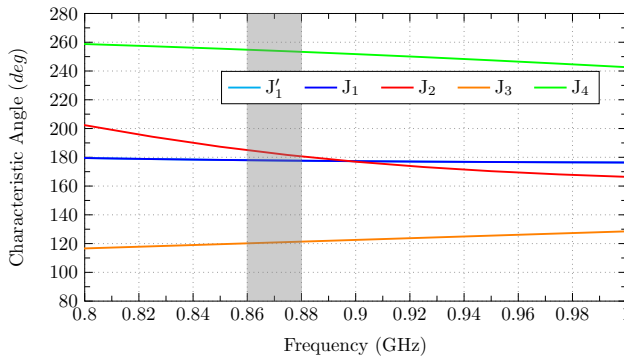
(b)

Figure 7.7: a) Current distribution of Modes J_1-J_4 and, b) Characteristic angle of Modes J_1-J_4. J_1' (horizontal) is the degenerated mode of mode J_1 (vertical).

(a)

(b)
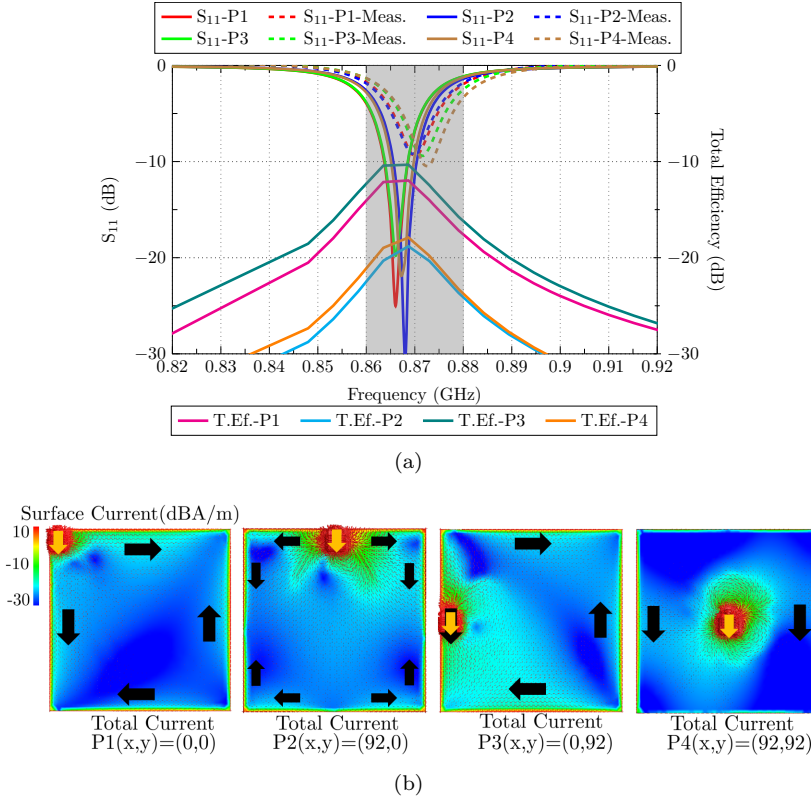
Figure 7.8: a) Reflection coefficient (S_{11}) and total efficiency for different (x,y) positions on a plane of a=200 mm, and b) Total current distribution of the antenna on different positions at resonance

The current distribution of mode J_1' is not depicted since it is the degenerated mode of J_1(vertical/horizontal modes). In Fig. 7.7(b), the operation band of the antenna is remarked in gray. As observed, mode J_1 has already resonated, mode J_2 is really close to resonance and mode J_3 and J_4 have not resonated yet. Mode J_1/J_1' and mode J_2 are potential candidates to be excited due to their proximity to resonance (α=180º). The antenna must be placed in a maximum current to excite any modes properly.

Fig. 7.8(a) describes the reflection coefficient (S_{11}) and the total efficiency obtained at the four analyzed positions. In terms of impedance matching, the antenna is stable, and it is not detuned when displaced. Regarding the total radiation efficiency, there is a considerable difference between each position due

to the excitation of different modes of the ground plane. Fig. 7.8(b) shows the total current distribution of the antenna at resonance in the analyzed positions. From the pictures, the dominant mode of the excited ground plane can be glimpsed. Still, for its confirmation, the correlation between the total and modal radiation patterns at 0.868 GHz is performed and detailed in Table 7.2.

$\rho_{n,T(x,y)}$	J_1	J_1'	J_2	J_3	J_4
P1(0,0)	0	0.12	0.29	0	0.1
P2(92,0)	0	0	0	0	0.2
P3(0,92)	0.28	0	0.5	0	0.05
P4(92,92)	0.45	0	0	0	0

Table 7.2: Correlation between total (plane+antenna) and modal (plane) fields.

The position P3 for the antenna gives the best efficiency results (-10.2 dB). It is placed at the current maximum of J_1 ($\rho = 0.28$) and J_2 ($\rho = 0.5$), and the current flow of the antenna (yellow arrow) has the same direction as the current flow of the mode of the plane (black arrow).

The following position is P1 with -12.5 dB of total efficiency. Mode J_2 ($\rho = 0.29$) is excited but at a lower level because the antenna is placed in a current minimum. Mode J_4 ($\rho = 0.1$) is excited because the antenna is placed in a current maximum, but this mode is still far from resonance. Position P2 has the lowest level of total efficiency (-19 dB) because either it is in a current minimum or the current flow of the antenna is perpendicular to the current flow of the modes. The only excited mode is mode J_4 ($\rho = 0.2$). The last position with a low total efficiency level (-17.5 dB) is P4 because it is only able to excite mode J_1 ($\rho = 0.45$) but not in the current maximum.

Study of an Electrically Small Ground Plane (a < $\lambda/4$).

The second study consists of analyzing an a=75 mm square ground plane with the antenna placed at the four positions: top-left corner P1(x,y)=(0,0), top-middle P2(x,y)=(30,0), left-middle P3(x,y)=(0,30) and center P4(x,y)=(30,30). The characteristic angles of the isolated ground plane modes are depicted in Fig 7.9(a). In this analysis, all the modes resonate at higher frequencies, and consequently, the efficiency's average value drops, as seen in Fig. 7.10(b). Only fundamental modes J_1 and J_1' can be excited, considering that the current distribution of these modes at the operating band is below resonance. They have a current null in the middle of a side, and currents flow through the perimeter in C-shape until they reach the null on the other side (see Fig. 7.9(b)). Table 7.3 details the correlation between modal and total fields.
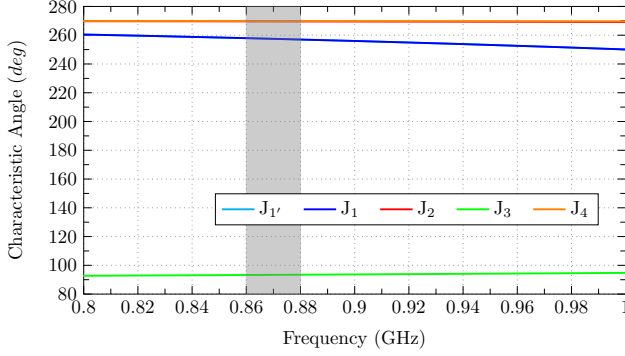
(a)
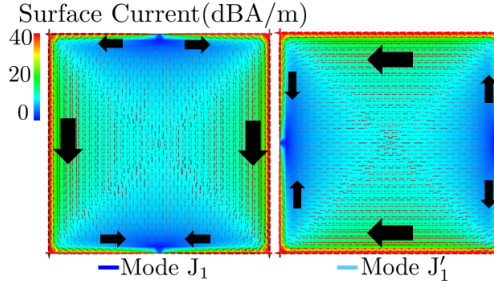
(b)

Figure 7.9: a) Characteristic angles of mode J_1-J_4, and b) Current distribution of modes J_1 and J_1' at the operating band.

$\rho_{n,T(x,y)}$	J_1	J_1'
P1(0,0)	0	0.55
P2(30,0)	0.1	0
P3(0,30)	0.45	0.2
P4(30,30)	0.35	0

Table 7.3: Correlation between total (plane+antenna) and modal (plane) fields.

Regarding impedance matching, the resonance frequency of the simulated results is slightly displaced to a higher frequency than the results obtained in the previous analysis. The measured results resonate at lower frequencies and have lower matching levels than the simulated results due to fabrication

tolerances (Fig. 7.10(b)). Measured results in both ground planes show a stable resonance frequency.

(a)

(b)
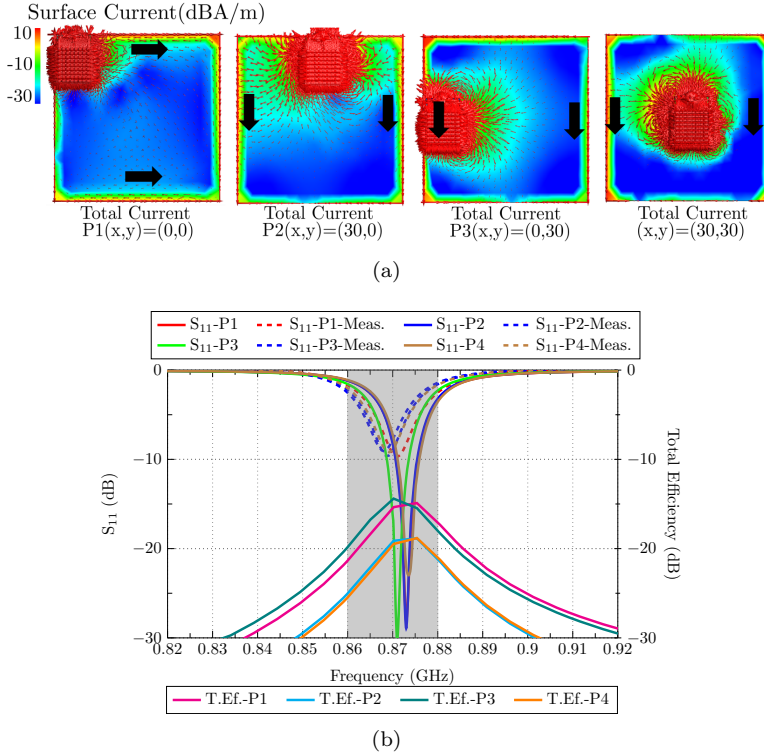
Figure 7.10: a) The total current distribution of the antenna on different positions at resonance on a plane of a=75 mm and, b) Reflection coefficient (S_{11}) and total efficiency for different (x,y) positions on the plane.

For position P1(x,y)=(0,0) and P3(x,y)=(0,30), the highest values of efficiency are obtained (-15 dB). In the case of P1 mode, J_1' ($\rho = 0.55$) is highly excited, and for P3 modes, $J_1(\rho = 0.45)$ is excited at a higher level. After all, the antenna is placed in the current maximum with the same current direction and $J_1'(\rho = 0.2)$ in a lower level because it has the same current direction but is placed in the minimum. On the contrary, at P2(x,y)=(30,0) and P4(x,y)=(30,30) positions, they show a -19.5 dB total efficiency because they are not properly exiting the ground plane. P2 slightly excites mode J_1 ($\rho = 0.1$) because it has the same current flow of the mode, but it is in a current minimum. P4 has slightly more correlation for J_1 ($\rho = 0.35$) because it is

placed where the currents are more intense but not in the optimum maximum position.

7.3 LTCC 2.4 GHz On-Ground Chip Antenna

In this section, a miniaturized design is a corrugated (accordion-like) planar inverted F antenna (PIFA) embedded in a ceramic substrate and fabricated in LTCC technology with a total size of $10.3 \times 8 \times 2.45$ mm^3 ($0.067 \times 0.048 \times 0.019\lambda_0^3$). The antenna geometry is depicted in Fig. 7.11, and its dimensions are detailed in Table 7.4. The antenna is meant to be installed on a metallic plane with no clearance area requirement for IoT applications. Due to its reduced height and the absence of clearance, the bandwidth (25 MHz (1%) for S_{11}¡-6 dB) is compromised. It shows excellent frequency stability when the antenna is displaced on planes of different sizes.
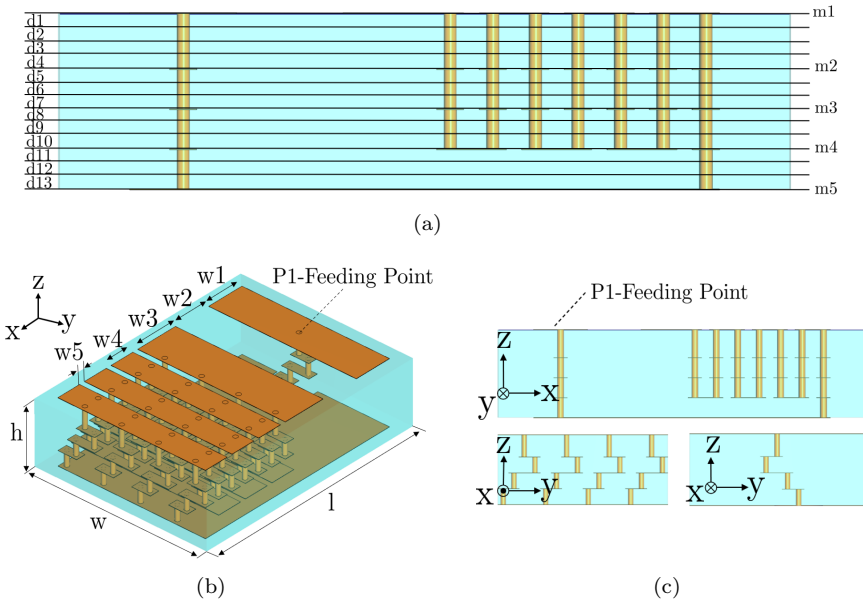
Figure 7.11: Geometry of the proposed low-profile LTCC chip antenna. The blue color represents the ceramic substrate, and the orange color represents the metallic layers and vias. a) Side view with all LTCC layers specified, b) Overall view of the antenna (Dimensions in Table 7.4), and c) Side views of the antenna.

162

l	w	h	w1	w2	w3	w4	w5
9.3	7	2.4	1.5	1.5	1.7	1	0.2

Table 7.4: Dimensions of the proposed chip antenna (unit: mm)

LTCC fabrication involves stacking glass-ceramic sheet layers, including metallic sheets, vias, and components. The proposed antenna comprises DuPont GreenTape 9k7 (er=7.1, tan=0.0009) low-loss glass ceramic dielectric tape, silver sheets, and silver vias. Fig. 7.11(a) describes the 13 stacked ceramics layers (d1-d13) with 112 μm or 224 μm thickness. Fig. 7.11(b) and 7.11(c) show the antenna's overall view and side views with the grooves/ridges creating the accordion shape. The antenna is meant to be placed on a PCB fed from below (see feeding point on Fig. 7.13(c) right) with an appropriate connector.

Figure 7.12: Picture of the fabricated antenna.

For the design process, miniaturization is obtained using four ridges and three grooves to increase the electric length of the antenna and reduce its size. The design process is depicted in Fig. 7.13(b).

In this section, the radiation properties of the antenna in terms of matching and total efficiency are studied depending on the location of the proposed design in different-sized ground planes. The analysis quantifies the degradation of the radiation properties if an antenna is not placed properly. We provide both a theoretical (using CMA) and experimental study using characteristic modes analysis to analyze which modes of the ground plane are excited.

Three ground plane sizes are studied: an electrically large (a=b=100 mm $> \lambda/2$), an electrically small (a=b=30 mm $< \lambda/4$), and a thin (a=100 mm and b=20 mm) ground plane. Fig. 6.3 depicts the three copper ground planes with the proposed antenna used for the experimental analysis.

We analyze the isolated ground plane with CMA and correlate the radiated fields of each mode to the total radiated fields of the ground plane, including the chip antenna in different positions. The correlation is then used as a metric to quantify approximately which mode of the ground plane is excited.

(a)   (b)

(c)
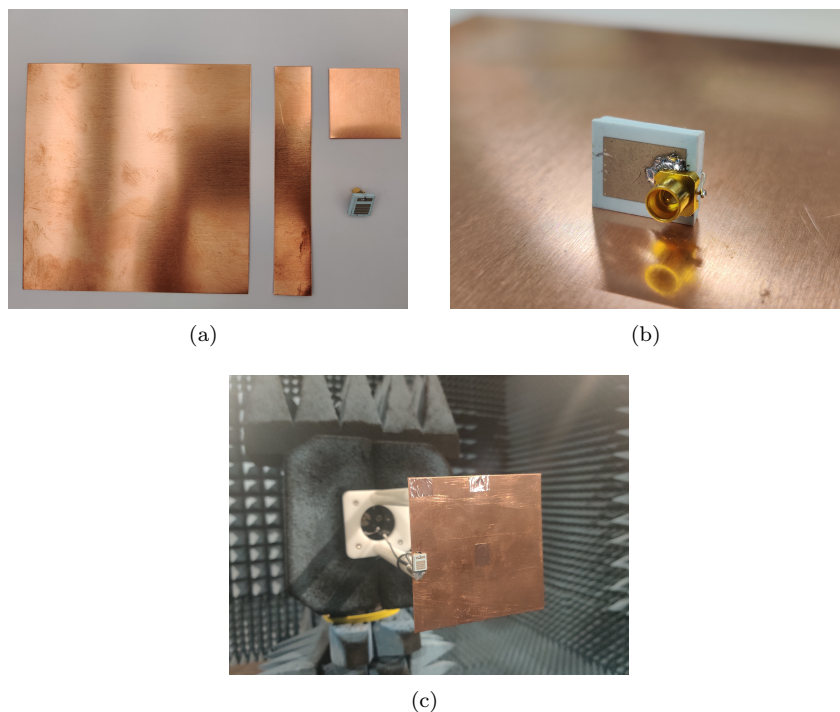
Figure 7.13: Pictures of the: a) Analyzed ground planes manufactured with copper sheets and the fabricated antenna, b) Connectorized antenna, c) Measurement set-up in the an-echoic chamber.

Large Ground Plane a=b=100 mm CMA

The first analysis is based on the square electrically large ground plane with a=b=100 mm dimensions corresponding to a$> \lambda/2$. For the study, four positions of the antenna are considered: top-left corner P1(x,y)=(0,0), top-middle P2(x,y)=(45,0), left-middle P3(x,y)=(0,45), and center P4(x,y)=(45,45). In Fig. 7.14(a), the evaluation set-up is detailed.

The initial step focuses on the CMA of the isolated square ground plane. In Fig 7.14(b) and 7.15, each mode's characteristic angle and current distribution are depicted, respectively. The gray bar in Fig. 7.14(b) indicates the band where the proposed antenna works. At that frequency, modes J_1/J'_1, which are the fundamental modes (vertical/horizontal modes), have already resonated and have values close to 0° and they have the potential to be excited. Mode J_2 also resonates before the operating band and has values of characteristic

(a)

(b)

Figure 7.14: a) Evaluated 100x100 mm^2 with the antenna in four different positions on the ground plane, and b) Characteristic angles of the analyzed modes (J$_1$-J$_5$).

angle close to 0. It is a mode with four nulls on the corners of the plane and a maximum in the middle of the edges, and it is also a potential candidate. Mode J$_3$ is considered the loop mode, which is resonant at higher frequencies, and due to its highly inductive behavior and high-frequency resonance, it is generally not excited. Modes J$_4$ and J$_5$ resonate at higher frequencies. Still, they may be excited because they are not far from resonance, and their capacitive behavior at the operating band can be compensated. Mode J$_4$ has four current nulls in the middle of the four edges, and mode J$_5$ has the same four nulls and four

165
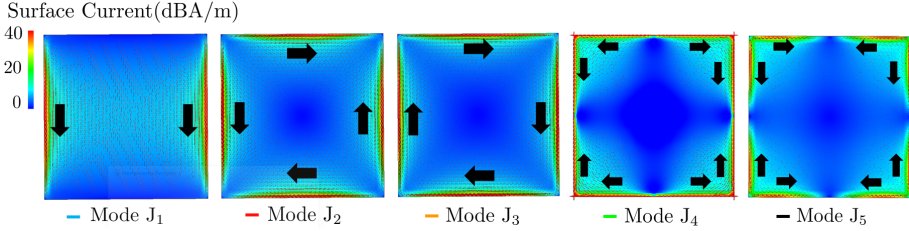
Figure 7.15: Current distribution of the analyzed modes (J_1-J_5). J_1' is equivalent to J_1 but rotated 90° (degenerated).

nulls in the corners. Since the ground plane is considered electrically big, all the mentioned modes can be potentially excited due to their relative proximity to resonance.

Once the ground plane is analyzed, the antenna is placed in the four analyzed positions, and the reflection coefficient (S_{11}) and the total efficiency are calculated and depicted together in Fig. 7.3. The result for the S_{11} parameter shows a very narrow bandwidth operating band (24 MHz for $S_{11} < -6$ dB) and high stability with no detuning nor bandwidth degradation when the antenna is displaced.

The total efficiency is greatly affected by the position of the antenna. The highest value (-8.5 dB) of total efficiency is obtained when the antenna is placed

Figure 7.16: Reflection coefficient (S_{11}) and Total Efficiency of the antenna located in the four analyzed positions.

(a)

(b)

Figure 7.17: a) Reflection coefficient (S_{11}) and Total Efficiency of the antenna located in the four analyzed positions, b) Correlation (detailed in Eq. 7.1) of total and modal fields, and c) Total current distribution of the antenna in the four positions.

in P3(x,y)=(0,45). In Fig. 7.17(a), the correlation between the total fields with each modal field is depicted, and in case of (x,y)=(0,45) modes J_1, J_2 and J_4 are excited. The first two present higher correlation because the antenna is placed at a current maximum for both modes and mode J_4 at a minimum. The second higher value (-10.2) is obtained when the antenna is placed in P1(x,y)=(0,0), where only mode J_4 is properly excited because only mode J_4 has a current maximum in the corner of the ground plane. Lastly, for the position P2(x,y)=(45,0) and P4(x,y)=(45,45), the lowest total efficiency value (-12 dB) is obtained. For P2(x,y)=(45,0), only mode J_5 is excited and at a low level because it has a current minimum. All the other modes are not excited because the current flow of the antenna is orthogonal to the current flow of

all the modal fields. For P4(x,y)=(45,45), the antenna is placed where most modes have a null. Only mode J_1 can be excited because its current flow is in the same direction as the antenna, but it is not in the current maximum.

Figure 7.18: Radiation patterns at resonance when the antenna is placed in: a) P1(x,y)=(0,0), b) P2(x,y)=(45,0), c) P2(x,y)=(0,45) and, d) P4(x,y)=(45,45).

The total currents in the four positions with the antenna are depicted in Fig. 7.17(b) for its visual comparison with the modes. The radiation patterns for planes $\phi=0°$ and $\phi=90°$ are also depicted for all the analyzed positions from Fig. 7.18(a) to Fig. 7.18(d).

As a first conclusion, the best position for the antenna is the middle left position P3(x,y)=(0,45) because most of the first analyzed modes of the ground plane, which are close to resonance, exhibit a current maximum in the perimeter of the ground plane and especially in the middle of each side. In addition, the antenna's current flow has the same direction as the modal currents.

Small ground plane a=b=30 mm CMA

The second subsection analyzes a square electrically small ground plane with a=b=30 mm dimensions corresponding to a< $\lambda/4$. Identically as in the previous subsection, the same four positions of the antenna are considered: top-left corner P1(x,y)=(0,0), top-middle P2(x,y)=(12,0), left-middle P3(x,y)=(0,12) and center P4(x,y)=(12,12) detailed in Fig. 7.19(a).

(a)

(b)
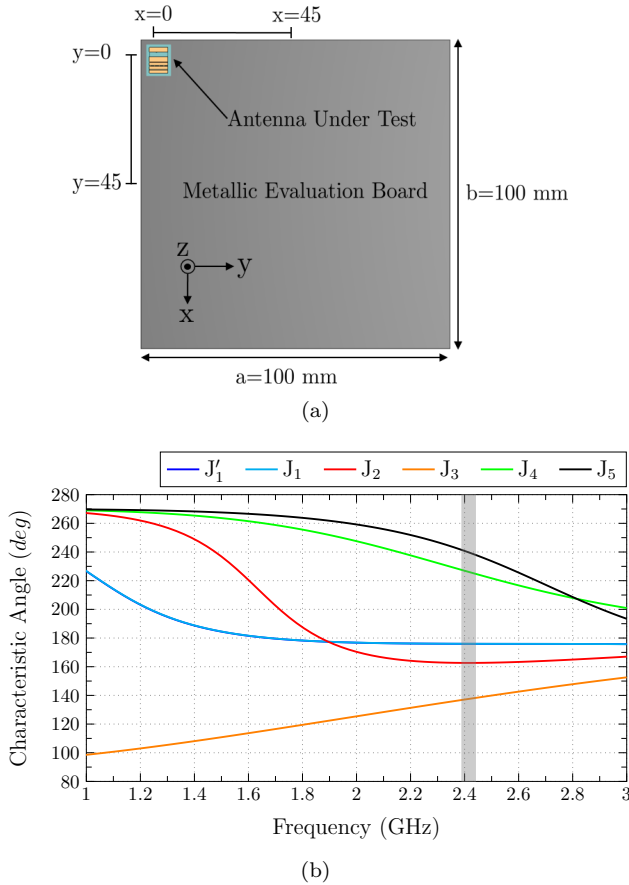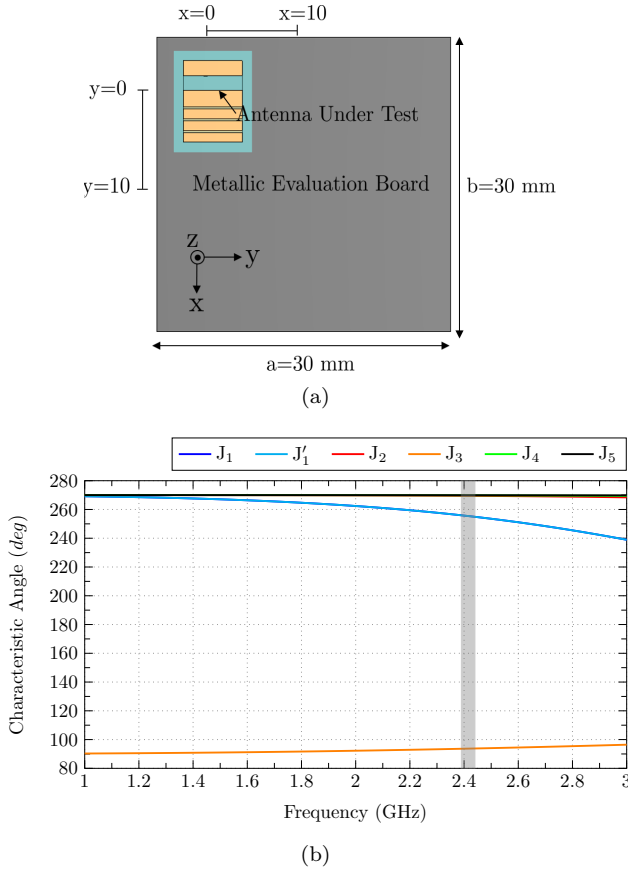
Figure 7.19: a) Evaluated 30x30 mm^2 with the antenna in four different positions on the ground plane and, b) Characteristic angles of the analyzed modes (J$_1$-J$_5$).

The CMA of the isolated plane shows that at the operating band (gray band of Fig. 7.19(b)), all the modes have not resonated yet due to the limited size of the plane. Only modes J$_1$ and J$_1'$ have a lower value of characteristic angle,
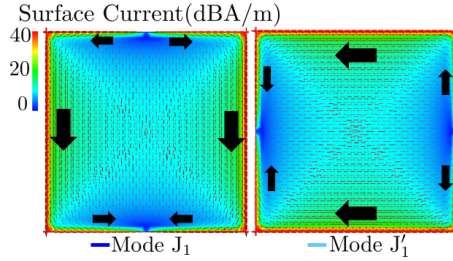
Figure 7.20: Current distribution of mode J_1 and J_1'.

and they will be the only modes that will be excited. Fig. 7.20 represents the current distribution of modes J_1 and J_1' at 2.4 GHz.

Since the modes are far from resonance, it can be observed that currents are not only flowing vertically or horizontally (like at resonance) but also have an external path beginning in the current minimum in the middle of a side and flowing through the edge of the perimeter (C-shape path) until the middle of the other side is null.

After the ground plane analysis, the antenna is analyzed in the four positions. The reflection coefficient (S_{11}) and the total efficiency are depicted together in Fig. 7.21. The result for the S_{11} parameter shows the same narrow

(a)
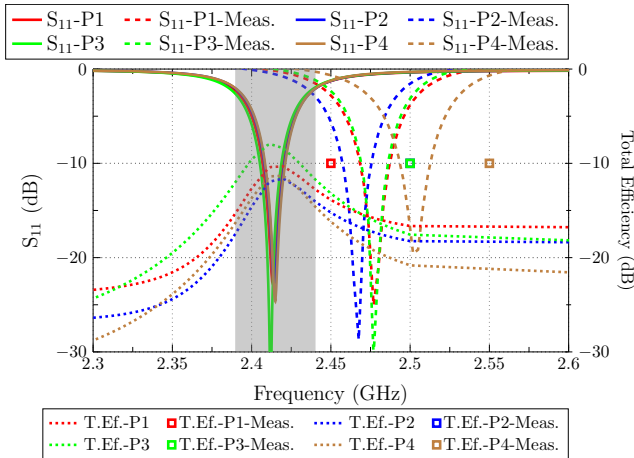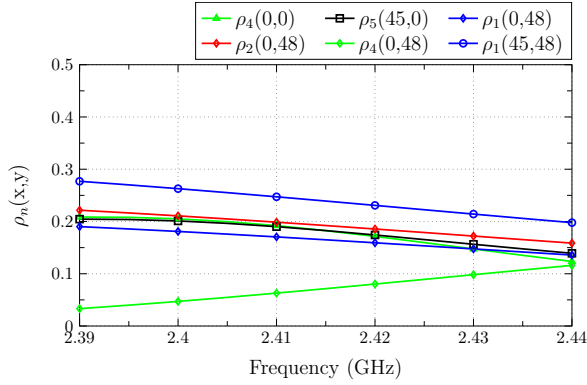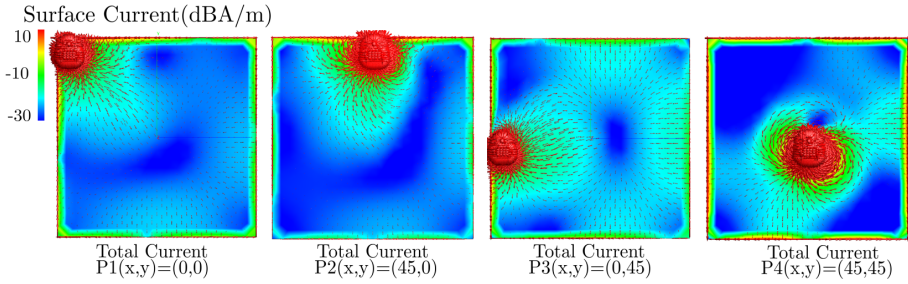
Figure 7.21: Reflection coefficient (S_{11}) and Total Efficiency of the antenna located in the four analyzed positions.

(a)

(b)
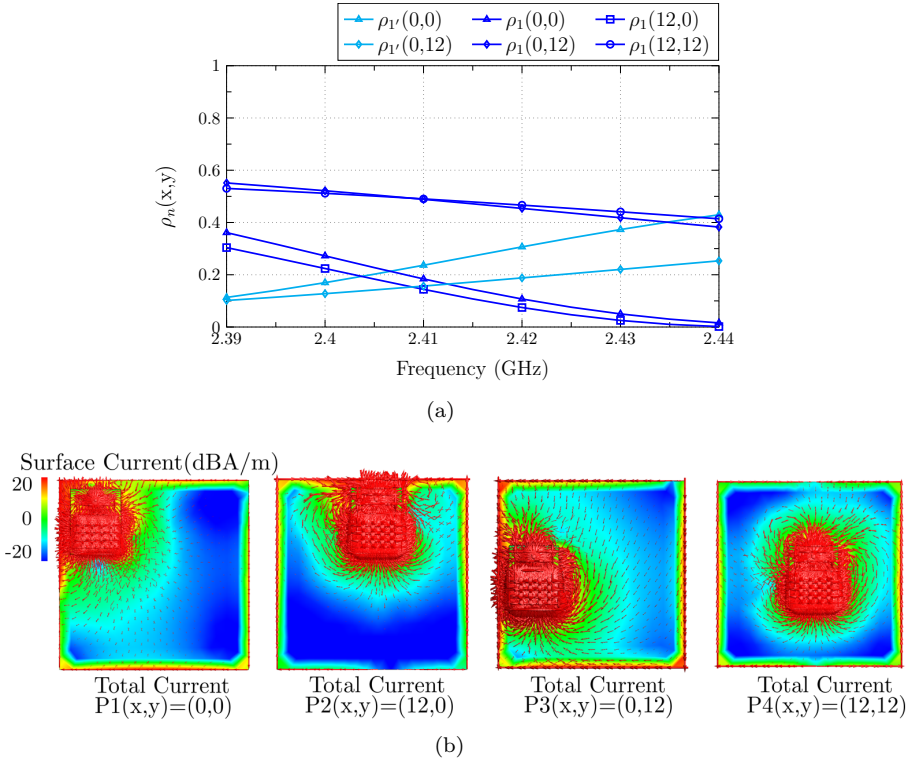
Figure 7.22: a) Correlation of total and modal fields, and b) Total current distribution of the antenna in the four positions.

bandwidth operating band (24 MHz for $S_{11} < -6$ dB) as in the electrically large ground plane and high stability with no detuning nor bandwidth degradation even when the antenna is displaced in such a limited ground plane.

The total efficiency is also affected by the position of the antenna. With a simple inspection of the two modes (J_1/J_1'), it is possible to guess which position is more suitable for getting the highest total efficiency. The position P3(x,y)=(0,12) obtains the highest value (-9.5 dB) because the antenna is placed in the middle of J_1 current maximum, and also, the current flow of the antenna follows the current flow of the mode. In addition, mode J_1' is excited with a lower level because it has a current null in that position. Still, the prolongation of the mode creates an additional current path (which appears at such low frequencies) in phase with the current flow of the antenna. The following efficiency values are -11.4 dB and -11.5 for positions P1(x,y)=(0,0)

171

and P4(x,y)=(12,12), respectively. For P1(x,y)=(0,0), the antenna is placed not in a current minimum nor a maximum for modes J_1 and J'_1. Both modes are excited at a low level because the antenna current flow has the same direction as the modes but is not placed in any current maximums. In the case of P4(x,y)=(12,12), only mode J_1 is excited with medium level because even though it has the same current flow as the mode, it is not placed in the exact current maximum (edge). The worst result of total efficiency (-13.5 dB) is obtained by P2(x,y)=(12,0) with a current minimum for mode J_1 (with antenna current flow in phase) and a maximum of J'_1 but with the current flow is orthogonal to the mode. Only mode J_1 is excited but at a poor level.

The total currents in the four positions with the antenna are depicted in Fig. 7.22(b) for its visual comparison with the modes. The radiation patterns for planes $\phi=0°$ and $\phi=90°$ are also depicted for all the analyzed positions in Fig. 7.23.
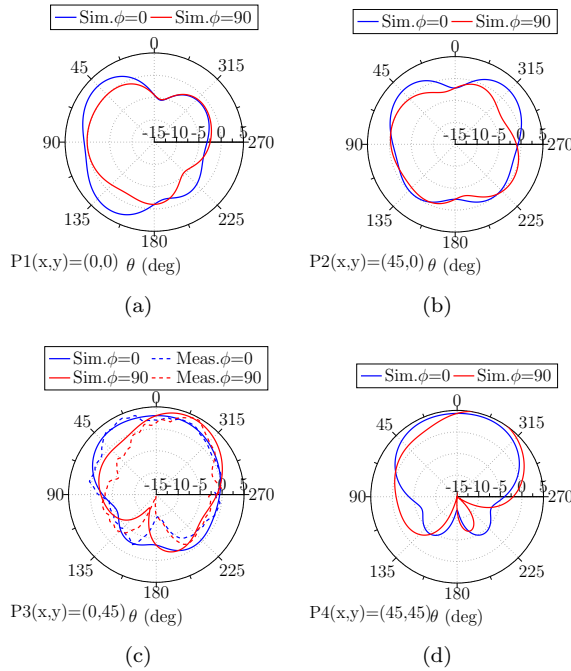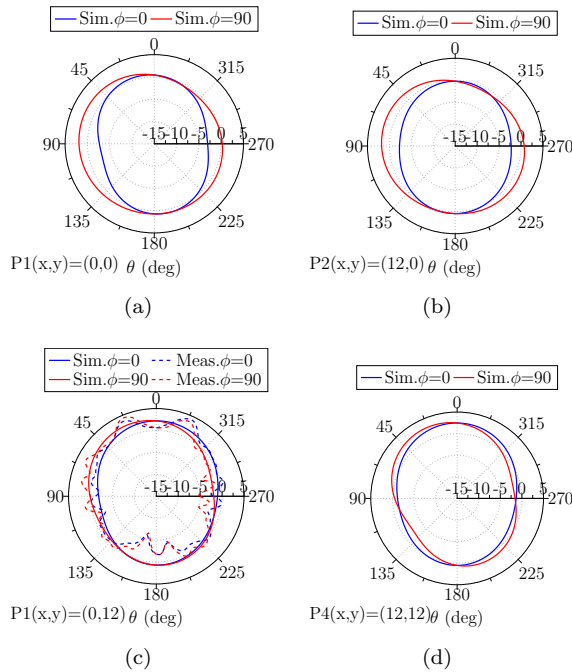

Figure 7.23: radiation patterns at resonance when the antenna is placed in: d) P1(x,y)=(0,0), e) P2(x,y)=(12,0), f) P2(x,y)=(0,12) and, g) P4(x,y)=(12,12).

After the second analysis, it can be stated that another time the best position for the antenna placement is the middle-left position because the antenna

is placed in the current maximum of mode J_1, and the current flow of the antenna is parallel to the current flow in the maximum of the mode. The worst position is the top-middle P2(x,y)=(12,0) because either the current flow is orthogonal to the current maximum flow of J_1' or, in the case of J_1, it is in a current minimum.

Long Ground Plane a=15 mm and b=100 mm CMA

The last subsection analyzes an electrically long ground plane with dimensions of a=15 mm and b=100 mm. In this study, due to the reduced width (a) of the plane, only two positions are analyzed: top P1(x,y)=(0,0) and middle P2(x,y)=(0,45). In each position, the antenna is placed in two orthogonal positions (see Fig. 7.24).
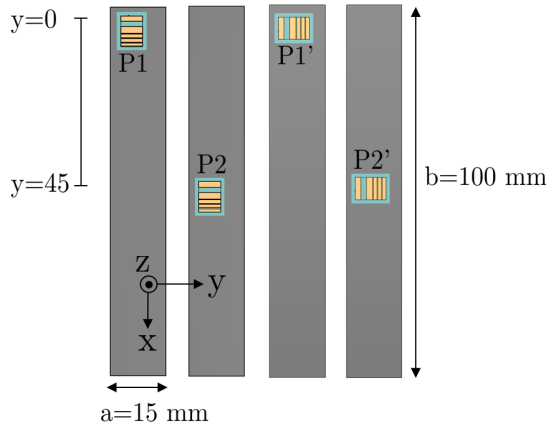
Figure 7.24: Evaluated 15x100 mm^2 ground plane with the antenna in two different positions and polarization.

Observing the characteristic angles of the modes of the long ground plane, it can be observed that mode J_1 is resonant before the operating band, and mode J_2 is close to resonance. The other modes resonate at high frequencies, and by a first impression, it can be stated that only modes J_1 and J_2 will be present in the analysis. Mode J_1 has a current distribution of the vertical mode (see Fig. 7.25(b)), with nulls in the top and bottom edges and maximums in the middle of the left and right sides. Mode J_2 presents a current minimum in the middle of the right/left sides and a current maximum in the top and bottom edges. Mode J_3 corresponds to the loop mode, and mode J_4 is a higher-order mode with four current nulls and four maximums. The total currents, including

the antenna, are also depicted in Fig. 7.25(c) for a visual comparison between modal and total currents.

(a)

(b)

(c)
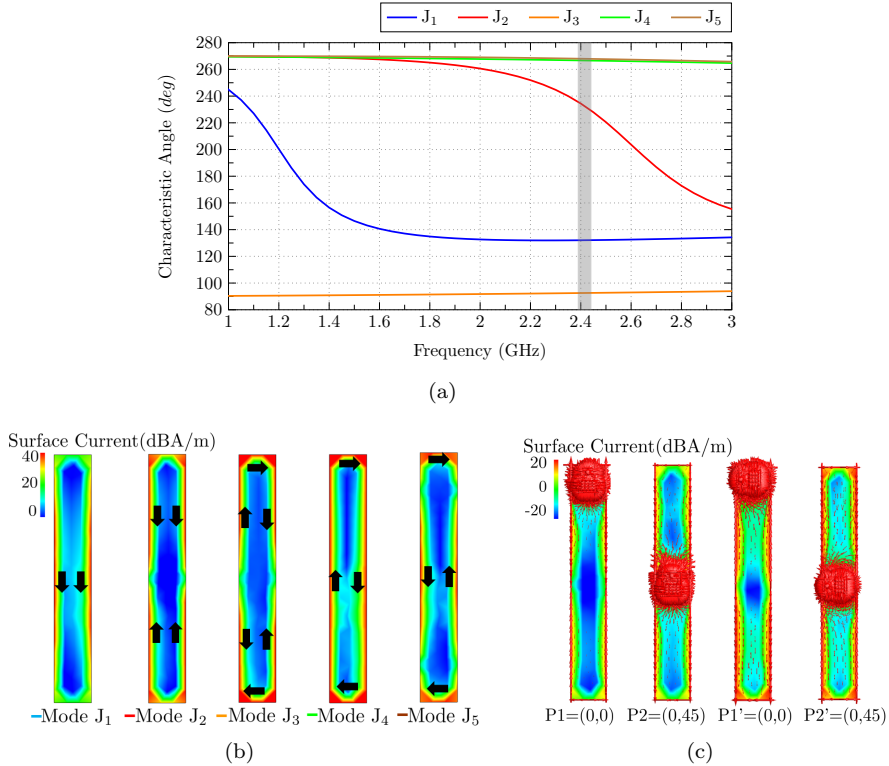
Figure 7.25: a) Characteristic angles of the analyzed modes (J_1-J_5), b) Current distribution of modes J_1-J_5, and c) Total current distribution of the antenna in the four positions.

Regarding matching (Fig. 7.26), results show the same stability as in the previous studies, with no detuning observed when the antenna is displaced or the polarization is changed.

The total efficiency results have the highest dynamic range values analyzed in all the performed studies. On the one hand, the best total efficiency results (-7.6 dB and -7.8 dB) observed in Fig. 7.26 are obtained by the position P1'(x,y)=(0,0) and P2(x,y)=(0,45). Analyzing the correlation (Fig. 7.27), it can be observed that for (x,y)=(0,0)', mode J_2 is perfectly excited because the antenna is placed parallel to the top edge. A current maximum flows in the same direction as the antenna currents. For P2(x,y)=(0,45) position, the
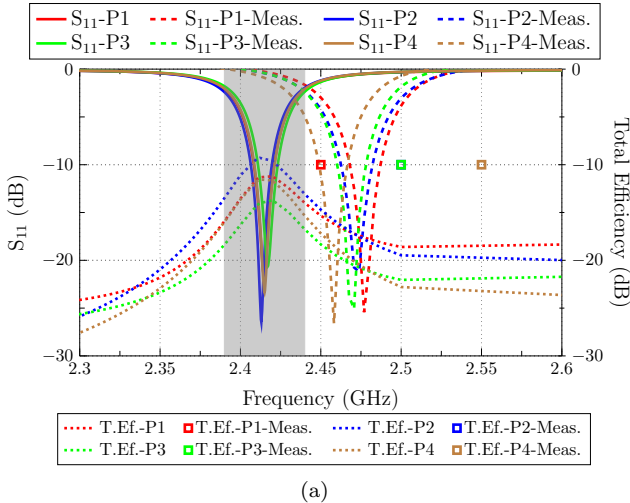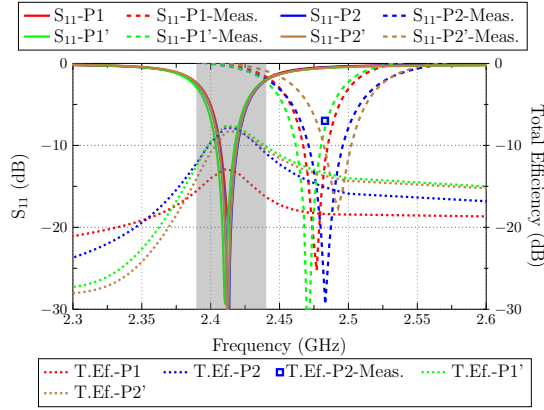
Figure 7.26: Reflection coefficient (S_{11}) and Total Efficiency of the antenna located in the four analyzed positions.

antenna is exciting mode J_1 because it is placed in the middle of the left and right sides, and since the plane is very narrow, both maximums are excited. The following total efficiency value is obtained for the P2'(x,y)=(0,45) position, where mode J_2 is excited but not at the same level because it is placed in the current minimum. Although it is placed in the maximum for J_1, the current flow of the antenna is orthogonal to the currents of this mode. The worst total efficiency value (-12.9 dB) is observed for P2(x,y)=(0,45) positions. The reason for such a low level is due to the position where mode J_1 has a current minimum and mode J_2 has its maximum on the top edge, but it is orthogonal to the current flow of the antenna.
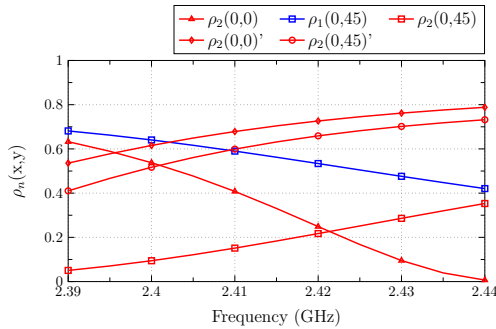
Figure 7.27: Correlation (detailed in Eq. 7.1) of total and modal fields.

175

The radiation patterns for planes $\phi=0°$ and $\phi=90°$ are also depicted for all the analyzed positions in Fig. 7.28.
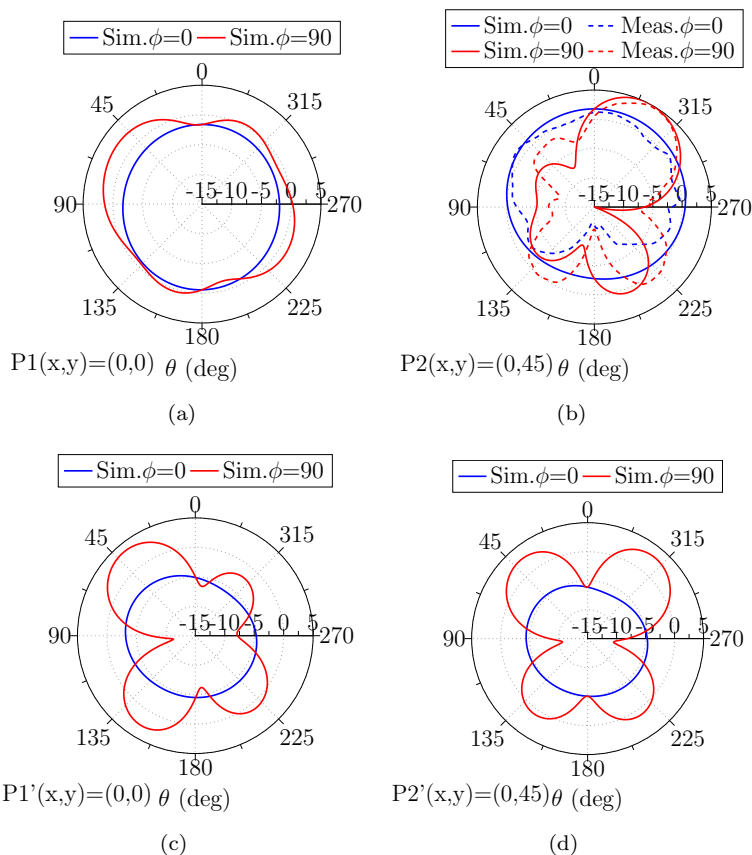
Figure 7.28: Radiation patterns at 2.4 GHz for: a) P1(x,y)=(0,0), b) P2(x,y)=(45,0), c) P1'(x,y)=(0,0) and, d) P2'(x,y)=(0,45).

The information gathered in the last analysis shows that the antenna position greatly impacts the efficiency of narrow ground planes. If the antenna is placed in the correct position, always considering the current distribution of the modes close to resonance and the current flow of the antenna, high correlation and efficiency values are obtained.

7.4   LTCC 3.6 GHz On-Ground Chip Antenna

This section presents another on-ground antenna that does not require a clearance area to be installed. It is compact with a total volume of $0.12 \times 0.06 \times 0.03\lambda_0^3$. It is meant to be installed in highly size-limited devices and resonates at 3.6 GHz for IoT applications. The fabrication process has been realized using LTCC technology. LTCC fabrication process consists of stacking multiple glass-ceramics sheets layers and, in this case, DuPont GreenTape 9k7 (ϵ_r=7.1, tan δ=0.0009) low loss glass ceramic dielectric tape, silver sheets, and silver vias are employed.
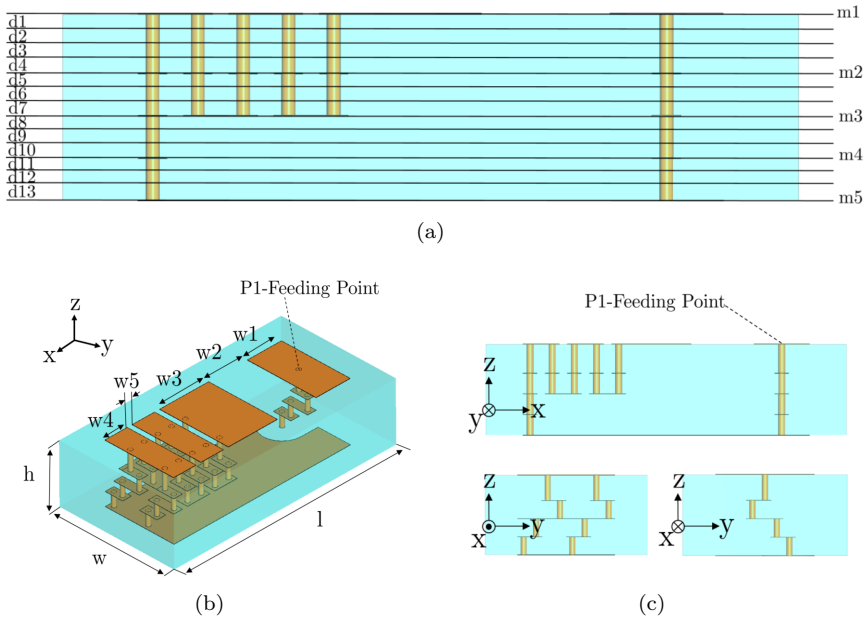
Figure 7.29: Geometry and dimensions of the proposed low-profile LTCC chip antenna (perspective view on top and side view on the bottom). Blue represents the substrate, and orange represents the metallic layers and vias. a) Side view with all LTCC layers specified, b) Overall view of the antenna, and c) Side views of the antenna.

The proposed LTCC low-profile antenna is a capacitively fed meandered planar inverted F antenna (PIFA) embedded in a ceramic substrate, and the geometry of the antenna is shown in Fig. 7.29(a). Fig. 7.29(b) depicts the layer distribution of the 13 ceramic sheets, five metallic sheets, and vias. Two

l	w	h	w1	w2	w3	w4	w5
9.75	5	2.44	1.50	1.70	2.15	0.98	0.22

Table 7.5: Dimensions of the proposed 3.6 GHz chip antenna (unit: mm)

Figure 7.30:   Front and back view of the fabricated antenna.

vertical grooves/ridges can be observed to miniaturize the antenna. The vias are connected with a zig-zag to avoid bulge effects on the fabrication process.
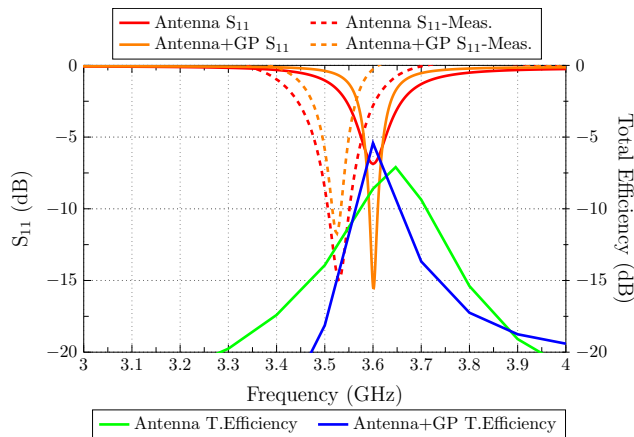
Figure 7.31:   Reflection coefficient S_{11}(dB) and Total efficiency of the simulated and fabricated antenna.

The fabrication process has been done with LTCC technology, and the manufactured antenna is depicted in Fig. 7.30 next to a 1 euro cent. The reflection coefficient (S_{11}) and the total efficiency of the simulated and fabricated antenna are depicted in Fig. 7.31 with good agreement. Better matching and total efficiency are observed when the antenna is connected to an infinite ground plane. In addition, the radiation patterns of the isolated antenna and the antenna on the infinite ground plane are depicted in Fig. 7.32.
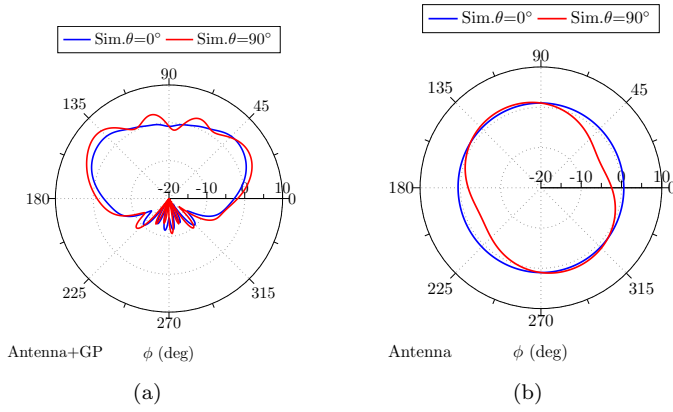
Figure 7.32: a) Radiation pattern of the antenna installed in an infinite ground plane, and b) Radiation pattern of the isolated antenna.

In conclusion, this chapter has successfully addressed the design, fabrication, and allocation study of three LTCC on-ground chip antennas for the 868 MHz, 2.4 GHz, and 3.6 GHz bands for IoT applications. In addition, a novel CMA-based methodology for their allocation on a device has been utilized. The study shows stable antennas when reallocated and a considerable drop in efficiency, which can reach a 10 dB difference if the antennas are not installed in the correct location.

Chapter 8

Conclusions

In this section, The main conclusions obtained throughout the thesis are listed by chapter. All the objectives established at the beginning of the thesis have been achieved, and it is worth summarizing the main conclusions that were extracted.

In **Chapter 1**, the state of the art of the two main applications of the thesis has been introduced:

- There is a growing demand for indoor access point antennas with highly isolated ports showing high efficiency for 5G MIMO applications. Most solutions are based on dual-polarized antennas; alternatives with more ports are required.

- The bloom of IoT applications has led to an exponential demand for small antennas to be installed in size-limited devices. Chip antennas emerged as a candidate to fill this need. Manufacturers provide general guidelines for their installation but without further information regarding the physical insight of the antenna's performance.

Chapter 2 addresses the Theory of Characteristic Modes and presents the main parameters used in CMA. In addition, a deep analysis on the state of the art on characteristic modes has been presented, obtaining the following conclusions:

- CMA is a handy tool for designing and integrating multiple antennas on a single platform, such as a smartphone, tablet, or CubeSat. Many solutions use CMA to isolate antennas by strategically placing them to excite different platform modes. In addition, many re-configurable antenna solutions have also been designed with CMA.

- CMA has been lately used for meta-surface design because it can be optimized independently and without feeding.

- A new trend in the decomposition of characteristic modes with alternative numerical techniques and numerical methods has widened the limitation of the only use of the MoM.

In **Chapter 3**, a brief introduction to wideband monopoles has been carried out. In addition, a circular wideband monopole has been used to feed a square ground plane, placing them on the corner and in the middle of a side to analyze with CMA how a feeding element (monopole) excites different modes of the fed structure (ground plane). The following conclusions are extracted:

- A monopole connected to a ground plane can be considered a capacitive feeding. It must be placed at a current minimum to excite any ground plane mode. Depending on the location of the monopole, different modes of the ground plane are excited.

- For the first time, a new strategy for studying which mode of the ground plane is excited is applied using the correlation between the total radiated fields (antenna+wideband) and modal radiated fields (ground plane). The correlation avoids the CMA, including the feeding (monopole), which saves time and resources, especially when the feeding becomes complex, and the modal calculation does so.

In **Chapter 4** the design of wideband multiple-fed indoor access point antennas for 5G MIMO applications have been addressed. The following conclusions have been obtained:

- A design procedure to design cavity-backed antennas from a square plane with the use of CMA has been successfully applied, simplifying the design process of this kind of structure. Three cavity-backed antennas with two monopoles, four monopoles, and two dipoles have been successfully designed using this design procedure.

- Cavity-backed designs are limited in miniaturization due to the minimum distance that must be left to isolate all the ports.

- Cavity-backed antenna designs present complex and time-demanding simulations when the number of ports is high.

In **Chapter 5**, two novel methodologies based on CMA have been presented to overcome some limitations when designing cavity-backed designs from the previous chapter. In addition, the MIMO channel was also studied using a proposed cavity-backed design. The following conclusions have been obtained:

- A novel methodology based on CMA has been used for identifying the nature of the coupling between ports. Decomposing the total currents and fields into modal currents and modal fields has provided valuable information to identify modes contributing to the coupling. The methodology has been applied to increase the isolation between ports of a four-port wide-band antenna with unidirectional and independent radiation patterns by adding an x-shape block, which does not permit the existence of a mode that contributes to the coupling between ports.

- A novel methodology (sector unit cell methodology) based on the subdivision of an N-port cavity with radial symmetry into N sector unit cells has been presented for N-port MIMO antenna designs for 5G/Wi-Fi indoor access point applications. The methodology simplifies the design and simulation process thanks to the approach based on the analysis of two contiguous cells. With the study of two contiguous cells, the performance of the N-port antenna can be predicted. Five designs of N-port open cavities with circular (N=4), square (N=4), hexagonal (N=6), octagonal (N=8), and teeth-saw (N=8) shapes have been successfully designed with the use of the proposed methodology. The matching and isolation correlation between the unit cell approximation and the complete design has been confirmed to be high.

- The proposed sector unit cell methodology introduces a significant simplification of the simulation and design process and a systematic strategy for designing complex and time-demanding cavity-based designs with a high number of ports. As a reference, the simulation of the 8-port octagonal design takes 4h 0m 14s, the simulation of two unit cells 8m 57s and a unit cell 4m 6s in a computer with 16 GB of RAM and an Intel Core i7-8700 CPU. The benefits of using the unit cell approximation methodology are justified.

- The calculation of the channel capacity of a 4X4 MIMO system in the presence of mutual coupling has been addressed with a previously designed antenna.

- The envelope correlation coefficient (ECC) in different propagation conditions modeled by several angular distributions (uniform, Gaussian, and Laplacian) have been successfully calculated.

Chapter 6 presents the fundamental basis of small antennas and the classical miniaturization techniques. The main advances of the last decades in the small antenna field are presented. In addition, a parametric study for the correct installation of a classic chip antenna is addressed.

- The industry and the constrain on the space where the antenna is installed have triggered the demand for chip antennas, which are miniaturized antennas generally embedded in ceramic substrates that permit their installation as a surface-mounted device (SMD). Many chip solutions are provided with installation guidelines, but the physical insight into the performance of these antennas has still not been deeply studied.

- Multiple configurations of a chip antenna, including a terminal line, have been analyzed in terms of efficiency, and the best solutions depending on the scenario where the antenna is allocated have been presented.

Lastly, **Chapter 7** addresses the design and study of three LTCC on-ground chip antennas and a novel methodology for their allocation on a device. The following conclusions have been obtained:

- Three low profile on-ground (no clearance needed) chip antennas have been designed and fabricated with LTCC technology. With a 2.4 mm height and a limited size, they are designed for the 868 MHz, 2.4 GHz, and 3.6 GHz bands for IoT applications.

- A novel methodology based on CMA is presented using the correlation between the total radiated fields (antenna+ground plane) and modal radiated fields (ground plane), justifying the best position in terms of efficiency. The study shows stable antennas for detuning when displaced and a considerable drop in efficiency of up to 10 dB if the antennas are not installed in the optimum location.

Appendix A

Technical Results

A.1   JCR Indexed journals

- **J.Molins-Benlliure**, E.Antonino-Daviu, M.Cabedo-Fabrés, and M.Ferrando-Bataller. "On-ground Small LTCC Chip Antenna and its Placement on IoT Devices." *IEEE Antennas and Wireless Propagation Letters*, 22(9), 2065-2069, 2023.

- **J.Molins-Benlliure**, M.Cabedo-Fabrés, E.Antonino-Daviu, and M.Ferrando-Bataller. "Miniaturized On-Ground 2.4 GHz IoT LTCC Chip Antenna and Its Positioning on a Ground Plane." *Sensors*, 23(6), 3007, 2023.

- **J.Molins-Benlliure**, M.Cabedo-Fabrés, E.Antonino-Daviu, and M.Ferrando-Bataller. "Sector unit-cell methodology for the design of Sub-6 GHz 5G MIMO antennas." *IEEE Access*, 10, 100824-100836, 2022.

- **J.Molins-Benlliure**, E.Antonino-Daviu, M.Cabedo-Fabrés, and M.Ferrando-Bataller. "Four-port wide-band cavity-backed antenna with isolating X-shaped block for sub-6 GHz 5G indoor base stations." *IEEE Access*, 9, 80535-80545, 2021.

A.2   International Conferences

- **J.Molins-Benlliure**, E.Antonino-Daviu, M.Cabedo-Fabrés, and M.Ferrando-Bataller, "Low-Profile Chip Antennas for IoT Sensors." *IEEE Conference on Antenna Measurements and Applications (CAMA) (pp. 717-718). Genoa, Italy, 15-17 November 2023.*

- M.Ferrando-Bataller, **J.Molins-Benlliure**, M.Cabedo-Fabrés, and C.Peñafiel-Ojeda, "Analysis of cavity back antennas with characteristic modes." *URSI GASS 2023, Sapporo, Japan, 19-26 August 2023.*

- **J.Molins-Benlliure**, E.Antonino-Daviu, M.Cabedo-Fabrés, and M.Ferrando-Bataller, "LTCC On-Ground Chip Antenna for 3.6 GHz IoT Applications." *IEEE International Symposium on Antennas and Propagation and USNC-URSI Radio Science Meeting (AP-S/URSI) (pp. 1187-1188). Portland, Oregon, USA, 23-28 July 2023.*

- **J.Molins-Benlliure**, E.Antonino-Daviu, M.Cabedo-Fabrés, and M.Ferrando-Bataller. "Design of a 10-Port MIMO Antenna for 5G/WiFi Indoor Base Station Applications." *IEEE International Symposium on Antennas and Propagation and USNC-URSI Radio Science Meeting (AP-S/URSI) (pp. 713-714). Denver, Colorado, USA, 10-15 July 2022.*

- **J.Molins-Benlliure**, E.Antonino-Daviu, M.Cabedo-Fabrés, and M.Ferrando-Bataller, "Design of a MIMO 5G indoor base station antenna using unit cells." *16th European Conference on Antennas and Propagation (EuCAP) (pp. 1-4). Madrid, Spain, 27 March- 1 April 2022.*

- **J.Molins-Benlliure**, E.Antonino-Daviu, M.Cabedo-Fabrés, and M.Ferrando-Bataller "Eight-Port Wideband MIMO Antenna for Sub-6 GHz 5G Base Stations." *IEEE International Symposium on Antennas and Propagation and USNC-URSI Radio Science Meeting (APS/URSI) (pp. 839-840). Singapore, 4-10 December 2021.*

- **J.Molins-Benlliure**, E.Antonino-Daviu, M.Cabedo-Fabrés, and M.Ferrando-Bataller, "Design procedure for 5g/iot multiple-port cavity-backed antennas." *15th European Conference on Antennas and Propagation (EuCAP) (pp. 1-5). Dusseldorf (Virtual), Germany, 22-26 March 2021.*

- **J.Molins-Benlliure**, M.Cabedo-Fabrés, E.Antonino-Daviu, and M.Ferrando-Bataller. "Effect of the ground plane in UHF Chip antenna efficiency." *14th European Conference on Antennas and Propagation (EuCAP) (pp. 1-5). Copenhagen (Virtual), Denmark, 15-20 March 2020.*

- **J.Molins-Benlliure**, M.Cabedo-Fabrés, E.Antonino-Daviu, and M.Ferrando-Bataller. "Effect of the size and shape of the ground plane in small antennas efficiency." *International Workshop on Antenna Technology (iWAT) (pp. 1-4). Bucarest, Romania, 25-28 February 2020.*

- **J.Molins-Benlliure**, A.Llanga-Vargas, D.K.Park, M.Ferrando-Bataller, and M.Cabedo-Fabrés, "MIMO antenna for indoor low-band 5G base stations." *IEEE International Symposium on Antennas and Propagation*

and USNC-URSI Radio Science Meeting (APS/URSI) (pp. 151-152). Atlanta, Georgia, USA, 7-12 July 2019.

A.3   National Conferences

- **J.Molins-Benlliure** and M.Ferrando Bataller. "Sector Unit-Cell Methodology for the Design of Sub-6 GHz 5G MIMO Base Station Antennas. (Sesión Premio Jóvenes Científicos URSI 2022)" *XXXVII Simposio Nacional URSI 2022. Libro de actas (pp. 1-4). Málaga, Spain, 5-7 September 2022.*

- **J.Molins-Benlliure**, E.Antonino Daviu, M.Cabedo Fabres, M.Ferrando Bataller, L.Jofre-Roca, and L.Juan-Llacer. "Antena de cuatro puertos de banda ancha con bloque aislante para estaciones base 5G Sub-6 GHz." *XXXVI Simposio Nacional URSI 2021. Libro de actas (pp. 1-4). Vigo (Virtual), Spain, 20-24 September 2021.*

- **J.Molins-Benlliure**, M.Cabedo-Fabrés, E.Antonino-Daviu, M.Ferrando-Bataller, J.Romeu, L.Jofre-Roca. "Eficiencia de Radiación en Antenas tipo Chip para aplicaciones IoT en 5G." *XXXV Simposium Nacional de la Unión Científica Internacional de Radio URSI 2020. Libro de actas, 1-4. Málaga (Virtual), Spain, 2-4 September 2020.*

- **J.Molins-Benlliure**, A.Llanga-Vargas, D.K.Park, M.Ferrando-Bataller, M.Cabedo-Fabrés. "Antena MIMO para estación base 5G interior." *XXXIV Simposium Nacional de la Unión Científica Internacional de Radio URSI 2019. Libro de actas, 1-4. Sevilla, Spain, 4-6 September 2019.*

A.4   Projects

- **Antenas X-Wave Multimodo y Multihaz Reconfigurables para Sistemas de Comunicaciones y Sensores.** (UPV, 2020-2022)
  Proyecto de la Agencia Estatal de investigación. Ministerio de Ciencia, Innovación y Universidades.

- **Design and Fabrication of a LTE Antenna for its Integration in an Interphone Device.** (UPV, 2019-2020)
  Financed by Fermax.

- **Diseño de Antenas Multihaz de Alta Ganancia para los Sistemas de Comunicaciones de Nueva Generacion** (UPV, 2018-2019)
  Ministerio de Asuntos Economicos y Transformacion Digital.

- **Design and Fabrication of an ISM 868MHz/915 MHz Antenna for its Integration in an IoT Device.** (UPV, 2019-2020)
  Financed by Celestica.

- **Design of Antennas for 5G MIMO communication systems and their integration in a Huawei handset.** (UPV, 2018-2019)
  Financed by Huawei Technologies OY(Finland).

A.5 Fellowships

- **Ayuda para Contratos predoctorales para la Formación de Doctores 2017.** (UPV, 2018-2023)
  Project: Antenas X-Wave Multimodo y Multihaz Reconfigurables para Sistemas de Comunicaciones y Sensores.
  Proyecto de la Agencia Estatal de Investigación. Ministerio de Ciencia, Innovación y Universidades.

A.6 Awards

- Accésit (Second Prize): Premio Jóvenes Científicos
  XXXVII Simposio Nacional URSI Málaga 2022
  Contribution: "Sector Unit-Cell Methodology for the Design of Sub-6 GHz 5G MIMO Base Station Antennas."

References

[1] M. Agiwal, A. Roy, and N. Saxena, "Next generation 5G wireless networks: A comprehensive survey," *IEEE Communications Surveys & Tutorials*, vol. 18, no. 3, pp. 1617–1655, 2016.

[2] N. Al-Falahy and O. Y. Alani, "Technologies for 5g networks: Challenges and opportunities," *It Professional*, vol. 19, no. 1, pp. 12–20, 2017.

[3] G. Naik, J.-M. Park, J. Ashdown, and W. Lehr, "Next generation wi-fi and 5g nr-u in the 6 ghz bands: Opportunities and challenges," *IEEE Access*, vol. 8, pp. 153 027–153 056, 2020.

[4] J. Lee, E. Tejedor, K. Ranta-aho, H. Wang, K.-T. Lee, E. Semaan, E. Mohyeldin, J. Song, C. Bergljung, and S. Jung, "Spectrum for 5g: Global status, challenges, and enabling technologies," *IEEE Communications Magazine*, vol. 56, no. 3, pp. 12–18, 2018.

[5] N. Zhang, P. Yang, J. Ren, D. Chen, L. Yu, and X. Shen, "Synergy of big data and 5g wireless networks: Opportunities, approaches, and challenges," *IEEE Wireless Communications*, vol. 25, no. 1, pp. 12–18, 2018.

[6] M. Agiwal, A. Roy, and N. Saxena, "Next generation 5G wireless networks: A comprehensive survey," *IEEE Communications Surveys Tutorials*, vol. 18, no. 3, pp. 1617–1655, thirdquarter 2016.

[7] M. Shafi, A. F. Molisch, P. J. Smith, T. Haustein, P. Zhu, P. De Silva, F. Tufvesson, A. Benjebbour, and G. Wunder, "5g: A tutorial overview of standards, trials, challenges, deployment, and practice," *IEEE journal on selected areas in communications*, vol. 35, no. 6, pp. 1201–1221, 2017.

[8] R. Vannithamby and S. Talwar, *Towards 5G: Applications, requirements and candidate technologies.* John Wiley & Sons, 2017.

REFERENCES

[9] I. B. F. De Almeida, L. L. Mendes, J. J. Rodrigues, and M. A. Da Cruz, "5g waveforms for iot applications," *IEEE Communications Surveys & Tutorials*, vol. 21, no. 3, pp. 2554–2567, 2019.

[10] B. P. Kumar and U. K. Kommuri, "Review on 5g small cell base station antennas: Design challenges and technologies," *IEEE Access*, 2024.

[11] D. Muirhead, M. A. Imran, and K. Arshad, "A survey of the challenges, opportunities and use of multiple antennas in current and future 5g small cell base stations," *IEEE access*, vol. 4, pp. 2952–2964, 2016.

[12] U. Siddique, H. Tabassum, E. Hossain, and D. I. Kim, "Wireless backhauling of 5g small cells: Challenges and solution approaches," *IEEE Wireless Communications*, vol. 22, no. 5, pp. 22–31, 2015.

[13] S. Wu and F. Shang, "Broadband dual-polarized magnetoelectric dipole antenna with compact structure for 5g base station," *IEEE Access*, vol. 11, pp. 20 806–20 813, 2023.

[14] B. Feng, H. Li, K. L. Chung, L. Deng *et al.*, "A dual-polarized wideband ceiling-mount antenna with low gain variations and high isolation for 5g sub-6 ghz applications," *IEEE Transactions on Antennas and Propagation*, vol. 70, no. 9, pp. 8572–8577, 2022.

[15] D. Yang, H. Zhai, C. Guo, and C. Ma, "A novel differentially fed dual-polarized filtering magneto-electric dipole antenna for 5g base station applications," *IEEE Transactions on Antennas and Propagation*, vol. 70, no. 7, pp. 5373–5382, 2022.

[16] Y.-Y. Zhu, J. Wang, J.-X. Chen, and W. Wu, "A compact wideband dual-polarized antenna using monolithic dielectric for 5g base station application," *IEEE Antennas and Wireless Propagation Letters*, vol. 21, no. 9, pp. 1717–1721, 2022.

[17] N. Sghaier, L. Latrach, and A. Gharsallah, "Design of a dual-polarized uwb 5g nr antenna," *Wireless Personal Communications*, vol. 123, no. 2, pp. 1293–1310, 2022.

[18] W. An, X. Tian, J. Wang, and S. Wang, "Low-profile dual-polarized double-layer microstrip antenna for 5g and 5g wi-fi," *Micromachines*, vol. 14, no. 5, p. 942, 2023.

[19] F. T. Çelik, S. Joof, and K. Karaçuha, "A dual-polarized bandwidth enhanced filtering dipole antenna design for 5g," *IEEE Access*, 2023.

[20] M. Li, D. Li, C. Xu, H. Li, and F. Xu, "Band-notched dual-polarized antennas for 2g/3g/4g/5g base station using the gcpw dgs-dms hybrid filter," *IEEE Access*, 2024.

[21] R. Chelghoum, Z. Messai, A. Brahimi, N. Bourouba, J. M. Jiménez, and F. Bouttout, "Dielectric behavior characterization of re/batio3 using time domain spectroscopy: Application on high-performance dielectric resonator antennas," *ECS Journal of Solid State Science and Technology*, vol. 13, no. 4, p. 043018, 2024.

[22] Q. Liu, H. Liu, W. He, and S. He, "A low-profile dual-band dual-polarized antenna with an amc reflector for 5G communications," *IEEE Access*, vol. 8, pp. 24 072–24 080, 2020.

[23] S. X. Ta, D. M. Nguyen, K. K. Nguyen, C. Dao-Ngoc, and N. Nguyen-Trong, "A tripolarized antenna with ultra-wide operational bandwidth," *IEEE Transactions on Antennas and Propagation*, 2020.

[24] K.-L. Wong and G.-L. Yan, "Wideband three-port equilateral triangular patch antenna generating three uncorrelated waves for 5g mimo access points," *IEEE Access*, vol. 10, pp. 893–899, 2021.

[25] K.-L. Wong, X.-Q. Ye, and W.-Y. Li, "Wideband four-port single-patch antenna based on the quasi-tm 1/2, 1/2 mode for 5g mimo access-point application," *IEEE Access*, vol. 10, pp. 9232–9240, 2022.

[26] K.-L. Wong, J.-Z. Chen, and W.-Y. Li, "Four-port wideband annular-ring patch antenna generating four decoupled waves for 5G multi-input-multi-output access points," *IEEE Transactions on Antennas and Propagation*, 2020.

[27] K.-L. Wong, Z.-W. Tso, and W.-Y. Li, "Very-wide-band six-port single-patch antenna with six uncorrelated waves for mimo access points," *IEEE Access*, vol. 10, pp. 69 555–69 567, 2022.

[28] I. S. Udoh and G. Kotonya, "Developing iot applications: challenges and frameworks," *IET Cyber-Physical Systems: Theory & Applications*, vol. 3, no. 2, pp. 65–72, 2018.

[29] H.-D. Chen, J.-S. Chen, and Y.-T. Cheng, "Modified inverted-l monopole antenna for 2.4/5 ghz dual-band operations," *Electronics letters*, vol. 39, no. 22, pp. 1567–1568, 2003.

[30] J.-Y. Jan and L.-C. Tseng, "Small planar monopole antenna with a shorted parasitic inverted-l wire for wireless communications in the 2.4-, 5.2-, and 5.8-ghz bands," *IEEE Transactions on Antennas and Propagation*, vol. 52, no. 7, pp. 1903–1905, 2004.

REFERENCES

[31] Z. D. Liu, P. S. Hall, and D. Wake, "Dual-frequency planar inverted-f antenna," *IEEE Transactions on antennas and propagation*, vol. 45, no. 10, pp. 1451–1458, 1997.

[32] K.-L. Wong and K.-P. Yang, "Modified planar inverted f antenna," *Electronics letters*, vol. 34, no. 1, pp. 7–8, 1998.

[33] M. Fallahpour and R. Zoughi, "Antenna miniaturization techniques: A review of topology-and material-based methods," *IEEE Antennas and Propagation Magazine*, vol. 60, no. 1, pp. 38–50, 2017.

[34] H. A. Wheeler, "Fundamental limitations of small antennas," *Proceedings of the IRE*, vol. 35, no. 12, pp. 1479–1484, 1947.

[35] R. C. Hansen, "Fundamental limitations in antennas," *Proceedings of the IEEE*, vol. 69, no. 2, pp. 170–182, 1981.

[36] S. Noghanian and L. Shafai, "Control of microstrip antenna radiation characteristics by ground plane size and shape," *IEE Proceedings-Microwaves, Antennas and Propagation*, vol. 145, no. 3, pp. 207–212, 1998.

[37] R. Garbacz and R. Turpin, "A generalized expansion for radiated and scattered fields," *IEEE transactions on Antennas and Propagation*, vol. 19, no. 3, pp. 348–358, 1971.

[38] R. Harrington and J. Mautz, "Theory of characteristic modes for conducting bodies," *IEEE transactions on antennas and propagation*, vol. 19, no. 5, pp. 622–628, 1971.

[39] ——, "Computation of characteristic modes for conducting bodies," *IEEE Transactions on Antennas and Propagation*, vol. 19, no. 5, pp. 629–639, 1971.

[40] M. Cabedo-Fabres, E. Antonino-Daviu, A. Valero-Nogueira, and M. F. Bataller, "The theory of characteristic modes revisited: A contribution to the design of antennas for modern applications," *IEEE Antennas and Propagation Magazine*, vol. 49, no. 5, pp. 52–68, 2007.

[41] M. Cabedo-Fabrés, "Systematic design of antennas using the theory of characteristic modes," Ph.D. dissertation, 2008.

[42] R. F. Harrington and J. L. Harrington, *Field computation by moment methods*. Oxford University Press, Inc., 1996.

[43] F. A. Dicandia, S. Genovesi, and A. Monorchio, "Null-steering antenna design using phase-shifted characteristic modes," *IEEE Transactions on Antennas and Propagation*, vol. 64, no. 7, pp. 2698–2706, 2016.

[44] ——, "Advantageous exploitation of characteristic modes analysis for the design of 3-d null-scanning antennas," *IEEE Transactions on Antennas and Propagation*, vol. 65, no. 8, pp. 3924–3934, 2017.

[45] ——, "Efficient excitation of characteristic modes for radiation pattern control by using a novel balanced inductive coupling element," *IEEE Transactions on Antennas and Propagation*, vol. 66, no. 3, pp. 1102–1113, 2018.

[46] D. Wen, Y. Hao, H. Wang, and H. Zhou, "Design of a wideband antenna with stable omnidirectional radiation pattern using the theory of characteristic modes," *IEEE Transactions on antennas and propagation*, vol. 65, no. 5, pp. 2671–2676, 2017.

[47] H. Sheng and Z. N. Chen, "Improving radiation pattern roundness of a monopole antenna placed off-center above a circular ground plane using characteristic mode analysis," *IEEE Transactions on Antennas and Propagation*, vol. 69, no. 2, pp. 1135–1139, 2020.

[48] C. Zhao and C.-F. Wang, "Characteristic mode design of wide band circularly polarized patch antenna consisting of h-shaped unit cells," *IEEE access*, vol. 6, pp. 25 292–25 299, 2018.

[49] F. A. Dicandia and S. Genovesi, "Design of a transmission-type polarization-insensitive and angularly stable polarization rotator by using characteristic modes theory," *IEEE Transactions on Antennas and Propagation*, vol. 71, no. 2, pp. 1602–1612, 2022.

[50] Y. Luo, Z. N. Chen, and K. Ma, "Enhanced bandwidth and directivity of a dual-mode compressed high-order mode stub-loaded dipole using characteristic mode analysis," *IEEE Transactions on Antennas and Propagation*, vol. 67, no. 3, pp. 1922–1925, 2018.

[51] E. Safin and D. Manteuffel, "Manipulation of characteristic wave modes by impedance loading," *IEEE Transactions on Antennas and Propagation*, vol. 63, no. 4, pp. 1756–1764, 2015.

[52] T.-Y. Shih and N. Behdad, "Bandwidth enhancement of platform-mounted hf antennas using the characteristic mode theory," *IEEE transactions on antennas and propagation*, vol. 64, no. 7, pp. 2648–2659, 2016.

REFERENCES

[53] Z. Miers, H. Li, and B. K. Lau, "Design of bandwidth-enhanced and multiband mimo antennas using characteristic modes," *IEEE Antennas and Wireless Propagation Letters*, vol. 12, pp. 1696–1699, 2013.

[54] C. Wang, Y. Chen, and S. Yang, "Bandwidth enhancement of a dual-polarized slot antenna using characteristic modes," *IEEE Antennas and Wireless Propagation Letters*, vol. 17, no. 6, pp. 988–992, 2018.

[55] C. Deng, Z. Feng, and S. V. Hum, "Mimo mobile handset antenna merging characteristic modes for increased bandwidth," *IEEE Transactions on Antennas and Propagation*, vol. 64, no. 7, pp. 2660–2667, 2016.

[56] X. Zhao, S. P. Yeo, and L. C. Ong, "Planar uwb mimo antenna with pattern diversity and isolation improvement for mobile platform based on the theory of characteristic modes," *IEEE Transactions on Antennas and Propagation*, vol. 66, no. 1, pp. 420–425, 2017.

[57] M.-Y. Li, Y.-L. Ban, Z.-Q. Xu, J. Guo, and Z.-F. Yu, "Tri-polarized 12-antenna mimo array for future 5g smartphone applications," *IEEE Access*, vol. 6, pp. 6160–6170, 2017.

[58] D. Wen, Y. Hao, H. Wang, and H. Zhou, "Design of a mimo antenna with high isolation for smartwatch applications using the theory of characteristic modes," *IEEE Transactions on Antennas and Propagation*, vol. 67, no. 3, pp. 1437–1447, 2018.

[59] N. Peitzmeier, T. Hahn, and D. Manteuffel, "Systematic design of multimode antennas for mimo applications by leveraging symmetry," *IEEE Transactions on Antennas and Propagation*, vol. 70, no. 1, pp. 145–155, 2021.

[60] B. Yang and J. J. Adams, "Systematic shape optimization of symmetric mimo antennas using characteristic modes," *IEEE Transactions on Antennas and Propagation*, vol. 64, no. 7, pp. 2668–2678, 2015.

[61] D.-W. Kim and S. Nam, "Systematic design of a multiport mimo antenna with bilateral symmetry based on characteristic mode analysis," *IEEE Transactions on Antennas and Propagation*, vol. 66, no. 3, pp. 1076–1085, 2017.

[62] K. Li and Y. Shi, "A pattern reconfigurable mimo antenna design using characteristic modes," *IEEE Access*, vol. 6, pp. 43 526–43 534, 2018.

[63] Y. Liu, A. Ren, H. Liu, H. Wang *et al.*, "Eight-port mimo array using characteristic mode theory for 5g smartphone applications," *IEEE Access*, vol. 7, pp. 45 679–45 692, 2019.

[64] I. Szini, A. Tatomirescu, and G. F. Pedersen, "On small terminal mimo antennas, harmonizing characteristic modes with ground plane geometry," *IEEE Transactions on Antennas and Propagation*, vol. 63, no. 4, pp. 1487–1497, 2015.

[65] J. Dong, S. Wang, and J. Mo, "Design of a twelve-port mimo antenna system for multi-mode 4g/5g smartphone applications based on characteristic mode analysis," *IEEE Access*, vol. 8, pp. 90 751–90 759, 2020.

[66] F. H. Lin and Z. N. Chen, "Low-profile wideband metasurface antennas using characteristic mode analysis," *IEEE Transactions on Antennas and Propagation*, vol. 65, no. 4, pp. 1706–1713, 2017.

[67] X. Yang, Y. Liu, and S.-X. Gong, "Design of a wideband omnidirectional antenna with characteristic mode analysis," *IEEE Antennas and Wireless Propagation Letters*, vol. 17, no. 6, pp. 993–997, 2018.

[68] G. Gao, R.-F. Zhang, W.-F. Geng, H.-J. Meng, and B. Hu, "Characteristic mode analysis of a nonuniform metasurface antenna for wearable applications," *IEEE Antennas and Wireless Propagation Letters*, vol. 19, no. 8, pp. 1355–1359, 2020.

[69] T. Li and Z. N. Chen, "Metasurface-based shared-aperture 5g s-/k-band antenna using characteristic mode analysis," *IEEE Transactions on Antennas and Propagation*, vol. 66, no. 12, pp. 6742–6750, 2018.

[70] ——, "A dual-band metasurface antenna using characteristic mode analysis," *IEEE Transactions on Antennas and Propagation*, vol. 66, no. 10, pp. 5620–5624, 2018.

[71] F. H. Lin and Z. N. Chen, "A method of suppressing higher order modes for improving radiation performance of metasurface multiport antennas using characteristic mode analysis," *IEEE Transactions on Antennas and Propagation*, vol. 66, no. 4, pp. 1894–1902, 2018.

[72] K. Li, Y. Shi, H. Shen, and L. Li, "A characteristic-mode-based polarization-reconfigurable antenna and its array," *IEEE Access*, vol. 6, pp. 64 587–64 595, 2018.

[73] L. Zhang, Y. Sun, Y. He, S.-W. Wong, C. Mao, L. Ge, and S. Gao, "A quad-polarization reconfigurable antenna with suppressed cross polarization based on characteristic mode theory," *IEEE transactions on antennas and propagation*, vol. 69, no. 2, pp. 636–647, 2020.

REFERENCES

[74] W. Li, Y. Zhao, X. Ding, L. Wu, and Z. Nie, "A wideband pattern-reconfigurable loop antenna designed by using characteristic mode analysis," *IEEE Antennas and Wireless Propagation Letters*, vol. 21, no. 2, pp. 396–400, 2021.

[75] Z. Chen, W. Hu, K. Wei, L. Wen, Z. Hu, and S. Gao, "A wideband polarization-reconfigurable antenna using the combined characteristic modes and common/differential modes," *IEEE Antennas and Wireless Propagation Letters*, 2023.

[76] F. A. Dicandia and S. Genovesi, "A compact cubesat antenna with beam-steering capability and polarization agility: Characteristic modes theory for breakthrough antenna design," *IEEE Antennas and Propagation Magazine*, vol. 62, no. 4, pp. 82–93, 2020.

[77] ——, "Characteristic modes analysis of non-uniform metasurface superstrate for nanosatellite antenna design," *IEEE Access*, vol. 8, pp. 176 050–176 061, 2020.

[78] E. Safin and D. Manteuffel, "Advanced eigenvalue tracking of characteristic modes," *IEEE Transactions on Antennas and Propagation*, vol. 64, no. 7, pp. 2628–2636, 2016.

[79] Z. Miers and B. K. Lau, "Wideband characteristic mode tracking utilizing far-field patterns," *IEEE Antennas and Wireless Propagation Letters*, vol. 14, pp. 1658–1661, 2015.

[80] M. Capek, V. Losenicky, L. Jelinek, and M. Gustafsson, "Validating the characteristic modes solvers," *IEEE Transactions on Antennas and Propagation*, vol. 65, no. 8, pp. 4134–4145, 2017.

[81] L. Akrou and H. J. da Silva, "Enhanced modal tracking for characteristic modes," *IEEE Transactions on Antennas and Propagation*, vol. 67, no. 1, pp. 356–360, 2018.

[82] M. Masek, M. Capek, L. Jelinek, and K. Schab, "Modal tracking based on group theory," *IEEE Transactions on Antennas and Propagation*, vol. 68, no. 2, pp. 927–937, 2019.

[83] X. J. Chen, Y. M. Pan, and G. D. Su, "An advanced eigenvector-correlation-based tracking method for characteristic modes," *IEEE Transactions on Antennas and Propagation*, vol. 69, no. 5, pp. 2751–2758, 2020.

[84] Y. Kuang, Q. S. Cheng, and Z. N. Chen, "Characteristic mode-guided trust-region-based optimization for mode manipulation in dual-band

metantenna design," *IEEE Transactions on Antennas and Propagation*, 2023.

[85] Q. Wu, "Computation of characteristic modes for dielectric bodies using volume integral equation and interpolation," *IEEE Antennas and Wireless Propagation Letters*, vol. 16, pp. 2963–2966, 2017.

[86] D. Tayli, M. Capek, L. Akrou, V. Losenicky, L. Jelinek, and M. Gustafsson, "Accurate and efficient evaluation of characteristic modes," *IEEE Transactions on Antennas and Propagation*, vol. 66, no. 12, pp. 7066–7075, 2018.

[87] M. Gustafsson, L. Jelinek, K. Schab, and M. Capek, "Unified theory of characteristic modes—part ii: Tracking, losses, and fem evaluation," *IEEE Transactions on Antennas and Propagation*, vol. 70, no. 12, pp. 11 814–11 824, 2022.

[88] J. Lundgren, K. Schab, M. Capek, M. Gustafsson, and L. Jelinek, "Iterative calculation of characteristic modes using arbitrary full-wave solvers," *IEEE Antennas and Wireless Propagation Letters*, vol. 22, no. 4, pp. 799–803, 2022.

[89] M. Capek, J. Lundgren, M. Gustafsson, K. Schab, and L. Jelinek, "Characteristic mode decomposition using the scattering dyadic in arbitrary full-wave solvers," *IEEE Transactions on Antennas and Propagation*, vol. 71, no. 1, pp. 830–839, 2022.

[90] N. P. Agrawall, G. Kumar, and K. Ray, "New wideband monopole antennas," in *IEEE Antennas and Propagation Society International Symposium 1997. Digest*, vol. 1.   IEEE, 1997, pp. 248–251.

[91] ——, "Wide-band planar monopole antennas," *IEEE transactions on antennas and propagation*, vol. 46, no. 2, pp. 294–295, 1998.

[92] C. R. Rowell and R. D. Murch, "A capacitively loaded pifa for compact mobile telephone handsets," *IEEE Transactions on antennas and Propagation*, vol. 45, no. 5, pp. 837–842, 1997.

[93] S.-S. Zhong, X.-L. Liang, and W. Wang, "Compact elliptical monopole antenna with impedance bandwidth in excess of 21: 1," *IEEE Transactions on Antennas and Propagation*, vol. 55, no. 11, pp. 3082–3085, 2007.

[94] K. Ray and Y. Ranga, "Ultrawideband printed elliptical monopole antennas," *IEEE transactions on antennas and propagation*, vol. 55, no. 4, pp. 1189–1192, 2007.

REFERENCES

[95] A. M. Abbosh and M. E. Bialkowski, "Design of ultrawideband planar monopole antennas of circular and elliptical shape," *IEEE transactions on antennas and propagation*, vol. 56, no. 1, pp. 17–23, 2008.

[96] M. N. Srifi, O. El Mrabet, F. Falcone, M. S. Ayza, and M. Essaaidi, "A novel compact printed circular antenna for very ultrawideband applications," *Microwave and Optical Technology Letters*, vol. 51, no. 4, pp. 1130–1133, 2009.

[97] M. Hammoud, P. Poey, and F. Colombel, "Matching the input impedance of a broadband disc monopole," *Electronics letters*, vol. 29, no. 4, pp. 406–407, 1993.

[98] Z. Chen, M. Ammann, M. Chia, and T. See, "Annular planar monopole antennas," *IEE PROCEEDINGS MICROWAVES ANTENNAS AND PROPAGATION*, vol. 149, no. 4, pp. 200–203, 2002.

[99] X. Liang, S. Zhong, W. Wang, and F. Yao, "Printed annular monopole antenna for ultra-wideband applications," *Electronics Letters*, vol. 42, no. 2, p. 1, 2006.

[100] M. Ammann, "Square planar monopole antenna," 1999.

[101] ——, "Control of the impedance bandwidth of wideband planar monopole antennas using a beveling technique," *Microwave and Optical Technology Letters*, vol. 30, no. 4, pp. 229–232, 2001.

[102] M. Ammann and Z. N. Chen, "A wide-band shorted planar monopole with bevel," *IEEE transactions on antennas and propagation*, vol. 51, no. 4, pp. 901–903, 2003.

[103] ——, "Wideband monopole antennas for multi-band wireless systems," *IEEE antennas and Propagation Magazine*, vol. 45, no. 2, pp. 146–150, 2003.

[104] M. John and M. Ammann, "Optimization of impedance bandwidth for the printed rectangular monopole antenna," *microwave and optical technology letters*, vol. 47, no. 2, pp. 153–154, 2005.

[105] K. P. Ray and Y. Ranga, "Printed rectangular monopole antennas," in *2006 IEEE Antennas and Propagation Society International Symposium.* IEEE, 2006, pp. 1693–1696.

[106] J. Jung, W. Choi, and J. Choi, "A small wideband microstrip-fed monopole antenna," *IEEE microwave and wireless components letters*, vol. 15, no. 10, pp. 703–705, 2005.

[107] J. Jung, K. Seol, W. Choi, and J. Choi, "Wideband monopole antenna for various mobile communication applications," *Electronics Letters*, vol. 41, no. 24, p. 1, 2005.

[108] K.-R. Chen, J.-S. Row *et al.*, "A compact monopole antenna for super wideband applications," *IEEE Antennas and Wireless Propagation Letters*, vol. 10, pp. 488–491, 2011.

[109] Z. Cui, Y.-C. Jiao, L. Zhang, and F.-S. Zhang, "The band-notch function for a printed ultra-wideband monopole antenna with e-shaped slot," *Microwave and Optical Technology Letters*, vol. 50, no. 8, pp. 2048–2052, 2008.

[110] Z. N. Chen and M. Chia, "Impedance characteristics of emc triangular planar monopoles," *Electronics Letters*, vol. 37, no. 21, p. 1, 2001.

[111] C.-C. Lin, Y.-C. Kan, L.-C. Kuo, and H.-R. Chuang, "A planar triangular monopole antenna for uwb communication," *IEEE Microwave and wireless components letters*, vol. 15, no. 10, pp. 624–626, 2005.

[112] Q.-X. Chu and L.-H. Ye, "Design of compact dual-wideband antenna with assembled monopoles," *IEEE Transactions on Antennas and Propagation*, vol. 58, no. 12, pp. 4063–4066, 2010.

[113] Z. N. Chen, "Impedance characteristics of planar bow-tie-like monopole antennas," *Electronics Letters*, vol. 36, no. 13, p. 1, 2000.

[114] J.-P. Lee, S.-O. Park, and S.-K. Lee, "Bow-tie wide-band monopole antenna with the novel impedance-matching technique," *Microwave and Optical Technology Letters*, vol. 33, no. 6, pp. 448–452, 2002.

[115] J. Evans and M. Amunann, "Planar trapezoidal and pentagonal monopoles with impedance bandwidths in excess of 10: 1," in *IEEE Antennas and Propagation Society International Symposium. 1999 Digest. Held in conjunction with: USNC/URSI National Radio Science Meeting (Cat. No. 99CH37010)*, vol. 3. IEEE, 1999, pp. 1558–1561.

[116] M. Ammanna, "The pentagonal planar monopole for digital mobile terminals; bandwidth considerations and modelling," 2001.

[117] K. Ray and S. Tiwari, "Ultra wideband printed hexagonal monopole antennas," *IET microwaves, antennas & propagation*, vol. 4, no. 4, pp. 437–445, 2010.

[118] A. A. Shaalan and M. Ramadan, "Design of a compact hexagonal monopole antenna for ultra—wideband applications," *Journal of Infrared, Millimeter, and Terahertz Waves*, vol. 31, pp. 958–968, 2010.

REFERENCES

[119] K. Chung, J. Kim, and J. Choi, "Wideband microstrip-fed monopole antenna having frequency band-notch function," *IEEE Microwave and Wireless Components Letters*, vol. 15, no. 11, pp. 766–768, 2005.

[120] W.-S. Lee, D.-Z. Kim, K.-J. Kim, and J.-W. Yu, "Wideband planar monopole antennas with dual band-notched characteristics," *IEEE Transactions on Microwave Theory and Techniques*, vol. 54, no. 6, pp. 2800–2806, 2006.

[121] J. Liu, S. Gong, Y. Xu, X. Zhang, C. Feng, and N. Qi, "Compact printed ultra-wideband monopole antenna with dual band-notched characteristics," *Electronics letters*, vol. 44, no. 12, pp. 710–711, 2008.

[122] S. Barbarino and F. Consoli, "Study on super-wideband planar asymmetrical dipole antennas of circular shape," *IEEE Transactions on Antennas and propagation*, vol. 58, no. 12, pp. 4074–4078, 2010.

[123] J.-N. Hwang and S.-J. Chung, "Isolation enhancement between two packed antennas with coupling element," *IEEE Antennas and wireless propagation letters*, vol. 10, pp. 1263–1266, 2011.

[124] M. Singh and M. S. Parihar, "A compact 4×4 MIMO antenna with high isolation for 5G application," in *2019 IEEE Asia-Pacific Microwave Conference (APMC)*.   IEEE, 2019, pp. 688–690.

[125] Z. Tang, J. Liu, R. Lian, Y. Li, and Y. Yin, "Wideband differentially fed dual-polarized planar antenna and its array with high common-mode suppression," *IEEE Transactions on Antennas and Propagation*, vol. 67, no. 1, pp. 131–139, 2018.

[126] M.-Y. Li, Y.-L. Ban, Z.-Q. Xu, G. Wu, K. Kang, Z.-F. Yu *et al.*, "Eight-port orthogonally dual-polarized antenna array for 5G smartphone applications," *IEEE Transactions on Antennas and Propagation*, vol. 64, no. 9, pp. 3820–3830, 2016.

[127] H. Jin, L. Zhu, H. Zou, Y. Luo, S. Xu, and G. Yang, "A wideband dual-polarized antenna and its array with electrically downtilt function for 5G sub-6 GHz communication applications," *IEEE Access*, vol. 8, pp. 7672–7681, 2019.

[128] H. Huang, Y. Liu, and S. Gong, "A broadband dual-polarized base station antenna with sturdy construction," *IEEE Antennas and Wireless Propagation Letters*, vol. 16, pp. 665–668, 2016.

[129] S. Fu, Z. Cao, X. Quan, and C. Xu, "A broadband dual-polarized notched-band antenna for 2/3/4/5G base station," *IEEE Antennas and Wireless Propagation Letters*, vol. 19, no. 1, pp. 69–73, 2019.

[130] L. Zhao, L. K. Yeung, and K.-L. Wu, "A coupled resonator decoupling network for two-element compact antenna arrays in mobile terminals," *IEEE Transactions on Antennas and Propagation*, vol. 62, no. 5, pp. 2767–2776, 2014.

[131] H. Piao, Y. Jin, and L. Qu, "A compact and straightforward self-decoupled MIMO antenna system for 5G applications," *IEEE Access*, vol. 8, pp. 129 236–129 245, 2020.

[132] Z. Ren, A. Zhao, and S. Wu, "MIMO antenna with compact decoupled antenna pairs for 5G mobile terminals," *IEEE Antennas and Wireless Propagation Letters*, vol. 18, no. 7, pp. 1367–1371, 2019.

[133] A. Zhao and Z. Ren, "Size reduction of self-isolated MIMO antenna system for 5G mobile phone applications," *IEEE Antennas and Wireless Propagation Letters*, vol. 18, no. 1, pp. 152–156, 2018.

[134] A. Alieldin, Y. Huang, S. J. Boyes, M. Stanley, S. D. Joseph, Q. Hua, and D. Lei, "A triple-band dual-polarized indoor base station antenna for 2G, 3G, 4G and sub-6 GHz 5G applications," *IEEE Access*, vol. 6, pp. 49 209–49 216, 2018.

[135] Y. Zhao, C. Rakluea, T. Hongnara, and S. Chaimool, "A compact dual-broadband multiple-input multiple-output (MIMO) indoor base station antenna for 2G/3G/LTE systems," *IEEE Access*, vol. 7, pp. 82 238–82 245, 2019.

[136] X. Chen, S. Zhang, and Q. Li, "A review of mutual coupling in MIMO systems," *IEEE Access*, vol. 6, pp. 24 706–24 719, 2018.

[137] B. T. Quist and M. A. Jensen, "Optimal antenna radiation characteristics for diversity and MIMO systems," *IEEE Transactions on Antennas and Propagation*, vol. 57, no. 11, pp. 3474–3481, 2009.

[138] S. Blanch, J. Romeu, and I. Corbella, "Exact representation of antenna system diversity performance from input parameter description," *Electronics letters*, vol. 39, no. 9, pp. 705–707, 2003.

[139] Y. Kim, H. Kim, I. Yoon, and J. Oh, "4 × 8 patch array-fed fr4-based transmit array antennas for affordable and reliable 5g beam steering," *IEEE Access*, vol. 7, pp. 88 881–88 893, 2019.

[140] M. E. Trampler, R. E. Lovato, and X. Gong, "Dual-resonance continuously beam-scanning x-band reflectarray antenna," *IEEE Transactions on Antennas and Propagation*, vol. 68, no. 8, pp. 6080–6087, 2020.

REFERENCES

[141] E. Ozturk and B. Saka, "Multilayer minkowski reflectarray antenna with improved phase performance," *arXiv preprint arXiv:2009.12343*, 2020.

[142] K. Singh, M. U. Afzal, M. Kovaleva, and K. P. Esselle, "Controlling the most significant grating lobes in two-dimensional beam-steering systems with phase-gradient metasurfaces," *IEEE Transactions on Antennas and Propagation*, vol. 68, no. 3, pp. 1389–1401, 2019.

[143] R. Harrington, "Time-harmonic electromagnetic fields/harrington rf–new-york, chichester," 2001.

[144] M. K. Joshi, S. K. Vyas, T. Tiwari, and R. Bhattacharjee, "Optimal design of a coaxial cavity based on quality-factor maximization for high-power coaxial magnetron in x-band," *IEEE Transactions on Plasma Science*, vol. 46, no. 3, pp. 503–510, 2018.

[145] Z. Li, J. Han, Y. Mu, X. Gao, and L. Li, "Dual-band dual-polarized base station antenna with a notch band for 2/3/4/5g communication systems," *IEEE Antennas and Wireless Propagation Letters*, vol. 19, no. 12, pp. 2462–2466, 2020.

[146] Y. Li, C. Wang, H. Yuan, N. Liu, H. Zhao, and X. Li, "A 5g mimo antenna manufactured by 3-d printing method," *IEEE Antennas and Wireless Propagation Letters*, vol. 16, pp. 657–660, 2016.

[147] L. J. Chu, "Physical limitations of omni-directional antennas," *Journal of applied physics*, vol. 19, no. 12, pp. 1163–1175, 1948.

[148] R. Collin and S. Rothschild, "Evaluation of antenna q," *IEEE Transactions on Antennas and Propagation*, vol. 12, no. 1, pp. 23–27, 1964.

[149] J. S. McLean, "A re-examination of the fundamental limits on the radiation q of electrically small antennas," *IEEE Transactions on antennas and propagation*, vol. 44, no. 5, p. 672, 1996.

[150] R. Fante, "Quality factor of general ideal antennas," *IEEE Transactions on Antennas and Propagation*, vol. 17, no. 2, pp. 151–155, 1969.

[151] R. Hansen and R. Collin, "A new chu formula for q," *IEEE Antennas and Propagation Magazine*, vol. 51, no. 5, pp. 38–41, 2009.

[152] D. M. Pozar, "New results for minimum q, maximum gain, and polarization properties of electrically small arbitrary antennas," in *2009 3rd European Conference on Antennas and Propagation*. IEEE, 2009, pp. 1993–1996.

[153] D. F. Sievenpiper, D. C. Dawson, M. M. Jacob, T. Kanar, S. Kim, J. Long, and R. G. Quarfoth, "Experimental validation of performance limits and design guidelines for small antennas," *IEEE Transactions on Antennas and Propagation*, vol. 60, no. 1, pp. 8–19, 2011.

[154] R. M. Fano, "Theoretical limitations on the broadband matching of arbitrary impedances," *Journal of the Franklin Institute*, vol. 249, no. 1, pp. 57–83, 1950.

[155] D. Rhodes, "On the stored energy of planar apertures," *IEEE Transactions on Antennas and Propagation*, vol. 14, no. 6, pp. 676–683, 1966.

[156] W. Geyi, P. Jarmuszewski, and Y. Qi, "The foster reactance theorem for antennas and radiation q," *IEEE Transactions on Antennas and Propagation*, vol. 48, no. 3, pp. 401–408, 2000.

[157] A. D. Yaghjian and S. R. Best, "Impedance, bandwidth, and q of antennas," *IEEE Transactions on Antennas and Propagation*, vol. 53, no. 4, pp. 1298–1324, 2005.

[158] H.-H. Kim, K.-Y. Kim, J.-H. Lee, and J.-M. Woo, "Surface-mounted chip dielectric ceramic antenna for pcs phone," in *2000 5th International Symposium on Antennas, Propagation, and EM Theory. ISAPE 2000 (IEEE Cat. No. 00EX417)*.   IEEE, 2000, pp. 582–585.

[159] W. Choi, S. Kwon, and B. Lee, "Ceramic chip antenna using meander conductor lines," *Electronics Letters*, vol. 37, no. 15, p. 1, 2001.

[160] K. Asakura, T. Oida, and H. Mandai, "Chip-antenna," Feb. 22 2000, uS Patent 6,028,568.

[161] K. Watanabe, T. Tsuru, S. Kanba, T. Suesada, and Y. Dakeya, "Chip antenna and radio equipment including the same," Aug. 7 2001, uS Patent 6,271,803.

[162] H. J. Kim, S. J. Yoon, J. W. Choi, C. Y. Kang, and S. H. Sim, "Ceramic chip antenna," Nov. 18 2003, uS Patent 6,650,303.

[163] L. P. de Rochemont, "Ceramic antenna module and methods of manufacture thereof," Jul. 29 2008, uS Patent 7,405,698.

[164] D. Yim and S. Park, "Small internal ceramic chip antenna for imt-2000 handsets," *Electronics Letters*, vol. 39, no. 19, p. 1, 2003.

[165] C.-C. Lin, Y.-J. Chang, H.-R. Chuang *et al.*, "Design of a 900/1800 mhz dual-band ltcc chip antenna for mobile communications applications," *Microwave journal*, vol. 47, no. 1, p. 78, 2004.

REFERENCES

[166] K.-L. Wong and C.-H. Chang, "Surface-mountable emc monopole chip antenna for wlan operation," *IEEE transactions on antennas and propagation*, vol. 54, no. 4, pp. 1100–1104, 2006.

[167] J.-I. Moon and S.-O. Park, "Small chip antenna for 2.4/5.8-ghz dual ism-band applications," *IEEE Antennas and Wireless Propagation Letters*, vol. 2, pp. 313–315, 2003.

[168] Y. Dakeya, T. Suesada, K. Asakura, N. Nakajima, and H. Mandai, "Chip multilayer antenna for 2.45 ghz-band application using ltcc technology," in *2000 IEEE MTT-S International Microwave Symposium Digest (Cat. No. 00CH37017)*, vol. 3.   IEEE, 2000, pp. 1693–1696.

[169] C.-L. Tang, "2.4/5.2 ghz dual-band chip antenna for wlan application," in *2005 IEEE Antennas and Propagation Society International Symposium*, vol. 1.   IEEE, 2005, pp. 454–457.

[170] K.-L. Wong and C.-H. Chang, "Wlan chip antenna mountable above the system ground plane of a mobile device," *IEEE Transactions on antennas and Propagation*, vol. 53, no. 11, pp. 3496–3499, 2005.

[171] J. Lee, C. Jeon, and B. Lee, "Design of ceramic chip antenna for bluetooth applications using meander lines," in *IEEE Antennas and Propagation Society International Symposium (IEEE Cat. No. 02CH37313)*, vol. 4. IEEE, 2002, pp. 68–71.

[172] J.-I. Moon and S.-O. Park, "The design of small size chip ceramic dielectric antenna for bluetooth application," in *IEEE Antennas and Propagation Society International Symposium. Digest. Held in conjunction with: USNC/CNC/URSI North American Radio Sci. Meeting (Cat. No. 03CH37450)*, vol. 2.   IEEE, 2003, pp. 954–957.

[173] P. Mendes, A. Bartek, J. Burghartz, and J. Correia, "Novel very small dual-band chip-size antenna for wireless sensor networks," in *Proceedings. 2004 IEEE Radio and Wireless Conference (IEEE Cat. No. 04TH8746)*. IEEE, 2004, pp. 419–422.

[174] S. Sim, C. Kang, S. Yoon, Y. Yoon, and H. Kim, "Broadband multilayer ceramic chip antenna for handsets," *Electronics Letters*, vol. 38, no. 5, p. 1, 2002.

[175] S. Mei and Z. Y. Ping, "A chip antenna in ltcc for uwb radios," *IEEE transactions on antennas and propagation*, vol. 56, no. 4, pp. 1177–1180, 2008.

[176] D.-H. Kwon, Y. Kim, M. Hasegawa, and T. Shimamori, "A small ceramic chip antenna for ultra-wideband systems," in *2004 International Workshop on Ultra Wideband Systems Joint with Conference on Ultra Wideband Systems and Technologies. Joint UWBST & IWUWBS 2004 (IEEE Cat. No. 04EX812)*. IEEE, 2004, pp. 307–311.

[177] K.-W. Khoo, Z. N. Chen, A. C. W. Lu, V. Sunappan, and L. L. Wai, "Miniaturized multilayer uwb antennas on ltcc," *IEEE transactions on antennas and propagation*, vol. 57, no. 12, pp. 3988–3992, 2009.

[178] J. Lee and J. K. Park, "Compact uwb chip antenna design using the coupling concept," *Progress In Electromagnetics Research*, vol. 90, pp. 341–351, 2009.

[179] D. Kearney, M. John, and M. J. Ammann, "Miniature ceramic pifa for uwb band groups 3 and 6," *IEEE Antennas and Wireless Propagation Letters*, vol. 9, pp. 28–31, 2010.

[180] ——, "Miniature ceramic dual-pifa antenna to support band group 1 uwb functionality in mobile handset," *IEEE transactions on antennas and propagation*, vol. 59, no. 1, pp. 336–339, 2010.

[181] Y.-Q. Zhang, Y.-X. Guo, and M. S. Leong, "A novel multilayer uwb antenna on ltcc," *IEEE transactions on antennas and propagation*, vol. 58, no. 9, pp. 3013–3019, 2010.

[182] M. Sun, Y. P. Zhang, and Y. Lu, "Miniaturization of planar monopole antenna for ultrawideband radios," *IEEE Transactions on Antennas and Propagation*, vol. 58, no. 7, pp. 2420–2425, 2010.

[183] Y.-J. Ren, "Ceramic based small lte mimo handset antenna," *IEEE Transactions on Antennas and Propagation*, vol. 61, no. 2, pp. 934–938, 2012.

[184] S.-C. Chen and K.-L. Wong, "Small-size wideband chip antenna for wwan/lte operation and close integration with nearby conducting elements in the mobile handset," *Microwave and Optical Technology Letters*, vol. 53, no. 9, pp. 1998–2004, 2011.

[185] C.-L. Hu, W.-F. Lee, Y.-E. Lee, C.-F. Yang, and S.-T. Lin, "A compact multiband inverted-f antenna for lte/wwan/gps/wimax/wlan operations in the laptop computer," *IEEE Antennas and Wireless Propagation Letters*, vol. 9, pp. 1169–1173, 2010.

[186] C.-L. Hu, D.-L. Huang, H.-L. Kuo, C.-F. Yang, C.-L. Liao, and S.-T. Lin, "Compact multibranch inverted-f antenna to be embedded in a laptop

computer for lte/wwan/imt-e applications," *IEEE Antennas and Wireless Propagation Letters*, vol. 9, pp. 838–841, 2010.

[187] K.-L. Wong and C.-T. Lee, "Wideband surface-mount chip antenna for eight-band lte/wwan slim mobile phone application," *Microwave and Optical Technology Letters*, vol. 52, no. 11, pp. 2554–2560, 2010.

[188] M. W. Lee, K. Leung, and Y. Chow, "Low cost meander line chip monopole antenna," *IEEE transactions on antennas and propagation*, vol. 62, no. 1, pp. 442–445, 2013.

[189] Taoglas "https://www.taoglas.com/".

[190] Würth Elektronik "https://www.we-online.com/en".

[191] Johanson Technology "https://www.johansontechnology.com".

[192] Yageo "https://www.yageo.com/en/Product/Index/wireless/antenna".

[193] Antenova "https://www.antenova.com/".

[194] Ignion "https://ignion.io/".

[195] P. Vainikainen, J. Ollikainen, O. Kivekas, and K. Kelander, "Resonator-based analysis of the combination of mobile handset antenna and chassis," *IEEE Transactions on Antennas and Propagation*, vol. 50, no. 10, pp. 1433–1444, 2002.

[196] P. Vainikainen, J. Ollikainen, O. Kivekäs, and I. Kelander, "Performance analysis of small antennas mounted on mobile handset," in *COST-259 Final Workshop-The Mobile Terminal and Human Interaction, Bergen, Norway, April 2000*, 2000, p. 8.

[197] O. Kivekas, J. Ollikainen, T. Lehtiniemi, and P. Vainikainen, "Bandwidth, sar, and efficiency of internal mobile phone antennas," *IEEE Transactions on Electromagnetic compatibility*, vol. 46, no. 1, pp. 71–86, 2004.

[198] J. Villanen, J. Ollikainen, O. Kivekas, and P. Vainikainen, "Coupling element based mobile terminal antenna structures," *IEEE Transactions on Antennas and Propagation*, vol. 54, no. 7, pp. 2142–2153, 2006.

[199] D. Manteuffel, A. Bahr, and I. Wolff, "Investigation on integrated antennas for gsm mobile phones," in *Millennium Conference on Antennas & Propagation, ESA, AP2000, Davos, Switzerland*, 2000.

[200] A. Cabedo, J. Anguera, C. Picher, M. Ribó, and C. Puente, "Multiband handset antenna combining a pifa, slots, and ground plane modes," *IEEE Transactions on Antennas and Propagation*, vol. 57, no. 9, pp. 2526–2533, 2009.

[201] A. Andújar, J. Anguera, and C. Puente, "Ground plane boosters as a compact antenna technology for wireless handheld devices," *IEEE Transactions on Antennas and Propagation*, vol. 59, no. 5, pp. 1668–1677, 2011.

[202] C. R. Rowell and R. D. Murch, "A compact pifa suitable for dual-frequency 900/1800-mhz operation," *IEEE Transactions on antennas and propagation*, vol. 46, no. 4, pp. 596–598, 1998.

[203] J. Anguera, C. Picher, A. Bujalance, and A. Andújar, "Ground plane booster antenna technology for smartphones and tablets," *Microwave and Optical Technology Letters*, vol. 58, no. 6, pp. 1289–1294, 2016.

[204] R. Hossa, A. Byndas, and M. Bialkowski, "Improvement of compact terminal antenna performance by incorporating open-end slots in ground plane," *IEEE Microwave and Wireless Components Letters*, vol. 14, no. 6, pp. 283–285, 2004.

[205] M. Abedin and M. Ali, "Modifying the ground plane and its effect on planar inverted-f antennas (pifas) for mobile phone handsets," *IEEE Antennas and Wireless Propagation Letters*, vol. 2, pp. 226–229, 2003.

[206] B. Sanz-Izquierdo, J. C. Batchelor, and R. J. Langley, "Multiband printed pifa antenna with ground plane capacitive resonator," *Electronics letters*, vol. 40, no. 22, pp. 1391–1392, 2004.

[207] E. Antonino-Daviu, M. Cabedo-Fabres, M. Ferrando-Bataller, and J. Herranz-Herruzo, "Analysis of the coupled chassis-antenna modes in mobile handsets," in *IEEE Antennas and Propagation Society Symposium, 2004.*, vol. 3. IEEE, 2004, pp. 2751–2754.

[208] E. Antonino-Daviu, C. Suarez-Fajardo, M. Cabedo-Fabrés, and M. Ferrando-Bataller, "Wideband antenna for mobile terminals based on the handset pcb resonance," *Microwave and optical technology letters*, vol. 48, no. 7, pp. 1408–1411, 2006.

[209] M. Cabedo-Fabres, A. Valero-Nogueira, E. Antonino-Daviu, and M. Ferrando-Bataller, "Modal analysis of a radiating slotted pcb for mobile handsets," in *2006 First European Conference on Antennas and Propagation*. IEEE, 2006, pp. 1–6.

REFERENCES

[210] J.-Q. Zhu, Y.-L. Ban, R.-M. Xu, J.-W. Lian, Y. Zhang, Z. Nie *et al.*, "A useful methodology to convert the smartphone metal cover into an antenna booster for nfc applications," *IEEE Transactions on Antennas and Propagation*, vol. 67, no. 7, pp. 4463–4473, 2019.

[211] Z.-X. Xia, K. W. Leung, N. Yang, and K. Lu, "Compact dual-frequency antenna array with large frequency ratio," *IEEE Transactions on Antennas and Propagation*, vol. 69, no. 4, pp. 2031–2040, 2020.

[212] M. Xue, W. Wan, Q. Wang, and L. Cao, "Low-profile wideband millimeter-wave antenna-in-package suitable for embedded organic substrate package," *IEEE Transactions on Antennas and Propagation*, vol. 69, no. 8, pp. 4401–4411, 2021.

[213] C. Zhou, W. Yang, Q. Xue, Y. Liu, Y. Xu, and W. Che, "Millimeter-wave wideband dual-polarized ltcc antenna array based on metasurfaces for beam-scanning applications," *IEEE Transactions on Antennas and Propagation*, 2022.

[214] M. Imbert, J. Romeu, M. Baquero-Escudero, M.-T. Martinez-Ingles, J.-M. Molina-Garcia-Pardo, and L. Jofre, "Assessment of ltcc-based dielectric flat lens antennas and switched-beam arrays for future 5g millimeter-wave communication systems," *IEEE Transactions on Antennas and Propagation*, vol. 65, no. 12, pp. 6453–6473, 2017.

[215] J. Qian, M. Tang, Q. Chen, Y.-P. Zhang, and J. Mao, "Integration of s/ka/d-band antennas in ltcc with a cylindrical radome for triband applications," *IEEE Transactions on Antennas and Propagation*, vol. 67, no. 9, pp. 5781–5789, 2019.

[216] H.-T. Chou, S.-J. Chou, J. D. Deng, C.-H. Chang, and Z.-D. Yan, "Ltcc-based antenna-in-package array for 5g user equipment with dual-polarized endfire radiations at millimeter-wave frequencies," *IEEE Transactions on Antennas and Propagation*, vol. 70, no. 4, pp. 3076–3081, 2021.

[217] Y. Zhang, W. Yang, Q. Xue, J. Huang, and W. Che, "Broadband dual-polarized differential-fed filtering antenna array for 5g millimeter-wave applications," *IEEE Transactions on Antennas and Propagation*, vol. 70, no. 3, pp. 1989–1998, 2021.

[218] J. Zhu, Y. Yang, C. Chu, S. Li, S. Liao, and Q. Xue, "Low-profile wideband and high-gain ltcc patch antenna array for 60 ghz applications," *IEEE Transactions on Antennas and Propagation*, vol. 68, no. 4, pp. 3237–3242, 2019.

[219] F. F. Manzillo, M. Śmierzchalski, L. Le Coq, M. Ettorre, J. Aurinsalo, K. T. Kautio, M. S. Lahti, A. E. Lamminen, J. Säily, and R. Sauleau, "A wide-angle scanning switched-beam antenna system in ltcc technology with high beam crossing levels for v-band communications," *IEEE Transactions on Antennas and Propagation*, vol. 67, no. 1, pp. 541–553, 2018.

[220] S. Liao and Q. Xue, "Dual polarized planar aperture antenna on ltcc for 60-ghz antenna-in-package applications," *IEEE Transactions on Antennas and Propagation*, vol. 65, no. 1, pp. 63–70, 2016.

[221] J. Zhu, Y. Yang, S. Li, S. Liao, and Q. Xue, "Single-ended-fed high-gain ltcc planar aperture antenna for 60 ghz antenna-in-package applications," *IEEE Transactions on Antennas and Propagation*, vol. 67, no. 8, pp. 5154–5162, 2019.

[222] Y. Shi, W. Feng, H. Wang, W. Che, Q. Xue, J. Wang, J. Zhang, X. Qian, M. Zhou, and B. Cao, "Novel *w*-band ltcc transition from microstrip line to ridge gap waveguide and its application in 77/79 ghz antenna array," *IEEE Transactions on Antennas and Propagation*, vol. 67, no. 2, pp. 915–924, 2018.

[223] X.-C. Wang, C.-W. Yu, D.-C. Qin, and W.-Z. Lu, "*w*-band high-gain substrate integrated cavity antenna array on ltcc," *IEEE Transactions on Antennas and Propagation*, vol. 67, no. 11, pp. 6883–6893, 2019.

[224] B. Cao, Y. Shi, and W. Feng, "W-band ltcc circularly polarized antenna array with mixed u-type substrate integrated waveguide and ridge gap waveguide feeding networks," *IEEE Antennas and Wireless Propagation Letters*, vol. 18, no. 11, pp. 2399–2403, 2019.

[225] Laboratory for high frequency LTCC circuits (LCAF) "https://ltcc.webs.upv.es/".